The design and analysis of radial inflow turbines implemented within low temperature organic Rankine cycles

Martin White

Submitted for the degree of Doctor of Philosophy
City University London
School of Mathematics, Computer Science & Engineering
Department of Mechanical Engineering & Aeronautics
September 2015

This page is left intentionally blank.

Contents

List of Tables viii

List of Figures xiv

Nomenclature xxv

1 Introduction 1

1.1 Background . . . 1
1.1.1 Thermodynamics of the organic Rankine cycle . . . 1
1.1.2 Applications . . . 3
1.1.3 Expanders for organic Rankine cycles . . . 4
1.2 Project scope and objectives . . . 5
1.3 Thesis structure and scientific contributions . . . 6
1.4 Publications . . . 8

2 Literature Review 11

2.1 Introduction . . . 11
2.2 Modelling the organic Rankine cycle . . . 11
2.2.1 Thermodynamic analysis of the organic Rankine cycle . . . 11
2.2.2 Working fluid selection . . . 14
2.2.3 Thermodynamic modelling . . . 18
2.2.4 Component modelling . . . 22
2.2.5 Optimisation . . . 25
2.3 Expanders for organic Rankine cycles . . . 27
2.3.1 Turboexpanders . . . 27
2.3.2 Volumetric expanders . . . 29
2.3.3 Summary of commercial expanders . . . 30
2.3.4 Summary of experimental expanders . . . 33
2.4 Design and analysis of ORC radial inflow turbines . . . 37
2.4.1 Background theory . . . 37
2.4.2 Design of ORC radial inflow turbines . . . 46
2.4.3 CFD studies on ORC turbines . . . 48
2.4.4 Off-design modelling of ORC radial inflow turbines . . . 50
2.5 Conclusions . . . 52

3 Thermodynamic modelling and optimisation **55**
3.1 Introduction . . . 55
3.2 Structure of the ORC model . . . 56
3.3 Thermodynamic modelling . . . 57
3.3.1 Cycle analysis . . . 60
3.3.2 Pump modelling . . . 62
3.3.3 Evaporator modelling . . . 63
3.3.4 Turbine modelling . . . 69
3.3.5 Condenser modelling . . . 72
3.4 Optimisation . . . 73
3.4.1 Optimisation strategy . . . 74
3.4.2 Defining the objective function . . . 74
3.5 Optimisation case study . . . 79
3.5.1 Optimisation setup . . . 79
3.5.2 Verification of the objective function . . . 81
3.5.3 Working fluid selection . . . 87
3.5.4 Optimisation results . . . 87
3.6 Conclusion . . . 96

4 Radial turbine development **97**
4.1 Introduction . . . 97
4.2 Rotor one-dimensional design . . . 98
4.2.1 Rotor inlet thermodynamics . . . 101
4.2.2 Rotor outlet thermodynamics . . . 102
4.2.3 Rotor outlet geometry . . . 103
4.2.4 Rotor inlet geometry . . . 106
4.3 Rotor three-dimensional design . . . 106
4.3.1 Rotor three-dimensional construction . . . 107
4.3.2 Prediction of meanline parameters . . . 107
4.4 Stator design . . . 109
4.4.1 Stator outlet . . . 109
4.4.2 Stator throat . . . 110
4.4.3 Stator inlet . . . 112
4.4.4 Stator design inputs . . . 112
4.5 Case study: Ideal gas turbine . . . 114
4.6 Case study: Subsonic ORC turbine . . . 117
4.6.1 ORC turbine design . . . 117
4.6.2 ORC turbine CFD simulation . . . 127
4.6.3 Validation of turbine design . . . 138
4.6.4 Validation of the prediction of meanline parameters . . . 146
4.7 Conclusion . . . 150

5 Application of similitude theory to ORC turbines 151
5.1 Introduction . . . 151
5.2 Similitude theory . . . 152
5.3 ORC turbine performance mapping . . . 158
5.4 Similitude scaling case study: R245fa . . . 161
5.5 Similitude scaling case studies: R123 and R1234yf . . . 176
5.6 Conclusions . . . 179

6 Implementation of turbine performance map 183
6.1 Introduction . . . 183
6.2 Turbine modelling . . . 184
6.2.1 Windage losses . . . 184
6.2.2 Diffuser design . . . 185
6.2.3 Diffuser performance analysis . . . 188
6.2.4 Updated turbine performance map . . . 189
6.3 Thermodynamic modelling . . . 193
6.4 R245fa case study . . . 195
6.5 Alternative working fluids . . . 203
6.6 Conclusions . . . 207

7 Conclusions and recommendations for further work 209
7.1 Conclusions . . . 209
7.1.1 Development of the ORC model . . . 210
7.1.2 Development of the turbine design model . . . 210
7.1.3 Investigating the off-design behaviour of ORC turbines . . . 211
7.2 Further work . . . 212
7.2.1 Improvements to the ORC model . . . 212
7.2.2 Improvements to the turbine model and candidate design . . . 213
7.2.3 Improvements to off-design modelling of ORC turbines . . . 214
7.2.4 Development of experimental test rigs . . . 214

Bibliography 215

Appendix A Heat transfer and pressure drop correlations 229
A.1 Heat transfer correlations . . . 229
A.2 Pressure drop correlations . . . 233

Appendix B Turbine three-dimensional design 237
B.1 Construction of the rotor . . . 237
B.2 Construction of the stator . . . 241

Appendix C Validation of turbine design model for ideal gases 243
C.1 Ideal gas turbine design . . . 243
C.2 CFD validation . . . 247

Appendix D Cubic equations of state **253**

List of Tables

2.1 Common ORC fluids as suggested by Colonna et al. (2015) 15

3.1 Sizing optimisation binary matrix. 77
3.2 Sizing optimisation study fixed inputs. 80
3.3 Optimisation study variables. 80
3.4 Reference values for the investigation of objective function 1. 81
3.5 Reference values for the investigation of objective function 2. 84
3.6 Sizing optimisation reference values. 86
3.7 Sizing optimisation screened working fluids. 88
3.8 Sizing optimisation results. 89

4.1 Summary of the default stator design inputs used during turbine development. 114
4.2 Thermodynamic inputs for the air turbine case study. 115
4.3 Comparison between of the intended design and CFD results for the air turbine case study. 115
4.4 Thermodynamic inputs for the R245fa turbine case study. 118
4.5 Inputs into the rotor design program for the R245fa turbine case study. . . 123
4.6 Outputs from the rotor design program for the R245fa turbine case study. . 124
4.7 Rotor geometrical inputs for the R245fa turbine case study. 126
4.8 Stator geometry for the R245fa turbine case study. 127
4.9 Comparison between the intended design and the steady-state CFD results for the R245fa turbine case study. 137
4.10 Sensitivity analysis considering the number of time steps per blade pass required for the unsteady design point CFD simulation. 138

5.1 Thermodynamic summary of the operating points selected for the R245fa similitude theory study. 161
5.2 Comparison between steady and unsteady CFD simulations for case 8. . . . 165
5.3 Comparison between total inlet and static throat thermodynamic conditions. 168
5.4 Reduced blade Mach numbers (N/a^*) obtained using the updated similitude theory for the CFD results that were obtained at rotational speeds that maintained the original blade Mach numbers (N/a_{01}). Results are expressed as a percentage of the reduced blade Number at the original turbine design point. 169
5.5 Turbine inlet conditions for the R123 and R1234yf similitude studies. 178

6.1 Fixed inputs for the R245fa case study. 196
6.2 Summary of optimal operating points for R245fa case study. 201

C.1 Air parametric study inputs. 243
C.2 Turbomachinery inputs for the air turbine case study. 244
C.3 Outputs from the design program for the air turbine case study. 245
C.4 Rotor geometrical inputs for the air turbine case study. 245
C.5 Summary of the design point CFD results for the air turbine case study. . . 248

List of Figures

1.1 Schematic of the simple subcritical Rankine cycle. 2

2.1 Schematic of the various ORC power cycles represented on a T-s diagram. . 13
2.2 Schematic of the recuperated Rankine cycle. 14
2.3 Classification of fluids according to the slope of their saturated vapour dome. Fluids with negative, infinite and positive gradients are classified as 'wet', 'isentropic' and 'dry' fluids respectively. 16
2.4 Schematic of the ORC evaporator heat transfer process and the location of the pinch point. 22
2.5 Three-dimensional model of the screw expanders rotors (Smith et al., 2005). 29
2.6 Schematic of the operation of a scroll expander. 30
2.7 Summary of commercial ORC systems in terms of the generated power. . . 31
2.8 Summary of small-scale experimental ORC systems in terms of the generated power and expander efficiency. 36
2.9 Geometry of the radial turbine. 38
2.10 Expansion process through a turbine shown on an enthalpy-entropy diagram. 38
2.11 Geometry of the radial turbine rotor and velocity triangles. 39

3.1 Schematic of the ORC thermodynamic model. 56
3.2 The subritical, superheated ORC represented on a T-s diagram along with the heat source and heat sink temperature profiles, and the designated notation. 58
3.3 Sensitivity of the cycle performance to variations in the pump efficiency. . . 63
3.4 Schematic of the double-pipe counter-flow heat exchanger and the designated notation. 65
3.5 Schematic of the discretisation process applied to the preheating stage of the ORC. 67
3.6 Investigation of the number of discretised elements required for the heat exchanger model. 68
3.7 Variation in radial turbine isentropic efficiency with specific speed and specific diameter (Watson and Janota, 1982). 70
3.8 Comparison between using total and static conditions when estimating rotational speed and rotor diameter using specific speed and specific diameter. 72
3.9 ORC optimisation strategy. 75
3.10 Breakdown of initial objective function for four different cases. 82

3.11 Breakdown of modified objective function for seven different cases. 84
3.12 Comparison of the different optimisation cases considered for objective function 1 and objective function 2 in terms of net work and total heat exchanger area. The numbers represent the corresponding case number. 85
3.13 Variation in ORC performance with condensation pressure resulting from the sizing optimisation; A) turbine work; B) pump work; C) net work; D) pressure ratio. 90
3.14 Sizing optimisation results for the 15 working fluids considered. (Bars indicate the breakdown of the objective function; crosses indicate the condensation pressures. 91
3.15 Breakdown of the objective function from the sizing optimisation with the 15 working fluids considered. 92
3.16 Evaporator and condenser areas that resulted from the sizing optimisation for the 15 working fluids considered. 92
3.17 Turbine rotational speed and rotor diameter required for the optimised cycles that resulted from the sizing optimisation. 93

4.1 Schematic showing the geometrical area blocked by the blade at the rotor outlet. 105
4.2 Schematic of the stator geometry and airfoil definition. 113
4.3 Comparison between the intended design and CFD velocity triangles for the air turbine at the rotor leading and trailing edges. 116
4.4 Relationship between α_4, β_4 and Ma_4 to ensure no swirl at the rotor outlet for the ORC turbine. 120
4.5 Variation in Φ with ϵ and ϕ at different α_4 values. 121
4.6 Variation in ξ with ϵ and ϕ at different α_4 values. 121
4.7 Variation in N_s with ϵ and ϕ at different values of λ. 122
4.8 Variation in meridional rotor profiles with different values of λ. 123
4.9 Rotor quasi-normals and passage area distribution for the R245fa turbine. . 125
4.10 Camberline distribution and thickness distributions for the R245fa turbine. 126
4.11 Percentage deviation between the pressure predicted using the most common cubic equations of state and the actual pressure calculated using REFPROP for R245fa. 130
4.12 Percentage deviation between enthalpy predicted using the most common cubic equations of state and the actual enthalpy calculated using REFPROP for R245fa. 131
4.13 Grid independence study for the ORC turbine stator. 133
4.14 Grid independence study for the ORC turbine rotor with clearance gap. . . 134
4.15 Sensitivity study on the thermodynamic property table size used for CFD simulations. 134
4.16 Stator mesh for the final ORC stator design, consisting of 4.3×10^5 nodes. . 135
4.17 Rotor mesh of the final ORC rotor design, consisting of 8.5×10^5 nodes. . . 135

4.18 Determining where along the rotor blade path length the laminar-turbulent transition occurs. . . . 136
4.19 Comparison between the intended design and CFD velocity triangles at the rotor leading and trailing edges for the R245fa turbine. . . . 139
4.20 Deviation in rotor inlet velocity triangle with variations in α_4 and η_N. . . . 139
4.21 Contour of relative Mach number and relative velocity vectors on the mid-span of the R245fa turbine. . . . 142
4.22 R245fa stator blade loading at 50% span. . . . 143
4.23 R245fa blade loading at 10%, 50% and 90% span. . . . 144
4.24 Comparison between the velocity distributions predicted by the one-dimensional model and the results obtained for the no clearance CFD simulation. . . . 147
4.25 Comparison between blade angle and the flow angles for the clearance and no clearance CFD simulations. . . . 148
4.26 Contours of relative Mach number at the rotor outlet for the R245fa turbine. Top: no clearance; Bottom: clearance. . . . 149

5.1 Deviation in Reynolds number with variations in turbine total inlet conditions for R245fa assuming that the blade Mach number has been conserved. 155
5.2 Variation in thermodynamic properties over a range of operating conditions for superheated R245fa between operating point and design point. A) Percentage deviation in density. B) Percentage deviation in speed of sound. C) Percentage deviation in dynamic viscosity. D) Variation in compressibility factor. . . . 157
5.3 Variation of reduced flow coefficient with reduced head coefficient at 80%, 100% and 120% design blade Mach number for the candidate ORC turbine. 160
5.4 Variation of isentropic total-to-static efficiency with reduced head coefficient at 80%, 100% and 120% design blade Mach number for the candidate ORC turbine. . . . 160
5.5 Turbine total inlet conditions for the 8 cases defined for the R245fa similitude theory study. . . . 162
5.6 Comparison between the flow coefficient predicted by similitude theory and the flow coefficient found from the CFD results for the R245fa operating points. . . . 163
5.7 Comparison between the isentropic total-to-static isentropic efficiency predicted by similitude theory and the efficiency found from the CFD results for the R245fa operating points. . . . 163
5.8 Comparison between the CFD results for R245fa cases 6-8 and the non-dimensional performance curves used during the application of similitude theory. A) Case 6; B) Case 7; C) Case 8. . . . 167
5.9 Variation of reduced flow coefficient with reduced head coefficient at 50% and 150% design blade Mach number for the candidate ORC turbine. . . . 170
5.10 Variation of isentropic total-to-static efficiency with reduced head coefficient at 50% and 150% design blade Mach number for the candidate ORC turbine. 170

5.11 Interpolation method to determine turbine performance at alternative blade Mach numbers. 171
5.12 Comparison between the flow coefficient predicted by the updated similitude theory and the flow coefficient found from the CFD results for the R245fa operating points. 173
5.13 Comparison between the isentropic total-to-static isentropic efficiency predicted by the updated similitude theory and the efficiency found from the CFD results for the R245fa operating points. 173
5.14 Summary of the stator vane performance over a range of flow coefficients. Bottom group of data points refers to the throat whilst the top group of data points refers to the stator outlet set at the rotor inlet radius. The dashed lines represent the change from subsonic to supersonic operation. . . 174
5.15 Distribution of Mach number within the turbine stator for case 8 with a flow coefficient of 2.87×10^{-4}. 175
5.16 Comparison between the flow coefficient predicted by the updated similitude theory and the flow coefficient found from the CFD results for the R245fa operating points. Based on total-to-total conditions. 177
5.17 Comparison between the isentropic total-to-total isentropic efficiency predicted by the updated similitude theory and the efficiency found from the CFD results for the R245fa operating points. 177
5.18 Turbine inlet conditions for the R123 and R1234yf similitude studies overlaid onto contours showing the percentage deviation in Reynolds number. . 179
5.19 Comparison between the flow coefficient predicted by the updated similitude theory and the flow coefficient from the CFD results for the R123 operating points. 180
5.20 Comparison between the isentropic total-to-static isentropic efficiency predicted by the updated similitude theory and the efficiency found from the CFD results for the R123 operating points. 180
5.21 Comparison between the flow coefficient predicted by the updated similitude theory and the flow coefficient from the CFD results for the R1234yf operating points. 181
5.22 Comparison between the isentropic total-to-static isentropic efficiency predicted by the updated similitude theory and the efficiency found from the CFD results for the R1234yf operating points. 181

6.1 Schematic of the defined diffuser geometry. 186
6.2 Parametric study on the effect of the diffuser area ratio on turbine performance. 188
6.3 Updated turbine performance map showing relationship between the reduced head coefficient and reduced flow coefficient for different reduced rotational speeds. 192

6.4 Updated turbine performance map showing relationship between the reduced head coefficient and turbine efficiency for different reduced rotational speeds. . . . 192
6.5 Variation in net power produced as a function of pressure ratio for different heat source conditions. Top: fixed heat source mass flow rate of 1.0kg/s; Bottom: fixed heat source temperature of 380K. . . . 195
6.6 Contour of the net power produced by an ORC operating with the candidate turbine as a percentage of the maximum potential power. Heat source of water at 380K, and R245fa as working fluid. The black lines indicate the heat source mass flow rate in kg/s, whilst the black dot represents the point of optimal operation. . . . 197
6.7 The optimal percentage of net work and the corresponding reduced rotational speed for the candidate turbine operating with R245fa for a heat source of 380K over a range of ORC pressure ratios. . . . 198
6.8 Contour of the net power produced by an ORC operating with the candidate turbine as a percentage of the maximum potential power. Heat source of water at 360K, and R245fa as working fluid. The black lines indicate the heat source mass flow rate in kg/s, whilst the black dot represents the point of optimal operation. . . . 200
6.9 Contour of the net power produced by an ORC operating with the candidate turbine as a percentage of the maximum potential power. Heat source of water at 400K, and R245fa as working fluid. The black lines indicate the heat source mass flow rate in kg/s, whilst the black dot represents the point of optimal operation. . . . 200
6.10 Contour plot showing the percentage of maximum power that can be obtained using the candidate turbine design operating with R245fa for a range of heat source conditions. The black lines indicate the percentage of the design reduced rotational speed, whilst the black dots correspond to the optimal points discussed in Table 6.2. . . . 202
6.11 Cycle analysis results showing the heat source mass flow rates that can be accommodated by an ORC utilising the candidate turbine at each combination of heat source temperature and working fluid. Top left: summary of all results; top right: 360K; bottom left; 380K; bottom right; 400K. . . . 204
6.12 Results from each combination of heat source temperature and working fluid overlaid onto the turbine performance map. . . . 205
6.13 Cycle analysis results showing variation in cycle at the three different heat source temperatures. . . . 206

A.1 Simplified schematic of the evaporator geometry. . . . 232

B.1 Schematic of the hub and shroud meridional profiles. . . . 238

C.1 Camberline distribution and thickness distributions for the air turbine. . . . 246
C.2 Rotor quasi-normals and passage area distribution for the air turbine. . . . 247

C.3 Air stator blade loading at 50% span. 248
C.4 Air blade loading at 10%, 50% and 90% span. 249
C.5 Contour of relative Mach number and relative velocity vectors on the mid-span of the air turbine. 250
C.6 Comparison between the velocity distributions predicted by the one-dimensional model and the results obtained for the no clearance simulation. 250
C.7 Comparison between the blade angle and flow angles for the for the clearance and no clearance CFD simulations. 251

Acknowledgements

First and foremost I would like to thank my supervisor, Professor Abdulnaser Sayma, for his support during my time completing my PhD at City University London. Our discussions, and his regular advice and recommendations, have enabled me to develop an extensive knowledge in the relevant fields alongside developing important skills for my future professional career.

I would also like to thank the university for their continued support which enabled me to both complete my studies whilst attending a number of international conferences, and to the UK Engineering Physical Sciences Research Council (EPSRC) for funding this research.

I would also like to thank my colleagues, and fellow PhD students, whose interesting non-technical discussions often provided a welcome break from research.

Lastly, special thanks go to my family and friends, and in particular to Fabienne for her support during these last three years. In particular, for her understanding when I decided to return to university to pursue further study.

This page is left intentionally blank.

Declaration

I hereby declare that this thesis has not been and will not be submitted in whole or in part to another University for the award of any other degree. I also grant powers of discretion to the University Librarian to allow the thesis to be copied in whole or in part without further reference to the author. This permission covers only single copies made for study purposes, subject to normal conditions of acknowledgement.

Signature:

Martin White

This page is left intentionally blank.

Abstract

Over recent years, with growing concern over climate change, the need for energy which is sustainable, economical and in line with legalisation has led to a substantial surge of interest in organic Rankine cycles (ORC). With the ability to convert low temperature heat sources into power, ORC technology is at the forefront of many sustainable technologies such as biomass, solar, geothermal and waste heat recovery. Despite successful commercialisation for large-scale systems (> 200 kW_e), more development is required at the small-scale to realise its potential. For low temperature ($< 150°C$), low power applications, volumetric expanders are the preferred choice. However, for a 10 kW_e system, a well-designed radial inflow turbine could achieve a higher efficiency, and bridge an observed gap between the output powers of existing volumetric expander systems. This thesis investigates the design and analysis of radial inflow turbines for this application.

A thermodynamic ORC model is first developed, which combines cycle analysis with component design. This model is coupled with a multi-objective optimisation, and a novel objective function is developed that considers the trade-off between system performance and system complexity. Following a cycle analysis case study, a radial inflow turbine design method for ORC turbines is developed which extends existing ideal gas design methods to be applicable for real gases. Two candidate turbine designs are developed and are validated using computational fluid dynamics (CFD).

For small-scale systems to be economically feasible it is reasonable to assume that the same turbine will be implemented within a number of different systems. This requires off-design models, and the suitability of using non-dimensional performance maps, obtained using similitude theory, has been investigated using further CFD studies. This has led to the development of a modified similitude theory, suitable for subsonic ORC turbines. This modified similitude theory has been implemented within another thermodynamic model, and the results from a case study show how the same turbine can be effectively utilised within a number of different ORC systems. This is done by selecting a working fluid to match the available heat source.

Overall, this thesis successfully demonstrates the development of modelling methods for small-scale low temperature ORCs utilising radial inflow turbines. This has considered design and off-design performance models, and ultimately the results demonstrate how the economy of scale of these systems can be improved, aiding in the future commercialisation of the technology.

This page is left intentionally blank.

Nomenclature

Greek Symbols

α	Absolute flow angle	$^\circ$
α_c	Local heat transfer coefficient (heat sink fluid)	W m^{-2} K^{-1}
α_h	Local heat transfer coefficient (heat source fluid)	W m^{-2} K^{-1}
α_w	Local heat transfer coefficient (ORC working fluid)	W m^{-2} K^{-1}
β	Relative flow angle/blade angle	$^\circ$
ϵ	Rotor radius ratio	
η	Isentropic efficiency	%
η_o	ORC cycle efficiency	%
Γ	Rotor axial length ratio	
γ_3	Stator setting angle	$^\circ$
λ	Rotor outlet hub/tip radius ratio	
μ	Dynamic viscosity	Pa s
ν	Isentropic velocity ratio	
ω	Rotational speed	rad s^{-1}
Φ	Flow coefficient	
ϕ	Rotor relative velocity ratio	
Ψ	Blade loading coefficient	
ρ	Density	kg m^{-3}
τ	Torque	N m
θ	Camber angle	$^\circ$
ξ	Rotor meridional velocity ratio	

ζ	Turbomachinery loss coefficient	

Roman Symbols

Δh	Change in enthalpy	J kg^{-1}
ΔP	Pressure drop	Pa
$\Delta T_{\log}$	Log-mean temperature difference	K
ΔT_{sh}	Degree of superheat	K
$\dot{m}$	Mass flow rate	kg s^{-1}
BK	Rotor blockage factor	
Ma	Mach number	
Nu	Nusselt number	
PP	Heat exchanger pinch point	K
PR	Pressure ratio	
Pr	Prandtl number	
Re	Reynolds number	
A	Area	m^2
a	Speed of sound	m s^{-1}
b	Rotor blade height	m
c	Absolute velocity	m s^{-1}
c_{p}	Specific heat capacity at constant pressure	J kg^{-1}
c_{s}	Spouting velocity	m s^{-1}
C_{w}	Windage torque loss coefficient	
D	Rotor diameter	m
d_{h}	Heat exchanger hydraulic diameter	m
d_{i}	Tube inner diameter	m
d_{o}	Shell inner diameter	m
D_{s}	Specific diameter	
F	Martinelli parameter	
f	Friction factor	

g	Optimisation importance factors	
h	Enthalpy	J kg^{-1}
I	Rothalpy	J kg^{-1}
k	Thermal conductivity	W m^{-1} K^{-1}
K_{I}	Stator-rotor interspace parameter	
L	Length	m
M	Meridional distance	m
N	Rotational speed	rpm
n	Heat exchanger discretisation number	
N_{s}	Specific speed	
o	Throat width	m
P	Pressure	Pa
Q	Heat input	J
q	Vapour quality	
R	Specific gas constant	J kg^{-1}
r	Radius	mm
S	Pitch	m
s	Entropy	J kg^{-1} K^{-1}
T	Temperature	K
t	Thickness	m
U	Overall heat transfer coefficient	W m^{-2} K^{-1}
u	Blade velocity	m s^{-1}
V	Volumetric flow rate	m^3 s^{-1}
W	Work	J
w	Relative velocity	m s^{-1}
X	Exergy	J
Y	Total pressure loss coefficient	
Z	Blade count	

z	Axial location	m

Subscripts

$'$	Relative conditions
$*$	Choked conditions
0	Total conditions
θ	Tangential velocity component
01-06	Turbine locations (total thermodynamic properties)
1-6	Turbine locations (static thermodynamic properties)
5h	Rotor blade hub
5t	Rotor blade tip
c	Heat sink
c1-c3	Heat sink locations
co	Condensation
ev	Evaporation
h	Heat source
h1-h4	Heat source locations
l	Saturated liquid
le	Leading edge
m	Meridional velocity component
max	Maximum
N	Stator (nozzle)
n	Net
p	Pump
pc	Precool
ph	Preheat
q	Rotor quasi-normal
R	Rotor
ref	Reference value

s	Conditions following an isentropic process
sh	Superheat
t	Turbine
te	Trailing edge
th	Throat
ts	Total-to-static
tt	Total-to-total
v	Saturated vapour
w	ORC working fluid
w1-w4	ORC working fluid locations
wall	Heat exchanger wall

This page is left intentionally blank.

Chapter 1

Introduction

1.1 Background

The conventional steam Rankine cycle has long been in use to convert heat into mechanical power. It is therefore understandable that as our understanding has grown, the interest in using alternative working fluids has also grown. This has given rise to the organic Rankine cycle (ORC). The use of organic fluids permits lower temperature heat sources, typically between 80°C and 350°C, to be converted into mechanical power, with potential applications such as biomass combined heat and power, geothermal, solar power and waste heat recovery. In a recent study, Colonna et al. (2015) reviewed the evolution of ORC technology and accredited T. Howard as first patenting the idea in 1826. Much of the more recent growth of ORC technology is attributed to work conducted in Italy in the 1970's and 1980's (Angelino et al., 1984), which ultimately led to the successful commercialisation of large-scale ORC systems with power outputs in the order of a few hundred kilowatts (kW) and above (Turboden, 2013). In the last decade with increasing concern over climate change and the need for sustainable, efficient power systems, there has been a massive surge of interest in ORC technology, particularly at the smaller-scale. However, more development is still required to achieve successful commercialisation.

1.1.1 Thermodynamics of the organic Rankine cycle

The operating principle of the organic Rankine cycle directly follows the operating principle of the conventional Rankine cycle used in steam power plants and a schematic of a simple subcritical Rankine cycle is shown in Figure 1.1. The saturated or subcooled liquid

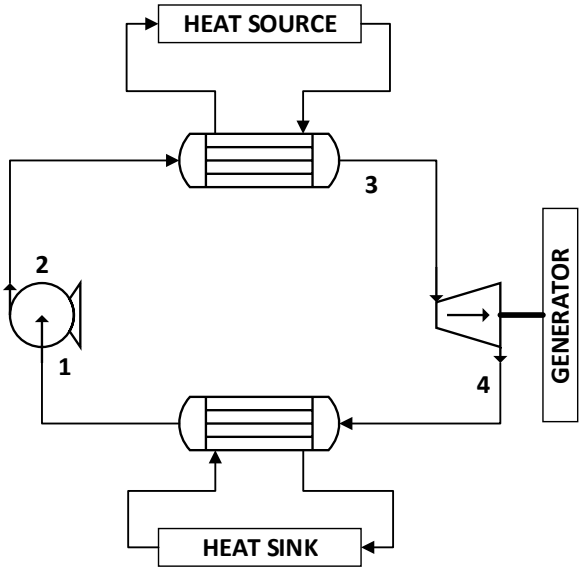

Figure 1.1: Schematic of the simple subcritical Rankine cycle.

is first pressurised in a pump, increasing the fluid pressure (1 to 2). The working fluid then passes through an evaporator where it absorbs the heat from the heat source. This process raises the temperature of the working fluid to the saturation temperature, fully evaporates the fluid before heating it to a superheated state (2 to 3). This high temperature, high pressure vapour then expands across an expander producing mechanical power, which can be converted into electricity using a generator (3 to 4). The working fluid then passes through a condenser where heat is rejected to a heat sink. During this process the working fluid is cooled to a saturated vapour and then fully condensed (4 to 1), before the cycle can then repeat.

The thermodynamic analysis of the Rankine cycle is given in more detail in Chapter 2, but ultimately the cycle performance is a function of four independent design variables:

- The condensation temperature
- The pressure ratio (i.e. the ratio of the evaporation and condensation pressures)
- The amount of superheat
- The working fluid

For a given working fluid the condensation temperature immediately determines the condensation pressure, whilst the pressure ratio then supplies the evaporation pressure and evaporation temperature. The amount of superheat then determines the expander inlet temperature, and the cycle is fully defined. An important indicator of the maximum

achievable efficiency of a thermodynamic cycle is the Carnot efficiency η_{carnot} (Equation 1.1). This says that to achieve the maximum efficiency the temperature difference between the hot and cold temperatures, denoted T_{h} and T_{c} respectively, should be maximised. This corresponds to minimising the condensation temperature, whilst maximising the pressure ratio. Ultimately, this means that for a higher heat source temperature, the cycle efficiency can be improved by increasing the pressure ratio. The Carnot efficiency also highlights a fundamental issue with low temperature ORCs, in that the small difference between the hot and cold temperatures inevitably leads to a high absolute temperature ratio ($T_{\text{c}}/T_{\text{h}}$), and low cycle efficiencies.

$$\eta_{\text{carnot}} = 1 - \frac{T_{\text{c}}}{T_{\text{h}}} \tag{1.1}$$

It is also important to note that the design variables also impact component design. For example, low condensation temperatures, and high pressure ratios can result in small temperature differences within the condenser and evaporator respectively, resulting in large heat exchangers. Similarly, the choice of working fluid can also significantly impact component design. These aspects are discussed comprehensively in Chapter 2, but ultimately it is clear that a trade-off between performance and system complexity exists, and that a suitable optimisation process is required to arrive at the optimal system configuration for a particular application.

1.1.2 Applications

The key advantage of the ORC over a conventional steam Rankine cycle is that it can convert lower temperature heat sources into mechnical power more economically. This opens up a wide range of applications that would not have been possible using steam. At this point it is also helpful to make the distinction between low temperature ($< 150°$C), and medium-to-high temperature applications ($> 150°$C). The possible applications are well discussed within a number of review papers (Tchanche et al., 2011; Vélez et al., 2012; Bao and Zhao, 2013; Quoilin et al., 2013; Colonna et al., 2015), but can be summarised as follows:

- Biomass/combined heat and power (CHP)
- Geothermal

- Ocean thermal energy conversion (OTEC)
- Solar energy
- Waste heat recovery

Details on current commercial ORC systems are provided in Chapter 2, however, generally speaking, the technology has been successfully commercialised for power outputs ranging from around 200 kW up to a few mega-watts, and these are typically implemented within biomass, geothermal and waste heat recovery applications. The implementations within biomass and waste heat recovery applications tend to operate at high temperatures, whilst the geothermal plants typically utilise low temperature heat sources.

At the smaller-scale, ORC technology has not yet been fully commercialised, although potential applications can again be classified into low and high temperature applications. With regards to high temperature applications there is interest in the development of domestic-scale biomass-fired ORCs for combined heat and power (Qiu et al., 2012), and for high temperature waste heat recovery from automotive internal combustion engines (Lang et al., 2013). There is of course also the opportunity to recover heat from the cooling water of these internal combustion engines using low temperature ORCs. More generally, the opportunity to recover waste heat is vast, with suitable heat sources ranging significantly in terms of both temperature and the thermal energy available (Campana et al., 2013; Department of Energy and Climate Change, 2014). Alongside low temperature waste heat recovery, there is also a significant interest in low temperature ORCs to convert solar energy into useful power (Orosz et al., 2009). These low cost systems can deliver sustainable, distributed energy in remote areas and developing countries.

Currently the successful commercialisation of ORC technology at this scale can only be realised by developing technical solutions which will not only improve the performance of existing systems, but can also improve the current economy of scale.

1.1.3 Expanders for organic Rankine cycles

The expander is the most critical component within an ORC since it generates the mechanical power. In general, there are two types of expanders, namely turboexpanders and volumetric expanders. Turboexpanders rely on the dynamic action of a rotating rotor, whilst volumetric expanders achieve expansion of the fluid through the cyclic change in volume of an expansion chamber.

Turbomachines are a technically mature technology, are compact, lightweight and can achieve high expansion efficiencies. However, at the smaller scale the required rotational speed can increase which may require high speed generators, whilst lower efficiencies can result from increased relative clearance gaps. By comparison, volumetric expanders have historically been obtained from the reverse operation of existing off-the-shelf compressors, which offers a low cost option, with lower rotational speeds than turboexpanders. However, the efficiency of these volumetric machines is inferior to turbomachines, which, considering the already low Carnot efficiency of ORCs, could have a significant effect on system performance.

Expander selection can be linked to the heat source temperature and power output. Although dependent on the working fluid, high temperature ORCs are generally characterised by high pressure ratios, where expansion can only be achieved using turbomachines. Similarly, turbomachines are almost exclusively used for all high power applications. For low temperature, low power applications there is a significant interest in volumetric expanders. This can mainly be attributed to the benefits of low cost and ease of installation, without giving much consideration to the expander efficiency. It is also worth highlighting that Chapter 2 discusses two different types of volumetric expanders, namely screw and scroll expanders. This review demonstrates that there exists a gap where the suitability of volumetric expanders has not been confirmed; scroll expanders have not been tested above a few kW, whilst screw expanders have not been tested below 20 kW.

1.2 Project scope and objectives

The aim of this project is to investigate and develop design and analysis modelling methods for turboexpanders implemented within small-scale, low temperature ORCs. Not only can the performance of a turboexpander eclipse the performance of existing volumetric expanders, but it can bridge an observed gap where the suitability of screw and scroll expanders have yet to be confirmed. This research project was part funded through the EPSRC and was originally motivated by the request of an industrial partner that was interested in developing ORC technology with power outputs between about 10 kW and 30 kW. Unfortunately, unforeseen circumstances led this partner to withdraw, however EPSRC funding permitted the research project to continue. This allowed the project to

investigate the design and analysis of ORC turboexpanders at a more fundamental level. The specific objectives for this project were set as follows:

- To design and implement an ORC design tool that builds on existing models within the literature by combining thermodynamic analysis, component design and multi-objective optimisation into a single ORC model.
- To design and implement a turbine design model suitable for the development of ORC specific turboexpanders. This model will be used to develop and validate a candidate turbine design for small-scale low temperature ORCs.
- To investigate the off-design behaviour of ORC turboexpanders, and to develop suitable models to predict off-design behaviour within ORC thermodynamic models.

Ultimately through the completion of this project, and through the delivery of the project objectives, it is hoped that a number of useful contributions to the research community will be made in terms of design and analysis modelling methods for small-scale low temperature ORCs.

1.3 Thesis structure and scientific contributions

This thesis consists of five chapters, which present the full progression of this research project. Following this introduction, a comprehensive review on the current state of the art of ORC technology, both within industry and academia, is presented in Chapter 2. This literature review is split into three sections, namely thermodynamic modelling and optimisation, the current status of commercial and experimental ORC expanders, and the modelling and analysis of ORC turbomachines. The outcome of this literature review is a number of key conclusions that both reinforce the project objectives, and give further insight into additional aspects that it is important to consider.

In Chapters 3 to 6 a number of different areas of this research project are discussed, with each research area being supported by a peer-reviewed conference or journal paper. Ultimately this work demonstrates the complete cycle of modelling a turbine within a small-scale low temperature ORC. Initial thermodynamic modelling and optimisation of the cycle leads to a design point specification which can then be used to obtain a complete turbine design. With a complete design, the off-design performance can then be evaluated,

and this analysis can be fed back into the thermodynamic model to assess the interaction between turbine and cycle performance.

In Chapter 3 a number of existing ORC modelling techniques are brought together into a single program that can analyse simple subcritical ORCs. Thermodynamic analysis is combined with a suitable equation of state, alongside individual component models to size each cycle component. This allows system performance, heat exchanger area and turbine rotational speed to be considered within one model. The ORC model is coupled to a multi-objective optimiser, and a novel objective function is defined which considers the trade-off between performance and system complexity. In the final section of Chapter 3 a case study is used to demonstrate how the ORC model and optimisation procedure can be used to select a suitable working fluid, and optimal cycle configuration for a particular heat source.

Although the ORC model can provide an initial indication of the turbine rotational speed, a more detailed design phase must be completed to obtain a complete turbine design, and this is presented in Chapter 4. This model generalises existing design methods, developed for ideal gases, to be applicable for any fluid by coupling the model with a suitable equation of state. Furthermore, this model builds on existing ORC turbine design methods by considering the stator and rotor three-dimensional geometry during the preliminary design, whilst a novel method to predict the relative velocity distribution within the rotor is developed. This enables more rapid design iterations before commencing with more detailed computational fluid dynamic (CFD) analysis. The turbine design model is validated using the commercial CFD code, ANSYS CFX, for two turbines operating with air and an organic fluid respectively.

For small-scale systems to be economically viable it will be necessary to implement the same turbine within a number of different cycle configurations to improve the economy of scale. This inevitably means operating a turbine under off-design conditions. However, off-design models for ORC turbines are overlooked within many existing studies. An investigation into whether similitude theory can be used to determine turbine performance following a change in the operating conditions or working fluid is presented in Chapter 5. The work presented here presents a significant contribution to the ORC community since, to the authors knowledge, the correct implementation, and validation of similitude theory to ORC turbines had not previously been demonstrated. Within this chapter, the

performance map for the ORC turbine is obtained from ANSYS CFX simulations, before further simulations are compared to predictions made using similitude theory. Ultimately, the output from this chapter is a modified similitude theory that is suitable for the off-design modelling of subsonic ORC turbines.

In Chapter 6 the aspects covered in the previous three chapters are brought together. A turbine performance map is implemented within an ORC thermodynamic model, and the modified similitude theory is used to predict performance over a range of operating conditions whilst using different working fluids. The model, when supplied with a particular heat source and working fluid, can determine the operating point at which the turbine operates most efficiently. This a useful and interesting contribution, which ultimately shows that the developed turbine can be effectively utilised within a range of different ORC system configurations, by simply selecting a working fluid to match the available heat source.

In Chapter 7 the final conclusions of this research project are summarised, and the deliverables from each chapter are evaluated against the project objectives, and the key conclusions drawn from the literature review. Finally, recommendations are made for the direction of future research.

1.4 Publications

Conference and journal publications

- White, M., and Sayma, A. I. (2015). System and component modelling and optimisation for an efficient 10kWe low-temperature organic Rankine cycle utilising a radial inflow expander. *Proceedings of the Institution of Mechanical Engineers, Part A: Journal of Power and Energy*, In Press:15, DOI: 10.1177/0957650915574211.

- White, M., and Sayma, A. I. (2015). The one-dimensional meanline design of radial turbines for small scale low temperature organic Rankine cycles. In *Proceedings of ASME Turbo Expo 2015: Turbine Technical Conference and Exposition*, 15-19$^{\text{th}}$ June, Montreal, Canada.

- White, M., and Sayma, A. I. (2015). The application of similitude theory for the performance prediction of radial turbines within small-scale low-temperature organic

Rankine cycles. *Journal of Engineering for Gas Turbines and Power*, 137(12):10.

- White, M., and Sayma, A. I. (2015). The impact of component performance on the overall cycle performance of small-scale low temperature organic Rankine cycles. In *9th International Conference on Compressors and their Systems*, 7-9th September, London, UK.

Workshop and poster presentations

- White, M., and Sayma, A. I. (2013). System modelling for a 10kWe ORC for heat recovery. In *Southampton Workshop on Heat Recovery Systems*, 16th May, Southampton, UK.

- White, M., and Sayma, A. I. (2013). System and component modelling for an efficient 10kWe ORC utilising a turbo-expander. In *2nd International Seminar on ORC Power Systems*, 7-8th October, Rotterdam, The Netherlands.

- White, M., and Sayma, A. I. (2015). Predicting radial turbine off-design performance within organic Rankine cycles (ORC) when operating conditions and working fluids change. In *Cambridge Workshop on Turbomachinery for Heat Recovery and Low-carbon Power*, 19th May, Cambridge, UK.

This page is left intentionally blank.

Chapter 2

Literature Review

2.1 Introduction

The surge of interest in ORCs over recent years has resulted in a very large number of research papers being published. Within this chapter the important aspects of ORC technology will be discussed, with reference to the most relevant of these papers. This chapter is split into three sections which review the modelling and analysis of the complete ORC system, expanders used in commercial and experimental ORCs, and then the modelling and analysis of ORC turboexpanders. At the end of this literature review the key issues surrounding the development of small-scale low temperature ORCs will be discussed, and these will complement the project objectives defined in Chapter 1.

2.2 Modelling the organic Rankine cycle

First and foremost, any analysis of a thermodynamic power cycle starts with an analysis of the complete cycle. This consists of a thermodynamic analysis of the ORC, alongside the criteria for selecting a suitable working fluid. Extrapolating this analysis it is also important to build in component models, and optimisation methods. This section will address these important aspects of ORC research.

2.2.1 Thermodynamic analysis of the organic Rankine cycle

A schematic of the simple subcritical Rankine cycle was shown in Figure 1.1, and this process can also be represented on a temperature-entropy ($T - s$) diagram, as illustrated in Figure 2.1A. For this simple cycle the pump work, heat absorbed, expander work and

heat rejected are denoted as W_p, Q_h, W_t and Q_c respectively and are given by the change in enthalpy h of the working fluid (Equations 2.1 - 2.4). It is convenient to express these parameters in terms of energy per unit mass flow rate $\dot{m}$.

$$\frac{W_\mathrm{p}}{\dot{m}} = h_2 - h_1 \tag{2.1}$$

$$\frac{Q_\mathrm{h}}{\dot{m}} = h_3 - h_2 \tag{2.2}$$

$$\frac{W_\mathrm{t}}{\dot{m}} = h_3 - h_4 \tag{2.3}$$

$$\frac{Q_\mathrm{c}}{\dot{m}} = h_4 - h_1 \tag{2.4}$$

The cycle thermal efficiency η_o is then given as the ratio of the net work produced by the cycle to the amount of heat input into the system (Equation 2.5).

$$\eta_\mathrm{o} = \frac{W_\mathrm{t} - W_\mathrm{p}}{Q_\mathrm{h}} \tag{2.5}$$

In the ideal cycle the compression and expansion processes occur isentropically, whilst the heat addition and rejection are both isobaric processes. In reality the performance of the Rankine cycle will deviate from this ideal cycle. The compression and expansion processes are no longer isentropic since loss mechanisms within both the pump and expander generate entropy. Furthermore, as the fluid passes through the evaporator and condenser it experiences a total pressure drop such that the heat addition and rejection are no longer isobaric processes. The non-isentropic behaviour of the pump and expander is accounted for by the pump and expander isentropic efficiencies, denoted η_p and η_t respectively, where the subscript 's' refers to the conditions following an isentropic compression or expansion.

$$\eta_\mathrm{p} = \frac{h_{2\mathrm{s}} - h_1}{h_2 - h_1} \tag{2.6}$$

$$\eta_\mathrm{t} = \frac{h_3 - h_4}{h_3 - h_{4\mathrm{s}}} \tag{2.7}$$

Alongside the simple subcritical cycle a number of alternative cycle configurations can also be considered. These systems come with added complexities but have the promise of greater cycle efficiencies than the simple cycle. These cycles are the recuperated, wet and supercritical cycles and these are also represented on a $T - s$ diagram in Figure 2.1. The system layout for the wet and supercritical cycles follow from Figure 1.1, whilst the

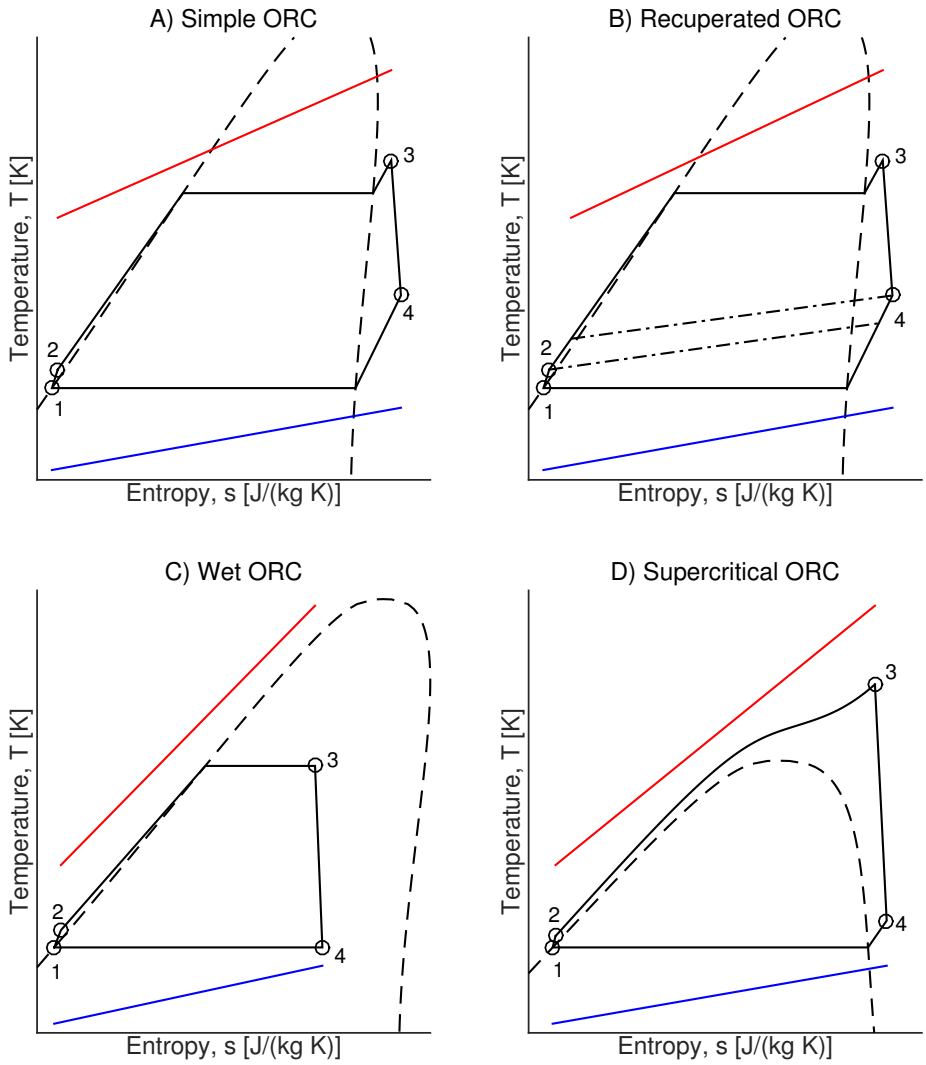

Figure 2.1: Schematic of the various ORC power cycles represented on a T-s diagram.

recuperator requires an additional component as demonstrated in Figure 2.2.

Within the recuperated cycle a recuperator is used to extract the heat still contained within the fluid at the expander outlet and use it to preheat the liquid leaving the pump before it enters the evaporator. This heat transfer is demonstrated by the dash-dot lines in Figure 2.1B. The advantage of this system is that the same power output can be produced for a smaller amount of input heat, thereby increasing the cycle efficiency whilst simultaneously reducing the condenser load. The disadvantage of such a system is the additional cost and weight of installing the recuperator.

The aim of both the wet and supercritical cycles is to obtain a better thermal match between the working fluid and heat source within the evaporator, thus reducing irreversibility and improving the overall cycle performance. Within the wet cycle this is achieved

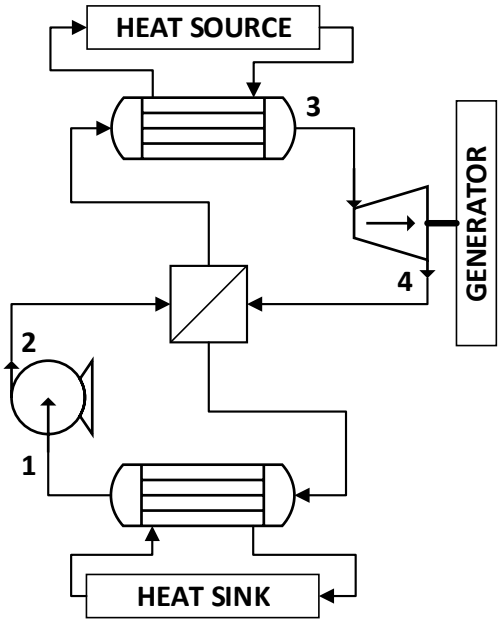

Figure 2.2: Schematic of the recuperated Rankine cycle.

by expanding the working fluid from a two-phase state. There also exists the trilateral cycle which is similar to the wet cycle but expands the fluid directly from a saturated liquid state. In the supercritical cycle two-phase conditions are avoided by compressing the working fluid to a pressure greater than the critical pressure. The difficulties associated with these cycles are that the wet cycle requires expanders that can operate with two-phase vapours, whilst the supercritical cycle requires very high operating pressures.

2.2.2 Working fluid selection

Due to the large range of potential applications, in terms of both the heat source temperature and the amount of heat available, it is arguable that the working fluid is one of the most critical components within the ORC, and this is highlighted by the abundance of research papers within the literature. The list of possible working fluids for an ORC is vast and covers a range of fluid groups such as hydrocarbons, hydrofluorocarbons, hydrochlorofluorocarbons, hydofluoroethers and siloxanes amongst others (Tchanche et al., 2011). Colonna et al. (2015) lists the most common working fluids found within commercial ORC plants, and this data is reproduced in Table 2.1 to give a flavour for the available fluids. A more comprehensive list can be found in ASHRAE (2009, 2010).

Badr et al. (1985) presented an early study on the selection of working fluids for an ORC, and discussed the properties that a working fluid should ideally exhibit. It is quickly

Table 2.1: Common ORC fluids as suggested by Colonna et al. (2015)

Fluid	Chemical formula	Molecular weight [g mol^{-1}]	Critical temperature [°C]	Critical pressure [bar]
toluene	C_7H_8	92.1	318.6	41.26
cyclo-pentane	C_5H_{10}	70.1	238.5	45.15
iso-pentane	C_5H_{12}	72.1	187.2	33.78
iso-butane	C_4H_{10}	58.1	134.7	36.29
MDM[1]	$C_8H_{24}Si_3O_2$	236.5	290.9	14.15
MM[2]	$C_6H_{18}OSi_2$	162.4	245.5	19.39
PP1[3]	C_6F_{14}	338.0	182.2	19.23
R245fa[4]	$C_3H_3F_5$	134.0	154.0	36.51
R134a[5]	$C_2H_2F_4$	102.0	101.1	40.59

[1] octamethyltrisiloxane [2] hexamethyldisiloxane
[3] perfluoro-2-methylpentane [4] 1,1,1,3,3-pentafluoropropane
[5] 1,1,1,2-tetrafluoroethate

established that there is no unique working fluid which will satisfy all the desired criteria and it is often down to the designer to select a fluid based on their own selection criteria. The desired properties discussed have been summarised in the following list. These same selection criteria have been reiterated within a number of more recent research papers (Husband and Beyene, 2008; Tchanche et al., 2011; Vélez et al., 2012; Quoilin et al., 2013; Bao and Zhao, 2013).

- First and foremost, the working fluid must result in an optimal thermal cycle efficiency resulting in an optimal conversion of the input heat into power
- The evaporation pressure should not be excessive to avoid high mechanical stress and expensive component design
- The condensation pressure should be above atmospheric pressure to avoid the requirement of operating the condenser under a vacuum
- The minimum ambient temperature should be above the fluids triple point
- High latent heat of vaporisation and high thermal conductivity are advantageous to achieve high heat transfer rates within the heat exchangers
- Low viscosity can help to reduce pressure drops within the system

- High fluid density results in low volume flow rates, permitting small cycle components to be designed, whilst minimising pressure losses downstream of the expander
- The slope of the fluids saturated vapour line should be close to vertical (see Figure 2.3). Fluids with a negative gradient require superheating to ensure the expansion finishes within the superheated region, whilst fluids with a positive gradient exit the expander with a large superheat requiring a large amount of pre-cooling prior to condensation.
- The fluid should be non-corrosive and compatible with the materials used for the construction of the system
- The fluid should be chemically stable within the operating range being considered
- The fluid should be non-toxic and non-flammable
- The fluid should have good lubrication properties
- The fluid should be low cost
- Although perhaps not a selection criteria, it should be noted that organic fluids generally have a lower enthalpy drop over a given pressure ratio compared to working fluids such as steam or air, which allows high pressure ratios to be achieved over a single turbine stage. Coupled with the low speed of sound of organic fluids, this can result in supersonic flows within the turbine which the designer should be aware of.

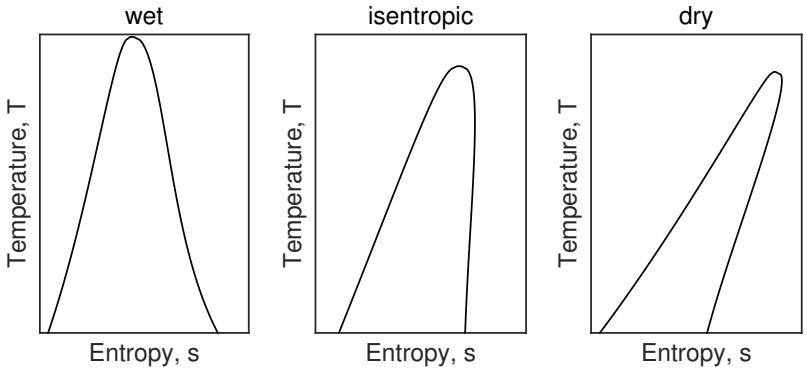

Figure 2.3: Classification of fluids according to the slope of their saturated vapour dome. Fluids with negative, infinite and positive gradients are classified as 'wet', 'isentropic' and 'dry' fluids respectively.

Alongside the properties already listed, it is also important to consider the environmental properties of the working fluid. Due to the Montreal and Kyoto protocols a number

of potential working fluids have already been banned, with others set to be phased out. A possible working fluid should therefore have a low environmental impact with a low global warming potential (GWP), a low atmospheric lifetime (ALT), and a low ozone depletion potential (ODP). With these considerations in mind, there has been a growing interest in hydrofluroolefins (HFO) as organic working fluids. These fluids have zero ODP, and very low GWP values. Liu et al. (2014) evaluated the thermodynamic performance of these fluids and classified them in terms of heat source temperature. The results suggested that these fluids can achieve a thermodynamic efficiency that is superior to that obtained with R245fa or R134a. McLinden et al. (2014) also discussed the potential of these fluids, and highlighted R1234yf and R1234ze as two common fluids that are available within the market. However, the authors also comment that HFOs are generally more difficult to manufacture, and will inevitably be more expensive to purchase.

With a large number of design criteria to meet, and a large array of possible working fluids available it is inevitable that a number of researchers have attempted to classify working fluids in a bid to recommend which working fluids would be optimal for particular applications. Tchanche et al. (2009) coupled a thermodynamic ORC model with working fluid considerations in a bid to recommend fluids for a low temperature solar ORC working with a heat source temperature of 90°C. After running the thermodynamic model each working fluid was scored against a number of criteria based on whether the result was in favour of the fluid or not. After completing this the author qualitatively accepted or rejected the fluids based on these scores. It was concluded that no fluid successfully met all criteria, but R134a was suggested as the most suitable candidate for this application, although R152a, butane and isobutane were also suggested as suitable candidates. Chen et al. (2010) reviewed thermodynamic cycles and working fluids for low temperature ORCs. The authors suggested the use of $T_c - \xi$ plots where ξ is the inverse of the gradient of the saturated vapour dome (i.e. ds/dT), and T_c is the fluids critical temperature. This allowed the classification of fluids in terms of whether they are dry, isentropic or wet, and whether they would be suitable for implementation within either a subcritical or supercritical ORC. Qiu (2012) considers fluid selection for a micro ORC for combined heat and power (CHP) applications. The authors ranked the desirable criteria for ORC working fluids according to their own interpretation and then developed a selection methodology which assumes that the suitability of a particular fluid is governed by its worst characteristic. Zhang et al.

(2014) commented that working fluid selection remains a subjective process, and proceeded to present a working fluid selection procedure that aimed to remove this aspect. Their results suggested R22 and R134a as suitable candidates. Recently Rödder et al. (2015) presented a systematic approach to working fluid selection. The authors established 22 criteria across 6 main categories within which to evaluate potential working fluids. By defining elimination criteria such as the minimum allowable condensation pressure, certain working fluids can be removed, before a ranking process was implemented to arrive at a final fluid selection. However, a limitation to both of the last two selection procedures was that there was a limited consideration of the thermodynamic performance of the considered fluids.

From these studies it becomes clear that the selection of an optimal working is a difficult process that relies on both a quantitative investigation of the cycle performance and a qualitative assessment on whether the safety, economical and environmental properties are suitable for a particular application. Perhaps understandably, there has been a significant amount of work within the literature that has focussed on the former, and this will be discussed within the next section. However it is important that the designer does not forget about the latter. Ultimately, it has been discussed within the literature that working fluid screening should remain an important stage when designing any ORC system (Quoilin et al., 2013).

To complete this section, it should also be mentioned that there is interest in the use of fluid mixtures as working fluids within ORCs. The advantage of mixtures is that their phase change under constant pressure is not isothermal permitting a greater thermal match with the heat source and a better cycle performance (Chys et al., 2012). However, this increased performance does come at the cost of increased cost and complexity. Another interesting area is the use of computer aided molecular design coupled with thermodynamic analysis to arrive at optimal working fluids (Papadopoulos et al., 2010), however this area is still in development.

2.2.3 Thermodynamic modelling

Alongside selecting the working fluid, the effect of the cycle operation parameters on the cycle performance, namely the condensation temperature, pressure ratio and amount of superheat, all need to be understood. A substantial amount of research within the

literature has focussed on this important aspect, and many of these studies follow a similar methodology. Generally speaking a thermodynamic model is developed, and then run over a range of operating conditions, using a range of different working fluids, for the same heat source and sink conditions. The results are then analysed resulting in recommendations for the optimal working fluid and cycle operating conditions.

Clearly, the main prerequisite for these studies is the accurate prediction of fluid properties for a range of possible working fluids. The majority of the working fluids considered do not obey the ideal gas law, so it is necessary to implement more complex equations of state. By far the most common approach is to use REFPROP, which is the industry standard for the calculation of working fluid properties and contains the most accurate equations of state for a large range of working fluids (Lemmon et al., 2013). CoolProp has also been recently developed, which is an open-source alternative to REFPROP (Bell et al., 2014). Another alternative is to model the fluid properties using cubic equations of state such as the Peng-Robinson or Redlich-Kwong models. These have been considered within a number of computational fluid dynamics (CFD) studies, such as those presented by Colonna et al. (2006) and Sauret and Gu (2014). Luján et al. (2012) modelled the expansion process for R245fa, a common ORC working fluid, and found that near the saturated vapour line these models accurately predicted the pressure to within 2%, and the enthalpy to with 2.5%, when compared to REFPROP.

In terms of thermodynamic modelling, Hung et al. (1997) demonstrated an early study on the effects of variable expander inlet conditions, and condensation temperatures for a range of organic fluids. Whilst cycle efficiency increases with pressure ratio and a reduction in condensation temperature, superheating was found to be detrimental and negligible for dry and isentropic fluids respectively. This was later validated experimentally by Yamamoto et al. (2001) who developed an ORC test rig operating with R123 as the working fluid. Saleh et al. (2007) developed a thermodynamic model and screened 31 different working fluids, and arrived at the same conclusion. However, the authors also report the benefit of including a recuperator to improve the overall cycle efficiency. In the same year Wei et al. (2007) investigated the effects of the heat sink flow conditions on the performance of an ORC, and showed that the power output and efficiency reduced with increasing ambient temperatures, and the degree of subcooling. The detrimental effect of superheating and subcooling was also noted in an experimental study conducted

by Quoilin et al. (2010), and it was suggested that these processes should be reduced to improve cycle efficiency.

In addition to considering the cycle performance in terms of the cycle efficiency a number of researchers have also considered the exergy efficiency of the cycle. The exergy, X, is defined as the amount of useful work that can be extracted from a particular fluid stream and is defined using Equation 2.8 (Cengel and Boles, 2007). Here $\dot{m}$ is the fluid mass flow rate and h and s are the fluid enthalpy and entropy. The terms h_{a}, T_{a} and s_{a} are the enthalpy, temperature and entropy of the fluid at ambient temperature and pressure. The first term in Equation 2.8 is therefore the total amount of thermal energy that would be released as a result of the fluid cooling from the heat source conditions to ambient conditions, whilst the second term is the amount of thermal energy that would be impossible to recovery due to the generation of entropy.

$$X = \dot{m}\left[(h - h_{\mathrm{a}}) - T_{\mathrm{a}}(s - s_{\mathrm{a}})\right] \tag{2.8}$$

Due to irreversibilities that occur within each cycle component there will be an exergy loss. The exergy efficiency then quantifies these losses giving an indication of the systems ability to convert the heat source into power. Hung (2001) extended his previous analysis to consider exergy, whilst Wei et al. (2007) and Dai et al. (2009) also conducted thermodynamic studies on exergy loss within the ORC. They found that the largest exergy loss is found within the evaporator and this was further demonstrated experimentally by Li et al. (2012). The analysis completed by Hung (2001) also showed that system efficiency and irreversibility have opposite trends with varying turbine inlet pressure, suggesting it is important to optimise the heat transfer process within the evaporator to achieve optimal cycle performance.

Running alongside the consideration of exergy loss, it is also important to consider the heat exchange between the heat source and the ORC working fluid. By considering the first law of thermodynamics, this can be represented as a simple energy balance (Equation 2.9). Here $\dot{m}_{\mathrm{w}}$ and $\dot{m}_{\mathrm{h}}$ represent the ORC and heat source mass flow rates respectively, h_2 and h_3 represent the working fluid enthalpy at the evaporator inlet and outlet, and h_{hi} and h_{ho} represent the heat source enthalpy at the evaporator inlet and outlet.

$$\dot{m}_{\mathrm{w}}(h_3 - h_2) = \dot{m}_{\mathrm{h}}(h_{\mathrm{hi}} - h_{\mathrm{ho}}) \tag{2.9}$$

For a specified heat source and cycle conditions, neither the ORC mass flow rate or heat source outlet conditions are known. Therefore to complete the evaporator design a pinch-point analysis is typically introduced. The pinch point is defined as the smallest temperature difference between the heat source and working fluid. Within a subcritical ORC this is typically found at the start of the evaporation process and this is shown in Figure 2.4. By defining this temperature difference it allows the working fluid mass flow rate to be established before calculating the heat source outlet temperature. The evaporator pinch point is strongly related to exergy efficiency with small values indicating a high exergetic efficiency and a high utilisation of the available heat. However, reducing the temperature difference within the evaporator increases the required heat transfer area and therefore cost. This trade-off between exergy efficiency and cost has been discussed by a number of researchers (Vaja and Gambarotta, 2010b; Quoilin et al., 2011; Wang et al., 2012). Quoilin et al. (2011) developed a thermodynamic ORC model that was coupled with sizing and economic models for the evaporator. An optimisation was completed with the intention of minimising the specific investment cost (€/kW), and it was found that the optimal pinch point was found to be below 10 K. However, it should be noted that this analysis was based on cost functions which may be overly simplistic, and indeed the authors highlight that the aim of the study was to present the method rather than an accurate economic study. Comparatively, Wang et al. (2012) constructed a similar model, but minimised the heat exchanger area per unit power (m^2/kW) instead of cost and found that optimal performance is obtained with pinch points of around 15 K.

In order to develop an economical ORC system, the most suitable objective should be to minimise the specific investment cost. However, cost functions for cycle components are not always available and therefore alternatives are required. Another parameter that is closely related to the pinch point is the evaporator effectiveness, and Srinivasan et al. (2010) stresses that the heat exchanger effectiveness is very important to achieve high heat recovery efficiencies. This has led authors such as Vaja and Gambarotta (2010b) to suggest that for ORC applications such as waste heat recovery it is more important

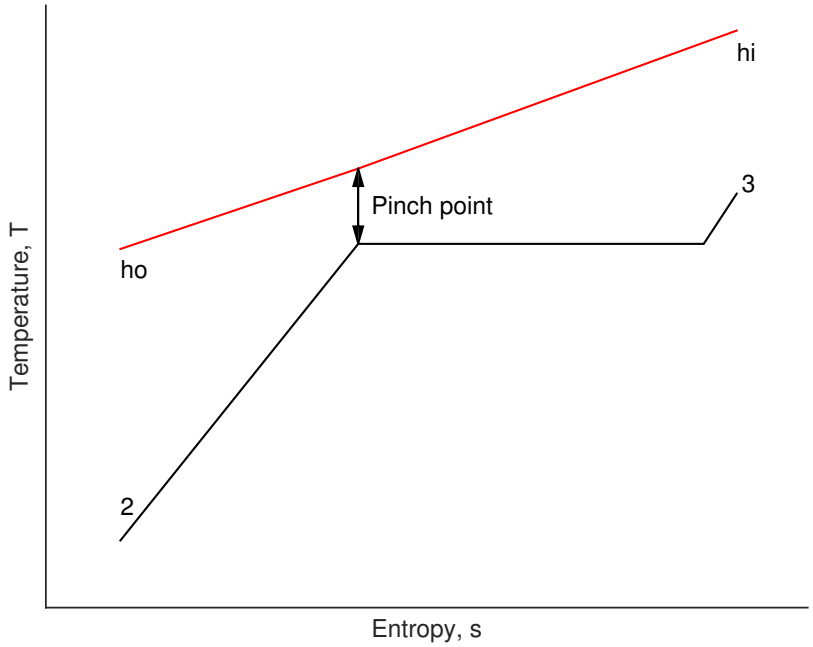

Figure 2.4: Schematic of the ORC evaporator heat transfer process and the location of the pinch point.

to maximise the global system efficiency, and therefore maximise the net power output, instead of maximising the ORC cycle efficiency. Here the global efficiency is the product of the evaporator effectiveness and the cycle efficiency. The result of maximising the system efficiency is that there exists an optimal pressure ratio at which optimal power can be produced from a given heat source. This was demonstrated by the study completed by Quoilin et al. (2011). To rephrase, above the optimal pressure ratio a greater cycle efficiency could be obtained, but this would be at the expense of the working fluid absorbing less heat from the available heat source resulting in less power. It has also been suggested that under this condition where the aim is to achieve maximum power, it may not be necessary to include a recuperator within the cycle (Quoilin et al., 2011; Dai et al., 2009), which would help to reduce installation costs for small-scale systems.

2.2.4 Component modelling

In addition to considering the thermodynamics of the cycle, it is also important to consider the component performance. Indeed, in Section 2.2.2 a number of working fluid selection criteria were noted, but these criteria can only be assessed by considering how the component design changes. Before discussing these aspects in more detail, it is helpful

to distinguish between two modelling scenarios that can be considered; namely component design and component off-design modelling. In the former scenario the cycle components must be designed to achieve the desired performance, whilst in the latter the component design is already defined, and a prediction of the performance is required.

Pump modelling

Within the published ORC research, the pump has received very little interest. More often than not, for both design and off-design modelling, the pump is assumed to operate with a constant pump isentropic efficiency across all operating conditions. Compared to a conventional steam Rankine cycle, the ratio of the specific work consumed by the pump to the specific work produced by the turbine in the ORC is much greater. This means that changes in the pump efficiency are not negligible, and this could have a significant impact on the cycle performance. Borsukiewicz-Gozdur (2013) studied pumping work in the ORC, and the results indicate that the pumping work could consume up to 15% of the turbine work, depending on the working fluid.

A few authors have considered pump performance, and this is typically in relation to dynamic modelling of the ORC (Wei et al., 2008; Vaja and Gambarotta, 2010a; Sun and Li, 2011). These authors generate non-dimensional performance maps based on pump scaling laws, which can predict the pump efficiency based on the ORC pressure ratio and mass flow rate. However, the construction of these curves requires data supplied by the manufacturer which is particular to a given pump. Of course, during cycle design this data is not typically available, leaving authors to assume pump efficiency values.

Expander modelling

As the component producing the work within the ORC, the expander is perhaps the most critical component. Since expander design is a particular focus of this research it is worth discussing the expander modelling in more detail, and this is completed in Sections 2.3 and 2.4. Therefore here it is suitable to just address the requirements for an expander model within ORC modelling.

Much like the pump, expander modelling within the literature has suffered from the common assumption of a constant isentropic efficiency. Although this may be a reasonable assumption for cycle design, where an expander can be designed to meet the ORC specific-

ation, it might still be useful to consider expander design aspects within the cycle analysis; such a study was completed by Sauret and Rowlands (2011). When considering off-design analysis, an expander off-design model is essential. Indeed, for small-scale systems it reasonable to assume that the same expander may be utilised within a range of different ORC applications. This could result in the cycle design point corresponding to operating conditions where the expander operates at off design. Clemente et al. (2012) combined thermodynamic and expander models to analyse the performance of small-scale ORCs. It was highlighted that ORC thermodynamic models are only accurate when variations in expander performance are taken into account.

Heat exchanger modelling

The heat exchanger models that have been developed within the literature can be grouped into three categories; steady-state sizing, steady-state performance and dynamic modelling.

In a steady-state sizing model the thermodynamic properties of the two fluids streams are already defined. The purpose of the heat exchanger model is to then determine the heat transfer area that is required to heat or cool the fluid streams to these desired conditions. Recalling Equation 2.9, the heat transferred between the two fluid streams can be related to the heat transfer area A using Newton's law of cooling (Equation 2.10). Here U is the overall heat transfer coefficient and $\Delta T_{\log}$ is the log-mean-temperature-difference, and therefore if these are both known the heat transfer area can be determined. Typically the complete heat transfer process is split into single-phase and two-phase heat transfer regions, and empirical correlations for local heat transfer coefficients are used.

$$Q = \dot{m}_{\mathrm{h}}(h_{\mathrm{hi}} - h_{\mathrm{ho}}) = U\ A\ \Delta T_{\log} \tag{2.10}$$

Hettiarachchi et al. (2007) and Wang et al. (2012) both constructed heat exchanger models using this method, however both show a general formulation that does not apply to a particular heat exchanger geometry. Quoilin et al. (2011) developed evaporator and condenser models suitable for the sizing of plate heat exchangers for small-scale low temperature ORCs, whilst Pierobon et al. (2013) developed a model to size shell-and-tube heat exchangers for implementation within MW-size ORCs. Karellas et al. (2012) developed a

model to size evaporators for supercritical ORCs, but further discretised the heat transfer process to account for variations in the fluid properties.

The second type of heat exchanger model that may be required in ORC simulations is a steady-state performance model. In this model the heat transfer area is already known, as are the inlet temperatures for both fluid streams. The purpose of a heat exchanger model is to then determine the temperature of each fluid at the heat exchanger outlet. This method is referred to as the $\epsilon - \text{NTU}$ method, and the implementation of this within an ORC model is demonstrated by Sun and Li (2011). Such a model is useful in a cycle optimisation study where the system components have already been defined.

The final model, implemented for dynamic modelling of the ORC, applies a one-dimensional differential energy and mass balance to the ORC heat exchangers to determine the temperature distribution as a function of space and time. A number of authors have demonstrated such models (Wei et al., 2008; Vaja and Gambarotta, 2010a; Zhang et al., 2012; Casella et al., 2013).

2.2.5 Optimisation

With a number of design variables available to the designer it is important to optimise both the cycle and component design to achieve an optimal system configuration. The most basic form of optimisation is a parametric optimisation where one variable is varied over a particular range whilst the other design variables remain fixed. An example of such a study was completed by Roy et al. (2010) who investigated the effects of the pressure ratio and amount of superheat on the net work produced and the cycle efficiency, while fixing the condensation temperature. He et al. (2012) completed a similar study, but instead of completing a parametric study the authors developed an analytical method to determine the optimal evaporating temperature to obtain the maximum net work.

Of course, when considering only the cycle performance there are only three design parameters (condensation temperature, pressure ratio and amount of superheat), which means a parametric study can be completed relatively quickly. However, when considering additional factors such as the heat source, the heat sink and the heat exchanger sizing, the complexity of the model increases, and so does the number of variables. This requires more complex methods of optimisation. Hettiarachchi et al. (2007) developed a model that coupled thermodynamic analysis with heat exchanger sizing. An optimisation was

then completed using the steepest descent method which optimised the evaporation and condensation pressures, and the fluid velocities within the evaporator and condenser. The objective was to minimise the heat exchanger area per unit power. This same strategy was later adjusted by Wang et al. (2012) who defined an objective function that considered minimising the heat exchanger area per unit power, but also maximising the system efficiency. This multi-objective optimisation was completed using a simulated annealing algorithm.

Dai et al. (2009) coupled an ORC thermodynamic model with a genetic algorithm to arrive at an optimal cycle configuration. For a fixed heat source, fixed ambient conditions, fixed component efficiencies and a fixed pinch point, the turbine inlet temperature and pressure was optimised to achieve the highest exergy efficiency. Rashidi et al. (2011) coupled a thermodynamic model of supercritical CO_2 cycles with an artificial neural network and a genetric algorithm. The objective of this optimisation was to find cycles that maximised the thermal efficiency, the exergy efficiency and the net work output. However, unlike the studies discussed in the previous paragraph, neither of these studies considered the heat exchanger geometry. In this instance an optimisation could result in a cycle that has a high efficiency, but would require excessively large heat exchangers.

Research at the University of Denmark has investigated the optimisation of ORCs for waste heat recovery in marine applications (Larsen et al., 2013; Pierobon et al., 2013). Larsen et al. (2013) developed a thermodynamic model and optimised the thermal efficiency according to the evaporation and condensation pressures using a genetic algorithm. The novelty in this approach was that the cycle layout (i.e. subcritical or supercritical) was an output from the optimisation. Pierobon et al. (2013) completed a more detailed optimisation by developing a heat exchanger model. This permitted a multi-objective optimisation of the thermal efficiency, the system cost and system size to be completed according to the condensation temperature, pressure ratio, the amount of superheat and the heat exchanger pinch points. Wang et al. (2013a) completed a similar study in which a multi-objective optimisation was completed using a genetic algorithm. The objectives were set as maximising the exergy efficiency of the cycle, whilst minimising the overall capital cost.

Sun and Li (2011) developed a more complete model which included off-design models for the pump, expander, evaporator and condenser. For a pre-determined set of com-

ponents the aim of this optimisation was to maximise either the net work output, or the cycle thermal efficiency, in relation to the working fluid and heat sink mass flow rates, and the evaporation pressure. Fixed heat source and ambient temperatures were assumed. It should be highlighted that such an optimisation is based on an existing system configuration, and is therefore not relevant to full cycle design. In such a case the trade-off between performance and cost can be removed since a pre-existing system implies the system costs are already known.

Ultimately, it is clear that a suitable optimisation strategy, used for system design, needs to consider the trade-off between thermodynamic performance, and system complexity by considering a multi-objective optimisation. Current studies have addressed this trade-off through either considering the heat exchanger area per unit power, or the system cost. However, minimising the heat exchanger area per unit power cannot guarantee that the cycle makes full utilisation of the available heat source, whilst the accuracy of cost functions may be questionable for small-scale ORC power systems. This is summarised in a review paper by Quoilin et al. (2013) which states that a major complexity with multi-objective optimisation is the definition of a suitable objective function.

2.3 Expanders for organic Rankine cycles

The expander is the most critical component within an ORC since it produces the mechanical work. For this reason, the design and analysis of ORC turbines has received a significant amount of attention, particularly for small-scale systems. Generally speaking, two types of expander are considered, and these are volumetric expanders and turboexpanders. Both of these expanders will now be discussed before completing a review of the current status of commercial and experimental ORC expanders.

2.3.1 Turboexpanders

In general, a turboexpander is a machine where the dynamic action of a rotating rotor accelerates the fluid passing through it, changing its direction and thus causing a reduction in the stagnation enthalpy. This change in energy produces torque on the shaft and generates useful mechanical power (Dixon, 2010). The rotor is preceded by a stationary stator which accelerates the flow, and delivers the flow to the rotor with a large absolute

tangential velocity. Through the rotor the absolute tangential velocity is reduced, and it is this reduction in absolute tangential velocity that determines the amount of useful mechanical power produced.

There are two main types of turboexpanders and these are referred to as axial and radial turbines. In an axial turbine the flow remains in the axial direction throughout the expansion and therefore maintains no radial velocity component. Comparatively, in a radial turbine the flow is mainly in the radial direction. By far the most common type of radial turbine is the radial inflow turbine where the flow enters the rotor in the radial direction, albeit with a tangential velocity, and is turned 90° through the rotor, leaving the rotor in the axial direction.

The advantage of the axial turbine is that it can achieve a high turbine efficiency over a wider range of rotational speeds than a radial turbine, whilst being able to easily accommodate multiple stages. In comparison, in a radial inflow turbine the reduction in radius allows a greater work output to be achieved over a single stage. Over the range of speeds where radial inflow turbines achieve a high efficiency it is hard to find a decisive advantage in either the radial or axial design (Dixon, 2010). In the 1960s and 1970s NASA undertook extensive research into small turbine design and concluded that radial inflow turbines are preferential over the axial design (Wood, 1963; Kofskey and Wasserbauer, 1966; Nusbaum and Kofskey, 1969; Rohlik, 1968). Radial inflow turbines are generally advantageous because they are compact, have good manufacturability, lightweight construction, can achieve high efficiencies over a single stage expansion, and provide a robust design. Furthermore, at the small-scale it is also noted that axial turbines require extremely thin blade trailing edges to achieve high efficiencies (Dunham and Panton, 1973).

The disadvantages associated with turbomachines largely relate to small-scale turbines. As the power rating reduces turbines can become expensive due to very high rotational speeds which may require high ratio gearboxes or high speed generators. Furthermore, as the turbine size reduces the relative clearances increase resulting in high tip clearance losses. This, alongside increased viscous losses, have a detrimental effect on turbine efficiency.

2.3.2 Volumetric expanders

The second group of expanders, called volumetric expanders, do not rely on the velocity of the fluid but instead expand the fluid through the cyclic change of volume of an expansion chamber. The most common volumetric expanders applied to ORCs are screw and scroll expanders.

A screw expander consists of two meshing helical rotors, as shown in Figure 2.5. As these rotors rotate a number of working fluid chambers are created between the rotors and the expander casing. The high pressure, high temperature gas enters at one end of the expander, and as the rotor rotates the volume of the working fluid chamber continually increases allowing the fluid to expand, producing mechanical power. The fluid is then discharged at the other side of the screw expander.

A scroll expander is formed from two identical scroll wraps which are constructed from an involute of a circle. After positioning the first scroll, the second is rotated by 180°, and then offset such that the two scrolls come into contact at a number of locations thus forming a number of working fluid chambers. The second scroll orbits around a central point which causes these contact points to move, creating a variation in the chamber volume. The construction of a scroll expander is demonstrated in Figure 2.6, which is also used to demonstrate how the expansion process occurs. Starting on the left of this figure, the high pressure, high temperature working fluid enters at the centre of the scrolls. As the second scroll moves anticlockwise more fluid is drawn into the scroll chamber, until a full revolution is completed at which point the chamber volume is shut-off from the

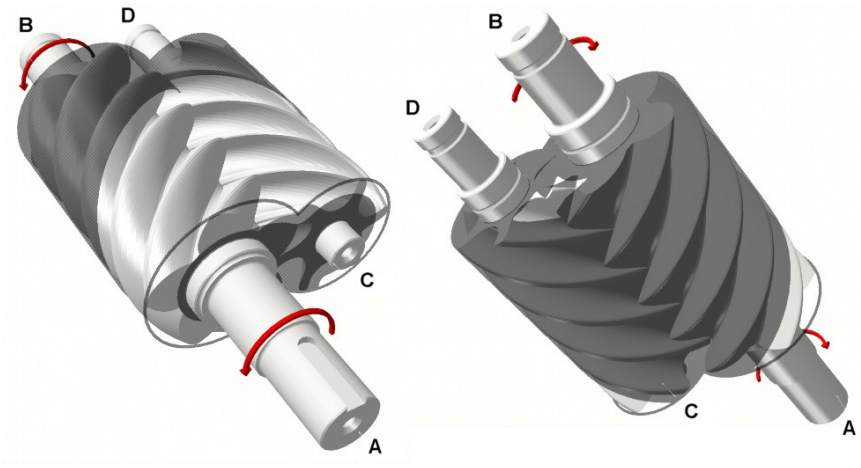

Figure 2.5: Three-dimensional model of the screw expanders rotors (Smith et al., 2005).

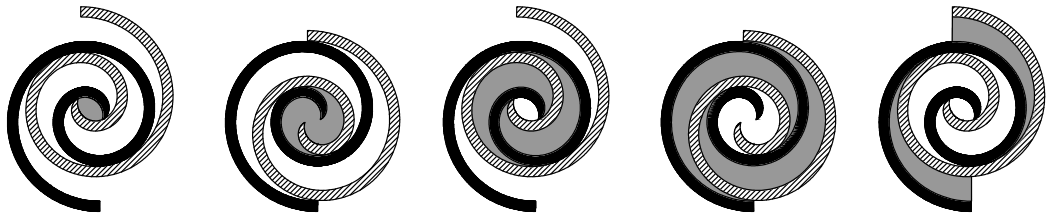

Figure 2.6: Schematic of the operation of a scroll expander.

inlet supply (this is demonstrated by the central plot in Figure 2.6). At this point the expansion of the fluid begins, and as the second scroll continues to rotate the chamber volume increases, thus expanding the fluid to lower pressure and generating mechanical power. Then finally, as the rotation continues, the outlet port opens and the fluid is discharged from the scroll.

Both screw and scroll expanders are both historically obtained by the reverse operation of existing screw and scroll compressors. The reverse operation of an off-the-shelf compressor delivers a simple, low cost alternative to turboexpanders, that generally have a low rotational speed, a low part count, are reliable, are already designed to operate with refrigerants and can tolerate two-phase conditions (Leibowitz et al., 2006; Lemort et al., 2009; Qiu et al., 2011; Clemente et al., 2012). Orosz et al. (2009) discusses that the conversion from an existing scroll compressor requires modifications such as lubricating the wraps and journal bearings, and the removal of features that would interfere with reverse operation. However it is noted that the required modifications vary from make and model and should be considered on a case-by-case basis.

The general disadvantage associated with volumetric machines is that the achievable expander efficiency is lower than turbomachines, which will impact the overall ORC performance. Furthermore, volumetric expanders have a fixed volume ratio which is determined by the expander geometry. Operating under ORC conditions which differ from this built-in volume ratio leads to either under or over expansion within the expander, which will reduce the expander efficiency even further.

2.3.3 Summary of commercial expanders

As discussed in Section 1.1.2 ORCs have been sufficiently developed to allow the commercialisation of the technology. The key manufacturers of ORC are summarised in Figure 2.7 in terms of the generated power, and the expander technology utilised.

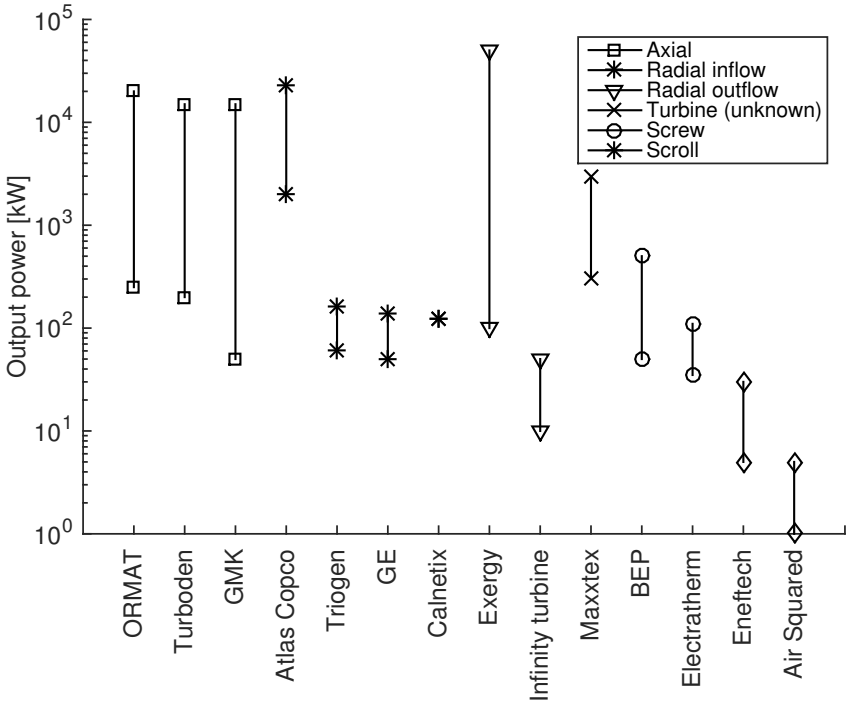

Figure 2.7: Summary of commercial ORC systems in terms of the generated power.

Much of the commercialisation of ORC technology can be attributed to ORMAT and Turboden. The ORMAT energy converter (OEC) has been installed in 75 countries, producing over 2000 MW of power from geothermal heat sources and waste heat. Their systems range from 250 kW to 20 MW and utilise a two-stage axial turbine (ORMAT, 2015). Similarly, Turboden have installed over 300 ORC units in 32 countries, producing over 400 MW of power from a variety of heat sources. Their systems range from 200 kW to 15 MW, and also utilise a multi-stage axial turbine (Turboden, 2013).

GMK also utilise a multi-stage axial turbine, and produce ORC systems for heat sources ranging from 100°C up to 300°C and produce power between 500 kW and 15 MW. They have also developed a smaller system producing between 35 kW and 60 kW which utilises waste heat from biogas engines (GMK, 2011).

There are also a number of companies utilising radial inflow turbines within ORC power systems. Atlas Copco implement radial turbines in ORC systems ranging from 2 MW up to 22.5 MW for geothermal and waste heat applications. Their turbines operate with adjustable guide vanes to allow more efficient turbine operation over a range of operating conditions (Atlas Copco, 2012). Triogen, GE and Calnetix all provide ORCs based on radial inflow turbines, but for smaller power outputs. The Calnetix system produces

125 kW from low temperature heat sources between 80°C and 170°C (Calnetix, 2014), whilst the GE system produces between 50 kW and 140 kW for an optimal turbine inlet temperature of 155°C (General Electric, 2014). The Triogen system is designed for higher temperature applications with heat source temperatures around 350°C, and produces a nominal power of 165 kW. The design consists of the pump, turbine and generator all directly coupled to the same shaft (Triogen, 2012), which is a concept that was first developed by Larjola (1995).

A more novel turboexpander that has been implemented within a number of commercial systems is the radial outflow turbine. In these turbines the fluid enters at the centre of the expander and moves outward in the radial direction, often across multiple stages. Exergy have commercialised this technology for power outputs ranging from 100 kW up to 50 MW, for applications ranging between 90°C and 260°C (Exergy, 2014).

Maxxtec provide ORC systems for high temperature applications around 300°C with power outputs between 300 kW and 3 MW (Maxxtec, 2014). These systems use a turboexpander, but the architecture of this turbine is not known.

As the system size reduces to a few hundred kW, there is interest in using alternative expanders to turboexpanders. BEP have developed ORC systems based on a screw expander capable of generating between 50 kW and 500 kW from heat sources between 80°C and 150°C (BEP, 2015). Similiarly, Electratherm have developed ORC systems based on a screw expander which can utilise waste heat, biomass, CHP, geothermal and solar heat sources. Their systems are capable of producing between 35 kW and 110 kW from heat sources between 77°C and 122°C (Electratherm, 2015).

At an even smaller scale, Eneftech have developed ORC-CHP systems which are based on the reverse operation of existing scroll compressors. Their systems utilise heat sources between 125°C and 150°C and can produce between 5 kW and 30 kW in addition to hot water (ENEFTECH, 2010). Although they do not develop the full ORC system, Air Squared provide scroll expanders that can produce power between 1 kW and 5 kW (Air Squared, 2015). For these small-scale systems, Infinity Turbines have commercialised turboexpanders for ORCs, delivering between 10 kW and 50 kW from low temperature heat sources. The turbine design is based on the radial outflow principle (Infinity Turbines, 2015).

Referring back to Figure 2.7, it is clear that ORC technology is sufficiently developed

for power outputs of around 100 kW and above, and for these systems turboexpanders are the most preferred expander technology. At lower powers, there have been a number of companies that have attempted to commercialise ORC systems, using a variety of expander architectures. However, these systems are either expensive bespoke systems, or are not installed in the large numbers required to confirm the widespread adoption of the technology. Furthermore, in a review by Qiu et al. (2011) it was highlighted that small-scale expanders are not commercially available or very expensive in form of prototype, and that this has led to a large amount of research focussed on the design and development of new expander technologies.

2.3.4 Summary of experimental expanders

Nguyen et al. (2001) and Yamamoto et al. (2001) both developed early experimental ORCs based on radial turbines for low temperature applications. Nguyen et al. (2001) achieved a power output of 1.47 kW with a turbine efficiency of 49.8%. The working fluid was n-pentane, whilst the evaporation temperature was 81°C and there was no superheat. Yamamoto et al. (2001) achieved a power output of 0.15 kW with a turbine efficiency of 48.0% respectively, operating with R123. Inoue et al. (2007) developed a radial inflow turbine with a focus on reducing costs by making the system as simple and compact as possible with a directly coupled generator and no particular speed control. An inverse design method optimised a 10 kW turbine which was validated with CFD before completing an experimental test. The results indicate that 13.5 kW was generated with a turbine efficiency of 80%. Pei et al. (2011) utilised a turbine designed in-house specifically for an ORC to achieve 1.1 kW with an efficiency of 62.5%. This system operated with R123, and the turbine inlet temperature was approximately 100°C. It was found that the turbine operated at off-design conditions, whilst condensation in the separator introduced droplets into the turbine which was detrimental to turbine performance. Further work by the authors obtained an efficiency of 68% with a better separator design (Li et al., 2012). Kang (2012) constructed a radial turbine for an ORC with a target power of 30 kW. The results from the experimental study show a power of 32.7 kW with a turbine efficiency of 78.7%, whilst operating with R245fa. However, it was believed that reducing heat and pressure losses could increase this efficiency further.

The relatively simple conversion of existing scroll compressors into expanders has led to

a number of experimental studies on scroll based ORCs. Johnston (2001) demonstrated the use of a scroll expander in a solar powered ORC using R123. The scroll expander generated a power of 2.81 kW with an expander efficiency of 65.1%. Saitoh et al. (2007) developed a similiar solar powered ORC using R113. The expander inlet temperature was 136°C, and the expander produced 0.45 kW, with a reported efficiency of 63%. Peterson et al. (2008) also implemented a scroll expander within an ORC, but reports a lower efficiency of 45%, whilst generating 0.2 kW. Lemort et al. (2009) developed a semi-empirical model to quantify losses within the scroll expander which was validated by experimental results. Mechanical losses may be reduced by better adapted tip seals, whilst pressure drop is found to be a main characteristic of scroll machines. A more detailed modelling might highlight how this pressure drop could be reduced through varying the expander geometry. Furthermore, the large flank clearance, a characteristic of kinematically rigid machines, leads to large leakage rates. Quoilin et al. (2010) combined this expander model with heat exchanger models to simulate, and experimentally validate a complete ORC model. A power output of 1.82 kW with a expander efficiency of 68% shows the viability of a scroll expander based ORC, but refrigerant leakage and a low volumetric performance are considered problematic. Wang et al. (2009) experimentally investigated a compliant scroll expander. Unlike the kinematically rigid design, a compliant design allows the two scrolls to contact, thus reducing clearance gaps, promoting sealing and improving volumetric efficiency. Results show an efficiency exceeding 70%, with rotational speed and pressure ratio only having a small effect on the performance. Orosz et al. (2009) experimentally characterised two scroll expanders, and reported expander efficiencies of up to 76%, whilst the power output was reported at 0.5 kW. The working fluids investigated were R245fa, and R123. Guangbin et al. (2010) modelled dynamic processes in scroll expanders, and results show that the stability of the expander is determined by the scrolls geometric parameters, and the design of the suction and discharge ports. It was concluded that further design modification such as suction port design and tighter radial and axial clearances could improve efficiency. Clemente et al. (2012) also developed and experimentally validated a scroll expander model before integrating it into a thermodynamic ORC model. Results showed high efficiencies were penalised by scroll performance which peaked at an expansion ratio of 3.5. The results indicate a power of 1.2 kW can be be obtained with an expander efficiency of 63%. Increasing the volume ratio by longer scroll wraps could

increase the expansion ratio at which peak scroll efficiency is obtained to further improve the ORC efficiency. Finally, in 2013 Bracco et al. (2013) and Declaye et al. (2013) both experimentally characterised scroll expanders operating with R245fa. The former report optimal expander efficiencies between 70% and 75% for power outputs between 1 kW and 1.5 kW, whilst the latter report an expander efficiency of 75.7% and a power output of 2.1 kW.

Ultimately, despite the low cost, and simplicity of operating existing scroll compressors in reverse, the problems facing the implementation of scroll expanders within ORCs relate to a relatively low expander efficiency. This is affected by high friction losses, pressure drops and internal leakage flows. These can be reduced by reducing clearances, and re-designing the suction and discharge ports.

Although most research has focussed on the development of radial inflow turbines and scroll expanders, there is also interest in other expansion devices. Much of the development on twin-screw machines, both compressors and expanders, has occurred at City University over the last few decades (Stosic et al., 2003; Smith et al., 2005). Through collaboration with Electratherm this has led to the development of screw expanders that are cost effective within the 20 kW and 50 kW range (Leibowitz et al., 2006). In this paper a system is designed for a heat source at 90°C, with R124 as the working fluid. The resulting system generated 24 kW with an expander efficiency of 71%. Wang et al. (2011) developed a single-screw expander, and preliminary results indicate a generated power of 5 kW with an overall efficiency of 32.5%. Qiu et al. (2012) modified an air-motor into a rotary-vane expander for implementation within an ORC for biomass applications. This expander has the advantages of a simple structure, easy manufacturing and low cost, but are not designed to operate with refrigerants, whilst the rotational speeds of these systems can be hysteretic. Their results indicate a power output of 0.86 kW with an expander efficiency of 53.9%.

The experimental systems developed within the literature have been summarised in Figure 2.8 in terms of power output and expander efficiency. Most notably it is clear that the scroll is the dominant expander technology for output powers below 3 kW, and the efficiency for these expanders is generally between 60% and 75%. Above this mark there has been limited development of scroll expanders. For powers above 20 kW screw expanders can achieve a reasonable performance, however they remain untested at lower

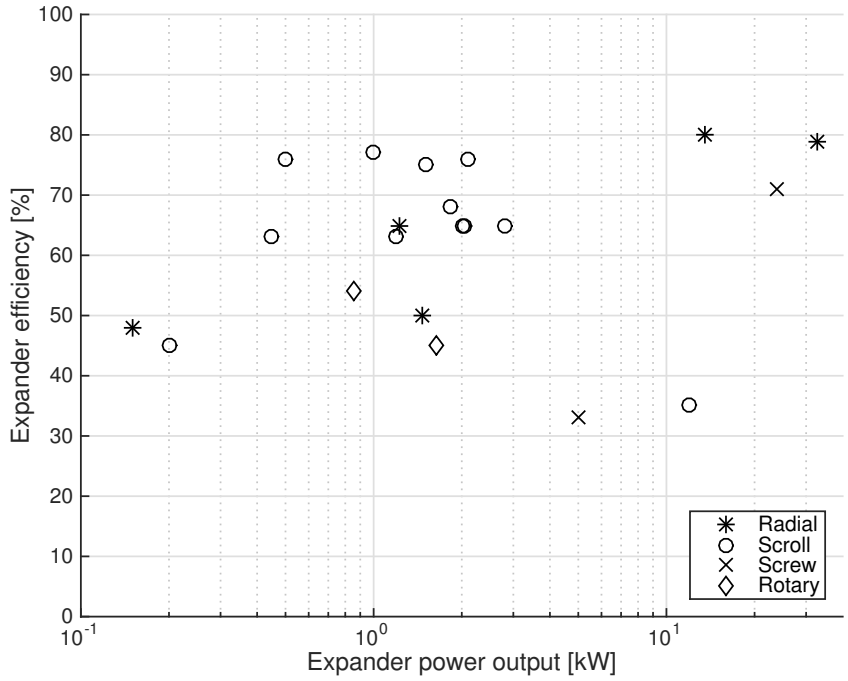

Figure 2.8: Summary of small-scale experimental ORC systems in terms of the generated power and expander efficiency.

powers. Furthermore, it is expected that as the power output reduces, and therefore screw size reduces, the relative clearances increase leading to higher leakage flows which will reduce the efficiency of the screw expander.

Comparatively, radial inflow turbines can obtain high efficiencies of around 80%, for power outputs of 10 kW and above. Below this point efficiency deteriorates, as indicated in Figure 2.8, presumably due to increasing clearance and viscous losses. The result of this literature review therefore indicates that at the power output of around 10 kW, the suitability of screw and scroll expanders has yet to be proved, whilst the development of an efficient radial turbine is a feasible proposition. Furthermore, it should be reiterated that scroll and screw expanders are obtained from the reverse operation of existing compressors, whilst a turbine designed specifically for an ORC could obtain a higher efficiency. It is also worth noting that the experimental studies on ORC turbines did not place any emphasis on turbine design, suggesting that there is room for further improvement.

2.4 Design and analysis of ORC radial inflow turbines

Radial inflow turbines are used in a large range of applications, covering a large range of power outputs, mass flow rates and rotational speeds (Dixon, 2010). Much of the development of these turbines is attributed to research conductied in the 1960's, particularly at NASA who implemented radial turbines within a Brayton cycle for space power systems (Wood, 1963; Kofskey and Wasserbauer, 1966; Nusbaum and Kofskey, 1969; Rohlik, 1968). Nowadays, the most significant interest in radial turbines is concerned with automotive turbocharges. However, as previously shown, with the ability to generate a greater work per stage than an axial turbine, and being able to operate with relatively low working fluid flow rates, there is a significant interest in utilising them as single stage ORC expanders.

2.4.1 Background theory

The expansion of the working through a radial inflow turbine occurs through a number of components, and the construction of these components is shown in Figure 2.9. The thermodynamic process can also be summarised using an enthalpy-diagram, and this is demonstrated in Figure 2.10.

The working fluid first enters a volute (station 1) which distributes the flow evenly around the periphery of the stator inlet (station 2) whilst introducing a tangential velocity component. The flow then accelerates through the stationary nozzle guide vanes (station 2 to 3) which are designed to deliver the flow to the rotor inlet (station 4) with a large tangential velocity component, and at the desired flow angle. In reality, the flow angle will change due to the expansion between the stator outlet, and rotor inlet, and this is labelled as the stator-rotor interspace (station 3 to 4). After entering the rotor inlet, the flow then expands through the rotating rotor, producing torque on the rotor shaft, before exiting at the rotor outlet (station 5). After exiting the rotor a diffuser can then be used to recover some of the kinetic energy of the flow, and increase the static pressure (station 5 to 6).

It should be noted that unlike the preceding stations, the variation in radius at the rotor exit (station 5) means that the flow conditions at the rotor exit cannot be assumed to be uniform. It is therefore important to select a suitable reference radius at which to take the relevant velocities and thermodynamic properties. The convention within radial

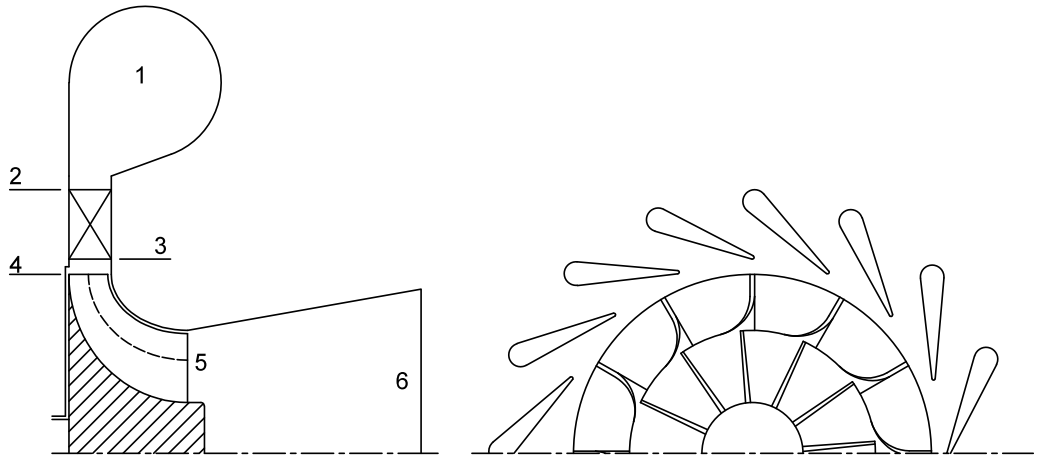

Figure 2.9: Geometry of the radial turbine.

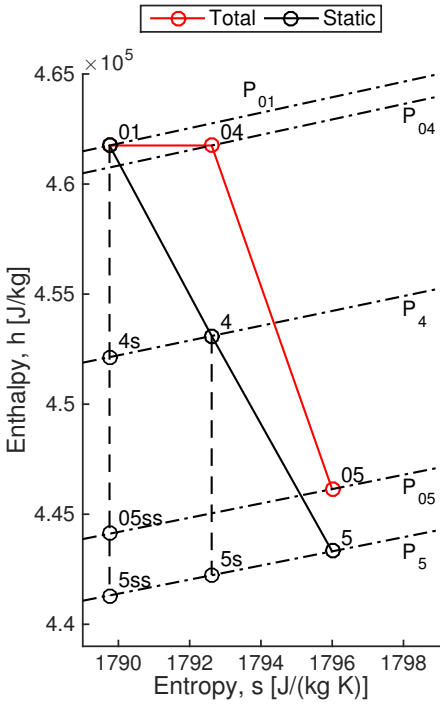

Figure 2.10: Expansion process through a turbine shown on an enthalpy-entropy diagram.

turbine design is to take the root mean square (rms) radius, and this convention is followed throughout this thesis. For simplicity when the subscript '5' is used to describe the rotor exit station, it therefore automatically corresponds to the value taken at the rms radius.

Of all the components, the turbine rotor is the most critical since it produces the work. The central aspect to the design of this rotor is the design of the rotor inlet and rotor outlet velocity triangles. Typical velocity triangles for a radial turbine are shown in Figure 2.11, along with the selected notation.

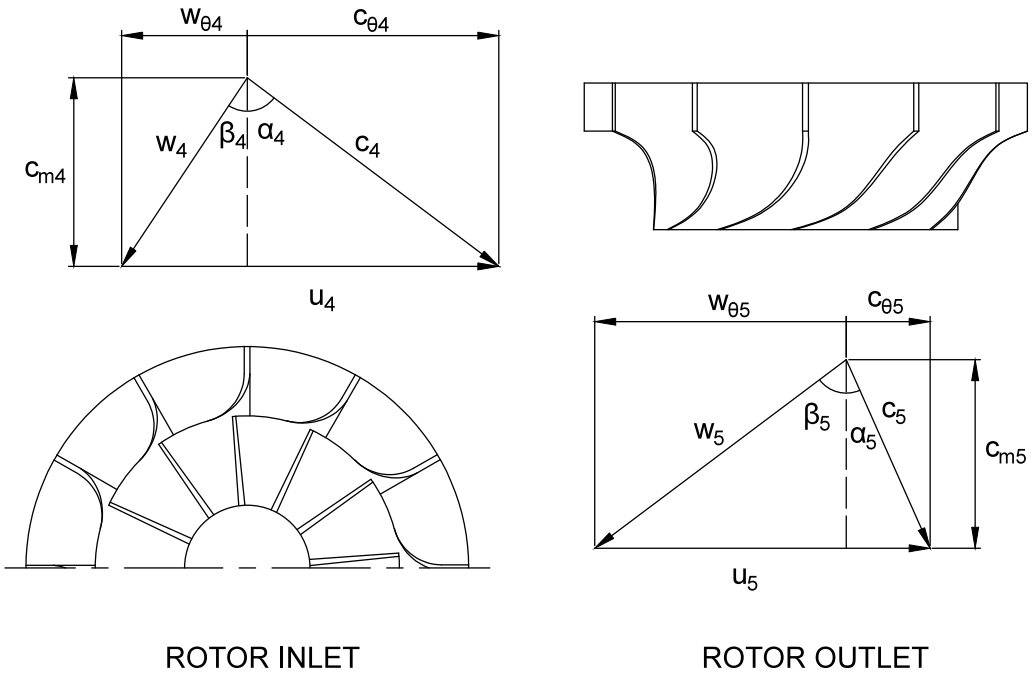

Figure 2.11: Geometry of the radial turbine rotor and velocity triangles.

The fluid enters the rotor inlet with an absolute velocity c_4, at an absolute flow angle α_4. This velocity is made up of a meridional velocity component $c_{\mathrm{m}4}$ and an absolute tangential velocity component $c_{\theta 4}$. It is assumed that the flow has no axial velocity and therefore $c_{\mathrm{m}4}$ is equal the radial velocity into the rotor. The rotor is rotating with a blade velocity u_4, which by vector subtraction supplies the velocity of the fluid relative to the rotation w_4. This is composed of the same meridional velocity, but with a relative tangential velocity component $w_{\theta 4}$. The relative flow angle is then denoted as β_4.

By the same discussion, the velocity triangle at the rotor oulet (taken at the rms radius) is obtained. Here the flow is assumed to leave the rotor axially, albeit with a absolute tangential velocity. Therefore the fluid has no radial velocity and the meridional velocity $c_{\mathrm{m}5}$ is equal to the axial velocity of the fluid.

Turbine isentropic efficiency

The overall aerodynamic performance of a turbine is described by the isentropic efficiency, which in general can be defined as the ratio of the work produced by the turbine to the maximum work that could be produced if the expansion was isentropic.

At the turbine exit the working fluid still contains kinetic energy, and therefore two definitions of the isentropic efficiency are required depending upon whether this exhaust

kinetic energy is recovered or not. The first definition is the total-to-total efficiency (Equation 2.11). This efficiency assumes that the kinetic energy of the fluid is recovered, and therefore the maximum work that could be produced is the isentropic enthalpy drop corresponding to total-to-total conditions.

$$\eta_{\mathrm{tt}} = \frac{h_{01} - h_{05}}{h_{01} - h_{05\mathrm{ss}}} \tag{2.11}$$

The second efficiency is the total-to-static efficiency (Equation 2.12). This efficiency assumes that the kinetic energy of the fluid at the turbine exit is lost, and therefore the maximum work is now the enthalpy drop corresponding to total-to-static conditions.

$$\eta_{\mathrm{ts}} = \frac{h_{01} - h_{05}}{h_{01} - h_{5\mathrm{ss}}} \tag{2.12}$$

Euler's turbine equation

Constructing a control volume around the rotor and then applying Newton's second law of motion, the torque τ generated on the rotor shaft can be equated to the rate of change of angular momentum of the fluid. For the steady flow through the rotor with a mass flow rate $\dot{m}$ this can expressed as follows, where r is the radius.

$$\tau = \dot{m}(r_4 c_{\theta 4} - r_5 c_{\theta 5}) \tag{2.13}$$

The rate of work done on the rotor by the fluid is then the product of the torque and rotational speed ω (Equation 2.14). Considering that the product $r\omega$ is equal to the blade velocity u, Euler's turbine equation is then obtained (Equation 2.15).

$$W = \tau\omega = \dot{m}\omega(r_4 c_{\theta 4} - r_5 c_{\theta 5}) \tag{2.14}$$

$$W = \dot{m}(u_4 c_{\theta 4} - u_5 c_{\theta 5}) \tag{2.15}$$

After applying some trigonometry to the velocity triangles shown in Figure 2.11 an expression for uc_θ can be obtained. Therefore an alternative expression for the work done on the rotor per unit mass can be obtained.

$$\frac{W}{\dot{m}} = \frac{1}{2}\left[(u_4^2 - u_5^2) - (w_4^2 - w_5^2) + (c_4^2 - c_5^2)\right] \tag{2.16}$$

Equation 2.16 is a useful equation to highlight the flow conditions that lead to a high specific work output. The first term $(u_4^2 - u_5^2)$ is a major contribution to the high specific power of a radial inflow turbine ($u_4 > u_5$), which highlights their advantage over outward flow ($u_4 < u_5$), and axial flow ($u_4 = u_5$) designs. Furthermore, a positive contribution to the specific power is obtained from accelerating the relative flow through the turbine ($w_5 > w_4$), whilst the absolute flow at the rotor outlet should be minimised ($c_5 < c_4$).

Rothalpy

Since the work per unit mass is equal to the change in total enthalpy ($h_{01} - h_{05}$), and the total enthalpy in the stator remains constant ($h_{01} = h_{04}$), the following can be deduced from Equation 2.15.

$$h_{04} - u_4 c_{\theta 4} = h_{05} - u_5 c_{\theta 5} \tag{2.17}$$

Considering that the total enthalpy is given by the static enthalpy and absolute flow velocity ($h_0 = h + \frac{1}{2}c^2$), whilst applying the same trigonometry used to deduce Equation 2.16, Equation 2.18 can be obtained. The result is a parameter called rothalpy I that appears to remain constant during the expansion through the rotor. This can be thought of as the summation of the total relative enthalpy ($h + \frac{1}{2}w^2$), and the energy associated with the blade velocity ($\frac{1}{2}u^2$).

$$h_4 + \frac{1}{2}\left(w_4^2 - u_4^2\right) = h_5 + \frac{1}{2}\left(w_5^2 - u_5^2\right) = I \tag{2.18}$$

Isentropic velocity ratio

Within turbomachinery the spouting velocity c_s is defined as the velocity that has a kinetic energy equal to the isentropic enthalpy drop through the turbine. Although this can be defined as either the total-to-total or total-to-static isentropic enthalpy drop, the more common definition used for radial turbines is the total-to-static term. For known inlet conditions, and a known total-to-static pressure ratio, c_s is easily obtained.

$$\frac{1}{2}c_\mathrm{s}^2 = h_{01} - h_{5\mathrm{ss}} \tag{2.19}$$

Considering Euler's equation, a nominal design is obtained when the flow enters the

rotor with no relative tangential velocity component (i.e. $c_{\theta 4} = u_4$), and leaves with no absolute tangential velocity component (i.e. $c_{\theta 5} = 0$). Therefore the work per unit mass is given by Equation 2.20. For an ideal turbine, this work per unit mass is also equal to the total-to-static isentropic enthalpy drop.

$$\frac{W}{\dot{m}} = u_4^2 = h_{01} - h_{5\mathrm{ss}} \tag{2.20}$$

From these parameters, the ratio of the blade velocity u_4 to the spouting velocity is easily obtained, and this is defined as the isentropic velocity ratio ν_{ts}.

$$\nu_{\mathrm{ts}} = \frac{u_4}{c_{\mathrm{s}}} = \frac{1}{\sqrt{2}} = 0.707 \tag{2.21}$$

For real turbine operation, optimal values for ν_{ts} are found to lie within the range $0.68 < \nu_{\mathrm{ts}} < 0.71$ (Dixon, 2010).

Designing the rotor velocity triangles

A key aspect of designing a radial inflow turbine is the design of the rotor inlet and outlet velocity triangles. To construct these a number velocity ratios can be used. Moustapha et al. (2003) recommends the use of three ratios, the first of which is the blade loading coefficient Ψ. This is defined as the ratio of absolute tangential velocity $c_{\theta 4}$, to the rotational velocity u_4. After some rearranging it can be shown Ψ is also related to η_{ts} and ν_{ts}.

$$\Psi = \frac{c_{\theta 4}}{u_4} = \frac{\eta_{\mathrm{ts}}}{2\nu_{\mathrm{ts}}^2} \tag{2.22}$$

Designing an ideal turbine with no swirl at the rotor outlet (i.e. $\eta_{\mathrm{ts}} = 1,\ \nu_{\mathrm{ts}} = 0.707$), implies $\Psi = 1$, so a more realistic value of η_{ts} therefore implies a value of Ψ slightly less than 1. The second velocity ratio of interest is the flow coefficient Φ, and this is defined as the ratio of the meridional velocity at the rotor outlet $c_{\mathrm{m}5}$, to the blade velocity u_4. Rodgers and Geiser (1987) correlated ν_{ts} and Φ against η_{ts} and found that optimal turbine performance was obtained when $\Phi = 0.25$.

$$\Phi = \frac{c_{\mathrm{m}5}}{u_4} \tag{2.23}$$

The third velocity ratio is the meridional velocity ratio ξ, and this is defined as the ratio of the meridional velocities at the rotor inlet and rotor outlet (i.e. $c_{\mathrm{m}4}$ and $c_{\mathrm{m}5}$). Generally, this has a value near unity (Moustapha et al., 2003).

$$\xi = \frac{c_{\mathrm{m}5}}{c_{\mathrm{m}4}} \tag{2.24}$$

It is also important to note another important design parameter, which is the incidence angle at the rotor inlet β_4. Experience has suggested that optimal performance is obtained when this angle is between $-20°$ and $-40°$ (Dixon, 2010). The use of Ψ, Φ and ξ does not allow direct control over this important parameter, and this has led to another feasible way to design the velocity triangles which involves directly specifying α_4 and β_4 (Atkinson, 1998; Aungier, 2006). However, by directly specifying α_4 and β_4 the designer does not have control over Ψ. It therefore seems that the decision to use velocity ratios, or to directly specify the flow angles, is largely a matter of preference, but it is important for the designer to verify after producing a design that the uncontrolled parameters remain within recommended limits.

Loss coefficients

The losses that occur within the stator and rotor passages can be accounted for by considering an enthalpy loss coefficient ζ. These are expressed as the ratio of the difference in enthalpy between an isentropic and real expansion, to the kinetic energy of the flow. The stator loss coefficient ζ_{N} is based on the absolute velocity of the fluid, whilst the rotor loss coefficient ζ_{R} is based on the relative flow velocity.

$$\zeta_{\mathrm{N}} = \frac{h_4 - h_{4\mathrm{s}}}{\frac{1}{2}c_4^2} \tag{2.25}$$

$$\zeta_{\mathrm{R}} = \frac{h_5 - h_{5\mathrm{s}}}{\frac{1}{2}w_5^2} \tag{2.26}$$

Alternatively, the stator losses can be defined by the stator isentropic efficiency η_{N} (Equation 2.27). Combining this with Equation 2.25 a simple relationship between ζ_{N} and η_{N} is found (Equation 2.28).

$$\eta_{\mathrm{N}} = \frac{h_{04} - h_4}{h_{04} - h_{4\mathrm{s}}} \tag{2.27}$$

$$\eta_{\mathrm{N}} = \frac{1}{1 + \zeta_{\mathrm{N}}} \tag{2.28}$$

For the rotor a similar expression cannot be derived because ζ_{R} is based on the relative velocity instead of the absolute. However, the rotor velocity ratio ϕ is introduced which is the ratio of the actual relative velocity w_5 to the relative velocity that would occur if the expansion through the rotor was isentropic $w_{5\mathrm{s}}$. From this a relation between ζ_{R} and ϕ can be obtained (Equation 2.30).

$$\phi = \frac{w_5}{w_{5\mathrm{s}}} \tag{2.29}$$

$$\zeta_{\mathrm{R}} = \frac{1}{\phi^2} - 1 \tag{2.30}$$

Specific speed and specific diameter

Two important design parameters that are often used during preliminary rotor design are the specific speed N_{s} and specific diameter D_{s}. These parameters are non-dimensional parameters that give an indication of the required rotor rotational speed ω, and rotor diameter D, to expand the specified fluid from the specified inlet conditions to the desired outlet conditions. These parameters are related to the volumetric flow rate at the rotor exit V, and the ideal enthalpy drop across the turbine Δh_{s}.

$$N_{\mathrm{s}} = \frac{\omega V^{1/2}}{\Delta h_{\mathrm{s}}^{3/4}} \tag{2.31}$$

$$D_{\mathrm{s}} = \frac{D \Delta h_{\mathrm{s}}^{1/4}}{V^{1/2}} \tag{2.32}$$

Performance prediction

The off-design performance of a radial inflow turbine is described by performance maps which plot how turbine isentropic efficiency and mass flow rate vary with pressure ratio and rotational speed. These performance maps should be generated through experimentation, although in the absence of an experimental test-rig they could also be generated using CFD. Having generated a performance map, it only applies for the rotational speeds,

turbine total inlet conditions, and working fluid that were used to generate the map. When considering turbine performance within cycle analysis this is not particularly helpful. To overcome this limitation, similitude theory is used to non-dimensionalise the performance map. Similitude theory has been successfully validated and is widely applied to ideal gases such as air (Moustapha et al., 2003). With care it can also be used to estimate the performance following a change of the working fluid, so long as the variation in thermodynamic properties of the two fluids is not significantly different (Aungier, 2006). The full mathematical details of similitude theory are discussed in detail in Chapter 5.

Loss models provide an alternate method to assess radial turbine performance. These require significantly less resources than experimental or CFD methods, but the accuracy is penalised by using one-dimensional flow concepts to simulate highly three-dimensional flow. These loss models break the loss coefficient previously described (i.e. ζ_R) into a number of different loss mechanisms, and details of these models can be found in Moustapha et al. (2003) and Aungier (2006). The loss mechanisms can be summarised as follows:

- Incidence losses occur the when the flow enters the rotor with a relative flow angle that is different to the optimal incidence angle, thus causing recirculation behind the rotor leading edge.

- The passage loss accounts for losses within the rotor passage and considers losses due to secondary flows and the growth of boundary layers on the rotor blade surfaces.

- Tip clearance losses occur due to the clearance gap that exists between the rotor blade shroud and the rotor casing. This gap creates a leakage path between the pressure and suction sides which introduces secondary flows within the rotor passage.

- Trailing edge losses occur as the flow expands from the rotor throat to a location just downstream of the rotor trailing edge. This sudden increase in area reduces the meridional velocity and results in a total pressure loss.

- Supersonic conditions will occur when the flow chokes at either the rotor or stator throat, and this will generate shock waves within the turbine.

- Windage loss is a parasitic loss that absorbs some of the work produced by the rotor, and is caused due to the clearance gap that exists between the rotor back face and the rotor casing.

2.4.2 Design of ORC radial inflow turbines

In Section 2.3 a number of experimental studies on ORC radial turbines were discussed. However, despite encouraging results from these articles, there was little emphasis on the turbine design, suggesting there is further room for improvement. Furthermore, from the literature it is clear that the design of radial inflow turbines operating with ideal gases is well understood, and this design process is summarised in a number of key texts (Whitfield and Baines, 1990; Moustapha et al., 2003; Dixon, 2010). However, much of this analysis relies on ideal gas assumptions which are not relevant to organic fluids. Therefore it is clear that to realise the potential of higher turbine efficiencies than screw or scroll expanders, it is necessary to develop radial inflow turbine design methods that are suitable for these non-ideal organic fluids. Much like the ORC thermodynamic modelling, the availability of accurate fluid properties remains a prerequisite to completing this analysis, and again the designer can turn to tools such as REFPROP, CoolProp or cubic equations of state for this purpose.

Badr et al. (1984) presented an early study on expander design for ORCs and characterised expanders using specific speed and specific diameter. This analysis cannot be used to obtain a complete rotor design, but it is useful during preliminary working fluid studies. Sauret and Rowlands (2011) used this method to compare how different working fluids effect the required turbine diameter and rotational speed. The results showed that for the same heat source the resulting expander design could change significantly; the optimal designs operating with R134a and n-pentane had rotor diameters of 74.6 mm and 144.3 mm respectively.

A more complete design methodology, often called a meanline design model, considers the velocity triangles and fluid properties at a variety of locations throughout the turbine. In terms of the rotor design, this corresponds to sizing the rotor inlet and rotor outlet to pass the required mass flow rate at the required thermodynamic conditions. Fiaschi et al. (2012) developed such a model that was coupled with REFPROP. This methodology was used to develop a 50 kW rotor for a range of working fluids, each with a fixed turbine inlet temperature of 147°C. Both Ventura et al. (2012) and Pan and Wang (2013) develop similar methodologies, however both papers also include loss models to predict the turbine performance. Later, Fiaschi et al. (2015) updated his previous work to include these loss models, whilst a more detailed model was also constructed for the design of the nozzle

guide vanes. In fact the combination of a meanline design model, coupled with these loss models, has recently been considered by a number of authors (Wang et al., 2013b; Hu et al., 2015; Rahbar et al., 2015; Erbas and Biyikoglu, 2015). Both Wang et al. (2013b) and Hu et al. (2015) have coupled the meanline turbine model with an ORC thermodynamic model, thus allowing the effect of varying turbine performance to be considered within cycle analysis studies. The aim here is to move away from the decoupled approach, thus allowing more optimal systems to be developed in a shorter time frame. In comparison, Rahbar et al. (2015) and Erbas and Biyikoglu (2015) have both coupled the meanline design model with an optimiser which allows the various design inputs to be optimised to obtain the best turbine design. Rahbar et al. (2015) completed the optimisation using a genetic algorithm to maximise the turbine efficiency for a range of different working fluids. Erbas and Biyikoglu (2015) also completed the optimisation using a genetic algorithm but considered instead a multi-objective optimisation. The first objective was to maxmise the design point efficiency, whilst the second objective was to optimise the part-load efficiency.

What becomes clear from these studies is that a number of researchers have developed meanline models for the design of ORC radial inflow turbines, and a considerable focus has been the inclusion of loss models. However, it is worth noting that these loss models are based on empirical data that has been obtained from tests completed on radial turbines operating with ideal gases. Therefore they have not been validated for the non-ideal gases found within ORC turbines. Indeed, Uusitalo et al. (2013) comments that to accurately evaluate the achievable turbine efficiency requires experimental information which is currently lacking. Another limitation with the meanline models that have been developed is that the main consideration is the design of the velocity triangles, and rotor dimensions, at the rotor inlet and outlet. Whilst these remain important, the rotor passage must also be effectively designed to ensure an efficient expansion. Typically this has either not been considered, or has been the result of more advanced techniques such as coupling a CFD solver to an optimiser.

Another important consideration when designing ORC turbines is the low speed of sound of the working fluid. At high pressure ratios this can result in supersonic flow, most notably within the stator passage. Up until now the papers reviewed have considered turbines for low and medium temperature ORC applications, and therefore the flow at the rotor inlet is either subsonic or transonic. Under such conditions a conventional stator

blade can be implemented, albeit accounting for any supersonic turning that may occur between the stator throat and rotor inlet (Moustapha et al., 2003). Having said this, the correct geometrical construction of the stator is important to ensure the flow enters the rotor at the correct flow angle, and this is something that has not been well addressed within the previously studies.

For higher temperature applications, such as waste heat recovery from internal combustion engines, a supersonic stator design is required. These stators blades are constructed with a subsonic converging section which accelerates the flow to the choked conditions, followed by a diverging section which expands the flow isentropically to the desired Mach number. Examples of such stator designs are given by Pasquale et al. (2013) and Wheeler and Ong (2013). The design of the rotor for these high temperature ORC turbines largely follows the same format as for low temperature applications, and examples can be found in Lang et al. (2013) and Costall et al. (2015). One point to note though is the significant change in density of the fluid from the rotor inlet to rotor outlet, which can result in very small blade heights at the rotor inlet, and very large blade heights at the rotor outlet, as observed in these studies.

Although not directly related to radial inflow turbines, it should also be mentioned that a large amount of work at the Politecnico di Milano has focussed on the design of turbomachines for high temperature ORCs. The design methodology combines a meanline design code, with a CFD throughflow code (Pini et al., 2013). This model has been used to design a novel 10 kW multi-stage radial outflow turbine with an expansion ratio of 45 (Casati et al., 2014), and the performance of this turbine has been investigated further in a more recent paper (Persico et al., 2015). The interest in this type of expander is that for high temperature applications with very large pressure ratios, the expansion process can be split over a number of subsonic, or transonic, stages instead of a single highly-supersonic radial inflow turbine stage.

2.4.3 CFD studies on ORC turbines

The application of computational fluids dynamics (CFD) to predict the performance of ORC turbine components goes hand-in-hand with their design. However, with the introduction of non-ideal working fluids this introduces certain complexities that need to be considered, and indeed the development of CFD techniques for ORC turbines has received

a fair amount of attention. Furthermore, as the critical point of an organic fluid is approached some fluids exhibit so-called non-classical behaviour, where classical behaviour is inverted leading to expansion shocks, and compression fans (Colonna et al., 2006). Arguably, for low to medium temperature heat sources the cycle operation remains sufficiently far from the critical point such that this non-classical behaviour will be avoided, and so this discussion is outside the scope of this study. None the less it remains an interesting topic and readers should refer to Colonna et al. (2006), Wheeler and Ong (2013) and Galiana et al. (2015) for more information.

In terms of CFD development, Hoffren et al. (2002) tailored an existing Navier-Stokes solver to apply to real gases and simulated the flow through a supersonic turbine stator. The solver required property tables to be constructed prior to the simulation which defined the relevant thermodynamic properties as a function of temperature and density. The results were found to agree reasonable well with one-dimensional design calculations. Colonna et al. (2006) completed CFD simulations using an in-house Euler solver, and investigated the effects of different equations of state on the resulting flow field. The results show that computations using either the Span-Wagner or Peng-Robinson-Stryjek-Vera eqautions were very similar, whilst a significant difference was found if the ideal gas law is used. Harinck et al. (2010) also simulated the flow within a supersonic ORC turbine stator, and compared the commercial Fluent code to two in-house codes, in addition to comparing the $k-\omega$ and $k-\epsilon$ turbulence models. It was found that the commercial code resulted in a much lower stator isentropic efficiency when compared to the in-house solvers. It was also found that the choice between the $k-\omega$ or $k-\epsilon$ turbulence model only had a minor influence on the flow field. These results were used to stress the need for experimental validation. Later, Harinck et al. (2013) used ANSYS CFX to complete a steady-state three-dimensional RANS simulation of an ORC turbine, and used REFPROP to generate property tables that were used during the simulation. The need for experimental validation was reiterated, however a qualitative analysis of the results resulted in an acceptance of the constructed model. Wheeler and Ong (2014) completed a similar study but compared steady-state and unsteady simulations of a transonic ORC turbine. Since experimental data on ORC turbines was not available, the solver was first validated considering a conventional gas-turbine radial turbine. For the two ORC turbines considered, the unsteady simulations resulted in a reduction in the turbine isentropic total-to-static

efficiency of 1.25% and 1.5% when compared to the steady-state simulations. This was attributed to a strong interaction between the stator trailing edge shocks and the rotor leading edge. Galiana et al. (2015) studied the trailing edge losses in ORC turbines in more detail. This study compared RANS and LES CFD simulations completed using Fluent to experimental results obtained using a Ludwieg tube. The application of LES showed a much better agreement with the experimental results than the RANS model.

Due to the interesting behaviour of organic fluids near the critical point, and the supersonic flows that are found within high temperature ORCs, much of the CFD analysis completed has been applied to these applications. For lower temperature applications Sauret and Gu (2014) completed a three-dimensional steady-state RANS simulation on an ORC turbine for geothermal applications. This simulation was completed using ANSYS CFX. The $k-\epsilon$ turbulence model was considered for robustness, whilst fluid properties were accounted for using the Peng-Robinson equation of state. However, the authors intended to replace this equation of state with REFPROP for future simulations. A similar study was also completed by Rahbar et al. (2014) who used CFD to evaluate rotor performance during the rotor design phase.

From this review of CFD studies, it is clear that a key issue to overcome is the availability of experimental test data for organic vapours, with which to validate CFD models. Alongside the experimental rig constructed by Galiana et al. (2015) a number of other authors are also in the process of constructing test rigs (Colonna et al., 2013; Spinelli et al., 2013; Reinker et al., 2015). No doubt these experimental test rigs will lead to further experimental data in the future. This will be important, not only validate the CFD solvers, but also to enhance our understanding of the behaviour of organic fluids within ORC turbines.

2.4.4 Off-design modelling of ORC radial inflow turbines

It was highlighted in Section 2.2.4 that a shortcoming within many papers is the assumption of a constant turbine efficiency. To overcome this, cycle analysis should be coupled with radial turbine off-design models. This is particularly true for small-scale systems where, due to the economy of scale, the same turbine may be implemented into a number of different ORC applications. Here the search for optimal cycle conditions may move turbine performance away from design conditions.

As described previously, turbine performance should be characterised experimentally. Whilst some studies have demonstrated experimental testing of small-scale low temperature ORC turbines (Inoue et al., 2007; Kang, 2012), limited off-design performance has been presented. More recently, experimental data has been used to generate performance curves, which were used for further cycle optimisation studies (Li et al., 2014). A similar study, but based on a scroll expander has also been undertaken (Declaye et al., 2013). In the absence of experimental testing, Sauret and Gu (2014) generated performance maps using CFD.

A number of authors have applied similitude theory to predict ORC turbine performance within off-design steady-state and dynamic models. Sun and Li (2011) implemented a model to predict turbine part-load operation which was originally developed for the part-load operation of gas turbines. Li et al. (2013) implemented a very similar model to investigate the leaving loss within ORC turbines at off-design conditions. Calise et al. (2013) also used similitude theory within an off-design assessment of turbine performance, whilst Manente et al. (2013) implemented the same model for a dynamic model used for control. However, a major shortcoming within all of these papers is that similitude is implemented using simplified non-dimensional parameters, derived from ideal gas relationships. Following from the practice within ideal gas applications, Reynolds number effects are also neglected. To the author's knowledge the application of similitude theory to the real gases found within ORCs has not currently been investigated or validated. Despite this, evaluating the suitability of similitude theory to real gas expanders is a critical aspect within ORC cycle analysis. If proven, it will permit turbine performance to be accurately predicted over a range of operating conditions, using alternative working fluids, using only one performance map. This significantly aids cycle design and optimisation, reducing the requirements for CFD or experimental studies to generate accurate performance maps. This is particularly pertinent for small-scale applications, since it is likely that the same turbine may be used within a number of different ORC configurations.

Loss models provide an alternate method to assess radial turbine performance. However, as discussed previously, these loss models are empirically based and their suitability to real gas applications has yet to be proven. The significance of turbine loss models for axial ORC turbines has been discussed by Klonowicz et al. (2014), but further work for radial turbines is required. If similitude is not found to be accurate, the further development

and validation of ORC radial turbine loss models will be essential.

2.5 Conclusions

From this review of the current commercial and research status of ORC technology, it is clear there is a significant interest in the development of small-scale systems for the conversion of solar energy, biomass and waste heat into useful power. Three key areas have been investigated, namely cycle modelling, expander selection and radial inflow turbines for ORCs. Within these three areas a number of key conclusions have been identified, and these are summarised below. These conclusions both reinforce the project objectives identified in Chapter 1, and highlight areas that should be addressed in order to deliver these objectives.

- The array of possible working fluids is vast, and there are a number of selection criteria to satisfy. There does not remain one optimal working fluid and therefore thermodynamic modelling and working fluid selection remain key aspects of any ORC project.

- The review of thermodynamic modelling has shown that both superheating and subcooling are detrimental to ORC performance. Furthermore, to derive optimal operating conditions the heat source stream must be included within the cycle modelling. Finally, although recuperation can improve the cycle efficiency, this may not be necessary for small-scale heat recovery applications.

- An ORC model needs to include individual component models. For cycle design these models must size the components, whilst for off-design these models need to predict component performance. For small-scale systems this is particularly true due to the requirement of implementing the same design into a number of different applications.

- It is important to couple the thermodynamic model and component models with an optimisation strategy to arrive at an optimal system configuration. A multi-objective optimisation should trade-off system performance against system complexity, however a major difficulty resides in the definition of a suitable objective function.

- Turboexpanders are the preferred expander for high power applications. For small-scale systems, volumetric expanders can be considered but these cannot match a radial inflow turbine in terms of expander efficiency. Furthermore, at a power output of 10 kW there appears to be a gap between the output of scroll and screw based cycles.

- Although the design of radial inflow turbines for ORCs has been considered within the literature, existing methods rely on empirical loss models that have not been validated for organic fluids. Furthermore, limited attention has been been placed on the three-dimensional geometry, which is equally important to obtain a high turbine efficiency.

- CFD analysis of ORC turbines requires an accurate thermodynamic model to account for variations in the fluid properties. Although there is a current lack of experimental validation, a number of authors have demonstrated the suitability of commercial codes such as ANSYS CFX and Fluent for the analysis of ORC turbines.

- Without validated loss models, the validation of similitude theory is critical to accurately predict the off-design performance of ORC turbines. To the authors knowledge this important aspect has not been investigated within the literature.

This page is left intentionally blank.

Chapter 3

Thermodynamic modelling and optimisation

3.1 Introduction

From the literature review it is clear that the development of an ORC thermodynamic model remains critical to any ORC development project. Not only should this model be able to determine the thermodynamic performance, but it must also consider the individual components in terms of either component sizing or component performance. Furthermore, a suitable multi-objective optimisation procedure should be developed which considers the trade-off between system performance and complexity. Ultimately, using this model a parametric study considering a variety of working fluids for a particular application can be undertaken, and this would lead to an optimal system configuration.

This chapter describes a model that addresses all of these points. The most significant contribution within this chapter is the development of a novel objective function that quantifies the trade-off between performance and complexity, without relying on economic models or compromising on the system power output. After describing the thermodynamic, component and optimisation models, a case study is evaluated for a small-scale low temperature ORC and a working fluid is recommended for this application. The research conducted within this chapter resulted in a publication in the Proceedings of the Institution of Mechanical Engineers, Part A: Journal of Power and Energy (White and Sayma, 2015a).

3.2 Structure of the ORC model

The ORC thermodynamic model developed is a steady state analysis program, written in FORTRAN. A schematic of the model is shown in Figure 3.1. The thermodynamic model contains a central cycle analysis function, connected to individual component models for the pump, evaporator, turbine and condenser. The central cycle analysis function completes the thermodynamic calculations such as determining fluid properties and cycle performance, whilst the individual component models determine the required heat transfer areas, the turbine rotational speed and the turbine rotor diameter.

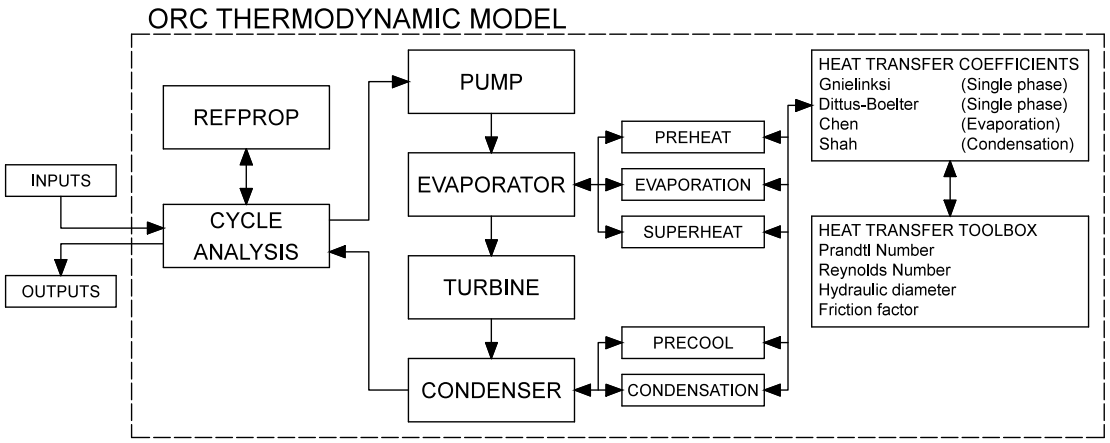

Figure 3.1: Schematic of the ORC thermodynamic model.

This modular approach is an advancement on many models considered within the literature, allowing component design aspects to be coupled with cycle performance. Furthermore, it enhances the model's versatility since it allows the future integration of alternative component models without requiring major modifications. For example, for cycle optimisation using existing components the heat exchanger and turbine models can be replaced with component off-design models, whilst alternative expanders such as volumetric devices, or different heat exchanger geometries such as plate, or shell-and-tube arrangements, could also be easily implemented. To further enhance the versatility of the model, low level functions are included for a variety of heat transfer coefficients, which connect to a heat transfer toolbox that can calculate the required non-dimensional parameters. The model is compiled along with the REFPROP subroutines allowing fluid properties for the heat source, heat sink and working fluid to be calculated.

3.3 Thermodynamic modelling

The ORC thermodynamic model predicts the performance of the overall cycle in addition to the individual components. To simplify the ORC simulation model a number of assumptions have been made. These are listed below, along with the reasoning behind each assumption.

- Cycle operation remains subcritical (i.e. below the critical point). Although supercritical cycles offer a better match to the heat source, the higher pressures increase system complexity and present safety concerns.

- The working fluid at the pump inlet is assumed to be a saturated liquid. In reality a small degree of sub-cooling will be required to prevent cavitation, however the impact of sub-cooling on cycle performance is small.

- For continuity within this thesis it is assumed that the expansion process always occurs through a turbine. However, the thermodynamic analysis presented here is equally applicable to volumetric expanders except for Section 3.3.4, which is specific to radial turbines.

- The working fluid at the turbine inlet is either a saturated or superheated vapour as two-phase conditions should be avoided for radial turbines. For this reason the fluid is also assumed to remain within the superheated vapour region during the expansion process. Any potential working fluids whose saturated vapour dome has a negative gradient will therefore require sufficient superheating.

- No phase change of the heat source or heat sink is permitted as this can significantly affect the size of the heat exchangers.

- Pressure losses are neglected within the cycle analysis. However, these are calculated after completing the heat exchanger design to verify the feasibility of the resulting heat exchanger geometry. In reality any pressure losses will increase the required pump work.

- The heat exchangers are assumed to be double-pipe counter-flow heat exchangers, as opposed to more realistic geometries such as plate or shell-and-tube. The aim of the heat exchanger model is to predict the required heat transfer area, enabling

a quantitative comparison of different cycle conditions and their impact on heat transfer area, instead of providing a fully optimised heat exchanger design.

- Heat losses to the surroundings are neglected.
- Steady state conditions are assumed.

The resulting ORC is represented on a temperature-entropy ($T-s$) diagram in Figure 3.2, along with the heat source and heat sink temperature profiles. This figure also displays the notation used throughout this chapter.

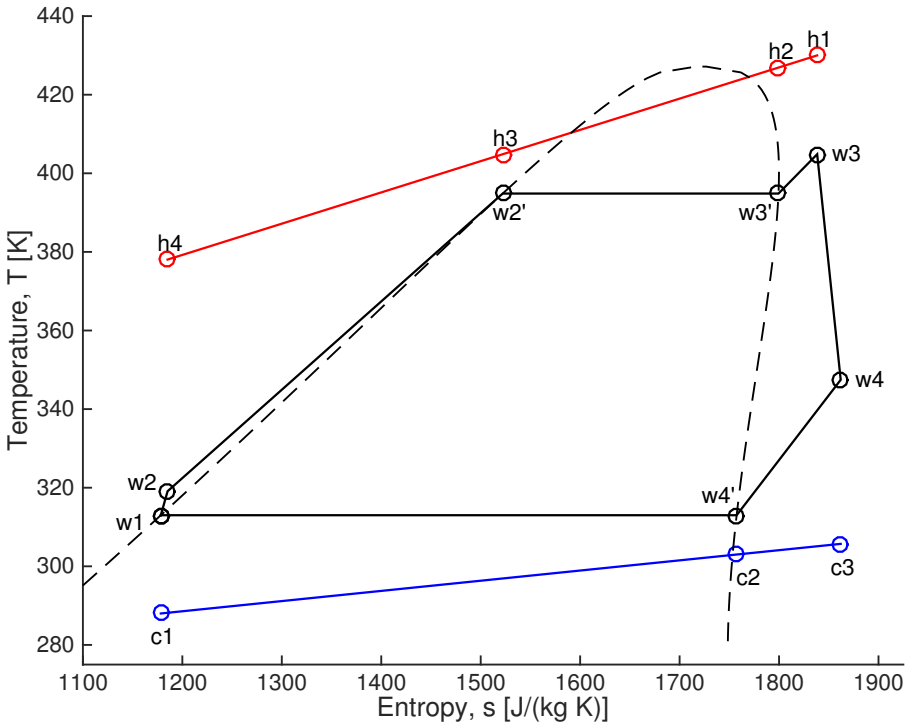

Figure 3.2: The subritical, superheated ORC represented on a T-s diagram along with the heat source and heat sink temperature profiles, and the designated notation.

There are a number of inputs required to simulate the ORC. The model requires a defined heat source and heat sink, and five thermodynamic variables, which can be used to control the cycle performance. Since the focus is on cycle design and component sizing, the pump and turbine efficiencies are both specified. Both the evaporator and condenser are modelled as double-pipe counter-flow heat exchangers with fixed pipe diameters and wall thicknesses. The heat exchanger sizing then determines the required pipe length. The required inputs are summarised as follows:

- The available heat source conditions
  - Heat source fluid
  - Input heat source temperature T_{h1}
  - Heat source pressure P_{h}
  - Heat source mass flow rate $\dot{m}_{\mathrm{h}}$
- The available heat sink conditions
  - Heat sink fluid
  - Input heat sink temperature T_{c1}
  - Heat sink pressure P_{c}
  - Heat sink mass flow rate $\dot{m}_{\mathrm{c}}$
- ORC thermodynamic variables
  - Working fluid
  - Condensation temperature T_{w1}
  - Pressure ratio PR
  - Amount of superheat ΔT_{sh}
  - Evaporator pinch point PP_{h}
- Component efficiencies
  - Pump isentropic efficiency η_{p}
  - Turbine isentropic efficiency η_{t}
- Heat exchanger dimensions
  - Inner diamaters $d_{\mathrm{i,h}}$, $d_{\mathrm{i,c}}$
  - Outer diameters $d_{\mathrm{o,h}}$, $d_{\mathrm{o,c}}$
  - Wall thicknesses t_{h}, t_{c}

After completing the cycle analysis, the thermodynamic model outputs a number of parameters that can be used to assess cycle and component performance. These are as follows.

- Net work produced W_{n}
- ORC cycle efficiency η_{o}
- ORC mass flow rate $\dot{m}_{\mathrm{w}}$
- Condenser pinch point PP_{c}
- Heat exchanger areas
  - Total evaporator area A_{h}
  - Total condenser area A_{c}
- Turbine model outputs
  - Turbine rotational speed N
  - Turbine rotor diameter D

3.3.1 Cycle analysis

Before the individual ORC components are individually modelled, the central ORC model first determines the majority of the working fluid properties within the cycle. The calculation of thermodynamic properties requires two state properties to be known, in addition to the working fluid. The two known properties can be any combination of temperature T, pressure P, enthalpy h, entropy s, density ρ and vapour quality q. Throughout this thesis, this calculation will be specified with the notation given by Equation 3.1, where $\mathbf{y}$ is a vector of the unknown properties, and x_1 and x_2 are the two known state properties. This has been formulated for a generic equation of state, although REFPROP is used within this model, which is the industry standard for determining fluid properties for a large range of fluids.

$$\mathbf{y} = \mathrm{EoS}(x_1, x_2, \mathrm{fluid}) \tag{3.1}$$

The pump inlet conditions (P_{w1}, h_{w1}, s_{w1}) are automatically defined by the input condensation temperature T_{w1}, and the selected working fluid. It is assumed that the fluid enters the pump as a saturated liquid so the vapour quality q_{w1} is set to 0.

$$[P_{\mathrm{w1}}, h_{\mathrm{w1}}, s_{\mathrm{w1}}] = \mathrm{EoS}(T_{\mathrm{w1}}, q_{\mathrm{w1}}, \mathrm{fluid}) \tag{3.2}$$

The pump compresses the working fluid from the inlet pressure to the outlet pressure defined by the input pressure ratio PR. The enthalpy after an isentropic compression h_{w2s} is obtained using the outlet pressure and inlet entropy.

$$P_{\mathrm{w2}} = P_{\mathrm{w1}} \times \mathrm{PR} \tag{3.3}$$

$$h_{\mathrm{w2s}} = \mathrm{EoS}(P_{\mathrm{w2}}, s_{\mathrm{w1}}, \mathrm{fluid}) \tag{3.4}$$

The isentropic efficiency of the pump η_{p} is defined as the ratio of the isentropic enthalpy change to the real enthalpy change. Therefore, if the isentropic pump efficiency is known, the pump outlet conditions are easily obtained.

$$h_{\mathrm{w2}} = h_{\mathrm{w1}} + \frac{h_{\mathrm{w2s}} - h_{\mathrm{w1}}}{\eta_{\mathrm{p}}} \tag{3.5}$$

$$[T_{\mathrm{w}2}, s_{\mathrm{w}2}] = \mathrm{EoS}(P_{\mathrm{w}2}, h_{\mathrm{w}2}, \mathrm{fluid}) \tag{3.6}$$

The evaporator uses the input heat source to raise the temperature of the working fluid from the pump outlet temperature, to the design turbine inlet temperature. This process can be broken into three distinct processes; single-phase preheating, two-phase evaporation and single-phase superheating. Assuming no pressure loss occurrs during each process, the pressure within the evaporator remains constant ($P_{\mathrm{w}3} = P_{\mathrm{w}2}$). Therefore the saturated liquid conditions (location w2′), and saturated vapour conditions (location w3′) can be obtained by setting the vapour quality equal to 0 and 1 respectively. The evaporator outlet conditions are supplied by the input superheat degree ΔT_{sh}.

$$[T_{\mathrm{w}2'}, h_{\mathrm{w}2'}, s_{\mathrm{w}2'}] = \mathrm{EoS}(P_{\mathrm{w}2}, q_{\mathrm{w}2'}, \mathrm{fluid}) \tag{3.7}$$

$$[T_{\mathrm{w}3'}, h_{\mathrm{w}3'}, s_{\mathrm{w}3'}] = \mathrm{EoS}(P_{\mathrm{w}3}, q_{\mathrm{w}3'}, \mathrm{fluid}) \tag{3.8}$$

$$T_{\mathrm{w}3} = T_{\mathrm{w}3'} + \Delta T_{\mathrm{sh}} \tag{3.9}$$

$$[h_{\mathrm{w}3}, s_{\mathrm{w}3}] = \mathrm{EoS}(T_{\mathrm{w}3}, P_{\mathrm{w}3}, \mathrm{fluid}) \tag{3.10}$$

The turbine is the most critical component within the ORC. The high pressure, high temperature working fluid vapour expands to the condensation pressure ($P_{\mathrm{w}4} = P_{\mathrm{w}1}$) producing work. The turbine isentropic efficiency η_{t} is defined as the ratio of the real enthalpy change across the turbine, to the enthalpy change for an isentropic expansion. The enthalpy after an isentropic expansion $h_{\mathrm{w}4\mathrm{s}}$ is determined using the outlet pressure and inlet entropy. If the expander efficiency is known, the turbine outlet conditions are therefore obtained.

$$h_{\mathrm{w}4\mathrm{s}} = \mathrm{EoS}(P_{\mathrm{w}4}, s_{\mathrm{s}3}, \mathrm{fluid}) \tag{3.11}$$

$$h_{\mathrm{w}4} = h_{\mathrm{w}3} - \eta_{\mathrm{t}}(h_{\mathrm{w}3} - h_{\mathrm{w}4\mathrm{s}}) \tag{3.12}$$

$$[T_{\mathrm{w}4}, s_{\mathrm{w}4}] = \mathrm{EoS}(P_{\mathrm{w}4}, h_{\mathrm{w}4}, \mathrm{fluid}) \tag{3.13}$$

Finally, the condenser then rejects the heat still contained within the working fluid to a cold sink, lowering the temperature from the turbine outlet temperature to the con-

densation temperature, before converting the fluid from a saturated vapour to a saturated liquid. This process is split into two processes, single-phase precooling and two-phase condensation. Again, assuming no pressure loss, the pressure within the condenser remains constant ($P_{w1} = P_{w4}$), therefore the saturated vapour conditions (location w4′) are obtained by setting the vapour quality equal to 1.

$$[T_{w4'}, h_{w4'}, s_{w4'}] = \text{EoS}(P_{w4}, q_{4'}, \text{fluid}) \tag{3.14}$$

The work absorbed by the pump W_p, the work produced by the turbine W_t, and the heat absorbed in the evaporator Q_h, all expressed per unit mass flow rate $\dot{m}_w$, are then given by a change in enthalpy (Equations 2.1 - 2.4). The net work W_n is then the difference between the turbine and pump work, and the thermal efficiency η_o is given by Equation 2.5.

3.3.2 Pump modelling

Throughout this research, the pump is modelled assuming a constant value for η_p. This keeps the pump modelling simple, allowing the pump outlet conditions to be calculated using Equation 3.5. Reductions in η_p will result in a higher amount work being absorbed by the pump leading to a reduction in both W_n and η_o.

By completing a simple cycle analysis study the sensitivity of the cycle performance to variations in η_p can be examined. Following from the literature review that showed R245fa to be a popular working fluid for low temperature applications, this has been selected as the working fluid. Furthermore, there has been shown to be little benefit in superheating ORCs so only a small superheat ($\Delta T_{sh} = 2$ K) has been allowed to ensure full vaporisation at turbine inlet. A target turbine isentropic efficiency has been set at $\eta_t = 80\%$, whilst the condensation temperature has been set to $T_{w1} = 313$ K. With these fixed inputs, the analysis outlined in Section 3.3.1 was undertaken for a range of pump efficiencies and pressure ratios. A baseline of $\eta_p = 70\%$ was selected and the percentage deviations in W_n and η_o for changes in η_p were obtained at each PR. The results are shown in Figure 3.3.

From this figure it is clear that if η_p remains between 50% and 90% the percentage deviation in η_o for a PR of 6 is small, ranging from -1.7% to $+1.0\%$. This corresponds to η_o ranging from 10.9% to 11.2%. Similarly the percentage deviation in W_n ranges between

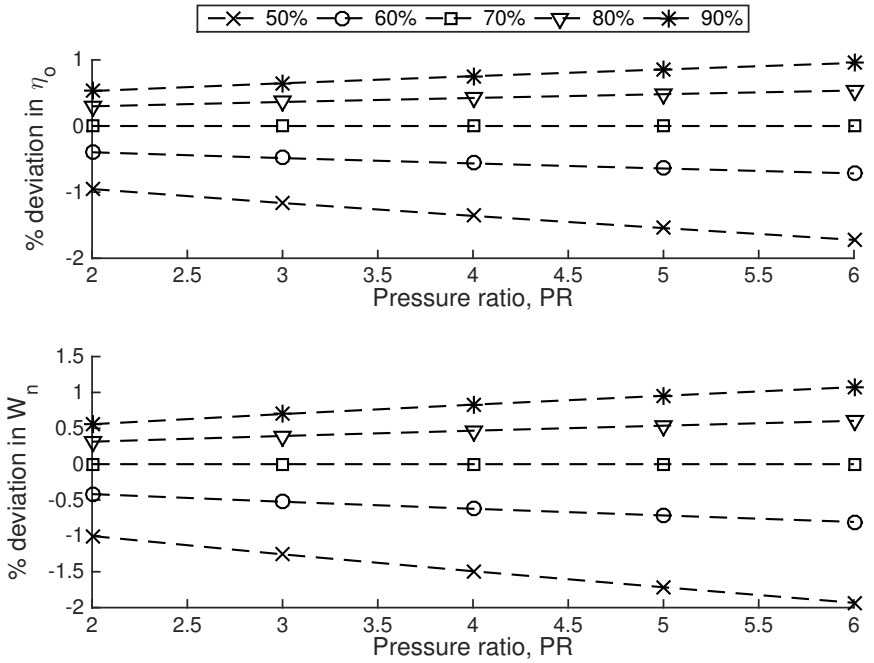

Figure 3.3: Sensitivity of the cycle performance to variations in the pump efficiency.

-1.9% and $+1.1\%$, corresponding to a physical range between 25.0 kW and 25.7 kW. It is clear that the impact of η_p on the cycle performance becomes greater as the pressure ratio increases. For low temperature ORC applications the pressure ratio is most likely to lie within the range of 2 to 4, so the resulting deviation will be smaller. Furthermore, a wide range of pump efficiencies were selected for this analysis, although in reality operation between 60% and 80% may be more realistic, further reducing the deviations. Overall, the deviations observed are not considered significant, therefore validating the assumption of a constant pump efficiency throughout this work, and this value been set at the baseline of $\eta_\mathrm{p} = 70\%$.

3.3.3 Evaporator modelling

The evaporator is divided into three heat transfer processes, and the ORC working fluid properties at the start and end of each of these processes have already been determined. The aim of the evaporator modelling is to establish the working fluid mass flow rate $\dot{m}_\mathrm{w}$ that can be heated to the required turbine inlet conditions using the specified heat source, and to then calculate the required heat exchanger area A_h.

The evaporator pinch point $\mathrm{PP_h}$ is the minimum temperature difference within the

evaporator, and this occurs at the point where the working fluid starts to evaporate. It is therefore defined as $\mathrm{PP_h} = T_{\mathrm{h3}} - T_{\mathrm{w2'}}$, and can be easily visualised in Figure 3.2.

Applying the first law of thermodynamics to the preheat, evaporation and superheat processes, results in a set of simultaneous equations (Equations 3.15 - 3.17). For an input value for $\mathrm{PP_h}$ these can be solved for $\dot{m}_{\mathrm{w}}$, and the heat source enthalpies h_{h2} and h_{h4}. This in turn leads to the temperatures T_{h2} and T_{h4}.

$$\dot{m}_{\mathrm{w}}(h_{\mathrm{w2'}} - h_{\mathrm{w2}}) = \dot{m}_{\mathrm{h}}(h_{\mathrm{h3}} - h_{\mathrm{h4}}) \tag{3.15}$$

$$\dot{m}_{\mathrm{w}}(h_{\mathrm{w3'}} - h_{\mathrm{w2'}}) = \dot{m}_{\mathrm{h}}(h_{\mathrm{h2}} - h_{\mathrm{h3}}) \tag{3.16}$$

$$\dot{m}_{\mathrm{w}}(h_{\mathrm{w3}} - h_{\mathrm{w3'}}) = \dot{m}_{\mathrm{h}}(h_{\mathrm{h1}} - h_{\mathrm{h2}}) \tag{3.17}$$

Where,

$$T_{\mathrm{h3}} = T_{\mathrm{2'}} + \mathrm{PP_h} \tag{3.18}$$

$$h_{\mathrm{h3}} = \mathrm{EoS}(T_{\mathrm{h3}}, P_{\mathrm{h}}, \mathrm{fluid_h}) \tag{3.19}$$

$$h_{\mathrm{h1}} = \mathrm{EoS}(T_{\mathrm{h1}}, P_{\mathrm{h}}, \mathrm{fluid_h}) \tag{3.20}$$

$$T_{\mathrm{h2}} = \mathrm{EoS}(P_{\mathrm{h}}, h_{\mathrm{h2}}, \mathrm{fluid_h}) \tag{3.21}$$

$$T_{\mathrm{h4}} = \mathrm{EoS}(P_{\mathrm{h}}, h_{\mathrm{h4}}, \mathrm{fluid_h}) \tag{3.22}$$

Having obtained the heat source and working fluid temperature distributions within the evaporator it is possible to estimate the heat transfer area required for each heat transfer process. Generalising the problem, the total thermal energy Q transferred to the working fluid for any heat transfer process is given by Equation 3.23, where U is the overall heat transfer coefficient, A is the heat transfer area and ΔT_{log} is the log-mean temperature difference. The subscripts 'i' and 'o' refer to the working fluid at the inlet and outlet respectively, whilst 'hi' and 'ho' refer to the heat source inlet and outlet respectively.

$$Q = \dot{m}_{\mathrm{w}}(h_{\mathrm{o}} - h_{\mathrm{i}}) = U\ A\ \Delta T_{\mathrm{log}} \tag{3.23}$$

Where;

$$\Delta T_{\log} = \frac{\Delta T_{\mathrm{a}} - \Delta T_{\mathrm{b}}}{\ln\left(\frac{\Delta T_{\mathrm{a}}}{\Delta T_{\mathrm{b}}}\right)} \tag{3.24}$$

$$\Delta T_{\mathrm{a}} = T_{\mathrm{hi}} - T_{\mathrm{o}}$$

$$\Delta T_{\mathrm{b}} = T_{\mathrm{ho}} - T_{\mathrm{i}}$$

From Equation 3.23 it should be clear that if U is known it is a simple matter to find A. The value for U is a function of the two fluid steams and the heat exchanger geometry. The evaporator is assumed to be a double-pipe counter-flow heat exchanger, and a schematic of this geometry along with the designated notation is shown in Figure 3.4. This construction consists of two concentric pipes with inner diameters of d_{i} and d_{o} respectively, with the wall thickness of the inner pipe denoted as t. The ORC working fluid enters the inner pipe at T_{i} and is heated to T_{o} by the transfer of heat from the heat source. The heat source travels in the opposite direction through the annular space between the two pipes, reducing from T_{hi} to T_{ho}. The required heat transfer area A is defined as the surface area of the inner wall of the inner pipe, and this area is related to the length of pipe required L, since $A = \pi d_{\mathrm{i}} L$. It should be noted that since d_{i} is a fixed input, the calculation of A is actually the result of calculating L. However, for simplicity it will be referred to as a calculation of the area.

For this geometry, U can be calculated by splitting the heat transfer process into three

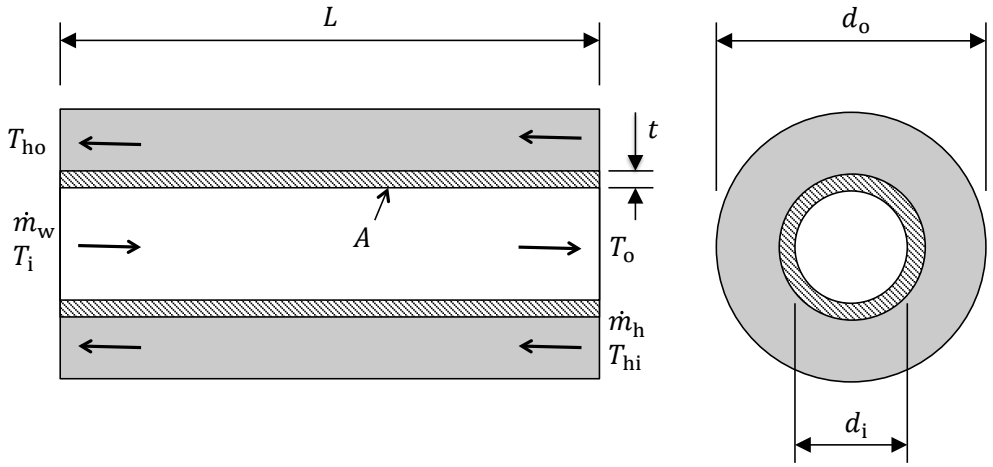

Figure 3.4: Schematic of the double-pipe counter-flow heat exchanger and the designated notation.

thermal resistances consisting of two convection terms either side of the inner pipe wall, and a conduction term through the wall. This has been expressed mathematically using Equation 3.25, where the first, second and third terms correspond to the convection on the inner wall, conduction through the wall, and convection on the outer wall respectively.

$$\frac{1}{U} = \frac{1}{\alpha_{\mathrm{w}}} + \frac{A \ln\left(\frac{d_{\mathrm{i}} + 2t}{d_{\mathrm{i}}}\right)}{2\pi k_{\mathrm{wall}} L} + \frac{d_{\mathrm{i}}}{(d_{\mathrm{i}} + 2t)} \frac{1}{\alpha_{\mathrm{h}}} \tag{3.25}$$

The term k_{wall} is the thermal conductivity of the wall material, whilst α_{w} and α_{h} refer to the local heat transfer coefficients on the inner and outer walls of the inner pipe respectively. These terms correspond to the ORC working fluid and heat source fluid streams respectively, and are calculated using common empirical correlations for single-phase heat transfer and two-phase evaporation. It is the calculation of these local heat transfer coefficients that distinguishes the three heat transfer processes of preheating, evaporation and superheating from each other. For the ORC working fluid, the preheating and superheating processes require a single-phase heat transfer correlation, whilst the two-phase evaporation requires an alternative correlation. The Gnielinski correlation is used for single-phase heat transfer, whilst the Chen correlation is used for two-phase evaporation. The correlations have been implemented according to Ghiaasiaan (2007), the details of which can be found in Appendix A.

Applying the general methodology outlined above to each heat transfer process, the heat transfer area required for preheating A_{ph}, evaporation A_{ev}, and superheating A_{sh} can each be obtained. The total heat transfer area required for the whole evaporator A_{h} is therefore just the summation of these individual areas.

$$A_{\mathrm{h}} = A_{\mathrm{ph}} + A_{\mathrm{ev}} + A_{\mathrm{sh}} \tag{3.26}$$

The calculation of the heat exchanger area requires a number of fluid properties, such as the density, specific heat capacity, thermal conductivity and viscosity, to be known. However, within each heat transfer process these properties do not remain constant. To account for these variations each heat transfer stage is further split into a number of discrete elements. The methodology outlined above is then applied to each element in turn, resulting in a more accurate prediction for the required heat transfer area. This

discretisation process will now be discussed with reference to the preheat stage, although the notation is equally applicable to the evaporation and superheat processes.

The first step is to calculate the total enthalpy change in the ORC working fluid, and then divide this by the number of specified discrete elements n. For the preheater the change in enthalpy of the working fluid within each element is therefore $(h_{\mathrm{w2'}} - h_{\mathrm{w2}})/n$. The calculation procedure then starts at the pinch point since the conditions of both fluids at this location are known, and then works back towards the preheat inlet. In general, the enthalpies of both fluids at the inlet and outlet of each element are obtained using Equations 3.27 - 3.30. The subscripts have the same meaning as before, with the introduction of 'j' to represent the j'th element. This process is presented graphically in Figure 3.5.

$$h_{\mathrm{o,j}} = h_{\mathrm{i,j-1}} \tag{3.27}$$

$$h_{\mathrm{i,j}} = h_{\mathrm{o,j}} - \frac{h_{\mathrm{w2'}} - h_{\mathrm{w2}}}{n} \tag{3.28}$$

$$h_{\mathrm{ho,j}} = h_{\mathrm{hi,j-1}} \tag{3.29}$$

$$h_{\mathrm{hi,j}} = h_{\mathrm{ho,j}} - \frac{\dot{m}_{\mathrm{w}}(h_{\mathrm{o,j}} - h_{\mathrm{i,j}})}{\dot{m}_{\mathrm{h}}} \tag{3.30}$$

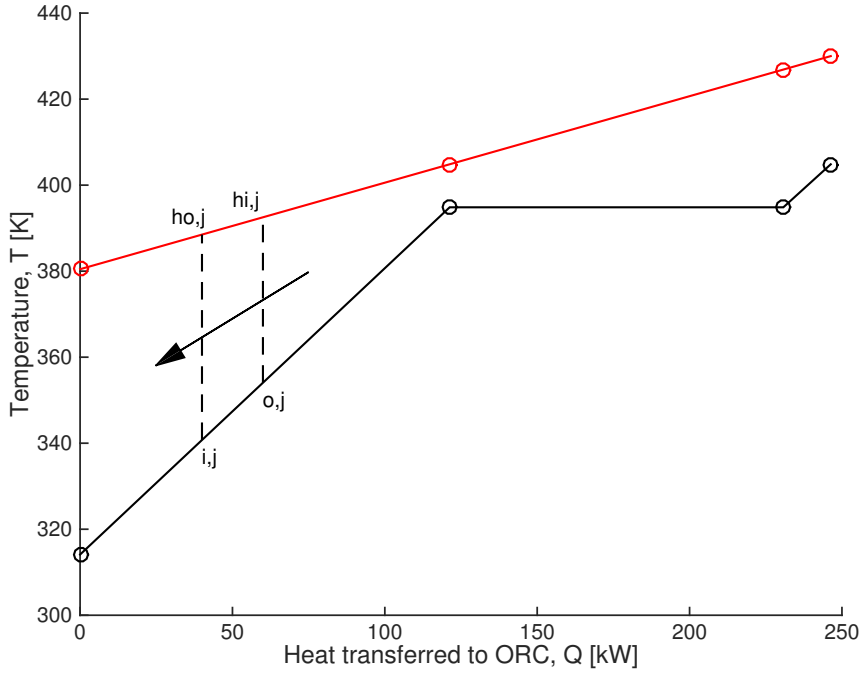

Figure 3.5: Schematic of the discretisation process applied to the preheating stage of the ORC.

With the enthalpies obtained, it is a simple matter to obtain the fluid temperature distributions using REFPROP, before using Equations 3.23 - 3.25 to find the required heat transfer area for each discrete element. After completing this analysis for the preheating, evaporation and superheating processes an improved estimate for the total evaporator heat transfer area A_{h} is given by Equation 3.31.

$$A_{\mathrm{h}} = \sum_{\mathrm{j}=1}^{n} A_{\mathrm{ph,j}} + \sum_{\mathrm{j}=1}^{n} A_{\mathrm{ev,j}} + \sum_{\mathrm{j}=1}^{n} A_{\mathrm{sh,j}} \tag{3.31}$$

It is important to select a suitable value for n, since a higher value will result in a more accurate prediction of A_{h}, but will also require a longer simulation time. To select a suitable value another parametric investigation has been completed. R245fa was again selected as the working fluid and the following parameters have been fixed: $T_{\mathrm{w1}} = 313$ K, $\Delta T_{\mathrm{sh}} = 2$ K, $\mathrm{PP_h} = 15$ K, $\eta_{\mathrm{p}} = 70\%$ and $\eta_{\mathrm{t}} = 80\%$. For a range of pressure ratios the ORC working fluid mass flow rate was estimated based on a target power of 10 kW, and these ORC cycle configurations were matched to a suitable heat source. With the mass flow rate known, the heat exchanger cross sectional areas were then selected to maintain the same mass flux (i.e. $\dot{m}/A$) for each pressure ratio. This then provided the required pipe

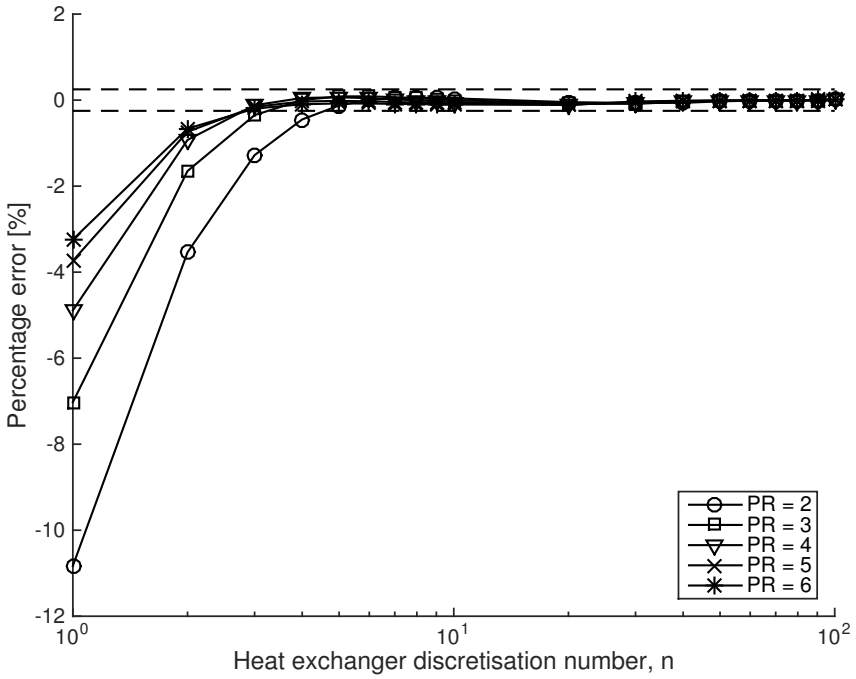

Figure 3.6: Investigation of the number of discretised elements required for the heat exchanger model.

diameters. With these inputs the evaporator model was ran with discretisation numbers ranging from 1 to 100, and the results are shown in Figure 3.6. Here the results are shown by the percentage deviation from the final values obtained with a discretisation number of 100. The straight dashed lines correspond to a percentage error of ±0.25%. From Figure 3.6 it is clear that for a discretisation number greater than 10, the error remains below 0.25%. This percentage error is sufficiently small so $n = 10$ has been selected for all future studies. Selecting a higher value would result in a higher computational cost, which may not be significant when analysing one particular cycle configuration, but would have an impact during optimisation studies.

3.3.4 Turbine modelling

Within cycle analysis the working fluid properties at the turbine outlet can be obtained if the turbine isentropic efficiency η_t is known (Equation 3.12). For cycle design it is suitable to specify a target value for η_t, and then design the turbine to achieve this value. In this instance it is helpful for a turbine model, implemented within the cycle analysis model, to establish whether it is feasible to design such a turbine. The purpose of this turbine design model is to therefore provide preliminary estimates for the rotational speed ω and rotor diameter D of a radial turbine that would efficiently expand the working fluid from the expander inlet conditions to the specified condensation pressure. Specific-speed N_s and specific-diameter D_s are used for this purpose, and were defined in Section 2.4.1. If values are assigned for N_s and D_s, Equations 2.31 and 2.32 can be rearranged for ω and D respectively, where the volumetric flow rate at the rotor exit is given by $V = \dot{m}_w/\rho_4$, and Δh_s is the ideal enthalpy drop across the turbine.

$$\omega = \frac{N_s \Delta h_s^{3/4}}{V^{1/2}} \tag{3.32}$$

$$D = \frac{D_s V^{1/2}}{\Delta h_s^{1/4}} \tag{3.33}$$

Watson and Janota (1982) correlated η_t against N_s and D_s, and their results are shown in Figure 3.7. It is worth noting that the data used to obtain Figure 3.7 refers to ideal gas turbines, so some caution should be advised when considering organic fluids. None the less, this figure suggests that optimal efficiencies above 80% are achieved with $0.4 < N_s < 0.8$ and $3 < D_s < 5$. Throughout this chapter it is assumed that designing a turbine with

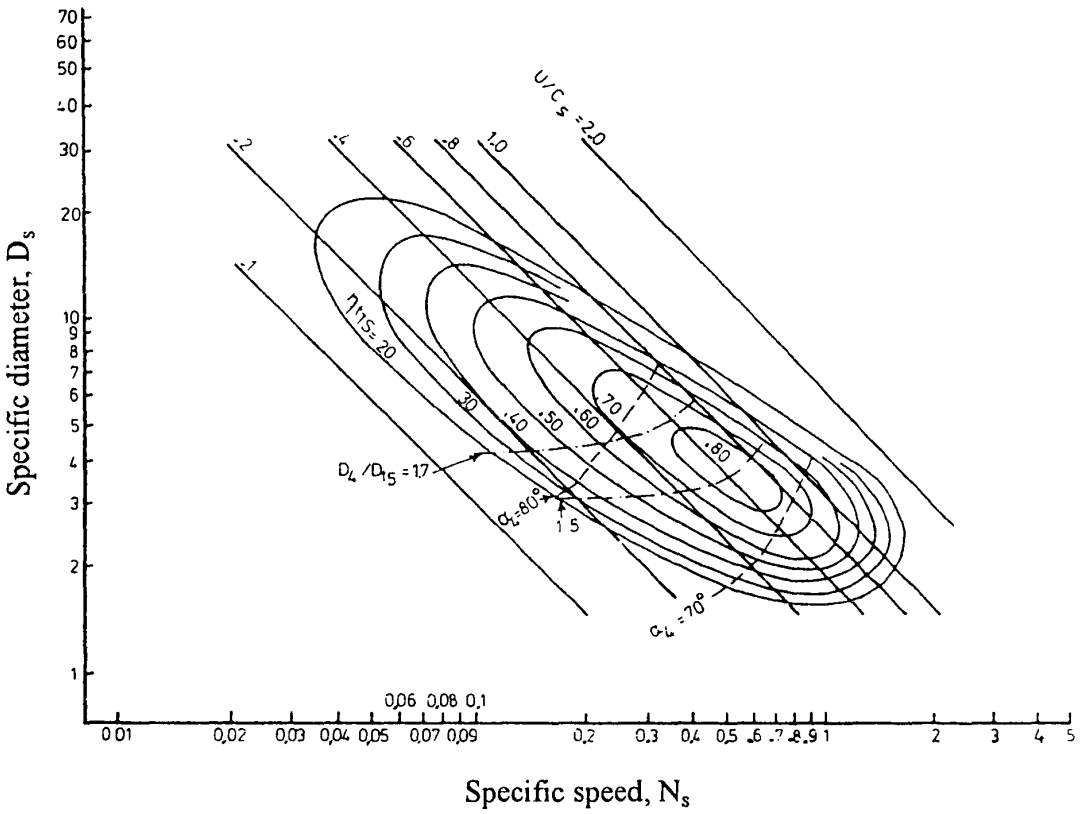

Figure 3.7: Variation in radial turbine isentropic efficiency with specific speed and specific diameter (Watson and Janota, 1982).

N_s and D_s values within this range is achievable. Therefore the turbine efficiency remains fixed at $\eta_t = 80\%$. The centre point of Figure 3.7 correlates to $N_s = 0.6$ and $D_s = 3.33$, which can be input into Equations 3.32 and 3.33.

At this point it is important to make the distinction between total and static fluid conditions. Throughout this chapter the speed of the fluid is assumed to be negligible such that the total and static properties of the fluid are approximately equal. However, within the turbine the velocity significantly increases so this assumption is no longer acceptable. When defining Equations 2.31 and 2.32 the density used to calculate V should be the static value, whilst Δh_s should be the total-to-static isentropic enthalpy drop. This introduces uncertainty into the calculation since the static properties at the rotor exit are unknown, and rely on knowing the velocity of the fluid at the rotor exit. This in turn is a function of the rotor exit geometry which is only obtained after more detailed design. However, the purpose of this preliminary sizing using N_s and D_s is to provide initial estimates for ω and D, which can be used to assess the feasibility of using a radial turbine for the specified thermodynamic conditions. After selecting a thermodynamic cycle more detailed

radial turbine design will follow, and this will lead to a final design, which is likely to have values for ω and D that will vary slightly from this initial estimate anyway. It was therefore assumed that it is reasonable to use the total density, and total-to-total isentropic enthalpy drop to arrive at these initial estimates.

To validate this assumption the initial estimates using total conditions have been compared to final estimates obtained using static conditions. The working fluid has been set as R245fa, whilst $T_{\mathrm{w1}} = 313$ K and $\Delta T_{\mathrm{sh}} = 2$ K was assumed. Following from Figure 3.7 it was assumed that $N_{\mathrm{s}} = 0.6$, $D_{\mathrm{s}} = 3.4$ and $\eta_{\mathrm{t}} = 80\%$. For a range of pressure ratios the thermodynamic properties at the turbine inlet and outlet were calculated and the mass flow rate was estimated assuming a 10 kW turbine power output. This provides a preliminary estimate for D and ω to based on total conditions.

To calculate the static properties two common turbomachinery design parameters are used. The isentropic velocity ratio ν and flow coefficient Φ were defined in Section 2.4.1 and define the rotor tip velocity and axial velocity at the rotor outlet using the total-to-static isentropic enthalpy drop through the turbine. Rodgers and Geiser (1987) correlated ν and Φ against η_{t} and found that optimal turbine performance was obtained at $\nu = 0.7$ and $\Phi = 0.25$. Assuming these values allows the static conditions to be calculated, although this process requires iteration since the static pressure is unknown. Initially it is assumed that the total and static pressures are equal, which provides an initial estimate for the rotor outlet flow velocity. Since the total enthalpy at the rotor outlet is known this supplies the static enthalpy and in turn the static pressure. Using this static pressure the process can then be repeated and iterated until convergence. This then supplies the final estimate for D and ω.

The results from this comparison are shown in Figure 3.8. It is clear that the initial estimate continually underestimates the rotor diameter, whilst overestimating the rotor rotational speed. The deviation increases as the pressure ratio increases because a higher pressure ratio corresponds to a higher total-to-static enthalpy drop and therefore a higher flow velocity at the rotor exit. However, it is also clear that the deviation is not significant. Considering that these estimates will be further refined during the detailed design phase it is clear that the estimation using total conditions is accurate enough for the intended purpose.

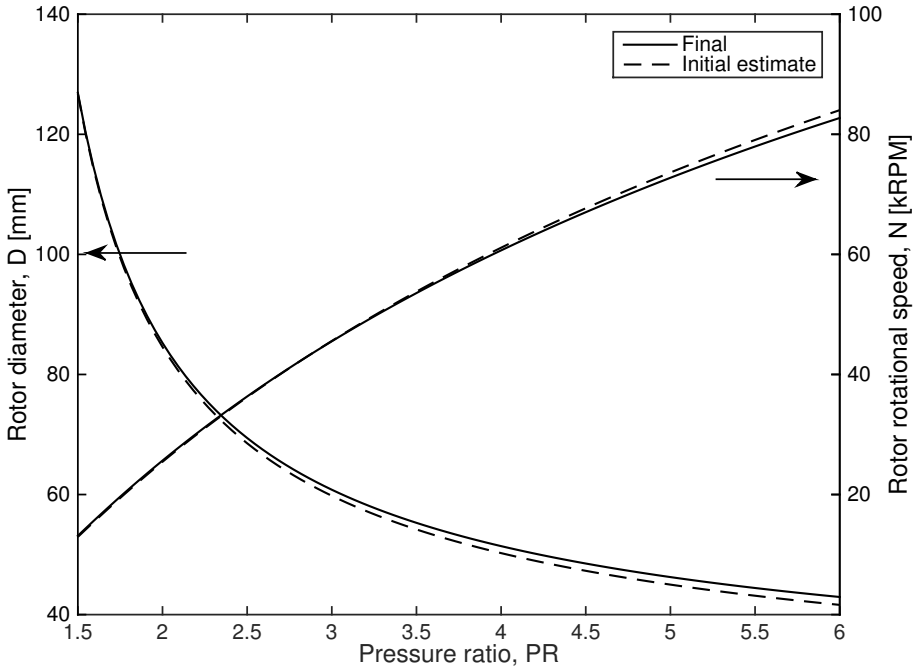

Figure 3.8: Comparison between using total and static conditions when estimating rotational speed and rotor diameter using specific speed and specific diameter.

3.3.5 Condenser modelling

The condenser transfers the heat that is still contained within the working fluid after expansion and dumps this into a cold reservoir before the complete cycle can start again. Much like the evaporation process this is an isobaric process, with the fluid cooling from a superheated vapour at the expander outlet to a saturated liquid at the pump inlet. This process can be divided into two processes; precooling and condensation.

With the heat sink conditions supplied, and the working fluid properties and the ORC mass flow rate already known, the purpose of the condenser model is to determine the required condenser heat transfer area A_c to cool the working fluid down to the required pump inlet conditions. Unlike the evaporator, the condenser pinch point ($PP_c = T_{w4'} - T_{c2}$) cannot be used to control the condenser area, since this is automatically defined by the known conditions. Instead the pinch point, and therefore condenser area can be indirectly controlled by selecting a suitable condensation temperature T_{w1}.

Applying the first law of thermodynamics to the precooling and condensation processes leads to Equations 3.34 and 3.35, which can be solved for the heat sink enthalpies h_{c2} and

h_{c3}. This in turn leads to the temperatures T_{c2} and T_{c3}.

$$\dot{m}_w(h_{w4} - h_{w4'}) = \dot{m}_c(h_{c3} - h_{c2}) \tag{3.34}$$

$$\dot{m}_w(h_{w4'} - h_{w1}) = \dot{m}_c(h_{c2} - h_{c1} \tag{3.35}$$

Where,

$$T_{c2} = \text{EoS}(P_c, h_{c2}, \text{fluid}_c) \tag{3.36}$$

$$T_{c3} = \text{EoS}(P_c, h_{c3}, \text{fluid}_c) \tag{3.37}$$

$$\text{PP}_c = T_{w4'} - T_{c3} \tag{3.38}$$

With the temperature profiles of both the working fluid and heat sink both defined, the same methodology outlined for the evaporator can be repeated to calculate the total heat transfer area A_c. The precooling and condensation heat transfer processes again require suitable correlations for the local heat transfer coefficients for single-phase and two-phase condensation. Here the Gnielinski correlation is again used for single-phase heat transfer whilst the Shah correlation is used for two-phase condensation. The details of which are found in Appendix A. In order to improve accuracy, the heat transfer processes are again discretised so the complete condenser area is then as follows:

$$A_c = \sum_{j=1}^{n} A_{pc,j} + \sum_{j=1}^{n} A_{co,j} \tag{3.39}$$

3.4 Optimisation

In order to arrive at an optimal ORC system configuration for a particular heat source and heat sink, it is critical to couple the ORC thermodynamic model with an optimisation procedure. The most primitive method of optimisation available is to conduct a parametric study where one parameter is varied over a specified range whilst the remaining parameters remained fixed. However, due to the large number of potential variables with the ORC, and the strong interdependencies between these variables, a more sophisticated optimisation strategy is required.

3.4.1 Optimisation strategy

MINUIT is a numerical minimisation program that has been developed at CERN. It is designed to find the minimum value of a multi-parameter function, and it is especially suited to handle difficult optimisation problems (James, 1994). One of the main advantages of MINUIT is that it contains a number of different minimisation algorithms that can be used in conjunction with each other to ensure a final optimal function value is obtained. More details of the available optimisers can be found in the user guide (James, 1994). The source files are publicly available and can be directly coupled to the ORC model allowing the minimisation of any user-defined objective function.

The optimisation strategy that couples the ORC model with MINUIT is shown in Figure 3.9. Presuming that an objective function has been defined, this ORC optimisation strategy can be summarised as follows. First the heat source and heat sink are defined, along with any other parameters that remain fixed through the optimisation. The design parameters that can be varied are then initialised in terms of an upper and lower bound, a starting value and an initial step size. MINUIT then runs the ORC thermodynamic model with an initial group of inputs and calculates the objective function value. The input values are then varied according to the initial step size and the process repeated. The aim is to move in a direction that results in a lower objective function value, and therefore more optimal system configuration. This process repeats until the reduction in the objective function value is lower than a specified tolerance, at which point the optimisation is complete, and the optimised cycle configuration is output.

From this simple overview, it is clear that the key aspect in designing the optimisation strategy is to define a suitable objective function. The definition of this function depends upon whether the intention is to optimise a cycle utilising existing components, or to obtain a complete new system design. Within this chapter the focus is on designing a system and therefore only the second scenario will be discussed.

3.4.2 Defining the objective function

For sizing optimisation an objective function is required that maximises cycle performance, whilst minimising system complexity. System performance can be measured by the cycle efficiency η_{o}, or the net work output W_{n}, whilst complexity is closely related to cost, and manifests itself through larger heat exchangers and increasing rotor rotational speeds that

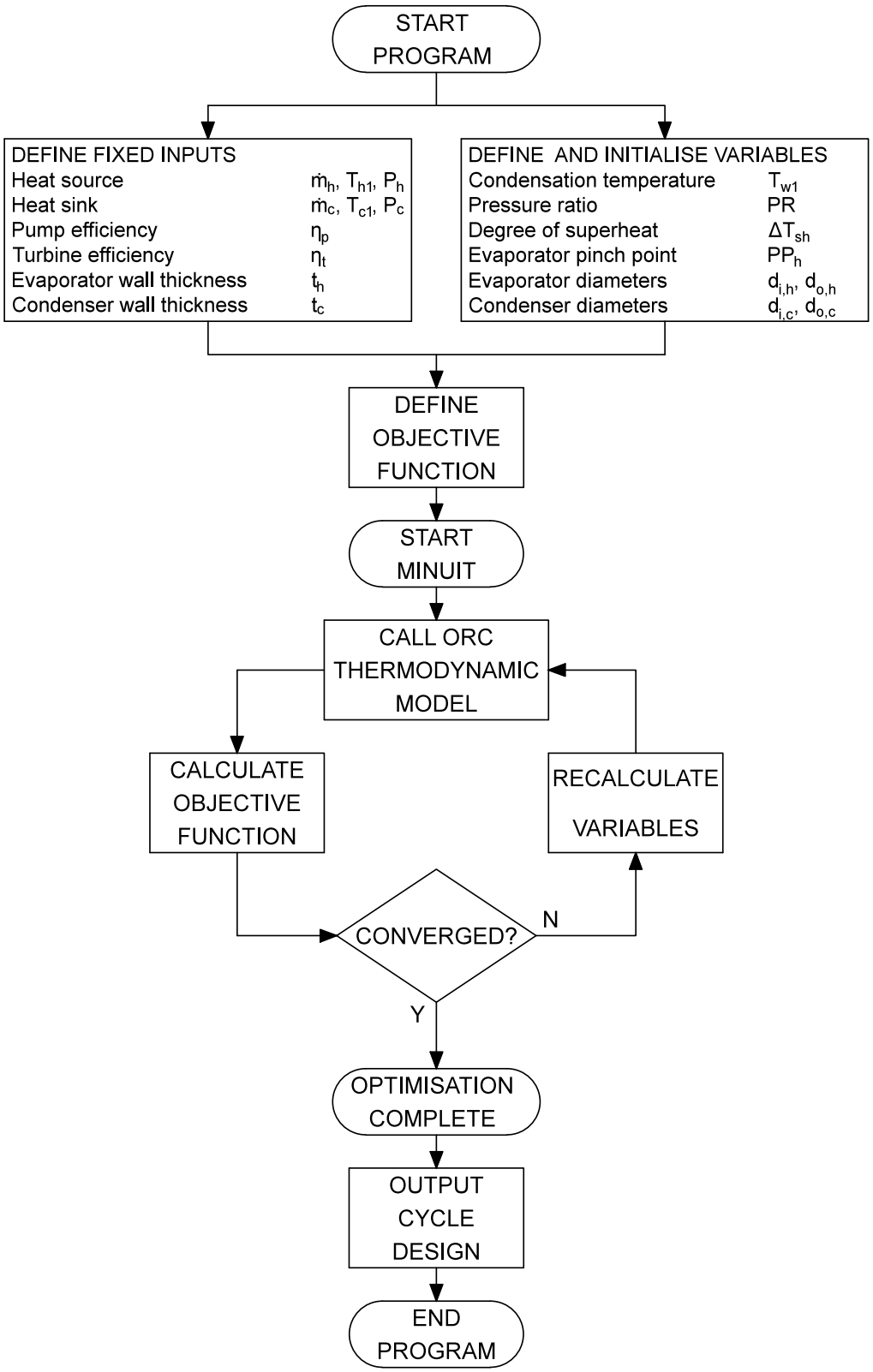

Figure 3.9: ORC optimisation strategy.

require high speed generators. The objective function must therefore quantify the trade-off between these aspects to obtain an optimal system configuration. Compared to cycle optimisation using existing components, sizing optimisation requires significantly more optimisation variables. This is because the heat exchanger dimensions, and evaporator pinch point can be varied. This of course adds further complexity to the optimisation problem.

It should be noted that it has been widely shown that η_{o} and W_{n} do not share an optimal point because the interaction between the heat source and working fluid is not considered when calculating η_{o}. An optimal cycle efficiency could result in a poor utilisation of the available heat source, whilst a lower cycle efficiency could absorb much more thermal energy, and produce a higher net work. For most ORC applications such as waste heat recovery or solar, it is important to achieve the best utilisation of the heat source, and therefore maximise the work output, so W_{n} has been selected as the most suitable measure of cycle performance. However, for applications such as combined heat and power where the remaining heat is utilised, cycle efficiency might be more appropriate.

Maximising W_{n} will inevitably lead to small pinch points and large heat exchangers. Therefore the objectives of a sizing optimisation should be to:

- Maximise net work output W_{n}
- Minimise evaporator area A_{h}
- Minimise condenser area A_{c}
- Minimise expander rotational speed N

Wang et al. (2012) demonstrated one example of an objective function that considers the trade-off between performance and heat exchanger areas, by minimising the heat exchanger area per unit power ($(A_{\mathrm{h}} + A_{\mathrm{c}})/W_{\mathrm{n}}$). However, this approach has the potential to lead to systems with small heat exchangers that do not make full utilisation of the available heat source.

In order to define an alternative objective function, the first step is to rank the four objectives using a binary matrix. Ultimately the aim of this binary matrix is to obtain an importance factor for each objective, denoted g, that can be used within the optimisation. This process is demonstrated in Table 3.1 for the four objectives being considered. At each element within the matrix the row objective is compared to the column objective. If

the row objective is considered more important than the column objective that element is filled with a 1, otherwise it is filled with a 0. After completing the whole matrix, the number of 1's in each row are summed up and then normalised by adding 1. This normalisation ensures that the lowest ranked objective is still considered even its tally is zero. The importance factors are then obtained by dividing the normalised values by the sum of all the normalised values.

Table 3.1: Sizing optimisation binary matrix.

	A_c	A_h	N	W_n	$\sum$ 1's	$\sum$ 1's + 1	g
A_c	x	0	1	0	1	2	0.2
A_h	1	x	1	0	2	3	0.3
N	0	0	x	0	0	1	0.1
W_n	1	1	1	x	3	4	0.4
					Total	10	1

With the importance factors obtained, an objective function can be expressed as the summation of each objective, multiplied by its corresponding importance factor g (Equation 3.40). Here the numerical subscripts are introduced to distinguish the importance factors from each other. Again the distinction between maximising and minimising an objective should be highlighted, requiring that the reciprocal of W_n is minimised. Reference factors, denoted with the subscript 'ref' have been introduced. These are required to scale each objective so it is within a similar order of magnitude. In the absence of scaling, the importance factors become meaningless.

$$\min \; f(\mathbf{x}) = g_1 \left[\frac{W_{n,ref}}{W_n}\right] + g_2 \left[\frac{A_h}{A_{h,ref}}\right] + g_3 \left[\frac{A_c}{A_{c,ref}}\right] + g_4 \left[\frac{N}{N_{ref}}\right] \tag{3.40}$$

Where;

$$\mathbf{x} = \left[\begin{array}{cccccccc} T_{w1} & PR & \Delta T_{sh} & PP_h & d_{i,h} & d_{o,h} & d_{i,c} & d_{o,c} \end{array} \right]$$

To evaluate the suitability of Equation 3.40 a sizing optimisation problem was considered, the details of which are discussed in detail in Section 3.5. From this study two main conclusions were drawn. Firstly, the contribution of each term within Equation 3.40

did not align with the defined importance factors. For example, the net work output has an importance factor of 0.4, and therefore it was intended that the first term in Equation 3.40 would contribute to 40% of the objective function value. However, it was found that this term was consistently more than 65% of the overall objective function. The second issue was that Equation 3.40 was found to be sensitive to the reference values selected. Small heat exchanger area reference values resulted in small systems that did not fully utilise the available heat source, therefore producing lower power outputs. This suggested that an alternative objective function was required. The objectives for this new objective function are listed below, and the resulting objective function is defined by Equation 3.41. The aim is that this objective function would accurately capture the interaction between the heat exchanger area and net work output, without significantly reducing the work produced by the cycle.

- Maximise net work output W_{n}
- Minimise evaporator area per net work output $A_{\mathrm{h}}/W_{\mathrm{n}}$
- Minimise condenser area per net work output $A_{\mathrm{c}}/W_{\mathrm{n}}$
- Minimise rotor rotational speed N

$$\min \ f(\mathbf{x}) = g_1 \left[\frac{W_{\mathrm{n,ref}}}{W_{\mathrm{n}}}\right] + g_2 \left[\frac{W_{\mathrm{n,ref}}}{W_{\mathrm{n}}}\frac{A_{\mathrm{h}}}{A_{\mathrm{h,ref}}}\right] + g_3 \left[\frac{W_{\mathrm{n,ref}}}{W_{\mathrm{n}}}\frac{A_{\mathrm{c}}}{A_{\mathrm{c,ref}}}\right] + g_4 \left[\frac{N}{N_{\mathrm{ref}}}\right] \tag{3.41}$$

The evaluation of this objective function is also detailed in Section 3.5. Overall, Equation 3.41 was found to be a significant improvement on Equation 3.41. Not only did the results for this objective function align better with the importance factors, it was also less sensitive to variations in the reference values selected.

Despite initial confirmation of Equation 3.41 as a suitable objective function, it should be highlighted that the chosen objective function is not ideal as objective ranking and scaling requires a qualitative understanding of the problem, thereby relying on designer experience. A more accurate method should quantify system complexity by developing economic models that could estimate the cost of each component. An objective function of minimising the system cost per unit work could then be used. However, these models are not currently available, or are not sufficiently accurate to provide realistic results. Therefore the development of the objective function described by Equation 3.41 is a novel contribution to the field of ORC optimisation, offering a method to arrive at a system

configuration that balances system performance with system complexity. This helps to satisfy the need for suitable objective functions for this sort of optimisation problem that has been highlighted by Quoilin et al. (2013).

3.5 Optimisation case study

An optimisation case study will now be explored, which will demonstrate how the thermodynamic modelling developed in Section 3.3 and the optimisation strategy developed in Section 3.4 can be combined together to arrive at an optimal cycle configuration for a particular heat source and sink.

3.5.1 Optimisation setup

Within a typical ORC design problem, the aim is to generate the optimal cycle configuration for a specified heat source and heat sink. The first steps within this case study were therefore the definition of a suitable heat source and heat sink. The focus within this project is low temperature ORCs, so a heat source consisting of pressurised water at $T_{\mathrm{h}} = 390$ K and $P_{\mathrm{h}} = 200$ kPa has been defined. The cold sink was assumed to be water at $T_{\mathrm{c}} = 288$ K, and at atmospheric pressure $P_{\mathrm{c}} = 101$ kPa. The heat source and heat sink mass flow rates were then estimated to provide a net power of around 10 kW. This corresponded to a heat source mass flow rate of $\dot{m}_{\mathrm{h}} = 0.75$ kg/s, and a cold sink mass flow rate of $\dot{m}_{\mathrm{c}} = 1.5$ kg/s. Following from the discussion in Sections 3.3.2 and 3.3.4 the pump and turbine isentropic efficiencies were set to $\eta_{\mathrm{p}} = 70\%$ and $\eta_{\mathrm{t}} = 80\%$ respectively. In selecting this turbine efficiency it is therefore assumed that for all working fluids considered it will be possible to design a turbine with an optimal specific speed and specific diameter. Overall, all of the fixed inputs for this sizing optimisation study are summarised in Table 3.2.

In addition to specifying the fixed parameters required for the optimisation, it was also important to specify the optimisation variables, and the starting values and step sizes of these variables. These are shown in Table 3.3. The variables selected for this study are the four main cycle variables (T_{w1}, PR, ΔT_{sh} and $\mathrm{PP_h}$), and the heat exchanger geometries. Of course, the working fluid is also a variable but it is not possible to include this in the optimisation. Instead the optimisation process will be ran for each candidate working

Table 3.2: Sizing optimisation study fixed inputs.

Parameter		Value	Units
Heat source fluid		water	
Heat source temperature	T_{h1}	390	K
Heat source pressure	P_{h}	200	kPa
Heat source mass flow rate	$\dot{m}_{\mathrm{h}}$	0.75	kg s^{-1}
Heat sink fluid		water	
Heat sink temperature	T_{c1}	288	K
Heat sink pressure	P_{c}	101	kPa
Heat sink mass flow rate	$\dot{m}_{\mathrm{c}}$	1.5	kg s^{-1}
Pump isentropic efficiency	η_{p}	70	%
Turbine isentropic efficiency	η_{t}	80	%
Evaporator wall thickness	t_{h}	1.0	mm
Condenser wall thickness	t_{c}	2.0	mm

Table 3.3: Optimisation study variables.

Parameter		Start value	Step size	Units
Condensation temperature	T_{w1}	310	10	K
Pressure ratio	PR	3.0	0.25	
Degree of superheat	ΔT_{sh}	15	5	K
Evaporator pinch point	PP_{h}	15	5	K
Evaporator tube inner diameter	$d_{\mathrm{i,h}}$	60	10	mm
Evaporator shell inner diameter	$d_{\mathrm{o,h}}$	100	10	mm
Condenser tube inner diameter	$d_{\mathrm{i,c}}$	80	10	mm
Condenser shell inner diameter	$d_{\mathrm{o,c}}$	120	10	mm

fluid, and the resulting cycle configurations can then be compared. This comparison will then highlight the most suitable cycle configuration.

The starting values are the values that MINUIT uses during the first calls to the ORC thermodynamic model. It is therefore important to select values that have a high probability of resulting in feasible a cycle configuration. For this reason a superheat of 15 K was specified to ensure that expansion would always remain within the superheated region, even if wet a working fluid is selected. Furthermore, the heat exchanger diameters were set at relatively large values such that the pressure drops within the heat exchangers would be within the allowed tolerance, so the ORC thermodynamic model would not fail. The values for T_{w1}, PR and PP_{h} were set according to user experience.

The step size controls the optimisation search space within the first few iterations of

MINUIT, and the selection of a suitable value is a slight trade-off between computation time and accuracy. On the one hand a small step size will result in a smaller search space at the start of the optimisation which may result in the optimiser taking a longer time to converge. On the other hand, too large a step size could result in the optimiser moving too far from its current location, resulting in the program to fail. The values in Table 3.3 were selected after some initial trial runs, and these were found to offer a fair compromise between computation time and accuracy.

3.5.2 Verification of the objective function

With the sizing optimisation case study defined the suitability of the defined objective functions can now be investigated. Both objective functions are clearly dependent upon the reference values and therefore it is important to investigate how the selected values affect the optimisation. For clarity the objective functions defined by Equations 3.40 and 3.41 will be referred to as objective function 1 and objective function 2 respectively.

For objective function 1, three optimisation cases were selected, each using different reference values, and these are defined in Table 3.4. For this investigation, two common ORC working fluids have been selected, namely R245fa and R123, whilst the importance factors used in the optimisation were set according to the values obtained in Table 3.1. For each case in Table 3.4, the optimisation procedure was then run and the overall objective function value, and the contributions of each term to this overall value, were obtained. These results are summarised in Figure 3.10.

Table 3.4: Reference values for the investigation of objective function 1.

Case number	$W_{\mathrm{n,ref}}$	$A_{\mathrm{h,ref}}$	$A_{\mathrm{c,ref}}$	N_{ref}
1	50	4	4	20000
2	25	2	2	10000
3	20	2	4	30000

From Figure 3.10 it is clear that the breakdown of the objective function does not match the defined importance factors. For all three cases, over 65% of the objective function is made up by the net power output, whilst the importance factor is only 0.4. Furthermore, although being the least important objective, the rotational speed term accounts for a relatively large percentage of the overall objective function compared to

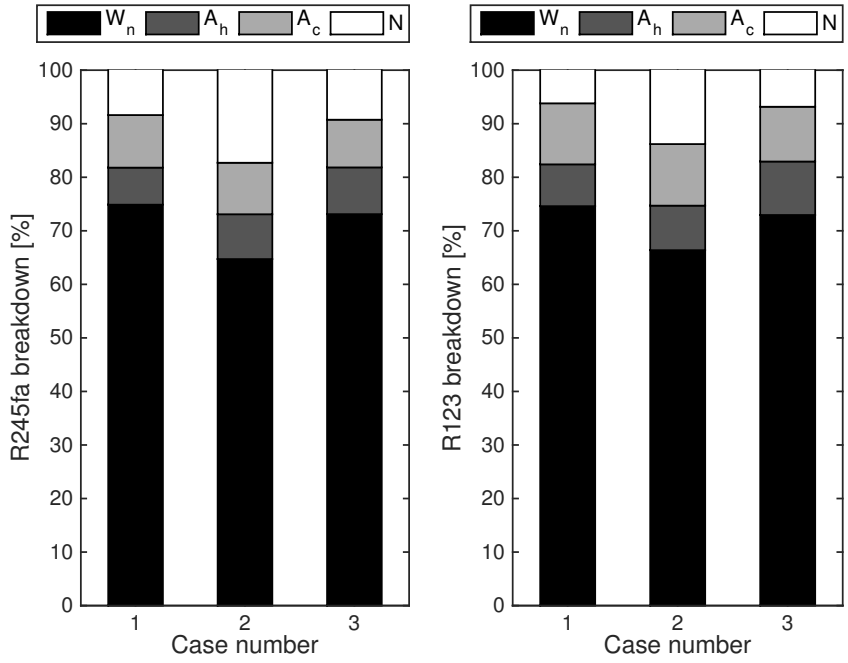

Figure 3.10: Breakdown of initial objective function for four different cases.

the heat exchanger areas. This suggests that objective function 1 does not arrive at an optimal configuration that trades-off heat exchanger area and net power output by the ratios intended by the binary matrix.

When comparing the optimised cycles obtained for cases 1, 2 and 3 the values for the net work produced by the cycle are 8.75 kW, 5.66 kW and 5.91 kW for R245fa, and 8.70 kW, 5.64 kW and 5.82 kW for R123 respectively. Comparatively, the total heat exchanger areas for cases 1, 2 and 3 are 8.81 m^2, 4.15 m^2 and 4.37 m^2 for R245fa, and 10.23 m^2, 4.55 m^2 and 5.11 m^2 for R123 respectively. This clearly shows that the objective function is sensitive to changes in the reference values, with low heat exchanger reference values resulting in smaller heat exchangers, and a 35% reduction in the net work produced by the cycle.

However, what is clear from Figure 3.10, and the resulting net work outputs and heat exchanger areas, is that the objective function does not appear to be sensitive to changes in the working fluid. This suggests that it is suitable to use to the same reference values when applying the same objective function to different ORC working fluids.

During the investigation of objective function 1 it became clear that selecting reference values relied to a large extent on educated guesses. For the study of objective function

2 this was improved by introducing three additional parameters that can be used to determine suitable reference values. It is intended that these parameters will generalise the optimisation procedure by being applicable to a range of different sizing optimisation applications. The first parameter, denoted x_1, is the ratio of the reference net work value to the maximum work that could be produced. This is known as the exergy and was defined in Chapter 2, and for the known heat source this is given by Equation 3.42, where h_{h} and s_{h} are the enthalpy and entropy of heat source, and h_{a} and s_{a} are the enthalpy and entropy of the heat source fluid at atmospheric temperature T_{a} and pressure P_{a}.

$$X = \dot{m}_{\mathrm{h}} \left[(h_{\mathrm{h}} - h_{\mathrm{a}}) - T_{\mathrm{a}}(s_{\mathrm{h}} - s_{\mathrm{a}}) \right] \tag{3.42}$$

Where;

$$[h_{\mathrm{h}}, s_{\mathrm{h}}] = \mathrm{EoS}(T_{\mathrm{h}}, P_{\mathrm{h}}, \mathrm{fluid_h})$$

$$[h_{\mathrm{a}}, s_{\mathrm{a}}] = \mathrm{EoS}(T_{\mathrm{a}}, P_{\mathrm{a}}, \mathrm{fluid_h})$$

The second and third parameters, x_2 and x_3, are slightly more self-explanatory. The parameter x_2 is the ratio of the reference evaporator area to the reference condenser area, whilst x_3 is the ratio of the reference net work output to the reference total heat exchanger area. x_3 is therefore a measure of how much power can be produced per square meter of total heat exchanger area. With specified values for x_1, x_2 and x_3 Equations 3.43 - 3.45 can be used to determined the reference values to be used within objective function 2.

$$W_{\mathrm{n,ref}} = x_1 \; X \tag{3.43}$$

$$A_{\mathrm{c,ref}} = \frac{x_1 \; X}{x_3(1 + x_2)} \tag{3.44}$$

$$A_{\mathrm{h,ref}} = x_2 \; A_{\mathrm{c,ref}} \tag{3.45}$$

Although this method still requires the user to specify values for x_1, x_2 and x_3, thereby still relying on the designer's experience, it does generalise the problem allowing previous experience with different cycle configurations to help define the reference factors. This new method to generate the reference factors has been implemented to investigate objective function 2. Seven cases have been defined and these have been summarised in Table 3.5.

As for objective function 1, R245fa and R123 have been selected as the working fluids, whilst the importance factors were set according to Table 3.1. For each case in Table 3.5, the optimisation procedure was run and then the overall objective function value, and the contributions of each term to this overall value, were obtained. These results are summarised in Figure 3.11.

From Figure 3.11 the improvement made by objective function 2 is clear, with the breakdown of the objective function more closely matching the importance factors. Across all cases the net work output continually accounts for approximately 40% of the overall objective function, whilst the total heat exchanger area accounts for approximately 50%,

Table 3.5: Reference values for the investigation of objective function 2.

Case number	x_1	x_2	x_3	$W_{\mathrm{n,ref}}$	$A_{\mathrm{h,ref}}$	$A_{\mathrm{c,ref}}$	N_{ref}
1	0.25	0.50	2.00	11.56	1.93	3.85	25000
2	0.35	0.33	3.00	16.19	1.35	4.05	25000
3	0.50	0.40	2.50	23.12	2.64	6.61	25000
4	0.50	0.33	4.00	23.12	1.43	4.35	25000
5	0.50	0.67	5.00	23.12	1.85	2.78	25000
6	0.50	0.80	3.50	23.12	2.94	3.67	25000
7	0.49	1.00	4.09	22.5	2.75	2.75	25000

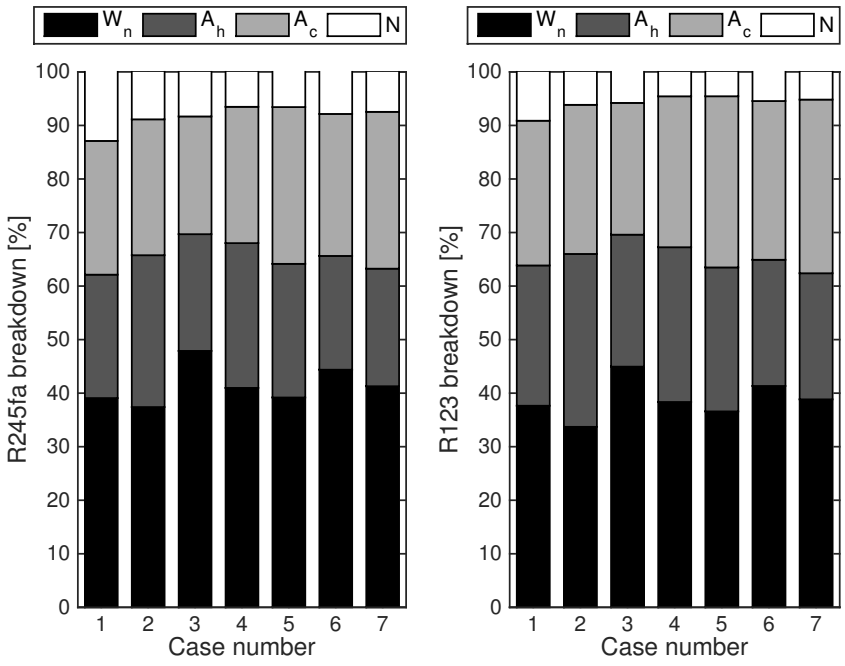

Figure 3.11: Breakdown of modified objective function for seven different cases.

leaving the expander rotational speed to account for the last 10%. This is well aligned with the importance factors of 0.4, 0.3, 0.2 and 0.1 for W_{n}, A_{h}, A_{c} and N respectively. Furthermore, the left and right hand graphs in Figure 3.11 are similar, again confirming that the reference values for this objective function are not sensitive to changes in working fluid.

Although Figure 3.11 shows that selecting different values for x_1, x_2 and x_3 results in slightly different breakdowns of the objective function, it is not clear which case number results in the most optimal design. To investigate this further, the resulting cycle configurations for each case number have been compared in Figure 3.12. This figure plots the net work produced against the total heat exchanger area for each case. The objective function 1 cases are also included, allowing a comparison between objective functions 1 and 2.

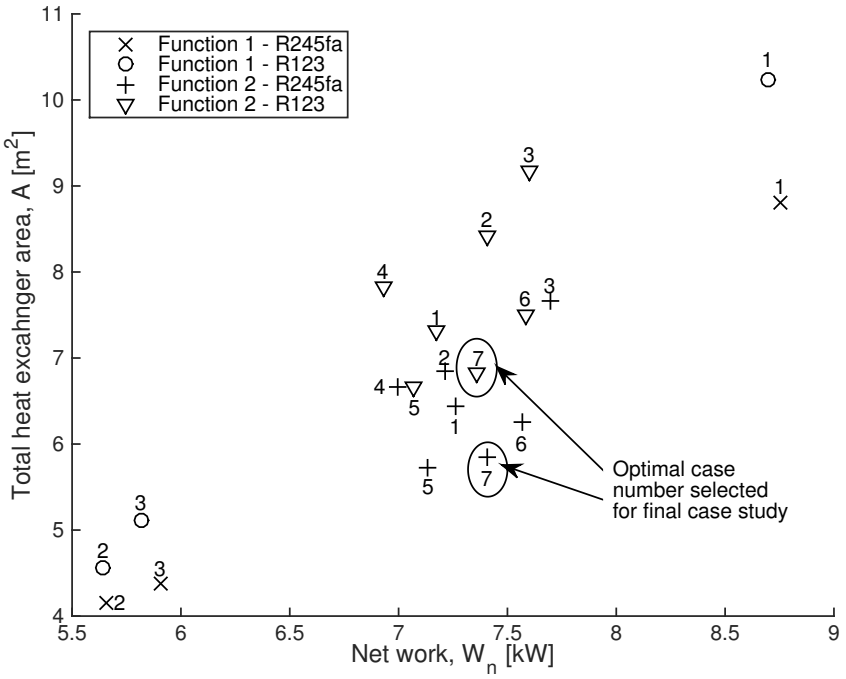

Figure 3.12: Comparison of the different optimisation cases considered for objective function 1 and objective function 2 in terms of net work and total heat exchanger area. The numbers represent the corresponding case number.

The first point to note is the comparison between the results obtained with objective function 1 and objective function 2. Objective function 1 shows a large spread of both net work output and the total heat exchanger area. This therefore visually demonstrates the sensitivity of objective function 1 to variations in the reference factors. By compar-

ison, all of the results for objective function 2 are more condensed with variations in net work between 6.99 kW and 7.56 kW for R245fa, and 6.93 kW and 7.59 kW for R123. Furthermore, the total heat exchanger area also shows less variation compared to objective function 1, with variations between 5.72 m^2 and 7.67 m^2 for R245fa, and 6.66 m^2 and 9.16 m^2 for R123. This demonstrates that the sensitivity of objective function 2 to changes in the reference parameters is not as severe as found for objective function 1. Therefore objective function 2 seems to more accurately model the trade-off between heat exchanger area and cycle performance.

Although it is clear that objective function 2 is an improvement on objective function 1, it is clear that the the selected values of x_1, x_2 and x_3 still have an impact on the resulting cycle configuration. In order to progress with the optimisation study it is required to select the case from Table 3.5 that results in the optimal cycle configuration. It should be clear that an optimal configuration should produce the maximum power with a relatively small heat exchanger area. Therefore, referring to Figure 3.12, it is found that for both R245fa and R123 the case that results in the most preferential cycle configuration is case 7, so this group of reference factors has been selected for the sizing optimisation case study. It is interesting to note that amongst the objective function 2 data points, this selected case results in the greatest work produced per unit area of heat exchanger, and this corresponds to 1.27 kW/m^2, and 1.08 kW/m^2 for R245fa and R123 respectively. The final parameters used to define the objective function for this optimisation study can therefore be summarised in Table 3.6. The optimisation for the defined heat source and sink with a wider array of working fluids can now be undertaken.

Table 3.6: Sizing optimisation reference values.

Objective		g	Reference	Units
Net power output	W_n	0.4	22.5	kW
Evaporator area	A_h	0.3	2.75	m^2
Condenser area	A_c	0.2	2.75	m^2
Rotor rotational speed	N	0.1	25000	rpm

3.5.3 Working fluid selection

Due to the large diversity of ORC applications and available working fluids, there is no single optimal working fluid, and fluid screening remains an important stage for any ORC project. A review of screening studies resulted in 50 potential pure fluids that have previously been considered for ORC applications. However, this list can be reduced by removing any fluids that have been banned by the Montreal and Kyoto protocols. By considering a realistic ORC condensation temperature of 313 K it was then possible to estimate the condensation pressure for the remaining fluids. Fluids with a condensation pressure below atmospheric pressure were ruled out due to the additional complexity of operating under a vacuum. Furthermore, by then considering a realistic ORC pressure ratio of 3 the ORC evaporation pressure for the remaining fluids could also be deduced. For simplicity subcritical ORCs are only being considered, immediately ruling out any remaining fluids with evaporation pressures above their critical pressure. This reduced the initial list of 50, down to the 18 fluids listed in Table 3.7.

In addition to pure fluids, there are also a large number of common refrigerant mixtures. However, these were immediately neglected as these are generally found to have high saturation pressures, near critical evaporator pressures or saturated vapour domes with a negative gradient.

3.5.4 Optimisation results

For each of the 18 fluids listed in Table 3.7 the sizing optimisation was then completed. The fixed inputs and variables were set according to Tables 3.2 and 3.3, whilst the objective function given by Equation 3.41 was setup using the parameters defined in Table 3.6. After completing each optimisation, the results were recorded, and these are summarised in Table 3.8.

Of the 18 fluids considered, 3 cases did not converge. Upon inspection, R134a and R152a both have negative gradient vapour domes, which require superheating to ensure a dry expansion. A condensation temperature of 313 K also leads to high condensation pressures of 10.1 and 9.1 bar respectively. R1234yf was also found to have a high condensation pressure, which after compression would result in operation close to the critical point.

For the converged solutions, the optimal condensation temperature ranges from 311.8 K

Table 3.7: Sizing optimisation screened working fluids.

Working Fluid		Series	ALT	ODP	GWP	Toxicity	Flammability	Molecular Mass	Critical Temperature [K]	Critical Pressure [bar]	Saturation Pressure at 313K [bar]	$\xi = \mathrm{d}s/\mathrm{d}T$ for PR = 4	Group
R123	2,2-dichloro-1,l,l-trifluoroethane	Ethane	1.3	0.02	77	B	1	153.0	456.8	36.6	1.5	0.34	HCFC
R124	2-chloro-1 ,I,I ,2-tetrafluoroethane	Ethane	5.8	0.022	609	A	1	136.5	395.4	36.2	5.9	0.07	HCFC
R141b	1,l-dichloro-1-fluoroethane	Ethane	9.3	0.11	725			117.0	477.5	42.1	1.3	0.15	HCFC
R142b	1-chloro-I,1-difluoroethane	Ethane	17.9	0.065	2310	A	2	100.5	410.3	40.6	5.2	-0.05	HCFC
R134a	1,1,1,2-tetrafluoroethane	Ethane	14	0	1430	A	1	102.0	374.2	40.6	10.1	-2.11	HFC
R152a	1,I -difluoroethane	Ethane	1.4	0	124	A	2	66.0	386.4	45.2	9.1	-1.74	HFC
R227ea	1,1,1,2,3,3,3-heptafluoropropane	Propane	34.2	0	3220			170.0	374.9	29.3	7.0	0.06	HFC
R236ea	1,1,1,2,3,3-hexafluoropropane	Propane						152.0	412.4	35.0	3.4	0.75	HFC
R236fa	1,1,1,3,3,3-hexafluoropropane	Propane	240	0	9810	A	1	152.0	398.1	32.0	4.4	0.54	HFC
R245ca	1,1,2,2,3-pentafluoropropane	Propane	6.2	0	693			134.1	446.6	39.3	1.7	0.70	HFC
R245fa	1,1,1,3,3-pentafluoropropane	Propane	7.6	0	1030	B	1	134.0	427.2	36.5	2.5	0.56	HFC
R1234ze	1,3,3,3-tetrafluoropropene	Propene						114.0	382.5	36.4	7.6	-0.33	HFO
R1234yf	2,3,3,3-tetrafluoropropene	Propene			4			114.0	367.9	33.8	10.1	NaN	HFO
R600	Butane	Hydrocarbons		0	1	A	3	58.1	425.1	38.0	3.8	1.11	HC
R600a	i-Butane	Hydrocarbons	0.41	0	20	A	3	58.1	407.8	36.3	5.3	0.90	HC
R601	Pentane	Hydrocarbons				A	3	72.2	469.7	33.7	1.2	1.75	HC
R601a	i-Pentane	Hydrocarbons	0.018	0	20	A	3	72.2	460.4	33.8	1.5	0.85	HC
RC318	Octafluorocyclobutane	Organic Compounds	0.01	0	1	A	1	200.0	388.4	27.8	4.9	0.84	PFC

Table 3.8: Sizing optimisation results.

Fluid	T_{w1}	P_{w1}	PR	ΔT_{sh}	PP_h	PP_c	$\dot{m}_w$	η_o	W_p	W_t	D	N	A_e	A_c	$d_{i,h}$	$d_{o,h}$	$d_{i,c}$	$d_{o,c}$
	K	bar		K	K	K	kg/s	%	kW	kW	mm	rpm	m^2	m^2	mm	mm	mm	mm
R123	314.1	1.60	3.10	0.00	13.59	13.05	0.50	7.88	0.17	7.52	65.74	40700	2.22	4.59	28.31	45.55	46.29	71.06
R124	313.3	5.96	2.84	0.01	12.99	11.37	0.64	7.85	0.77	8.52	39.72	63400	1.97	3.70	25.04	43.05	37.34	63.64
R141b	313.3	1.34	3.17	0.00	13.58	12.39	0.37	8.15	0.13	7.55	65.59	47400	2.05	3.96	27.45	45.16	43.38	68.18
R142b	314.2	5.38	2.68	0.01	12.80	12.40	0.45	7.83	0.55	8.06	38.49	75400	1.77	2.83	23.80	41.81	33.64	59.78
R227ea	316.4	7.68	2.73	0.00	13.83	13.78	0.92	6.84	1.32	8.66	40.51	52300	2.19	3.38	27.18	45.87	38.69	63.85
R236ea	315.0	3.57	2.93	0.00	13.59	13.65	0.57	7.45	0.41	7.75	47.86	53000	1.96	4.09	25.48	43.26	41.54	66.95
R236fa	315.5	4.69	2.83	0.01	13.69	13.79	0.64	7.29	0.60	7.89	44.24	54900	1.87	3.61	25.16	42.87	39.53	64.85
R245ca	314.8	1.83	3.18	0.00	13.07	13.46	0.44	7.70	0.19	7.63	59.20	48700	2.05	4.33	26.41	44.02	44.17	69.02
R245fa	314.9	2.65	3.09	0.01	13.13	13.48	0.47	7.67	0.29	7.70	50.99	54900	1.95	3.90	25.37	43.18	40.93	67.04
R1234ze	315.3	8.13	2.66	0.01	13.55	12.78	0.60	7.26	1.04	8.36	34.77	74000	1.59	2.40	23.55	41.18	32.05	57.77
Butane	314.9	3.97	2.61	0.00	12.94	13.38	0.25	7.60	0.41	7.83	38.67	100100	1.51	2.84	22.04	40.11	33.84	60.39
i-Butane	314.4	5.49	2.57	0.03	12.12	12.34	0.29	7.64	0.66	8.46	35.41	106000	1.74	3.19	22.49	41.04	33.75	60.71
Pentane	314.8	1.22	3.02	0.04	13.53	13.70	0.23	7.62	0.14	7.45	62.82	62100	1.71	3.77	25.20	42.48	42.92	67.34
i-Pentane	311.8	1.45	3.28	2.00	15.35	12.63	0.21	8.30	0.17	7.22	53.81	75100	1.35	4.12	22.83	40.04	41.49	67.11
RC318	314.2	5.07	3.16	0.01	11.72	13.42	0.83	7.60	0.91	8.65	44.89	49500	2.52	5.17	27.45	45.62	44.78	70.72
R134a	*	*	*	*	*	*	*	*	*	*	*	*	*	*	*	*	*	*
R152a	*	*	*	*	*	*	*	*	*	*	*	*	*	*	*	*	*	*
R1234yf	*	*	*	*	*	*	*	*	*	*	*	*	*	*	*	*	*	*

for isopentane to 316.4 K for R227ea. The evaporator and condenser pinch points range from 11.72 K for RC318 to 15.35 K for isopentane, and 11.37 K for R124 and 13.79 K for R236ea respectively. For all fluids the optimisation converges to a solution where the superheat is negligible. This confirms the widespread view that there is no thermodynamic benefit in superheating ORCs.

The remaining thermodynamic variable, the pressure ratio, shows the most variation with optimal values ranging from 2.57 for isobutane to 3.28 for isopentane. The relationship between pressure ratio and condensation pressure, pump work and expander work has been investigated in Figure 3.13. A strong correlation between increasing condensation pressure and increasing pump and expander work is found. The enthalpy change for a constant pressure ratio increases with increasing condensation pressure. Therefore, for the same mass flow rate the required pump work and achievable expander work must increase. Figure 3.13C shows the net effect of increased pump and expander work. It shows that these two effects cancel each other out, with only small variations in net power being obtained for the range of working fluids considered. Figure 3.13D shows the relation between condensation pressure and pressure ratio. Generally, with increasing condensation pressure, the optimal pressure ratio reduces.

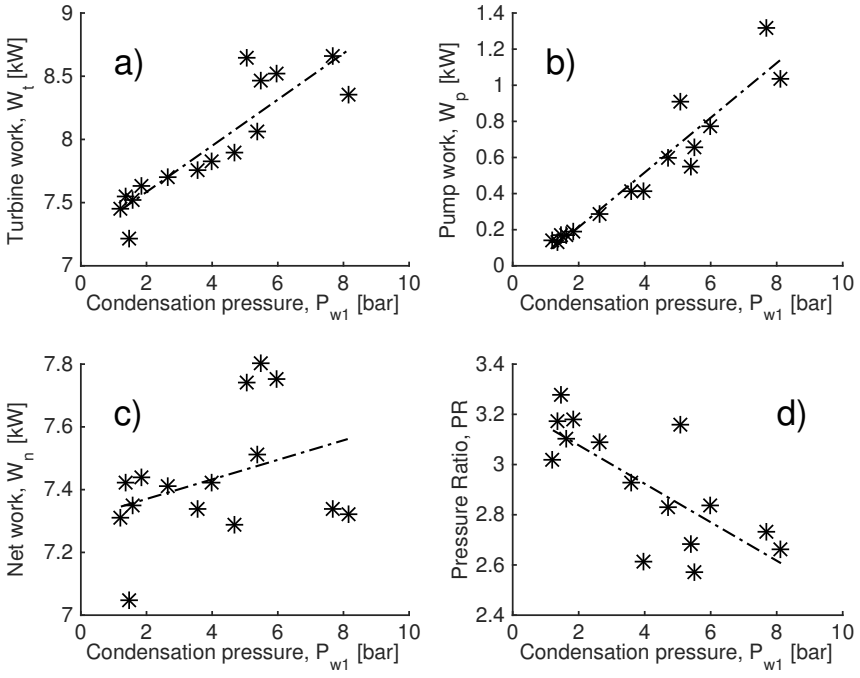

Figure 3.13: Variation in ORC performance with condensation pressure resulting from the sizing optimisation; A) turbine work; B) pump work; C) net work; D) pressure ratio.

Overall these results indicate that regardless of the optimal pressure ratio and condensation pressure, the optimisation converges to a solution with a similar net power output for all fluids. Coupled with the small variations in other thermodynamic variables, it seems the most suitable working fluid is the fluid that results in the most favourable expander and heat exchanger design. To investigate this further the results from the sizing optimisation are shown in terms of the objective function values and the objective function breakdown in Figures 3.14 and 3.15 respectively, whist the resulting heat exchanger and turbine designs are shown in Figures 3.16 and 3.17 respectively.

The bars in Figure 3.14 show the breakdown of the objective function for each fluid. It is immediately clear that the contribution from the net work output for each case remains approximately equal, further confirming that the optimisation is driven by the heat exchanger and turbine design. Moving from left to right in Figure 3.14, there is an obvious trend of an increasing contribution from the total heat exchanger area, leading to an overall rise in the total objective function. R1234ze, R142b and butane achieve the three lowest objective functions of 2.58, 2.69 and 2.74 respectively, and from Figure 3.16 it is clear that these three fluids have the smallest heat exchanger areas. This suggests that the optimisation is mainly driven by the minimisation of heat exchanger area.

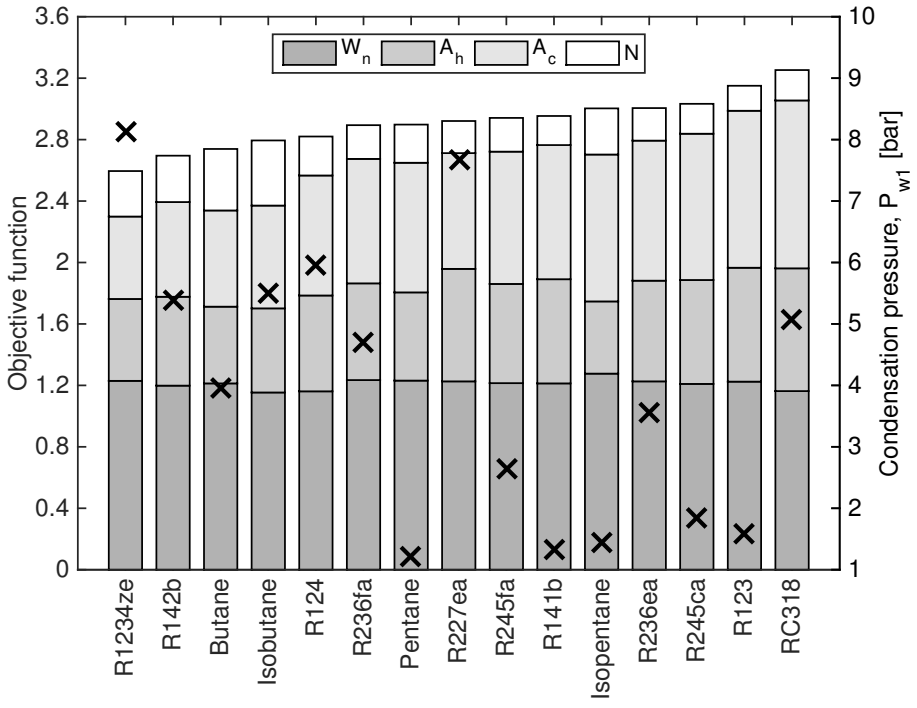

Figure 3.14: Sizing optimisation results for the 15 working fluids considered. (Bars indicate the breakdown of the objective function; crosses indicate the condensation pressures.

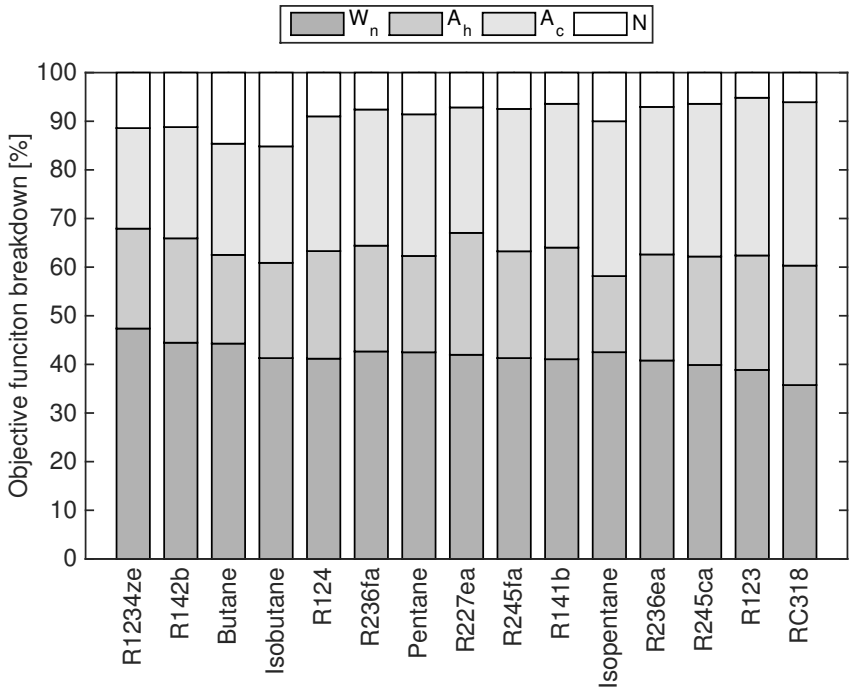

Figure 3.15: Breakdown of the objective function from the sizing optimisation with the 15 working fluids considered.

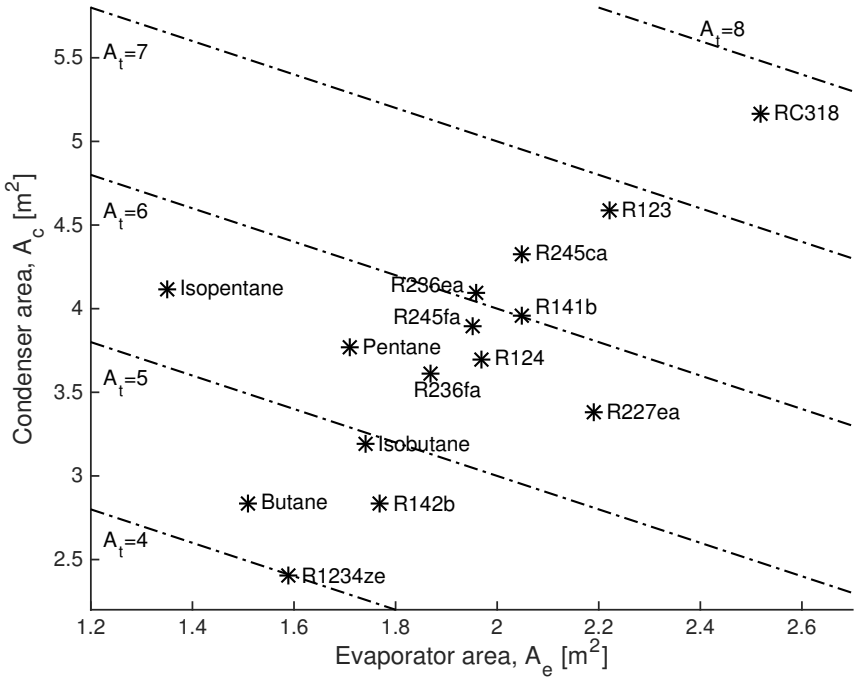

Figure 3.16: Evaporator and condenser areas that resulted from the sizing optimisation for the 15 working fluids considered.

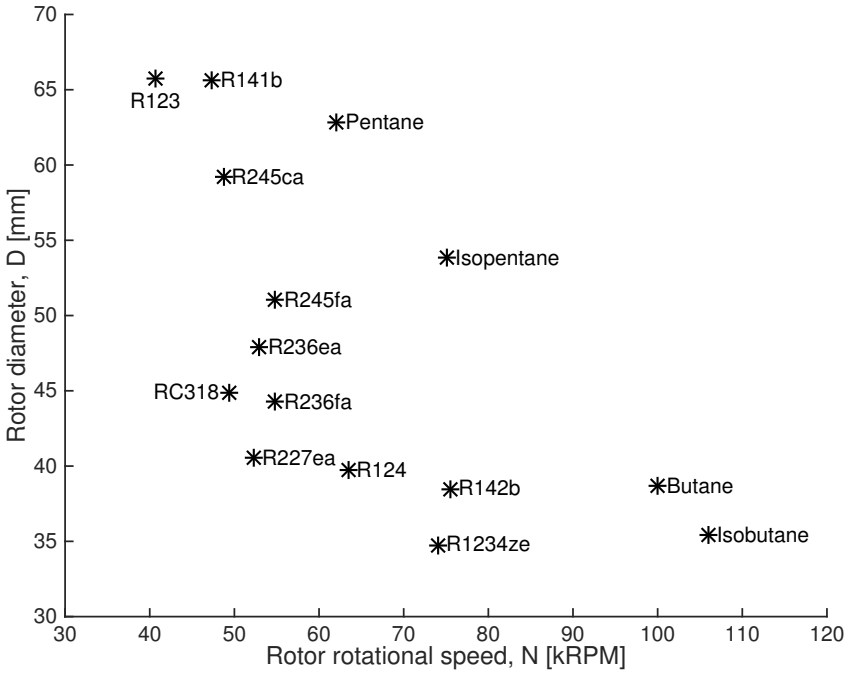

Figure 3.17: Turbine rotational speed and rotor diameter required for the optimised cycles that resulted from the sizing optimisation.

Upon inspection there was not found to be any significant correlation between smaller heat exchanger areas and higher pinch points, or smaller heat exchanger areas resulting from changes in the working fluid mass flow rate. This suggests that the minimisation of the heat exchanger area is largely dependent upon the predicted pressure loss, with a fluid that experiences a lower predicted pressure drop permitting a smaller pipe diameter to be used. This in turn results in a higher flow velocity, and therefore a better heat transfer. This is an interesting result that highlights that certain fluids may be a more optimal choice when considering the heat exchanger design. Of course, this study has considered a double-pipe counter-flow arrangement, but it would be interesting to extend this analysis to more complex, realistic, heat exchanger geometries such as a plate, or shell-and-tube arrangement.

In Figure 3.14 the working fluid condensation pressures have also been included. From these results it would appear that there is a relationship between a higher condensation pressure and a smaller heat exchanger area. This suggests that a higher condensation pressure might be advantageous in improving heat transfer, therefore reducing heat exchanger area.

Referring to Figure 3.15 it is clear that for all of the working fluids considered, the

breakdown of the objective function remains fairly similar. Despite slight variations from fluid to fluid, on average the net work output remains around 40% of the overall objective function, whilst the heat exchanger area is around 50% and the rotational speed term is the last 10%. This is again in line with the defined importance factors. This provides further verification that the defined objective function and reference values are suitable for a wider variety of working fluids that those considered in the previous section. Having said this, one issue that could be addressed further would be to address the balance between evaporator and condenser area. Within the binary matrix the evaporator area was ranked above the condenser area, although results show that a larger contribution to the objective function is found to be from the condenser area instead of the evaporator area. However, this is only a minor adjustment since the contribution in total area remains aligned with the summation of the evaporator and condenser importance factors.

In terms of the turbine design, rotor rotational speeds varying from $40,700$ rpm for R123, up to $106,000$ rpm for isobutane, whilst the rotor diameter varies from 34.77 mm for R1234ze, up to 65.74 mm for R123. There is also the general trend of increasing rotational speed resulting in smaller rotor diameters. If butane and isobutane are neglected none of the remaining fluids would require a rotational speed above $80,000$ rpm to operate at the optimal specific speed. Considering that similar sized radial turbines are used in turbochargers, and that these operate with rotational speeds up to $150,000$ rpm, it is clear that these rotational speeds are perfectly feasible. Of course, there will be the requirement for high speed generators or gearboxes.

Referring to Figure 3.14 it is clear that the four working fluids that have the lowest objective function are the fluids that require rotors with the higher rotational speeds. This indicates that during the optimisation, turbine rotational speed is sacrificed for reductions in heat exchanger area. This was to be expected to some extent due to the rotational speed being considered the least important objective.

Despite the higher rotational speed, the optimisation results for the defined objective function indicate that R1234ze would be the most suitable working fluid for the defined heat source and sink. However, referring to Figure 3.14 it also has the highest condensation pressure of 8.13 bar, which results in an expander inlet pressure of 21.64 bar. This creates more stringent design constraints, which may increase system complexity and cost. Comparatively R142b has the second lowest objective function and has condensation and

evaporation pressures of 5.38 bar and 14.47 bar respectively. However R142b is a HCFC and is to be phased out as a result of the Kyoto protocol.

Therefore, the main conclusion from this optimisation study using the defined objective function is that selecting the most suitable working fluid and therefore cycle configuration may not be as clear-cut as simply selecting the fluid that has the lowest objective function value. Even with the complex objective function additional factors such as operating pressures, environmental properties or fluid availability can impact the final decision. One potential method to enhance this optimisation procedure would be to adapt the objective function to include these additional factors. This would require an extension of the binary matrix, and the addition of further terms to Equation 3.41. However, this would significantly increase the complexity of the objective function and potentially introduce more uncertainties since these additional factors would need to be quantified. Having said this, it is worth noting that the condensation pressure is directly related the condensation temperature. Therefore in order to reduce operating pressures, a reduction in the condensation temperature would be required which would inadvertently result in smaller temperature differences in the condenser and larger heat exchanger areas. It is therefore obvious that the condensation pressure is not something that the designer has much control over.

Another option is to use the defined objective function and optimisation procedure to arrive at an optimal cycle configuration for each working fluid, and then rely on the designer to qualitatively identify the most suitable working fluid from the resulting cycle configurations, environmental properties, availability, and any other factors that might be important. Referring back to Figure 3.14, having ruled out R1234ze and R142b, the next fluids with the lowest objective functions are butane and isobutane. However, as discussed these both require rotor rotational speeds above $100,000$ rpm. The first working fluids with relatively low condensation pressures, and low rotor rotational speeds are R245fa and pentane. Both fluids sit within a group of fluids with similar heat exchanger configurations, with total evaporator and condenser areas of 1.75 m^2 and 3.77 m^2 for pentane, and 1.95 m^2 and 3.90 m^2 for R245fa respectively. The R245fa expander has a lower rotational speed and rotor diameter of $54,900$ rpm and 50.99 mm respectively, compared to $62,100$ rpm and 64.14 mm for Pentane. Based on this R245fa seems the most suitable considering that one objective was the reduction of rotor rotational speed, and that the R245fa rotor

has a smaller diameter and therefore requires less material. R245fa is available within the market, has widely been acknowledged as a suitable low temperature ORC working fluid, and has previously been employed in a number of experimental ORC studies. This study therefore further validates the suitability of R245fa for these applications.

3.6 Conclusion

Within this chapter an ORC model has been developed which addresses the key areas that were indentified from the literature review in Chapter 2. A novel objective function has been developed which quantifies the trade-off between system performance and complexity, and the use of this objective function has been demonstrated within an optimisation case study. Although relying on the designer to have a qualitative understanding of the system, this objective function satisfies a need for suitable objective functions for these optimisation problems, since accurate economic models are not yet sufficiently developed.

After running the optimisation for a range of working fluids, R1234ze was suggested as the optimal working fluid with reference to the novel objective function. However, working fluid selection is further complicated by considering qualitative factors, such as environmental properties and fluid availability amongst other considerations. It is therefore suggested that the optimisation procedure is used to obtain an optimal cycle configuration for each working fluid, and the designer must qualitatively identify the most suitable working fluid based on these optimisation results, alongside their own selection criteria. After taking these considerations into account, R245fa was highlighted as the most suitable working fluid for low temperature applications.

Chapter 4

Radial turbine development

4.1 Introduction

Having completed the thermodynamic analysis of the cycle, the next phase is to design a radial inflow turbine for small-scale low temperature ORCs. The literature review highlighted that existing turbine design methods should be adapted to account for non-ideal fluid properties, whilst more consideration needs to be given to the geometrical construction of the turbine. Furthermore, it is important to validate design models with accurate CFD codes, and the suitability of ANSYS CFX for this purpose has been demonstrated. However, it is important to select an accurate equation of state.

This chapter presents an ORC radial inflow turbine design methodology capable of providing a complete preliminary design of a turbine stator and rotor. The inclusion of REFPROP expands common design procedures to be applicable for any working fluid, whilst existing methods are considered, and improved where appropriate, in a bid to improve their accuracy. A novel contribution of this work is the consideration of the three-dimensional rotor geometry within this preliminary design phase, coupled with a method to predict the meanline velocity distribution within the rotor, which helps during the preliminary design phase without requiring more advanced design techniques. The design method is validated using three-dimensional RANS simulations completed in ANSYS CFX for two turbines operating with air and R245fa respectively. Fluid properties are accounted for by constructing fluid property tables using REFPROP, which uses the Helmholtz equation of state. The work presented in this chapter led to publishing a conference paper, presented at the 2015 ASME Turbo Expo (White and Sayma, 2015d).

4.2 Rotor one-dimensional design

The turbine rotor is the most critical component within a turbine, and understandably receives the most attention during the design process. The aim of the rotor one-dimensional design is to size the rotor inlet and outlet to efficiently expand the design mass flow rate from the specified inlet conditions to the desired outlet conditions. The geometry of a radial turbine, along with the expansion process as shown on an enthalpy-entropy diagram, and the specified notation used throughout this chapter were shown by Figures 2.9, 2.10 and 2.11.

Although the thermodynamic ORC model was created in FORTRAN, the turbine design model has been constructed in MATLAB. This has the advantage of being able to quickly and easily generate three-dimensional plots of the turbine geometry, in addition to having access to a wide range of built-in functions that aid in the three-dimensional construction of the turbine geometry.

The design process for the rotor is to first determine the velocity triangles, before calculating the thermodynamic properties of the working fluid at the rotor inlet and outlet. Once the velocities and thermodynamic properties have been established the rotor dimensions can then be determined. In general, this design procedure is well established within the literature. However, in order to complete the design the designer has a choice over which design variables to specify as inputs, and the choices made will now be justified. The thermodynamic inputs required for the turbine design are as follows:

- Working fluid
- Total inlet temperature T_{01}
- Total inlet pressure P_{01}
- Mass flow rate $\dot{m}$
- Total-to-static pressure ratio $\mathrm{PR}_{\mathrm{ts}}$

To establish the rotor velocity triangles and thermodynamic properties a number of design inputs are required. Closing each velocity triangles requires three design inputs, whilst the stator isentropic efficiency η_{N} is required to account for losses upstream of the rotor. The seven design inputs are as follows:

- Total-to-static isentropic velocity ratio ν_{ts}
- Rotor inlet absolute flow angle α_4

- Rotor inlet relative flow angle β_4
- Total-to-static isentropic efficiency η_{ts}
- Rotor radius ratio $\epsilon = r_4/r_5$
- Rotor velocity ratio ϕ
- Stator isentropic efficiency η_{N}

ν_{ts} was introduced in Section 2.4.1, and determines the inlet blade velocity u_4 as a function of the thermodynamic inputs. There are a number of ways to close this velocity triangle, however the approach adopted here is to directly specify α_4 and β_4. This allows control over the shape of the velocity triangle, whilst allowing the designer to directly control the incidence angle (Atkinson, 1998). This is an important design consideration with optimal values between $\beta_4 = -20°$ and $\beta_4 = -40°$ (Dixon, 2010).

To define the rotor outlet velocity triangle suitable values for η_{ts} and ϵ must be selected. It is important to select a realistic value for η_{ts} since this impacts the amount of swirl at the rotor outlet. Designing for an optimal specific speed, $N_{\mathrm{s}} = 0.6$, equates to $\eta_{\mathrm{ts}} = 85\%$ (Rohlik, 1968). After completing a design, the difference between the design value and the efficiency predicted by CFD will indicate the quality of this selection. Specifying ϵ permits a generalised rotor shape to be defined without being constrained by a rotational speed. This is useful for ORC turbines since rotational speeds are relatively low compared to similar size air turbines, which means that speed is less constrained by mechanical considerations. Optimal values are between $0.50 < \epsilon < 0.65$ (Rodgers and Geiser, 1987).

The final design parameter, ϕ, is defined as the ratio of the actual relative velocity at the rotor exit w_5, to the velocity that would occur if the expansion through the rotor was isentropic $w_{5\mathrm{s}}$ (Moustapha et al., 2003). It is a measure of the losses that occur within the rotor passage, and Dixon (2010) states that for well designed rotors $0.70 < \phi < 0.85$. As discussed within Section 2.4.1 there are alternative methods to close the velocity triangle such as defining the flow coefficient $\Phi = c_5/u_4$ or the meridional velocity ratio $\xi = c_{\mathrm{m}5}/c_{\mathrm{m}4}$. However it was found that when using these ratios it is sometimes possible to result in values of w_5 greater than $w_{5\mathrm{s}}$ suggesting that over-expansion would occur within the rotor.

To determine the rotor inlet and outlet dimensions a number of geometrical design inputs are required, and are summarised as follows.

- Rotor outlet hub/tip radius ratio $\lambda = r_{5\mathrm{h}}/r_{5\mathrm{t}}$

- Blade number Z_{R}
- Rotor inlet blade thickness ratio t_4/r_4
- Rotor outlet hub blade thickness ratio $t_{5\mathrm{h}}/r_4$
- Rotor outlet tip blade thickness ratio $t_{5\mathrm{t}}/r_4$
- Rotor axial length ratio $\Gamma = L/(r_{5\mathrm{t}} - r_{5\mathrm{h}})$

Although the velocity triangles have been determined, it is λ that determines the required rotor inlet diameter and therefore rotational speed. Again, using λ allows a generalised rotor shape to be defined, without being constrained by rotational speed, and values close to $\lambda = 0.4$ are recommended (Dixon, 2010; Fiaschi et al., 2012). In some applications the turbine rotor must be designed to operate at a specified rotational speed. In this case the rotational speed can be directly specified, leaving λ to be determined.

The designer has direct control over the rotor blade number Z_{R}, and ideally the number of blades should be sufficient to avoid flow reversal within the rotor passage. However, a large number of blades can result in a large blockage area at the rotor outlet, and high friction losses due to the large surface area in contact with the working fluid. Glassman (1976) employed the following empirical correlation to determine Z_{R} based on α_4.

$$Z_{\mathrm{R}} = \left(\frac{\pi}{30}\right)(110 - \alpha_4)\tan\alpha_4 \tag{4.1}$$

The remaining geometrical parameters express the rotor blade thickness at the rotor inlet, and the rotor outlet hub and tip as a fraction of the rotor inlet radius, and determine the rotor axial length. These non-dimensional parameters again allow a non-dimensional rotor shape to be defined without knowing the final rotor diameter. These inputs have been implemented according to suggestions made by Aungier (2006).

Having outlined the chosen design inputs for the rotor design, the rotor design procedure will now be described. As mentioned previously, rotor design methods are well established. However, these design methods rely extensively on ideal gas relationships, which are not suitable for organic fluids. The following sections outline the implementation of a rotor design model that replaces these ideal gas relationships with direct calls to a suitable equation of state. This permits thermodynamic properties to be calculated as functions of known parameters such as temperature, pressure, enthalpy and entropy.

4.2.1 Rotor inlet thermodynamics

The first step of the rotor inlet thermodynamic model is to establish the total enthalpy h_{01} and entropy s_{01} at the turbine inlet. The static pressure at the turbine exit P_5 is then determined by the input pressure ratio, $\mathrm{PR_{ts}}$. From this, the enthalpy corresponding to an isentropic expansion through the turbine, $h_{5\mathrm{ss}}$, is determined.

$$[h_{01}, s_{01}] = \mathrm{EoS}(T_{01}, P_{01}, \mathrm{fluid}) \tag{4.2}$$

$$P_5 = \frac{P_{01}}{\mathrm{PR_{ts}}} \tag{4.3}$$

$$h_{5\mathrm{ss}} = \mathrm{EoS}(P_5, s_{01}, \mathrm{fluid}) \tag{4.4}$$

The total-to-static isentropic enthalpy drop across the turbine and the input value for ν_{ts} then determines u_4. Having directly specifed α_4 and β_4 the remaining velocity components at the rotor inlet follow from trigonometry.

$$u_4 = \nu_{\mathrm{ts}} \sqrt{2(h_{01} - h_{5\mathrm{ss}})} \tag{4.5}$$

$$c_{\mathrm{m}4} = \frac{u_4}{\tan\alpha_4 - \tan\beta_4} \tag{4.6}$$

$$c_{\theta 4} = c_{\mathrm{m}4} \tan\alpha_4 \tag{4.7}$$

$$w_{\theta 4} = c_{\mathrm{m}4} \tan\beta_4 \tag{4.8}$$

$$c_4 = \sqrt{c_{\mathrm{m}4}^2 + c_{\theta 4}^2} \tag{4.9}$$

$$w_4 = \sqrt{c_{\mathrm{m}4}^2 + w_{\theta 4}^2} \tag{4.10}$$

Assuming adiabatic flow through the stator, the total enthalpy at the rotor inlet is equal to the turbine inlet enthalpy ($h_{04} = h_{01}$). The rotor inlet static enthalpy h_4 then follows from the absolute velocity c_4 (Equation 4.11), and the input stator efficiency determines the enthalpy following an isentropic expansion through the stator $h_{4\mathrm{s}}$.

$$h_4 = h_{04} - \frac{1}{2}c_4^2 \tag{4.11}$$

$$\zeta_{\mathrm{N}} = \frac{1}{\eta_{\mathrm{N}}} - 1 \tag{4.12}$$

$$h_{4\mathrm{s}} = h_4 - \frac{1}{2}\zeta_{\mathrm{N}} c_4^2 \tag{4.13}$$

With $h_{4\mathrm{s}}$ known, the static properties at the rotor inlet can then be determined. Having

determined the speed of sound a_4 the absolute Mach number Ma_4 and relative Mach number $\mathrm{Ma}_{4'}$ then follow.

$$P_4 = \mathrm{EoS}(h_{4\mathrm{s}}, s_{01}, \mathrm{fluid}) \tag{4.14}$$

$$[T_4, \rho_4, s_4, a_4] = \mathrm{EoS}(P_4, h_4, \mathrm{fluid}) \tag{4.15}$$

$$\mathrm{Ma}_4 = \frac{c_4}{a_4} \tag{4.16}$$

$$\mathrm{Ma}_{4'} = \frac{w_4}{a_4} \tag{4.17}$$

The final step of the rotor inlet thermodynamic model is to determine the rothalpy at the turbine inlet, I_4, based on the static enthalpy and the known velocities.

$$I_4 = h_4 + \frac{1}{2}(w_4^2 - u_4^2) \tag{4.18}$$

4.2.2 Rotor outlet thermodynamics

Following from radial turbine design convention, the rotor outlet conditions are determined at the root mean square (rms) radius. The rotor outlet blade velocity u_5 is obtained from the diameter ratio, ϵ. Combing the definition of η_{ts} (Equation 2.12) with Euler's turbomachinery equation (Equation 2.15), and rearranging for the absolute tangential velocity $c_{\theta 5}$, Equation 4.20 is obtained. The relative tangential velocity $w_{\theta 5}$ then follows.

$$u_5 = \epsilon\, u_4 \tag{4.19}$$

$$c_{\theta 5} = \frac{u_4 c_{\theta 4} - \eta_{\mathrm{ts}}(h_{01} - h_{5\mathrm{ss}})}{u_5} \tag{4.20}$$

$$w_{\theta 5} = c_{\theta 5} - u_5 \tag{4.21}$$

For this rotating machine rothalpy is conserved ($I_5 = I_4$). Since the static pressure at the rotor exit P_5 is known, the enthalpy following an isentropic expansion through the turbine $h_{5\mathrm{s}}$ can be determined using the rotor inlet entropy s_4 (Equation 4.22). The ideal relative velocity $w_{5\mathrm{s}}$ then immediately follows from the definition of rothalpy.

$$h_{5\mathrm{s}} = \mathrm{EoS}(P_5, s_4, \mathrm{fluid}) \tag{4.22}$$

$$w_{5\mathrm{s}} = \sqrt{2(I_5 - h_{5\mathrm{s}}) + u_5^2} \tag{4.23}$$

The input value for ϕ then supplies the actual relative velocity w_5, and the remaining velocity components and flow angles follow from trigonometry.

$$w_5 = \phi \; w_{5\mathrm{s}} \tag{4.24}$$

$$c_{\mathrm{m}5} = \sqrt{w_5^2 - w_{\theta 5}^2} \tag{4.25}$$

$$c_5 = \sqrt{c_{\mathrm{m}5}^2 + c_{\theta 5}^2} \tag{4.26}$$

$$\alpha_5 = \tan^{-1}\left(\frac{c_{\mathrm{m}5}}{c_{\theta 5}}\right) \tag{4.27}$$

$$\beta_5 = \tan^{-1}\left(\frac{c_{\mathrm{m}5}}{w_{\theta 5}}\right) \tag{4.28}$$

The static enthalpy at the rotor exit h_5 is then determined using Equation 4.29. This, along with the static pressure P_5, then supplies the remaining static properties, and the absolute and relative Mach numbers.

$$h_5 = I_5 - \frac{1}{2}(w_5^2 - u_5^2) \tag{4.29}$$

$$[T_5, \rho_5, s_5, a_5] = \mathrm{EoS}(P_5, h_5, \mathrm{fluid}) \tag{4.30}$$

$$\mathrm{Ma}_5 = \frac{c_5}{a_5} \tag{4.31}$$

$$\mathrm{Ma}_{5'} = \frac{w_5}{a_5} \tag{4.32}$$

The total properties at the rotor outlet are then obtained from the absolute velocity c_5, and the static properties h_5 and s_5.

$$h_{05} = h_5 + \frac{1}{2}c_5^2 \tag{4.33}$$

$$[T_{05}, P_{05}] = \mathrm{EoS}(h_{05}, s_5, \mathrm{fluid}) \tag{4.34}$$

4.2.3 Rotor outlet geometry

Having established the velocity triangles and thermodynamic properties, the turbine can now be sized to pass the required mass flow rate. Applying mass continuity, the required flow area at the rotor outlet A_5 can immediately be determined (Equation 4.35), and this flow area is equal to the total geometrical area at the rotor outlet minus the loss in area that is caused by blade blockage (Equation 4.36). The total geometrical area is the cross sectional area of the annular space with inner and outer radii of $r_{5\mathrm{h}}$ and $r_{5\mathrm{t}}$ respectively.

Here the subscripts 'h' and 't' refer to the rotor outlet blade hub, and blade tip locations respectively. The blade blockage is accounted for by the blockage factor BK_5, whilst the rms radius r_5 is related to the hub and tip radii by Equation 4.37.

$$A_5 = \frac{\dot{m}}{\rho_5 c_{\mathrm{m}5}} \tag{4.35}$$

$$A_5 = \pi(r_{5\mathrm{t}}^2 - r_{5\mathrm{h}}^2)(1 - \mathrm{BK}_5) \tag{4.36}$$

$$r_5 = \sqrt{\frac{r_{5\mathrm{t}}^2 + r_{5\mathrm{h}}^2}{2}} \tag{4.37}$$

Introducing λ and solving Equations 4.35 - 4.37 for r_5 results in Equation 4.38. The hub and tip radii then immediately follow.

$$r_5 = \sqrt{\frac{A_5(1+\lambda^2)}{2\pi(1-\mathrm{BK}_5)(1-\lambda^2)}} \tag{4.38}$$

To determine the geometrical blade blockage area, a method originally developed by Atkinson (1998) has been implemented within the rotor design model. Referring to Figure 4.1, the geometrical area blocked by each blade can be estimated as a trapezium with a height $(r_{5\mathrm{t}} - r_{5\mathrm{h}})$, and effective thicknesses of t_{eh} and t_{et} at the hub and tip respectively. The total area blocked by each blade at the rotor outlet is given by Equation 4.39, and the rotor outlet blockage factor is then defined by Equation 4.40.

$$A_{\mathrm{bb}} = \frac{1}{2}(r_{5\mathrm{t}} - r_{5\mathrm{h}})(t_{\mathrm{et}} + t_{\mathrm{eh}}) \tag{4.39}$$

$$\mathrm{BK}_5 = \frac{Z_{\mathrm{R}} A_{\mathrm{bb}}}{\pi(r_{5\mathrm{t}}^2 - r_{5\mathrm{h}}^2)} \tag{4.40}$$

For a known rotor inlet radius the values of $t_{5\mathrm{t}}$ and $t_{5\mathrm{h}}$ are determined from the input blade thickness ratios. However, this is the thickness normal to the blade angle β. Referring to Figure 4.1, t_{eh} and t_{et} are therefore given by Equations 4.41 and 4.42 respectively.

$$t_{\mathrm{eh}} = \frac{t_{5\mathrm{h}}}{\cos\beta_{5\mathrm{h}}} \tag{4.41}$$

$$t_{\mathrm{et}} = \frac{t_{5\mathrm{t}}}{\cos\beta_{5\mathrm{t}}} \tag{4.42}$$

Therefore, to determine the blockage area, the blade angles at the hub and tip therefore

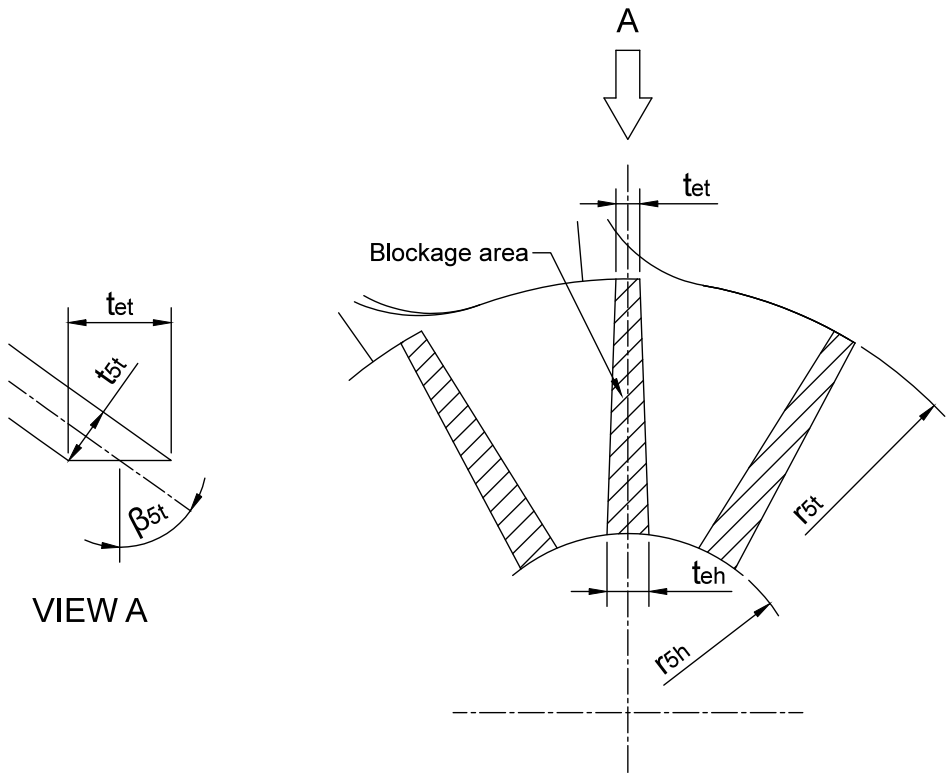

Figure 4.1: Schematic showing the geometrical area blocked by the blade at the rotor outlet.

need to be determined. For structural considerations, radial turbines are generally assumed to have radially fibered blades (Aungier, 2006). A consequence of this is that at any axial distance along the blade, the relationship given by Equation 4.43 must hold true. Therefore the hub and tip blade angles, denoted $\beta_{5\mathrm{h}}$ and $\beta_{5\mathrm{t}}$ respectively, can be found from the known values for r_5 and β_5 (Equations 4.44 and 4.45).

$$\frac{\tan\beta}{r} = \text{constant} \tag{4.43}$$

$$\beta_{5\mathrm{h}} = \tan^{-1}\left(\frac{r_{5\mathrm{h}}\tan\beta_5}{r_5}\right) \tag{4.44}$$

$$\beta_{5\mathrm{t}} = \tan^{-1}\left(\frac{r_{5\mathrm{t}}\tan\beta_5}{r_5}\right) \tag{4.45}$$

From the preceding discussion it should be apparent that iteration is required to arrive at the final rotor outlet dimensions. An initial guess assuming no blockage ($\mathrm{BK}_5 = 0$) results in an initial guess for $r_{5\mathrm{h}}$ and $r_{5\mathrm{t}}$, which in turn supplies the next estimate for for BK_5. This process is repeated until convergence.

Once the rotor radii are fully defined, the axial length of the rotor L is then given

by the input rotor length ratio Γ. Although the axial length does not impact the one-dimensional design, Γ can be used to control the passage area distribution during the three-dimensional design phase (Section 4.3).

$$L = \Gamma(r_{5\mathrm{t}} - r_{5\mathrm{h}}) \tag{4.46}$$

4.2.4 Rotor inlet geometry

Applying mass continuity at the rotor inlet determines the required flow area at the rotor inlet A_4 (Equation 4.47). Again, this is equal to the geometrical area minus the loss in area due to blade blockage. Since r_4 has already been defined by the outlet geometry, this leaves the required rotor inlet blade height b_4 to be determined (Equation 4.48). The turbine inlet blade thickness t_4 is assumed to be constant in the spanwise direction, and again the value is specified as a fraction of r_4.

$$A_4 = \frac{\dot{m}}{\rho_4 c_{\mathrm{m}4}} \tag{4.47}$$

$$b_4 = \frac{A_4}{2\pi r_4 - Z_{\mathrm{R}} t_4} \tag{4.48}$$

With the rotor inlet geometry fully defined the rotational speed of the turbine (in rpm), N, can then be determined.

$$N = \left(\frac{30}{\pi}\right)\omega = \left(\frac{30}{\pi}\right)\left(\frac{u_4}{r_4}\right) \tag{4.49}$$

4.3 Rotor three-dimensional design

Having sized the rotor inlet and outlet, the next design phase is to design the three-dimensional rotor passage. This rotor passage must be designed to minimise losses, and achieve a favourable blade loading distribution. This important aspect is often overlooked during preliminary design, and is often the result of more computationally expensive design methods such as CFD. The three-dimensional construction of the rotor consists of defining the meridional profiles, the camberline and the blade thickness distributions. These three curve sets, when superimposed onto each other, form the full rotor geometry. By controlling how these curves are defined, the shape and area distribution of the rotor passage can be controlled. Combining this geometrical construction with a method to predict the

resulting velocity distribution within the rotor allows the designer to quickly iterate and arrive at a suitable preliminary rotor passage design.

4.3.1 Rotor three-dimensional construction

Although the three-dimensional construction of ORC turbines has not been considered in detail in the literature, the three-dimensional construction of ideal gas turbines has been discussed. The definition of the relevant curve sets, in addition to the procedure to construct the rotor geometry, has been well discussed by both Atkinson (1998) and Aungier (2006), and the approach adopted here combines aspects from both methodologies. Subsequently, the key equations are described in Appendix B, whilst readers should refer to these references for more information.

4.3.2 Prediction of meanline parameters

After constructing the full rotor passage, the passage area distribution through the rotor can be determined, and this can be used to provide a preliminary estimate of the velocity distribution within the rotor. The first process is to construct a number of meanline quasi-normals on the meridional profile. To construct these, the co-ordinates of the hub and shroud profile curves are determined at 5% intervals of the total meridional path length, and these are connected by straight lines. The mid point of each line is determined and these locations correspond to the points at which the velocity distributions will be established. At each quasi-normal the meridional flow area, with and without blade blockage, can then be determined. The process of accounting for blade blockage is relatively involved, but has been well documented by Atkinson (1998). After calculating the passage area at each quasi-normal A_{q}, the complete rotor passage area distribution is then obtained. An example of the resulting meanline quasi-normals and passage area distribution is shown later on for the developed ORC turbine (Figure 4.9).

The approach adopted to predict the velocity distribution within the rotor is based on an approached suggested by Watson and Janota (1982). For this rotating machine the rothalpy I must remain constant, and this parameter is known from the rotor one-dimensional design. Therefore, the total relative enthalpy at each quasi-normal, $h_{0'}$, can be determined from the known rothalpy value, rotor rotational speed ω and the quasi-normal mid point radius r_{q} (Equation 4.50). The total relative enthalpy is related to

the static enthalpy h and the relative velocity w. For this analysis the rotor isentropic static-to-static efficiency η_{R} is also required and is defined by Equation 4.51. This can be determined from the rotor one-dimensional design.

$$h_{0'} = I + \frac{1}{2}(r_{\mathrm{q}}\omega)^2 = h + \frac{1}{2}w^2 \tag{4.50}$$

$$\eta_{\mathrm{R}} = \frac{h_4 - h_5}{h_4 - h_{5\mathrm{s}}} \tag{4.51}$$

To determine the relative velocity at each quasi-normal an iterative proceeded is required since neither h or w is known. As an initial guess, the total relative density, $\rho_{0'}$, is calculated based on $h_{0'}$, and assuming an isentropic expansion from the rotor inlet.

$$\rho_{0'} = \mathrm{EoS}(h_{0'}, s_4, \mathrm{fluid}) \tag{4.52}$$

An initial guess for the relative velocity is then obtained by applying mass continuity (Equation 4.53). For this analysis it is assumed that the relative flow within the rotor remains aligned with the blade such that the relative flow angle β is equal to the quasi-normal blade angle β_{q}. The applicability of this assumption will be analysed and confirmed later.

$$w = \frac{\dot{m}}{\rho_{0'} A_{\mathrm{q}} \cos\beta_{\mathrm{q}}} \tag{4.53}$$

The static enthalpy h follows from Equation 4.50, whilst the enthalpy associated with an isentropic expansion h_{s} can be obtained by assuming that η_{R} remains constant as the flow expands through the rotor (Equation 4.54). This in turn determines the static pressure P, then supplying a new estimate for the density ρ. This process is repeated until convergence, and then repeated for each quasi-normal.

$$h_{\mathrm{s}} = h_4 - \frac{h_4 - h}{\eta_{\mathrm{R}}} \tag{4.54}$$

$$P = \mathrm{EoS}(h_{\mathrm{s}}, s_4, \mathrm{fluid}) \tag{4.55}$$

$$\rho = \mathrm{EoS}(P, h, \mathrm{fluid}) \tag{4.56}$$

It should be clarified that the method outlined above cannot be relied upon to provide an accurate representation of the flow field within the rotor. This is because this meth-

odology applies one-dimensional flow theories to simulate a highly three-dimensional flow field. Furthermore, assuming that the flow remains aligned with the blade does not account for the flow entering the rotor with a certain amount of incidence, or for the flow deviation that is known to occur at the rotor outlet (Moustapha et al., 2003). However, the intention behind implementing this procedure is to aid in preliminary design. By calculating the rotor passage area distribution, and then estimating the velocity distribution, this procedure can be used to assess and then modify the passage geometry to avoid abrupt changes in the flow area, or unintentional areas of diffusion.

4.4 Stator design

The purpose of the stator is to deliver the flow to the rotor at the correct velocity, flow angle and thermodynamic conditions specified from the rotor design. The stator design therefore starts at the rotor inlet and works upstream.

4.4.1 Stator outlet

The stator-rotor interspace is the annular space between the stator exit (station 3) and rotor inlet (station 4), and this space allows the wakes downstream of the stator to mix out before entering the turbine. The optimal value is a trade-off between increased mechanical coupling at small distances, and increasing total pressure loss for larger distances (Moustapha et al., 2003). This trade-off is modelled by the interspace parameter K_{I}, and Watanabe et al. (1971) suggests that optimal performance is obtained when $K_{\mathrm{I}} = 2$. The stator outlet radius r_3 is then given by Equation 4.57.

$$r_3 = r_4 + K_{\mathrm{I}} b_4 \cos\left(\frac{\alpha_3 + \alpha_4}{2}\right) \tag{4.57}$$

Equation 4.57 requires iteration since the stator outlet flow angle α_3 is not known. As a first guess it is assumed that $\alpha_3 = \alpha_4$, resulting in an initial guess for r_3. Conservation of angular momentum (Equation 4.58) then supplies the tangential velocity component $c_{\theta 3}$, which then supplies the absolute velocity c_3. Within the stator-rotor interspace there is no work done, so assuming adiabatic flow ($h_{03} = h_{04}$) allows the static enthalpy h_3 to

be calculated (Equation 4.59).

$$r_3 c_{\theta 3} = r_4 c_{\theta 4} \tag{4.58}$$

$$h_3 = h_{03} - \frac{1}{2} c_3^2 \tag{4.59}$$

It is assumed that there is a negligible change in total pressure between the stator exit and rotor inlet, so the static entropy across the stator-rotor interspace remains constant ($s_3 = s_4$). This determines the density at the stator exit ρ_3 (Equation 4.60). This assumption is an over simplification since there will be losses associated with the abrupt area change at the stator exit and rotor inlet respectively, in addition to any profile loss along the side walls. However, this method has been successfully applied to the design of ideal gas radial turbines by Whitfield and Baines (1990) and Atkinson (1998). The suitability of this assumption for real gases will be verified later on on this chapter. By combining mass continuity between the stator exit and rotor inlet with Equation 4.58, a new estimate for α_3 can be obtained (Equation 4.61).

$$\rho_3 = \mathrm{EoS}(h_3, s_3, \mathrm{fluid}) \tag{4.60}$$

$$\tan \alpha_3 = \tan \alpha_4 \left(\frac{\rho_3}{\rho_4} \right) \left(\frac{1}{1 - \mathrm{BK}_4} \right) \tag{4.61}$$

With this new estimate the process outlined by Equations 4.57 - 4.61 can be repeated until α_3 has converged.

4.4.2 Stator throat

For axial turbines the cosine rule is widely used to determine the required stator throat width to supply the flow at the specified flow angle at the stator outlet. This rule applied to a radial turbine is stated by Equation 4.62, where o_{th} is the throat width and S_3 is the stator outlet pitch. S_3 is determined from the the number of stator blades, Z_{N}, and the stator outlet radius r_3. These parameters are shown later in Figure 4.2, alongside the full stator geometry.

$$o_{\mathrm{th}} = S_3 \cos \alpha_3 \tag{4.62}$$

$$S_3 = \frac{2\pi r_3}{Z_{\mathrm{N}}} \tag{4.63}$$

However, Equation 4.62 might be an over simplification for a radial turbine. Aungier (2006) suggests that for radial turbines the cosine rule should be adjusted to account for the change in angular momentum between the stator throat and the stator exit. This change in angular momentum is caused by the change in radius. For axial turbines, there is no change in radius, and therefore no change in angular momentum.

This correction is defined by Equation 4.64, where α_{th} is now the flow angle associated with the cosine rule (Equation 4.65), whilst r_{th} is the mean radius at the stator throat.

$$\tan \alpha_{\mathrm{th}} = \left(\frac{r_3}{r_{\mathrm{th}}} \right) \tan \alpha_3 \tag{4.64}$$

$$o_{\mathrm{th}} = \left(\frac{2\pi r_3}{Z_{\mathrm{N}}} \right) \cos \alpha_{\mathrm{th}} \tag{4.65}$$

Equation 4.64 can be derived by applying the conservation of mass between the stator throat and stator exit. Considering that the stator exit area is given by $A_3 = 2\pi r_3 b_3$, and the stator throat area is given $A_{\mathrm{th}} = Z_{\mathrm{N}} o_{\mathrm{th}} b_{\mathrm{th}}$, the following expression can be obtained.

$$\rho_{\mathrm{th}} c_{\mathrm{th}} \left(\frac{Z_{\mathrm{N}} o_{\mathrm{th}}}{2\pi r_3} \right) = \rho_3 c_3 \cos \alpha_3 \tag{4.66}$$

It is clear that the expression contained within the parentheses is equal to $\cos \alpha_{\mathrm{th}}$. Therefore, after expressing the absolute velocities c_{th} and c_3 in terms of the tangential velocity components and flow angles, Equation 4.67 can be obtained.

$$\frac{\rho_{\mathrm{th}} c_{\theta \mathrm{th}}}{\tan \alpha_{\mathrm{th}}} = \frac{\rho_3 c_{\theta 3}}{\tan \alpha_3} \tag{4.67}$$

After applying the conservation of angular momentum between the stator throat and stator exit ($r_{\mathrm{th}} c_{\theta \mathrm{th}} = r_3 c_{\theta 3}$), Equation 4.68 is finally obtained. This result is the same as Equation 4.64 apart from the density ratio that has been introduced. However, the density change between the stator throat and stator exit is assumed to be small, such that the two values are assumed to be approximately equal.

$$\tan \alpha_{\mathrm{th}} = \left(\frac{\rho_{\mathrm{th}}}{\rho_3} \right) \left(\frac{r_3}{r_{\mathrm{th}}} \right) \tan \alpha_3 \tag{4.68}$$

Equations 4.64 and 4.65 require iteration to arrive at the final stator throat width since neither α_{th} or r_{th} are known. An initial guess of $\alpha_{\mathrm{th}} = \alpha_3$ is assumed which supplies an

initial guess for the throat width using the cosine rule. A stator with this throat width is then constructed, and r_{th} can be determined numerically. This in turn supplies the next guess for α_{th}, and the process can be repeated until convergence.

The geometrical construction of the stator is shown in Figure 4.2. This construction is obtained by defining a single stator blade airfoil, which is then positioned so that the trailing edge is located at the stator outlet radius r_3, and then rotated about the trailing edge by the stator setting angle γ_3. A second blade can then be constructed by rotating this stator blade about the origin by $\theta = 2\pi/Z_{\text{N}}$. The value of γ_3 therefore needs to be selected to obtain the desired throat width, and this requires iteration. This iteration process, along with the mathematical description of the stator airfoil, can be found in Appendix B.

4.4.3 Stator inlet

With the stator geometry fully constructed the stator inlet radius r_2 can be determined numerically. The optimal incidence angle α^* at the stator leading edge is given by Equations 4.69 and 4.70. This expression is based on an empirical correlation that was developed by Emery et al. (1957) for axial compressor cascades. The parameters β_2 and β_3 refer to the blade angles at the stator inlet and outlet respectively.

$$i^* = \left(3.6\sqrt{\frac{10t_{\text{le}}}{c}} + \frac{|\beta_3 - \beta_2|}{3.4}\right)\sqrt{\frac{c}{S_3}} - \frac{|\beta_3 - \beta_2|}{2} \tag{4.69}$$

$$\alpha^* = \beta_2 - i^* \operatorname{sgn}(\beta_3 - \beta_2) \tag{4.70}$$

It is assumed that upstream components, such as a volute, will be designed to deliver the flow at this optimal incidence angle such that $\alpha_2 = \alpha^*$. Assuming minimal loss within the volute the total conditions at the stator inlet will be equal to the turbine inlet conditions ($T_{02} = T_{01},\ P_{01} = P_{02}$). This permits an iterative mass balance to undertaken using the known stator inlet flow area $A_2 = 2\pi r_2 b_2$ to determine the static properties and absolute velocity.

4.4.4 Stator design inputs

The inputs required to design the stator are listed in Table 4.1. These values shown are the default values that are used within this chapter to generate the stator blade geometry.

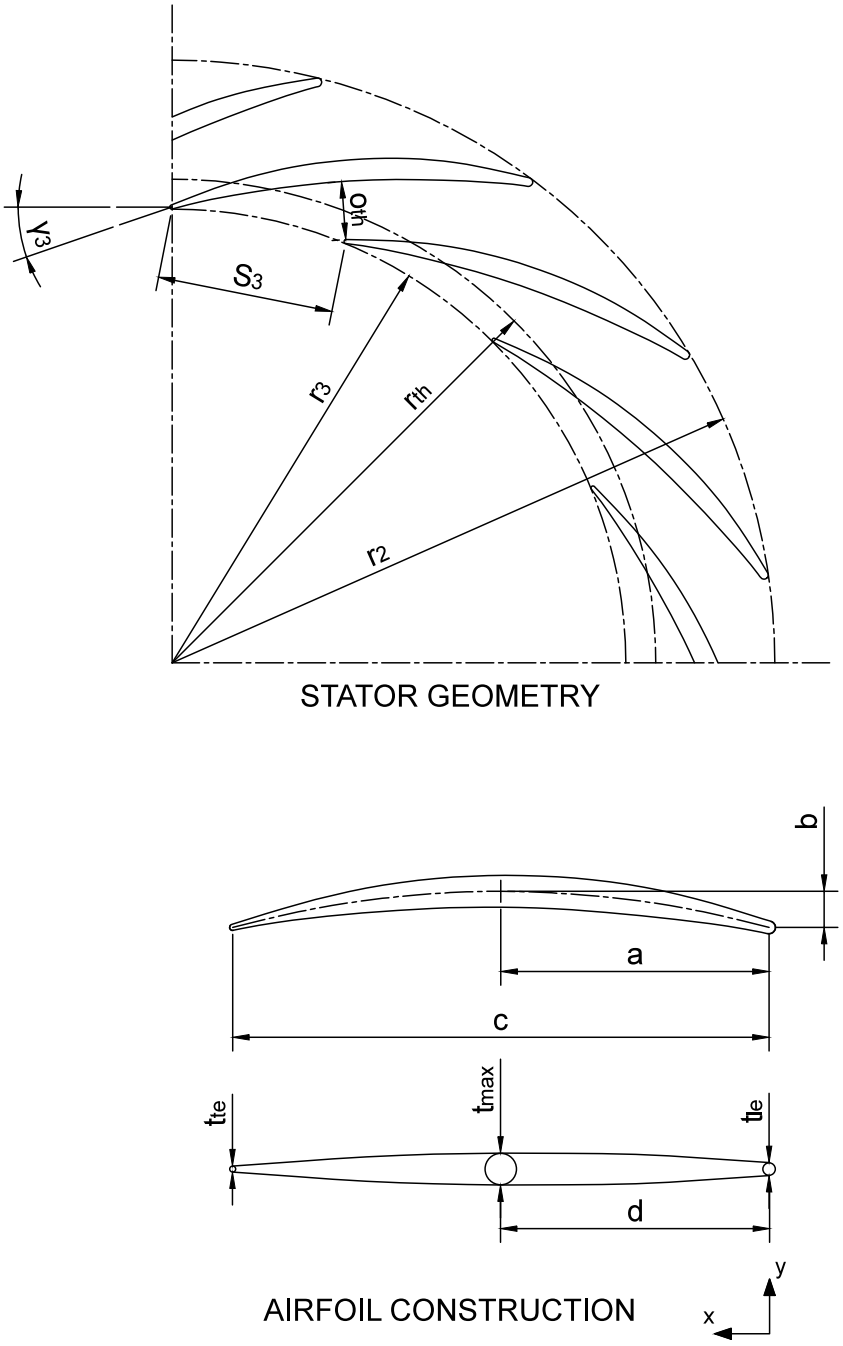

Figure 4.2: Schematic of the stator geometry and airfoil definition.

These values are selected based on recommendations made by Aungier (2006) who argues that these values should result in a suitable geometry for most applications. However it was found that the original suggestion for the stator exit pitch to chord ratio ($S_3/c = 0.75$) required a large number of stator blades to achieve suitable blade loading. For a small turbine a large number of stator vanes would be hard to machine, and therefore it was suitable to reduce this ratio to 0.5. The stator blade camber angle is set to zero, therefore assuming that there will be a volute upstream of the stator leading edge.

Table 4.1: Summary of the default stator design inputs used during turbine development.

Parameter		Value
Rotor-stator interspace parameter	K_I	2
Number of stator blades	Z_N	16
Stator blade camber angle	θ	0°
Normalised location of maximum camber	a/c	0.5
Normalised location of maximum thickness	d/c	0.4
Normalised leading edge thickness	t_le/c	0.025
Normalised trailing edge thickness	t_te/c	0.012
Normalised maximum thickness	t_max/c	0.04
Stator exit pitch to chord ratio	S_3/c	0.5

4.5 Case study: Ideal gas turbine

The design of radial turbines operating with ideal gases is much better understood than those operating with ORC working fluids. Therefore, before designing an ORC turbine it was decided to design a turbine operating with air. This turbine design has been evaluated at the design point using CFD, thus validating the design model.

The thermodynamic specification for the radial turbine is summarised in Table 4.2. These conditions refer to a radial turbine operating within an optimised micro gas turbine that would be used to convert concentrated solar power into mechanical power. This application is being considered within a research project that is currently being undertaken within the same research group at City University. It is assumed that a turbine can be designed with an optimal specific speed and specific diameter, such that a turbine with an isentropic efficiency of $\eta_\mathrm{ts} = 85\%$ could be achieved.

The design process, CFD setup and CFD analysis for both the air turbine, and the ORC turbine are very similar. Since the design and analysis of ORC turbines is the focus of

Table 4.2: Thermodynamic inputs for the air turbine case study.

Parameter		Value	Units
Fluid		Air	
Total inlet temperature	T_{01}	1073	K
Total inlet pressure	P_{01}	282.3	kPa
Mass flow rate	$\dot{m}$	0.1	kg s^{-1}
Pressure ratio	PR_{ts}	3.0	
Isentropic efficiency (ts)	η_{ts}	85.0	%

this research, and the design and CFD analysis of ideal gas turbines is well discussed within the literature, it is more appropriate to discuss the design process and CFD analysis with relation to the ORC turbine. Therefore only the key results from this ideal gas validation are discussed here, whilst more details are supplied in Appendix C.

After developing the rotor design and completing the CFD analysis, the intended performance was compared to the performance predicted by the CFD (Table 4.3). Following from the rotor one-dimensional design phase the design rotational speed was determined to be $135,587$ rpm, whilst the CFD analysis was completed for the design pressure ratio of 3.0. A large part of the rotor design process is designing the rotor velocity triangles, and therefore it is also suitable to compare the design velocity triangles with those predicted by CFD. This comparison is shown in Figure 4.3. The blade loading distributions, contours of Mach number and velocity vectors determined from the CFD analysis are included in Appendix C.

The rotor inlet velocity triangle predicted by the CFD matches well with the design point velocity triangle. There is a slight deviation in the absolute flow angle at the rotor inlet, whilst the estimated $\eta_N = 95.77\%$ is higher than the design value of $\eta_N = 91.62\%$.

Table 4.3: Comparison between of the intended design and CFD results for the air turbine case study.

Parameter		Design	CFD	Units
Rotational speed	N	135,587		rpm
Pressure ratio (ts)	PR_{ts}	3.0		
Mass flow rate	$\dot{m}$	0.100	0.104	kg s^{-1}
Isentropic efficiency (ts)	η_{ts}	85.00	84.74	%
Isentropic efficiency (tt)	η_{tt}	88.70	91.01	%
Stator isentropic efficiency	η_N	91.62	95.77	%

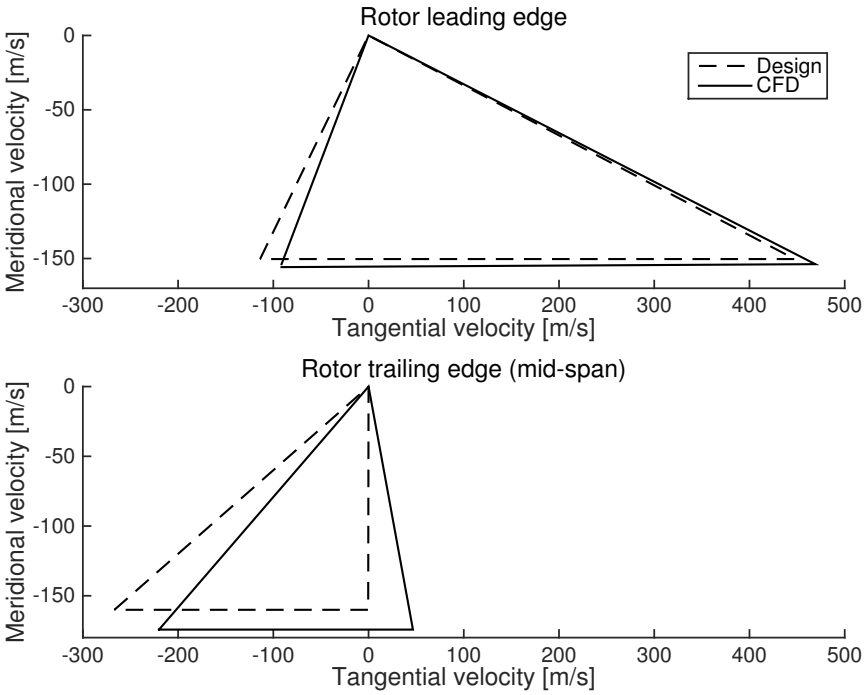

Figure 4.3: Comparison between the intended design and CFD velocity triangles for the air turbine at the rotor leading and trailing edges.

As will be shown in Section 4.6 the rotor inlet velocity is sensitive to small variations in these two parameters. Nonetheless, the overall deviation is sufficiently small, indicating that the stator design methodology is sufficient in providing a suitable design; particularly the use of the cosine rule with the radius adjustment ratio.

At the rotor outlet a larger deviation in the velocity triangles is observed. The CFD results predict an average relative flow angle at the rotor outlet mid-span of $-51.62°$, compared to the $-59.04°$ mid-span blade angle. This shows that the relative flow at the rotor outlet is not fully aligned with the blade as assumed, corresponding to a deviation of $-7.42°$. This deviation is due to the highly complex three-dimensional flow field at the rotor discharge that cannot be accurately estimated using a one-dimensional method. This will be discussed in more detail in Section 4.6. However, the measured deviation agrees well with values suggested by Moustapha et al. (2003). It is observed that this deviation results in an absolute tangential velocity component that introduces swirl at the rotor discharge.

Overall, the CFD results indicate that at the design total inlet conditions and total-to-static pressure ratio, the turbine, rotating at $135,587$ rpm will expand 0.104 kg s^{-1} of air with aerodynamic isentropic efficiencies of $\eta_{\text{ts}} = 84.72\%$ and $\eta_{\text{tt}} = 91.01\%$ respectively.

The higher mass flow rate is attributed to a lower total pressure loss within the turbine, suggested by the higher η_{tt} value compared to the design value of $\eta_{\mathrm{tt}} = 88.70\%$, calculated from the one-dimensional model outputs. Overall, the predictions made by the CFD are in good agreement with the design values, thereby validating the rotor and stator design tools for the design of a turbine operating with air. The small difference between η_{ts} predicted by the CFD and the design input confirms that $\eta_{\mathrm{ts}} = 85\%$ was a suitable value to select within the rotor one-dimensional design.

It should of course be noted that the efficiencies quoted here are purely the aerodynamic efficiencies calculated from the CFD results, which are based on the thermodynamic properties at the stator inlet and the rotor trailing edge. Therefore there is no consideration of the total pressure losses that will inevitably occur upstream of the stator in the volute, and downstream of the rotor trailing edge, which will both act to reduce the turbine efficiency. Additional windage losses, and mechanical losses in the transmission system will then reduce the overall turbine efficiency even further.

4.6 Case study: Subsonic ORC turbine

Having implemented the turbine design model, and validated the model for the design of an ideal gas turbine, a subsonic ORC turbine operating with R2454fa was then developed. This design has also been evaluated using CFD, thus validating the design method for subsonic turbines operating with organic fluids. At this point it should be highlighted that the aim of this part of the research was not to complete a full optimisation of the turbine design, but to arrive at a turbine design that would expand the working fluid whilst achieving a reasonable efficiency. From this candidate turbine design the performance map can be obtained which can be used in further thermodynamic cycle optimisation studies which can couple ORC cycle analysis with detailed turbine performance data.

4.6.1 ORC turbine design

From the sizing optimisation carried out in Chapter 3, R245fa was confirmed as a suitable working fluid for low temperature ORC applications. Although the results from this sizing optimisation study could have been used as the thermodynamic inputs for the turbine design model, the net work produced from this cycle was less than the original target

power of 10 kW. Therefore, a new thermodynamic specification has been defined and this has been summarised in Table 4.4. This refers to a 10 kW ORC with a condensation temperature of 40°C, and has been designed to utilise low temperature heat sources been 100 and 120°C. For this condensation temperature, and the defined pressure ratio, the saturation temperature at the turbine inlet pressure is 343.97 K. Although it has been shown that superheating is unnecessary for ORCs, the turbine inlet temperature has been increased to 350.00 K, corresponding to a superheat of 6.03 K. The reason for this is to ensure that the expansion through the turbine remains within the superheated region. Not only should two-phase conditions be avoided in turbomachines, but two-phase conditions may introduce uncertainties when running the CFD simulation.

Table 4.4: Thermodynamic inputs for the R245fa turbine case study.

Parameter		Value	Units
Fluid		R245fa	
Total inlet temperature	T_{01}	350	K
Total inlet pressure	P_{01}	623.1	kPa
Mass flow rate	$\dot{m}$	0.7	kg s^{-1}
Pressure ratio	PR_{ts}	2.5	
Isentropic efficiency (ts)	η_{ts}	85.0	%
Isentropic stator efficiency	η_N	95.0	%

For the thermodynamic specification in Table 4.4 it is expected that a turbine with an optimal specific speed and specific diameter can be obtained, so the target isentropic efficiency has been set to $\eta_{ts} = 85\%$. For the air turbine Equation 4.71 was used to estimate the total pressure loss within the stator, as recommended by Aungier (2006). However, Table 4.3 showed that this Equation over predicted the total pressure loss. Therefore for the ORC turbine the stator efficiency was directly set to $\eta_N = 95\%$.

$$P_{04} = P_{01} - \frac{\rho_{01}(h_{01} - h_{5ss})(1 - \eta_{ts})}{4} \tag{4.71}$$

Rotor one-dimensional design

With the thermodynamic inputs specified the first step was to define the rotor one-dimensional design. Again, it should be reiterated that the purpose of this research is not to obtain a fully optimised rotor geometry, but to obtain a design that will achieve a reasonable performance. Therefore, to develop this design a parametric study of the

design parameters has been completed, and this has led to a candidate rotor design.

As stated previously, it was expected that for the defined thermodynamic conditions an optimal specific speed and specific diameter can be achieved. Referring back to Figure 3.7, optimal turbine efficiencies are obtained when $N_\mathrm{s} = 0.6$ and $D_\mathrm{s} = 3.33$. Furthermore, combining the definitions of N_s and D_s (Equations 2.31 and 2.32), it can be shown that these values of N_s and D_s immediately supply the isentropic velocity ratio ν_ts.

$$\nu_\mathrm{ts} = \frac{N_\mathrm{s} D_\mathrm{s}}{2\sqrt{2}} = 0.707 \tag{4.72}$$

With ν_ts defined, the rotor inlet blade velocity immediately follows. An important design consideration for radial turbines is to ensure minimal swirl at the rotor outlet. This means $c_{\theta 5} = 0$, which from Euler's law (Equation 2.15) supplies $c_{\theta 4}$ and therefore the blade loading coefficient ($\Psi = c_{\theta 4}/u_4$). Considering the rotor inlet velocity triangle it can also be shown that to ensure no swirl the following relationship between the absolute and relative flow angles must hold (Equation 4.73). This relationship is plotted in Figure 4.4, along with the resulting rotor inlet absolute Mach number.

$$\tan\beta_4 = \tan\alpha_4 \left(1 - \frac{2\nu_\mathrm{ts}^2}{\eta_\mathrm{ts}}\right) \tag{4.73}$$

From this figure it is clear that as the absolute flow angle α_4 increases, the relative flow angle β_4 increases while the Mach number reduces. This is because the tangential velocity components $c_{\theta 4}$ and $w_{\theta 4}$ remain fixed, which means that as α_4 increases the meridional velocity component must reduce, leading to a lower absolute velocity and larger value for β_4. At low values of α_4 it is clear that the Mach number could exceed 1, which could complicate the stator design. Furthermore, it has been shown that for a radial turbine it is favourable for the flow to enter the rotor with a certain amount of incidence, and Dixon (2010) recommends values of β_4 between $-20°$ and $-40°$. From Equation 4.73 this suggests values of α_4 between 64° and 78°.

To establish the most suitable value for α_4 the analysis was extended to the rotor outlet. The rotor outlet velocity triangle is defined by the diameter ratio ϵ and the rotor velocity ratio ϕ. A parametric study of ϵ and ϕ at different values for α_4 was therefore undertaken which investigated how these parameters effect the flow coefficient Φ and the meridional velocity ratio ξ. The limits for ϵ and ϕ were set according to Dixon (2010).

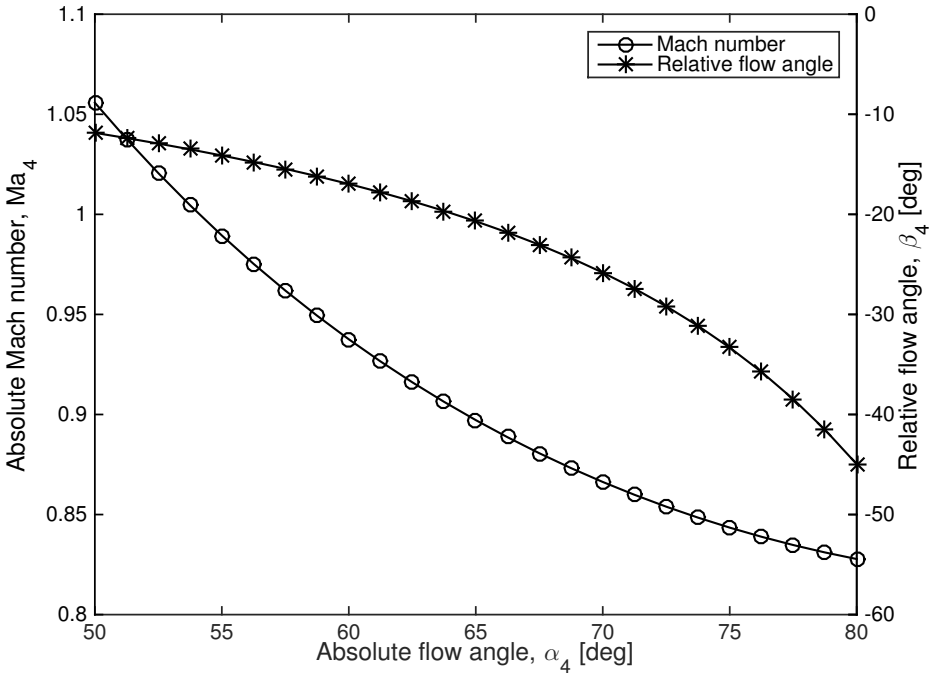

Figure 4.4: Relationship between α_4, β_4 and Ma_4 to ensure no swirl at the rotor outlet for the ORC turbine.

The resulting variations in Φ and ξ are shown in Figures 4.5 and 4.6 respectively. Optimal designs tend to have values of $\Phi = 0.25$ (Rodgers and Geiser, 1987) and $\xi = 1$ (Moustapha et al., 2003).

From Figure 4.5 it is clear that the variation in Φ with ϵ and ϕ is not sensitive to variations in α_4. This is because for fixed values of $c_{\theta 4}$ and u_4 the rotor inlet, and therefore rotor outlet, rothalpy will remain constant for any flow angle. Any slight variation in the flow coefficient with variations in α_4 is therefore only attributed to the slight change in the rotor inlet thermodynamic properties that occurs due to the change in the absolute velocity c_4. Overall from Figure 4.5, it is apparent that for this particular application it is possible to achieve a turbine design that will achieve $\Phi = 0.25$.

From Figure 4.6 it is clear the variation in ξ is more sensitive to variations in α_4. This was to be expected since a similar Φ distribution means that the rotor outlet meridional velocity $c_{\mathrm{m}5}$ remains similar for any value of α_4. However, as was noted previously a higher α_4 value corresponds to a lower rotor inlet meridional velocity $c_{\mathrm{m}4}$, therefore resulting a higher value for ξ. For $\alpha_4 = 65°$ it is clear that a value of $\xi = 1$ cannot be achieved, which would mean that a considerable reduction in the meridional velocity through the turbine would be required, whilst for $\alpha_4 = 80°$, $\xi = 1$ is achieved at low values of ϕ.

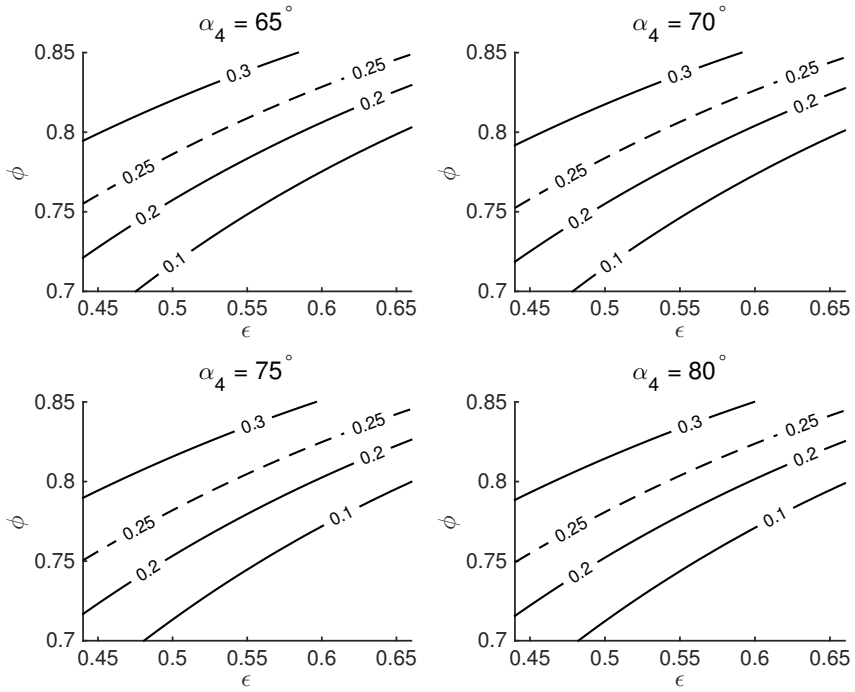

Figure 4.5: Variation in Φ with ϵ and ϕ at different α_4 values.

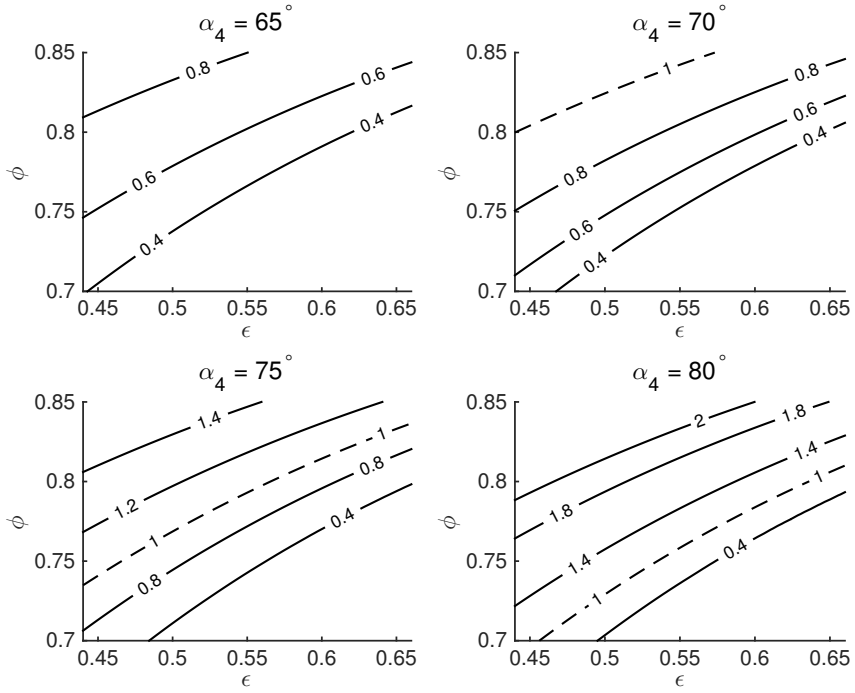

Figure 4.6: Variation in ξ with ϵ and ϕ at different α_4 values.

Since ϕ is a measure of the deviation from isentropic flow conditions through the rotor, this suggests that such a design would not be ideal. The results therefore indicate that $\alpha_4 = 70°$ and $\alpha_4 = 75°$ would be the most suitable absolute flow angles. Comparing Figures 4.5 and 4.6 it seems apparent that the lines corresponding to $\Phi = 0.25$ and $\xi = 1$ align better for $\alpha_4 = 75°$ than for $\alpha_4 = 70°$ therefore suggesting that the former would be the better choice. Furthermore, Aungier (2006) suggests that designs with $\xi < 1.5$ are equally permissible which also favours $\alpha_4 = 75°$.

The final rotor outlet design is also dependent on the value selected for the hub-to-shroud diameter ratio λ. Although the values selected for ϵ and ϕ determine the velocity triangle, λ controls the hub and shroud diameters, and therefore also the rotor inlet diameter. This in turn controls the rotor specific speed N_s. With $\alpha_4 = 75°$ selected, the parametric investigation of ϵ and ϕ was repeated for four values of λ and the resulting variations in N_s are shown in Figure 4.7.

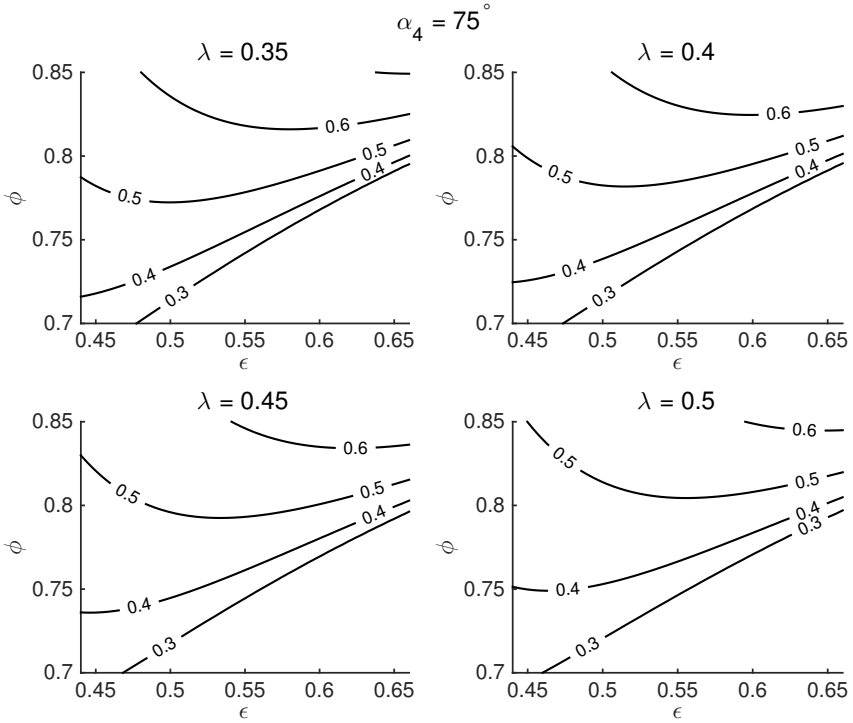

Figure 4.7: Variation in N_s with ϵ and ϕ at different values of λ.

Figure 4.7 shows that as λ reduces there is a larger range of ϵ and ϕ values that will result in the optimal specific speed of $N_s = 0.6$. For $\lambda = 0.5$, $N_s = 0.6$ is only achieved for high values of ϕ. This would require a well designed rotor passage to ensure minimal loss, which may not be realised in practice. The case with $\lambda = 0.35$ shows the largest range of

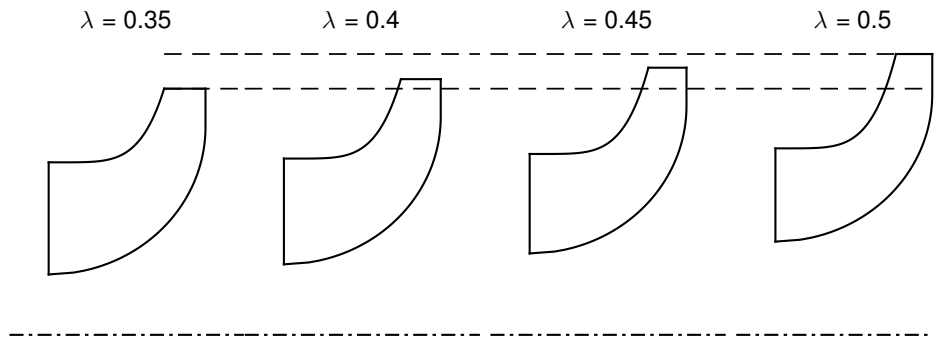

Figure 4.8: Variation in meridional rotor profiles with different values of λ.

ϵ and ϕ values that will result in an optimal specific speed, which suggests that this may be a suitable choice.

It is also interesting to consider the resulting turbine geometry, as viewed on the meridional plane. This has been shown in Figure 4.8 for the same set of λ values, where ϵ and ϕ are set to 0.525 and 0.825 respectively. Here the reduction in the rotor inlet radius is clear with reducing λ, indicating why $\lambda = 0.35$ enables a higher specific speed to be achieved.

Overall, the parametric study detailed in the previous pages enabled a rotor one-dimensional design to be established. After some additional manual refinement to some of the geometrical parameters, the final design inputs selected have been summarised in Table 4.5. The design outputs are summarised in Table 4.6.

The final turbine specific speed is 0.602, and this correlates well to the selected value of $\eta_{\text{ts}} = 85\%$. Furthermore, according to Aungier (2006) the flow coefficient Φ should be

Table 4.5: Inputs into the rotor design program for the R245fa turbine case study.

Parameter		Value
Isentropic velocity ratio	ν_{ts}	0.707
Rotor inlet absolute flow angle	α_4	75°
Rotor inlet relative flow angle	β_4	−33.32°
Rotor velocity ratio	ϕ	0.825
Rotor outlet/inlet diameter ratio	ϵ	0.525
Rotor outlet hub/shroud ratio	λ	0.347
Blade number	Z_{R}	12
Rotor inlet blade thickness	t_4/r_4	0.04
Rotor outlet hub blade thickness	$t_{5\text{h}}/r_4$	0.02
Rotor outlet shroud blade thickness	$t_{5\text{t}}/r_4$	0.01

Table 4.6: Outputs from the rotor design program for the R245fa turbine case study.

Parameter		Value	Units
Performance parameters			
Isentropic efficiency (tt)	η_{tt}	88.96	%
Work output	W_{t}	10.22	kW
Rotational speed	N	37,525	rpm
Specific speed	N_{s}	0.602	
Specific diameter	D_{s}	3.320	
Degree of reaction	R	0.597	
Blade loading coefficient	Ψ	0.850	
Flow coefficient	Φ	0.299	
Meridional velocity ratio	ξ	1.314	
Rotor dimensions			
Inlet radius	r_4	33.34	mm
Inlet blade height	b_4	5.28	mm
Outlet hub radius	$r_{5\mathrm{h}}$	8.11	mm
Outlet shroud radius	$r_{5\mathrm{t}}$	23.39	mm
Rotor flow angles			
Outlet absolute flow angle	α_5	0.000	°
Outlet hub relative flow angle	$\beta_{5\mathrm{h}}$	-39.10	°
Outlet shroud relative flow angle	$\beta_{5\mathrm{t}}$	-66.88	°
Rotor Mach numbers			
Inlet Mach number	Ma_4	0.843	
Outlet shroud Mach number	$\mathrm{Ma}_{5\mathrm{t}}$	0.726	

between 0.2 and 0.4, whilst the degree of reaction R should be between 0.45 and 0.65; both parameters are found to fall within this range. The meridional velocity ratio of $\xi = 1.314$ is higher than unity. However, this is not considered an issue since it is permissible for this ratio to range between 1 and 1.5. It is clear that the flow remains subsonic through the whole the rotor, so there should be no concerns with supersonic flows.

For the ORC turbine there is a significant reduction in rotational speed compared to the air turbine. This is attributed to the much lower enthalpy drop experienced for the organic fluid compared to enthalpy drop for air. This significantly reduces the rotor inlet blade speed to 131.0 m s^{-1} compared to 561.4 m s^{-1} for air, which should mean the structural analysis of the blade becomes less relevant. However, the ORC turbine designer must be aware of the possibility of supersonic flow due to the low speed of sound, in addition to the more complex sealing methods required to contain the organic fluid.

Rotor three-dimensional design

The rotor three-dimensional design was established through the manual variation of the meridional profile curves, camberline and blade thickness distributions. With the blade number and blade thicknesses at the rotor inlet and outlet established in Table 4.5, the available variables were the shroud meridional curve power factor n, the axial length ratio Γ and the blade thickness spline points. The camberline was defined by Equation B.3. A manual iteration of these parameters was undertaken, and this was coupled with the method to predict the velocity distribution within the rotor (Section 4.3.2). This was also combined with preliminary CFD analysis to evaluate the mass flow rate through the rotor at the design pressure ratio and rotational speed. The final rotor design was the design that resulted in the closest match to the design mass flow rate, whilst maintaining a reasonable velocity distribution within the rotor. The left hand side of Figure 4.9 displays the final rotor profile displayed on the meridional plane along with the meanline quasi-normals used to predict the velocity distribution within the rotor. The right hand side of Figure 4.9 displays the passage area distribution. Figure 4.10 displays the resulting camberline, blade angle and blade thickness distributions, whilst the final geometrical inputs used to construct the three-dimensional rotor are summarised in Table 4.7.

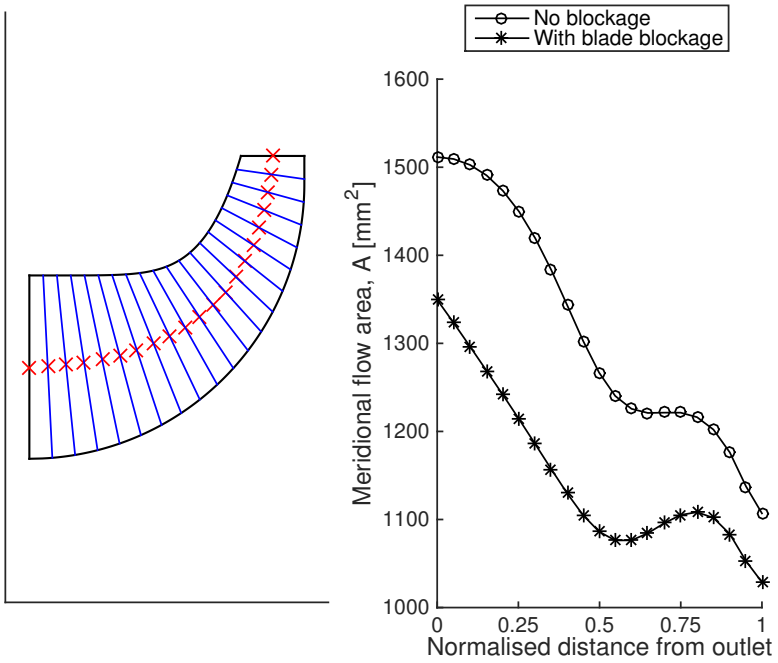

Figure 4.9: Rotor quasi-normals and passage area distribution for the R245fa turbine.

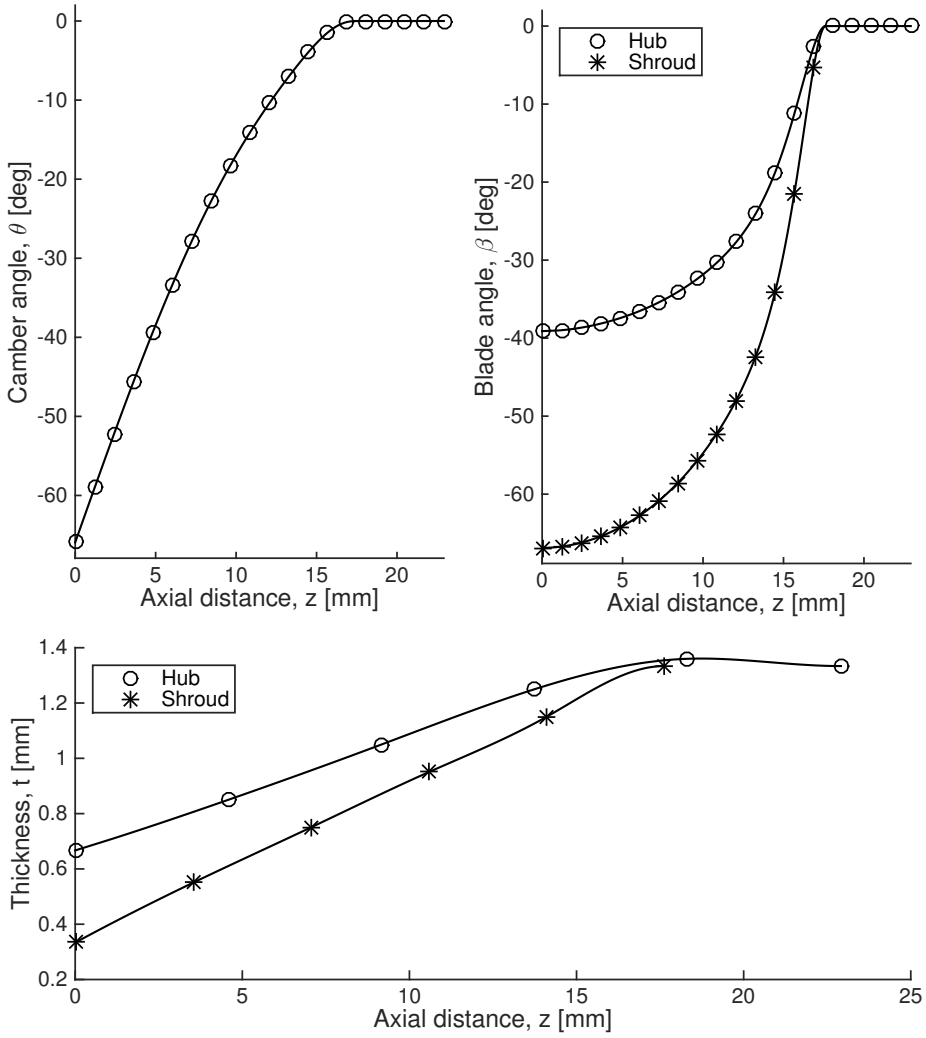

Figure 4.10: Camberline distribution and thickness distributions for the R245fa turbine.

Table 4.7: Rotor geometrical inputs for the R245fa turbine case study.

Axial length ratio	Γ	1.5
Shroud profile power factor	n	6.0
Camberline function		Equation B.3

Hub		Shroud	
Location	Thickness (mm)	Location	Thickness (mm)
$0.2L$	0.85	$0.2(L-b_4)$	0.55
$0.4L$	1.05	$0.4(L-b_4)$	0.75
$0.6L$	1.25	$0.6(L-b_4)$	0.95
$0.8L$	1.36	$0.7(L-b_4)$	1.15

Stator design

The default inputs in Table 4.1 were used to construct the stator, and this was originally completed with an stator-rotor interspace parameter of 2. However, it was found that this resulted in a small distance between the stator outlet radius and the rotor inlet radius. Whilst this is not a physical problem, it could result in numerical issues within the CFD solver since the rotor inlet domain radius would be very close to the rotor leading edge. To avoid this the stator-rotor interspace parameter was therefore increased to 4, and the stator was reconstructed. The final geometrical data for the stator is summarised in Table 4.8.

Table 4.8: Stator geometry for the R245fa turbine case study.

Parameter		Value	Units
Stator-rotor interspace	K_{I}	4.0	
Stator inlet radius	r_2	51.93	mm
Stator outlet radius	r_3	38.42	mm
Stator radius ratio	r_2/r_3	1.351	
Stator throat	o_{th}	3.494	mm
Stator throat radius	r_{th}	40.31	mm
Leading edge thickness	t_{le}	0.754	mm
Trailing edge thickness	t_{te}	0.362	mm
Stator setting angle	γ_3	6.381	$^\circ$

4.6.2 ORC turbine CFD simulation

With the rotor and stator design established, the performance of the turbine can be evaluated using CFD. The purpose of using CFD is to evaluate the turbine performance at the design point, which will enable a comparison between the intended turbine performance, and the actual performance achieved. This in turn will validate whether the developed model is suitable for the design of ORC turbines.

CFD setup

The CFD analysis of the turbine has been completed using ANSYS workbench. The ANSYS CFX solver is well suited to simulating flows within turbomachines, whilst BladeGen and TurboGrid can be used to construct and mesh the rotor and stator blades respectively.

Using the meridional profile curves, camberline and blade thickness defined in Section

4.3 the rotor geometry can be quickly constructed in BladeGen. Although it would have been possible to define these curve sets in BladeGen directly, their inclusion in the design model enhances the design models versatility, whilst allowing the meanline parameters to be predicted during the design process. Once the rotor is constructed the rotor shroud clearance gap is created by trimming the rotor blade by the desired clearance amount. The blade is trimmed to create the clearance gap as opposed to adding this clearance gap to the blade height to ensure conservation of the flow areas. The clearance was set to 0.4 mm, which according to Dixon (2010) is a suitable value that can be obtained by current manufacturing techniques. The stator blade was constructed in SolidWorks which was then imported into BladeGen.

The rotor and stator meshes were constructed using TurboGrid, which is a program specifically designed to provide high quality hexahedral meshes of turbomachine blades. Based on the rotor inlet conditions and rotor blade path length the flat plate Reynolds number is estimated at $\mathrm{Re_L} = 2.7 \times 10^6$, and therefore the boundary layer should be fully turbulent. The near wall spacing was set to $y^+ = 100$ to be in line with the selected turbulence model and scalable wall function.

With the meshes complete, a steady-state simulation of the stator, rotor and clearance gap was setup in ANSYS CFX. The mixing plane (stage) model was used to simulate the interface between the stator and rotor, and periodic boundaries were used for the stator and rotor blade passages. The time-step was set to the reciprocal of the rotational speed in rad s^{-1}. Minimal total pressure loss was assumed within the volute such that the conditions at the stator inlet were set to the turbine total inlet conditions. It was assumed that the volute delivered the flow to the stator leading edge at the optimal incidence angle and the flow angle upstream of the stator leading edge was then estimated by applying conservation of mass and angular momentum. The rotor outlet boundary condition was set according to the design mass flow rate.

For this analysis the standard $k - \epsilon$ turbulence model with scalable wall function was used, and this was selected over the SST turbulence model. The SST model combines a $k - \omega$ formulation within the boundary layer with the $k - \epsilon$ formulation within the freestream, allowing a better resolution of the flow field within the boundary layers. However Harinck et al. (2010) simulated real gas flows through an ORC turbine stator and results showed that the implementation of the $k - \omega$ turbulence model had little effect on the overall flow

field. The $k-\epsilon$ model was therefore selected since it converges faster, and this follows on from Sauret and Gu (2014) who also consider this model for its robustness with real gas applications.

Working fluid properties

One of the significant differences in the CFD setup for the ORC turbine compared to the air turbine is the calculation of the working fluid properties. For the air turbine the fluid is modelled as an ideal gas, and a constant value for the ratio of specific heats is assumed. However, for the ORC working fluid this model is no longer valid and therefore alternatives are required.

A common method employed in the ORC CFD studies found within literature is to use cubic equations of state to model the working fluid properties (Colonna et al., 2006; Sauret and Gu, 2014). These equations determine the pressure of the fluid as a function of temperature and specific volume, and are called cubic equations since, when rearranged for the volume, a cubic equation is obtained. The most common examples are the Peng-Robinson (PR) and Redlich-Kwong (RK) equations, although additional models such as the Redlich-Kwong-Soave (RKS) and Redlich-Kwong-Aungier (RKA) models have also been developed which aim to improve the accuracy of the original RK model. The mathematical description of these equations can be found in Appendix D. Within CFX all of these equations of state can easily be implemented. These models require the fluid properties at the critical point, in addition to the fluids acentric factor, to be specified. In order to determine the internal energy, enthalpy and entropy, the coefficients of a zero pressure polynomial also need to be defined. This polynomial expresses the variation in the specific heat capacity with temperature at zero pressure as a fourth order polynomial. For this purpose REFPROP is used to obtain suitable data points before MATLAB is used to then generate the fourth order polynomial curve fit.

The other option is to directly construct fluid property tables using REFPROP, which can then be made available to the CFX solver during the simulation. The advantage of constructing these property tables using REFPROP is that the equations of state used in REFPROP are more advanced and accurate than the cubic equations of state. However, this does require a license to the REFPROP software, whilst the information required for the cubic equations of state is readily available.

The accuracy of the cubic equations of state has been investigated in Figure 4.11 for R245fa. Here the pressures predicted using the ideal gas, PR, RKS and RKA equations of state are expressed in terms of the percentage deviation from the pressure obtained using REFPROP. The white area is the saturated vapour dome. The distributions found in this figure match well with those obtained by Luján et al. (2012) who completed a similar comparison for R245fa, therefore validating these results.

Firstly, the large deviation found using the ideal gas law clearly shows why it is not suitable to model the fluid as an ideal gas. For the remaining equations of state the percentage deviation remains less than 2% over the range of temperature and entropy values considered. The adapted RK models both show a similar error distribution with the highest deviation found close to saturated vapour line. For these cases as superheating increases the accuracy of these equations of state increases. It is also clear that the accuracy of the RKA model offers a slight improvement over the RKS equation of state. The PR equation of state shows a more interesting distribution with areas with a higher percentage error found near the saturated vapour line for low temperatures, and at increasing temperature and pressure. However, for saturated vapour conditions near the

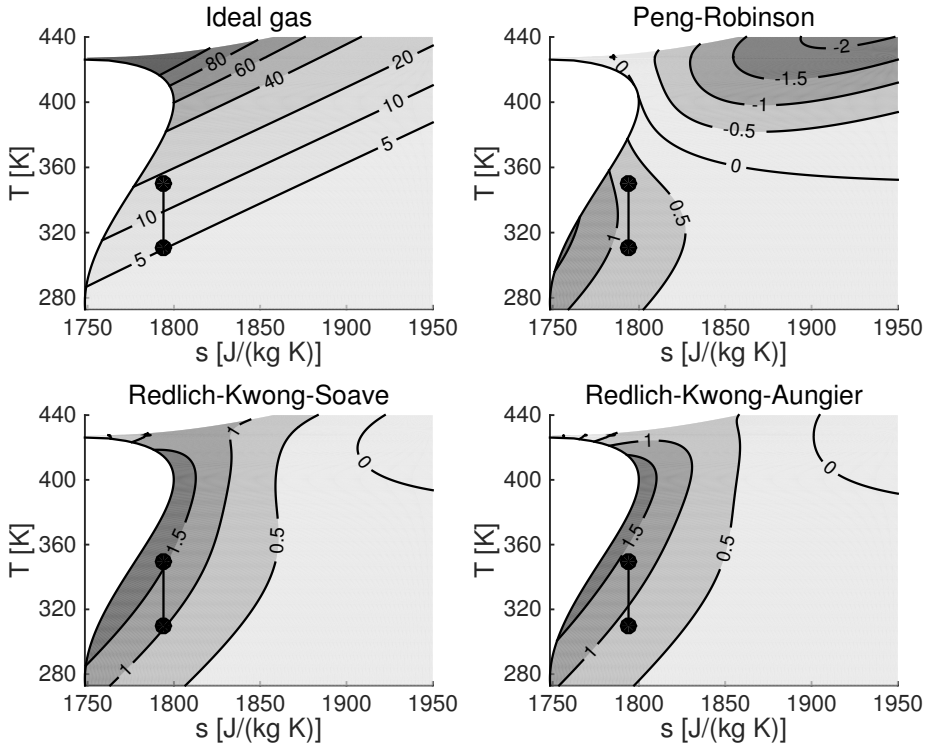

Figure 4.11: Percentage deviation between the pressure predicted using the most common cubic equations of state and the actual pressure calculated using REFPROP for R245fa.

critical point the deviation found for the PR equation of state is negligible.

The black vertical lines in Figure 4.11 represent the expected operating conditions for the ORC turbine. The top dot corresponds to the turbine total inlet conditions, whilst the bottom dot corresponds the turbine outlet conditions after an isentropic expansion to the design static pressure. From these lines it is clear that during the expansion process the percentage error in the pressure remains between 0.8% and 1.57% for all three equations of state. Of the three, it seems that the PR equation of state would be the most accurate for predicting pressure for this operating point.

Using the same equations of state the fluid enthalpy has also been calculated over the same range of temperature and entropy values. The calculation procedure is shown in Appendix D and requires the definition of the zero pressure polynomial as mentioned previously. The results are shown in Figure 4.12 and again the results are expressed in terms of the percentage deviation from the enthalpy value obtained using REFPROP.

Unlike the pressure calculation, the shape of the error distribution in enthalpy does not vary significantly between the PR and adapted RK models. Close to the saturated vapour line all three cubic equations of state over predict the fluid enthalpy, whilst the percentage

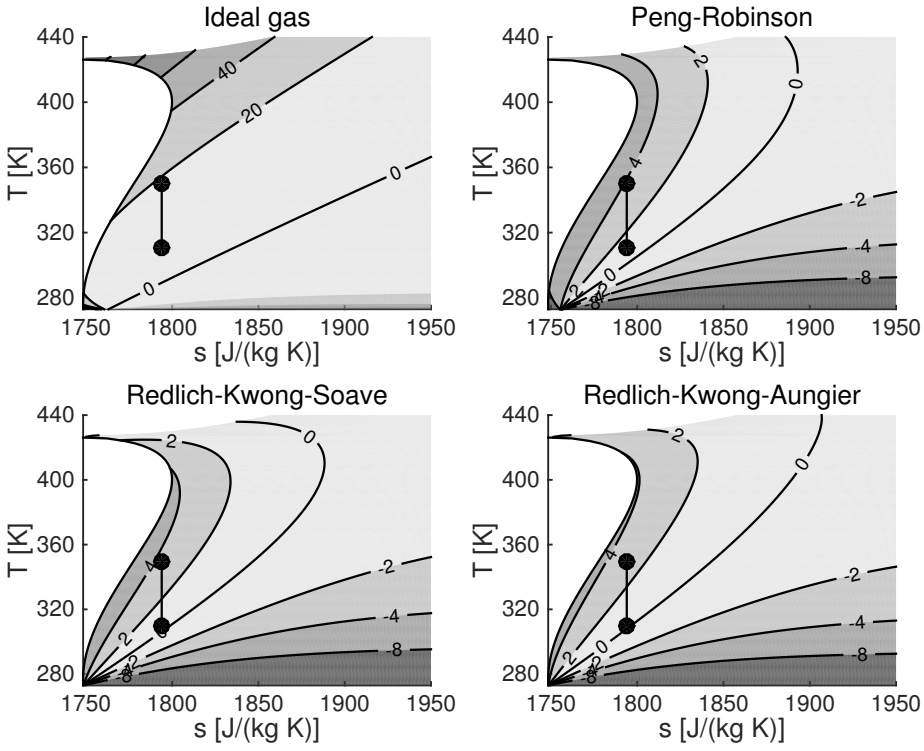

Figure 4.12: Percentage deviation between enthalpy predicted using the most common cubic equations of state and the actual enthalpy calculated using REFPROP for R245fa.

error reduces as superheating increases. Overall, there is a more significant deviation in the enthalpy calculation than that found for the pressure calculation, with maximum deviations above 4% found within the operating region that the ORC turbine would be expected to operate. Interestingly, the enthalpy estimations near the saturation line using the adapted RK models are more accurate than the PR model, whilst the opposite was found for the pressure estimations. It is again clear from Figure 4.12 that the RKA model offers a slight improvement over the RKS model.

However, from the investigation in Figures 4.11 and 4.12 it is clear that the operating point for the ORC turbine lies within regions with a relatively large deviation in the pressure and enthalpy values. Considering that a REFPROP license is available it is therefore obvious that constructing fluid property tables using REFPROP is the most accurate method for accounting for fluid properties within the CFD simulations.

Fluid property tables are constructed in accordance with the guidelines set out in the CFX solver modelling guide (ANSYS, 2013). Property tables are required for h, a, v, C_{v}, C_{v}, $\partial P/\partial v$, s, μ and k as a function of temperature and pressure, where v is the specific volume and C_{v} and C_{p} are the specific heats at constant volume and constant pressure respectively. The other parameters have the same definitions as before. To construct the tables the minimum and maximum temperatures and pressures are specified and these values must exceed the expected conditions within the turbine, but not by much. The number of elements used to construct the tables n is then defined such that the property tables are $n \times n$ arrays. Once a suitable mesh size has been established in the next section, a sensitivity study considering the property table size will be completed.

Grid independence study

The final rotor three-dimensional geometry was obtained after a manual iteration of the design parameters coupled to CFD analysis of the resulting turbine. During this design stage a grid independence study was also completed to ensure that the rotor and stator meshes were sufficient in size. Grid independence studies were completed for the stator, and for the rotor with clearance gap, and these studies were completed for the first iteration of the rotor three-dimensional design. Once an initial mesh had been created and the CFD simulation completed, the mass flow rate and isentropic efficiencies were calculated. The mesh was then refined and the simulation re-ran, and this was repeated until a grid

independent solution was obtained.

Figures 4.13 and 4.14 display the results from the grid independence studies for the stator and rotor respectively. In these figures the percentage deviations in the mass flow rate and isentropic efficiencies are given in relation to the values obtained with the finest mesh. For the stator the percentage errors for the mass flow rate and isentropic efficiency are less than 0.1% for a mesh greater than 1.5×10^5 nodes, and less than 0.04% for a mesh greater than 4.0×10^5 nodes. Due to this small percentage error it is therefore clear that a mesh of this size is suitable for the stator. Similarly, for the rotor with clearance gap, the percentage errors for the mass flow rate, total-to-static and total-to-total efficiencies are less than 0.1% for a mesh size greater than 4.0×10^5 nodes, and less than 0.025% for a mesh with more than 7.0×10^5 nodes. Again, due to this small percentage error it is clear that a mesh this size is suitable to simulate the rotor and clearance gap.

With the mesh size established, it was also possible to investigate the sensitivity of the results to variations in the size of the thermodynamic property tables. To do this the same simulation was ran with table sizes of $n = 25$, 50, 100 and 200. The percentage deviations in the mass flow rate and the turbine isentropic efficiencies are shown in Figure 4.15. The converged solution for $n = 25$ did not return reasonable results and has therefore been neglected. From the remaining results it is clear that a table size of 100 or more is adequate with the percentage error in mass flow rate and the isentropic efficiencies being less than 0.01% compared to the reference table size of 200.

After establishing the mesh and fluid property table sizes, the manual iteration of the rotor three-dimensional design was then completed and the final turbine geometry was

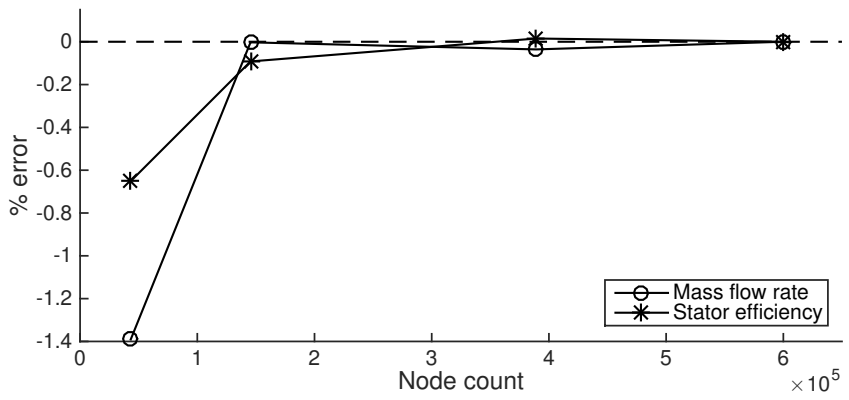

Figure 4.13: Grid independence study for the ORC turbine stator.

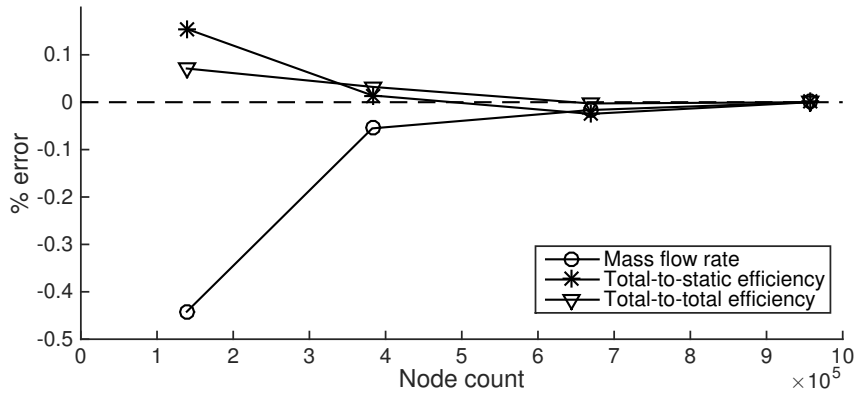

Figure 4.14: Grid independence study for the ORC turbine rotor with clearance gap.

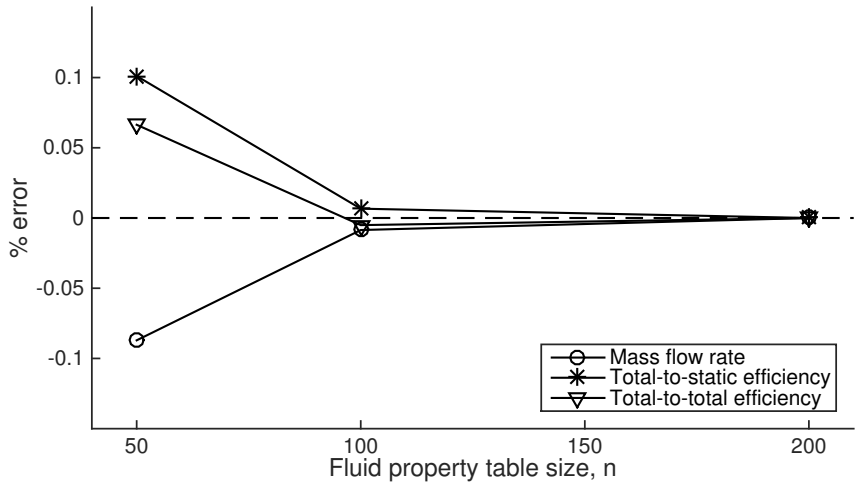

Figure 4.15: Sensitivity study on the thermodynamic property table size used for CFD simulations.

obtained. The single passage stator and rotor meshes used to simulate the final turbine design consisted of approximately 4.3×10^5 and 8.5×10^5 nodes respectively. These meshes are displayed in Figures 4.16 and 4.17 respectively.

Alongside establishing the required mesh and property table size, at this point it was also important to calculate the flat plate Reynolds number along the rotor blade surface to establish where the transition from laminar to turbulent flow occurs. This is shown in Figure 4.18 against the normalised path length with 0 and 1 corresponding to the rotor leading edge and trailing edge respectively. It is generally accepted that the laminar-turbulent transition along a flat plate occurs at $\mathrm{Re_x} \approx 5 \times 10^5$ (Cengel, 2008). This has been represented as a dashed line in Figure 4.18. From this it is clear that the transition occurs within the first 20% of the blade length, and therefore the assumption of fully

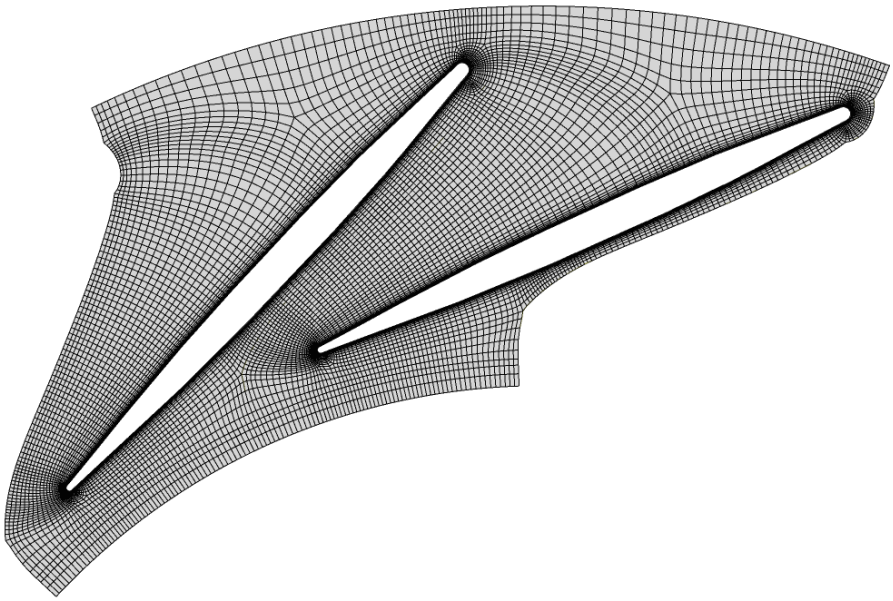

Figure 4.16: Stator mesh for the final ORC stator design, consisting of 4.3×10^5 nodes.

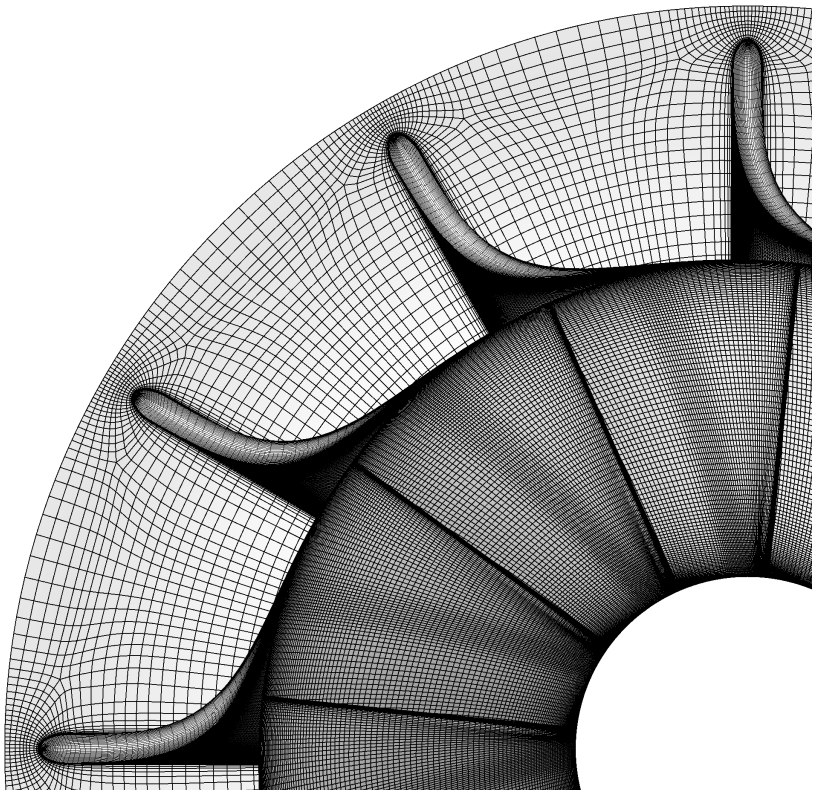

Figure 4.17: Rotor mesh of the final ORC rotor design, consisting of 8.5×10^5 nodes.

turbulent flow is not expected to affect of the accuracy of the CFD simulation. It is worth noting that for a similar size turbine operating with air this may not always be the case, which would introduce uncertainties within the CFD simulation if transition is not modelled.

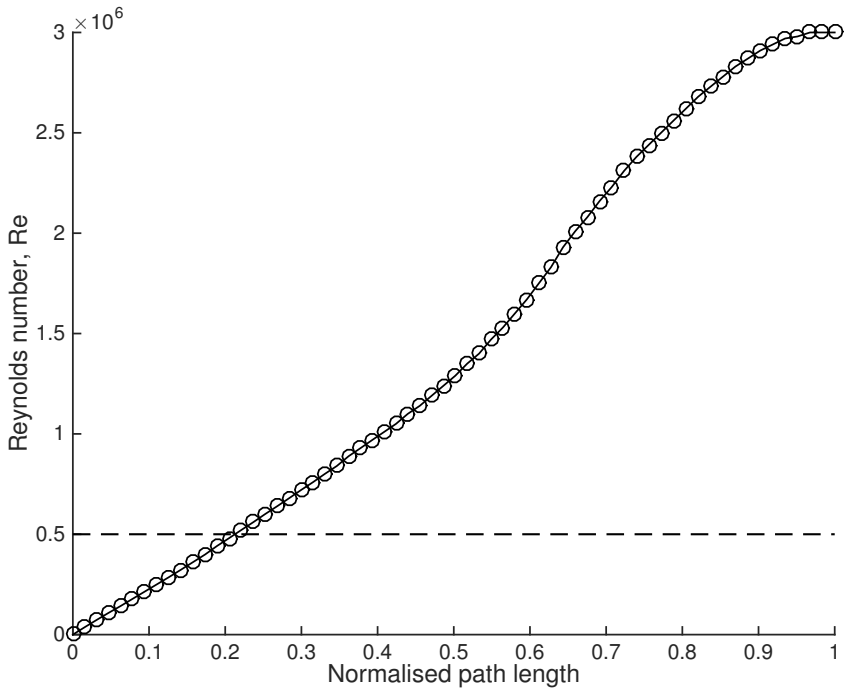

Figure 4.18: Determining where along the rotor blade path length the laminar-turbulent transition occurs.

Steady-state ORC simulation results

After establishing the required mesh and fluid property table size, the steady-state CFD simulation was completed and the CFD results are compared to the design values in Table 4.9. To allow a suitable comparison, the rotor outlet design values at the mid-span have been estimated by conserving rothalpy, and assuming a constant static pressure and meridional velocity across the rotor discharge. For the CFD results, total conditions and temperatures are mass flow averaged, whilst the static pressure and velocities are area averaged. The flow angles are then obtained from the area averaged meridional and respective tangential velocity components.

Unsteady CFD analysis

Before evaluating the CFD results it is important to confirm the suitability of the steady-state CFD simulation. To do this an unsteady simulation using a sliding plane to simulate the rotor-stator interface was also considered. The same boundary conditions used for the steady state simulation were selected. The stator-rotor blade ratio is 16:12, so the simulation was run with 4 stator passages and 3 rotor passages to ensure the pitch ratio

Table 4.9: Comparison between the intended design and the steady-state CFD results for the R245fa turbine case study.

Parameter		Design	CFD	Units
Rotor leading edge				
Total temperature	T_{04}	349.7	349.6	K
Total pressure	P_{04}	611.1	606.0	kPa
Static temperature	T_4	339.5	337.6	K
Static pressure	P_4	428.7	403.3	kPa
Absolute velocity	c_4	115.3	124.7	m s^{-1}
Absolute flow angle	α_4	75.00	75.67	°
Rotor trailing edge				
Total temperature	T_{05}	327.5	326.7	K
Total pressure	P_{05}	259.6	263.6	kPa
Static temperature	T_5	326.4	325.2	K
Static pressure	P_5	249.2	247.8	kPa
Absolute velocity	c_5	39.2	47.7	m s^{-1}
Absolute flow angle	α_5	0.00	6.35	°
Performance summary				
Rotational speed	N	37,525	37,525	rpm
Mass flow rate	$\dot{m}$	0.700	0.700	kg s^{-1}
Pressure ratio (ts)	PR_{ts}	2.50	2.51	
Isentropic efficiency (ts)	η_{ts}	85.00	84.87	%
Isentropic efficiency (tt)	η_{tt}	88.96	89.24	%

was equal to unity. This relates to a full 90° of the turbine geometry, and a complete mesh size of approximately 4.3×10^6 nodes. The unsteady simulation was run until the mass flow rate, and the mass averaged total and static parameters at the rotor inlet and discharge had converged. The total-to-static isentropic efficiency was calculated using Equation 2.12, permitting the convergence of the isentropic efficiency to be verified.

Initially a sensitivity study was undertaken to establish the number of time steps required per blade pass. Unsteady CFD results for 10, 25 and 40 time steps per blade pass were obtained and have been compared to the steady-state simulation in Table 4.10. The difference in the predicted mass flow and isentropic efficiency for 25 and 40 time steps is negligible, thus suggesting that 25 time steps is sufficient to capture the unsteady flow behaviour. When comparing the steady and unsteady results, the percentage differences in mass flow rate and isentropic efficiency are both less than 1%. Considering the additional time required to compute an unsteady solution, it was therefore concluded that the steady-state simulation is sufficiently accurate to capture the turbine performance.

Table 4.10: Sensitivity analysis considering the number of time steps per blade pass required for the unsteady design point CFD simulation.

Timesteps per	Steady		Unsteady		% Diff.	
blade pass	$\dot{m}$	η_{ts}	$\dot{m}$	η_{ts}	$\dot{m}$	η_{ts}
10			0.695	85.30	+0.504%	−0.755%
25	0.699	84.87	0.693	85.42	+0.946%	−0.643%
40			0.693	85.43	+0.939%	−0.656%

4.6.3 Validation of turbine design

Having confirmed the suitability of the steady-state simulation results shown in Table 4.9, the achieved performance can now be compared to the intended performance. For the first investigation the velocity triangles at the rotor leading and trailing edges have been compared (Figure 4.19). From this it appears that the rotor inlet velocity triangles match reasonably well, although some deviation between the design and CFD absolute flow angles is found, with the CFD predicting $\alpha_4 = 75.67°$ compared to the 75.00° design value. The estimated isentropic nozzle efficiency from the CFD is also slightly lower at 93.81% compared to the design value of 95.00%. The resulting velocity triangle shift increases the absolute velocity from 115.33 m s^{-1} to 124.6 m s^{-1}, corresponding to a reduction in static pressure from 428.69 kPa to 403.26 kPa.

Applying an iterative mass balance using the known rotor inlet flow area, it is possible to investigate how variations in α_4 and η_{N} can cause this observed deviation. Although this investigation adopts a simple one-dimensional approach, and cannot be relied upon to provide an accurate representation of the three-dimensional flow field, it can provide a useful insight into the sensitivity of the rotor inlet velocity triangle to variations in α_4 and η_{N}. By first assuming isentropic flow through the stator ($P_{04} = P_{01},\ h_{04} = h_{01}$), the defined value for α_4, along with the known mass flow rate and rotor inlet flow area, supplies an initial guess for the absolute flow velocity c_4, and static enthalpy h_4. The nozzle loss coefficient ζ_{N} then follows from η_{N} using Equation 2.28. This in turn supplies the enthalpy after an isentropic expansion $h_{4\text{s}}$, the static pressure P_4, and then the static entropy s_4. This then supplies the next guess for the rotor inlet total pressure P_{04}, and the process can be repeated until convergence. Results obtained using this method are shown in Figure 4.20.

The top graph in Figure 4.20 shows how the rotor inlet velocity triangle changes when

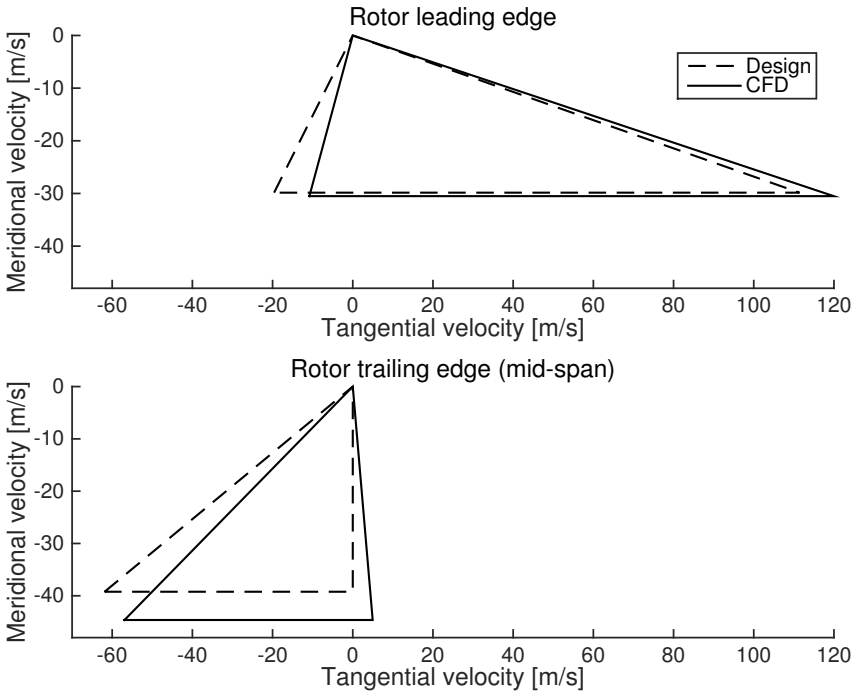

Figure 4.19: Comparison between the intended design and CFD velocity triangles at the rotor leading and trailing edges for the R245fa turbine.

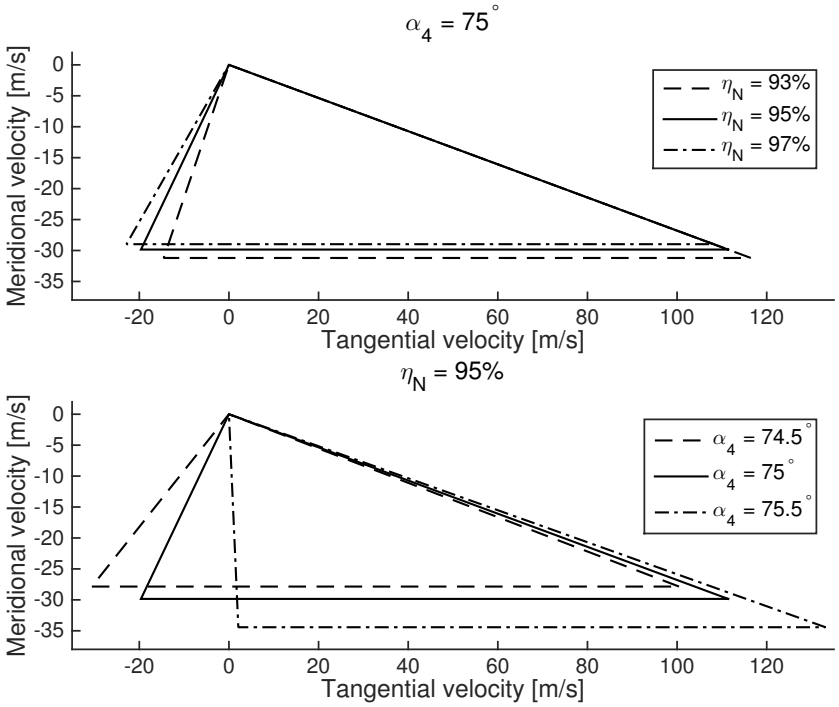

Figure 4.20: Deviation in rotor inlet velocity triangle with variations in α_4 and η_N.

η_N varies and α_4 remains fixed, whilst the bottom figure shows how variations in α_4 change the velocity triangle when η_N remains fixed. This figure clearly shows how small deviations can cause significant shifts in the rotor inlet velocity triangle away from the design point. Referring to the top graph, as η_N reduces the total pressure at the rotor inlet must reduce, which must lead to a lower density. Since the mass flow rate, area and flow angle remain fixed the meridional velocity must increase to conserve mass. This results in a larger absolute tangential velocity component and overall absolute velocity. For a fixed blade rotational speed, this requires the relative tangential velocity component to reduce, leading to a smaller relative flow angle.

Referring to the bottom graph in Figure 4.20, the sensitivity to variations in α_4 seems much greater, with a small variation in α_4 resulting in a large deviation in the velocity triangle. Considering mass continuity, the mass flux, $\dot{m}/A_4$, must remain constant, and is given by Equation 4.74.

$$\frac{\dot{m}}{A_4} = \frac{\rho_4 c_4}{\sqrt{1 + \tan^2 \alpha_4}} \tag{4.74}$$

For increases in α_4, the product $\rho_4 c_4$ must increase. For a defined total inlet enthalpy, an increase in c_4 reduces the static enthalpy, therefore reducing ρ_4. It was found that the rate of increase in c_4 is faster than the rate of decrease in ρ_4, leading to an overall increase in $\rho_4 c_4$ as c_4 increases. Therefore as α_4 increases, c_4 must increase, leading to increased meridional and absolute tangential velocity components. It is this shift in meridional velocity that is responsible for the obvious shift in the rotor inlet velocity triangle. For an increase in α_4 of just 0.5° from the design value, the increase in the meridional velocity, and absolute tangential velocity is enough to reduce the relative flow angle to almost zero.

With the CFD predicting both a reduction in η_N and an increase in α_4, the trends observed in Figure 4.20 help to explain the deviation observed in Figure 4.19. However, the deviation between the design and CFD results is not as severe as that predicted by Figure 4.20, as there is not a significant increase in the meridional velocity component for the CFD results. This is probably due to an over simplification of the flow field in the one-dimensional analysis.

Between the stator trailing edge and rotor leading edge the total pressure reduces from 616.8 kPa to 606.0 kPa, corresponding to a 1.76% reduction. For the air turbine the

reduction was from 276.4 kPa to 272.4 kPa, corresponding to a 1.45% reduction in total pressure. These results show that although the total pressure drop within the stator-rotor interspace is slightly larger for the ORC turbine, it is not a significant increase. Therefore it is not considered significant enough to affect the assumption of constant total pressure across the stator-rotor interspace.

Overall, from the analysis of the rotor inlet velocity triangle, it seems that the stator design method, coupled with the default inputs defined in Table 4.1, has resulted in a suitable stator design that delivers the flow at conditions close to the design point. In particular the application of the cosine rule, adjusted for the radius change, results in the stator supplying the flow at an absolute flow angle sufficiently close to the intended design value, albeit with a slightly lower isentropic efficiency.

At the rotor outlet a larger deviation in the thermodynamic properties and velocity triangles is observed. The CFD results predict an average relative flow angle at the rotor outlet mid-span of $-51.90°$, compared to the $-57.63°$ mid-span blade angle. This shows that the relative flow at the rotor outlet is not fully aligned with the blade as assumed, corresponding to a deviation of $-5.73°$. This deviation can be attributed to a number of highly three-dimensional flow features that are overlooked within a one-dimensional design methodology. Most notably is the inherent three-dimensionality of the flow that exists towards the rotor outlet. This is complicated further by the introduction of secondary flows as a result of the clearance gap, in addition to the deviation that can occur as the mean flow expands from the rotor throat to the rotor exit. The implementation of the cosine rule to estimate the rotor discharge flow angle based on the mean rotor pitch and rotor throat, may provide a more realistic prediction of the relative flow angle at the rotor discharge (Aungier, 2006). However, quantifying the degree of deviation remains complicated due to the complex nature of the flow. Moustapha et al. (2003) compared deviation angles for a number of experimental studies and found a range of values. More specifically, at the design rotational speed and an isentropic velocity ratio of $\nu_{\text{ts}} = 0.7$ a deviation of $-7.5°$ is suggested, which agrees well for the results obtained for this design.

At the rotor outlet the CFD meridional velocity has increased from the design value of 39.23 m s^{-1} to 44.63 m s^{-1}. This increase is caused by the development of boundary layers on the blade surfaces and end walls, which act to reduce the flow area requiring an increase in flow velocity to conserve mass. This corresponds to a 13.76% increase in meridional

velocity for the same mass flow rate. For the air turbine, the increase in meridional velocity was 8.85%, but this was experienced with an additional increase in mass flow rate. This may suggest that the boundary layer blockage is more significant within the ORC turbine. The consequence of the observed deviation and increased meridional velocity is to reduce the relative tangential velocity component, as observed in Figure 4.19. Since the rotational speed remains fixed, this introduces an absolute tangential velocity component, introducing swirl at the rotor discharge. At the mid-span the absolute flow angle predicted by the CFD results is 6.35°.

Figure 4.21 displays the CFD contours of relative Mach number alongside the relative velocity vectors. These have been displayed on the mid-span contour which has been translated onto the two-dimensional plane of meridional distance M and polar angle θ for clarity. The visible change in Mach number across stator and rotor interface is due to the change from an absolute frame of reference to a relative frame of reference. To accompany the discussion of Figure 4.21, the blade loading diagrams for the stator and

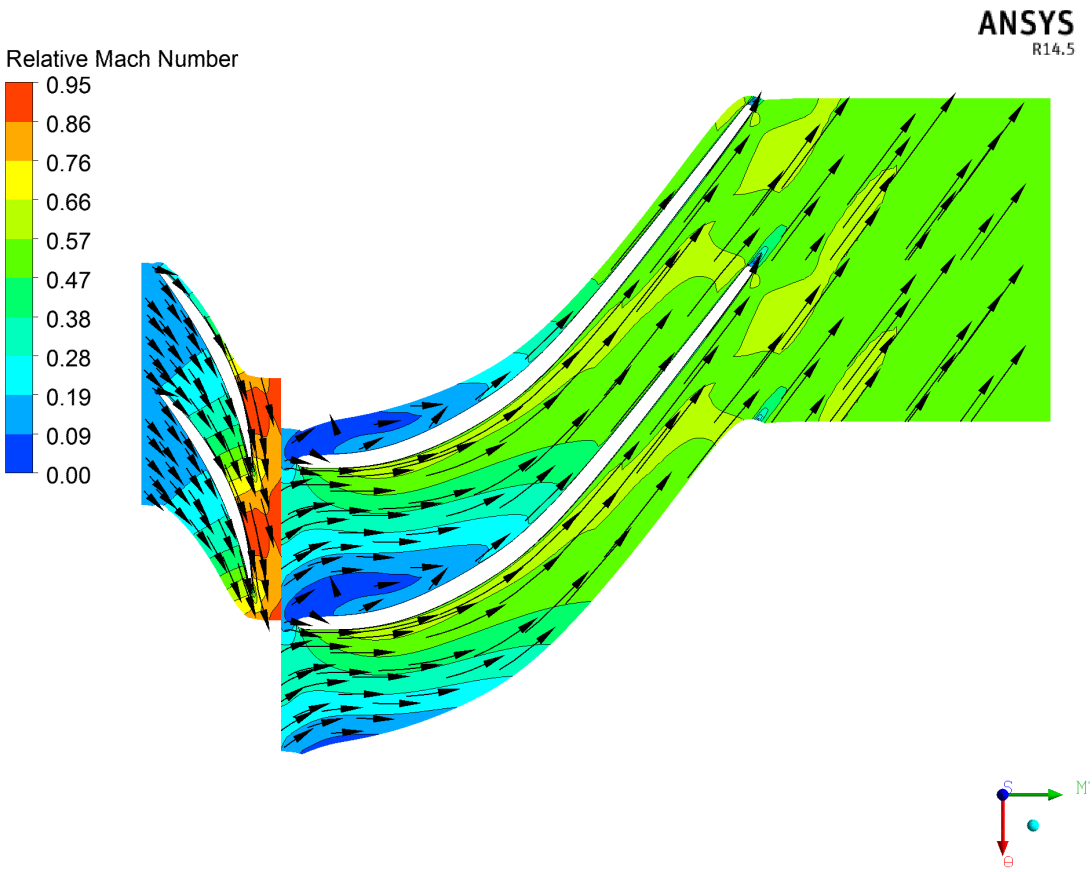

Figure 4.21: Contour of relative Mach number and relative velocity vectors on the midspan of the R245fa turbine.

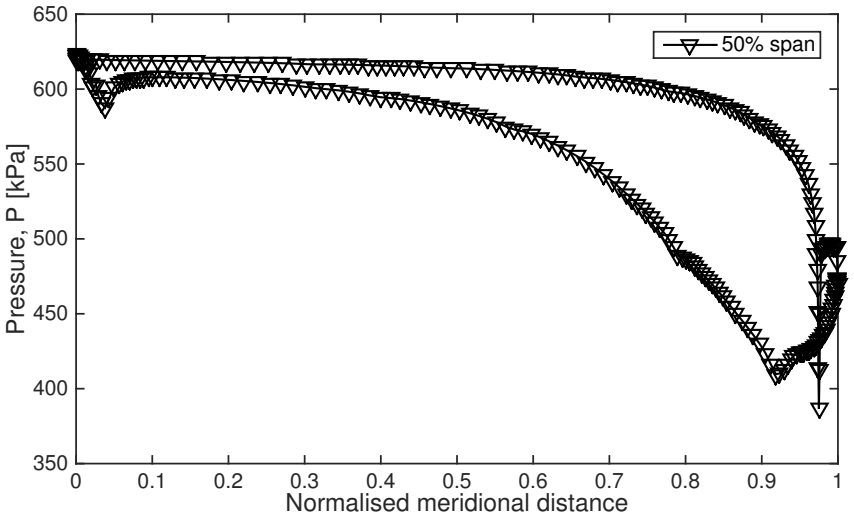

Figure 4.22: R245fa stator blade loading at 50% span.

rotor are shown in Figures 4.22 and 4.23. The top and bottom curves on the blade loading diagrams represent the static pressure variation on the pressure and suction surfaces of the blades respectively. A large area enclosed by these two curves is indicative of high loading and a high turbine work output. It is therefore advantageous to maintain a high pressure on the pressure side, and a low pressure on suction side, with high and low pressures corresponding to low and high relative velocities respectively. The flow through the stator is largely two-dimensional so the blade loading is shown only at the mid-span, whilst for the rotor the blade loading is shown at 10%, 50% and 90% of the blade span.

As the flow expands through the stator a higher velocity is continually maintained on the suction surface leading to the desired pressure difference across the stator blade. This is displayed by the relative Mach number distribution shown in Figure 4.21. Referring to Figure 4.22 the pressure difference during the first 40% of the stator passage is relatively low. This is due to the low velocity of the fluid at the stator inlet. However, as the flow expands and the velocity increases, the static enthalpy reduces as a function of the velocity squared, which leads to a more rapid reduction in pressure on both surfaces of the blade. However, since the velocity is higher on the suction side, the pressure on this surface reduces faster leading to the higher blade loading observed in Figure 4.22.

At the leading and trailing edges of the stator blade a smooth variation in the blade loading is not observed. The sharp change in static pressure observed on the suction surface just behind the leading edge is attributed to a slight deviation between the incoming flow

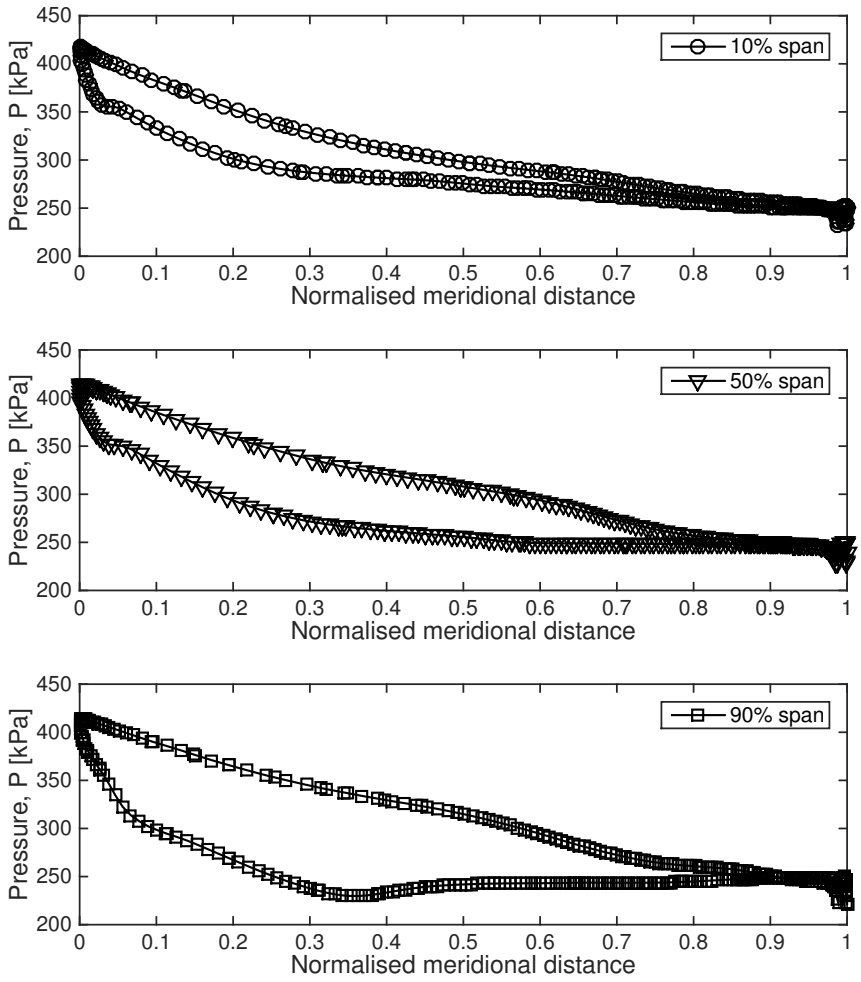

Figure 4.23: R245fa blade loading at 10%, 50% and 90% span.

angle and the optimal incidence angle for this stator blade. This might indicate a slight inaccuracy in Equations 4.69 and 4.70 in predicting α_2, or in the method of conserving mass and angular momentum to estimate the flow angle upstream at the stator leading edge. For this design point analysis, the deviation is not overly significant, but for the off-design analysis of a complete turbine, incidence losses could become more significant. This suggests that a larger leading edge radius is required, improving the stators tolerance to incidence. At the trailing edge, Figure 4.22 shows that as the the flow along the suction surface reaches a meridional distance of 0.9, it begins to slow, resulting in an increase in the static pressure. During this period the velocity along the pressure surface continues to increase resulting in a lower static pressure and a lower pressure difference across the blade. When the flow reaches the trailing edge it appears to separate on the suction surface, forming a wake. Moustapha et al. (2003) states that this is most likely due to the local pressure rise as the result of the sudden expansion that occurs at the trailing edge,

and suggests that this could be improved by implementing cambered blades.

Despite the issues discussed at the stator leading and trailing edge, on the whole a reasonable blade loading diagram is observed. This again confirms that the stator design method, using the default values listed in Table 4.1, has resulted in a viable stator geometry that achieves reasonable performance. Of course, more detailed optimisation could improve this design further.

Referring back to Figure 4.21, the relative velocity vectors show that the flow through the rotor aligns relatively well with the rotor blades, despite a small area of recirculation along the pressure surface just behind the rotor leading edge. This small recirculation suggests that the design β_4 value may have been slightly high, and this could be reduced to remove this small recirculation. The relative Mach number distribution shown in Figure 4.21 shows that for around the first 70% of the flow path length the flow travels faster along the suction surface than the pressure surface leading to a favourable blade loading. This is confirmed for the 50% span blade loading diagram in Figure 4.23. Figure 4.23 also demonstrates that this same behaviour is observed at 10% and 90% of the blade span. However, after around 70% of the path length a smaller difference between the static pressures on the pressure and suction surfaces is found, and this is found across the whole blade span. This is indicative of a low blade loading which is not favourable for a high power output. This may suggest that the rotor blade chord length may be too long, and this is partly the consequence of having a large blade overlap, which is clearly visible in Figure 4.21. The large blade overlap results from the selected camberline (Equation B.3), and therefore blade loading may be improved by using Equation B.5 to define the camberline instead. At the rotor trailing edge the blade loading diagrams again show a sudden change in the static pressures on the pressure and suction surfaces, although this is not as severe as that found for the stator. Again, this is attributed to the sudden expansion that occurs at the rotor trailing edge.

Overall, at the design rotational speed of $37,525$ rpm, and the design mass flow rate of 0.7 kg s^{-1}, the predicted total-to-static pressure ratio is 2.51, whilst the aerodynamic isentropic total-to-static efficiency is 84.87%. Again, it should be reiterated that the efficiencies discussed here are the aerodynamic efficiencies, not accounting for losses upstream and downstream of the stator inlet and rotor trailing edges respectively, windage losses and mechanical losses. The performance values obtained are in good agreement

with the specified design inputs of PR = 2.50 and η_{ts} = 85.00% respectively. From the one-dimensional design outputs the isentropic total-to-total efficiency was calculated as 88.96%, agreeing well with the CFD prediction of 89.24%. This validates the suitability of the design methodology for the design of a subsonic ORC turbine operating with R245fa. The small difference between the design and CFD efficiencies confirms that a suitable value for the total-to-static efficiency was selected as the design input. It should also be reiterated that the purpose of this research was not to obtain a fully optimised turbine design, but to obtain a turbine that would achieve a reasonable efficiency and it is felt that this has been achieved. However, the CFD analysis has shown areas that could be investigated to optimise this design further, such as developing a stator with a cambered blade, reducing the rotor inlet relative flow angle, and implementing an alternative camberline.

4.6.4 Validation of the prediction of meanline parameters

During the rotor design process the equations described in Section 4.3.2 were used to estimate the velocity distribution within the rotor, and this was used to aid in the preliminary design of the three-dimensional rotor passage. Having completed the CFD analysis, the velocity distribution within the rotor predicted by the CFD simulation can now be used to validate the method described in Section 4.3.2.

Upon first inspection, a comparison between the CFD results and the one-dimensional predictions showed large discrepancies due to the deviation between the blade and relative flow angles as the flow expands through the rotor. This deviation is again the result of the complex three-dimensional effects that cannot be accounted for using the one-dimensional model. This therefore confirms that the simple one-dimensional model presented cannot be relied upon to provide an accurate prediction of the resulting velocity distribution.

However, the interest in predicting the velocity distribution is to aid design, enabling quick assessment of the rotor geometry, allowing the designer to quickly spot problem areas such as large changes in flow area or regions of diffusion (Atkinson, 1998). It was therefore decided to simulate the rotor at the design conditions without the clearance gap, which should enable a better comparison with the one-dimensional model. The CFD simulation was setup in exactly the same way as before, but this time neglecting the clearance gap. The resulting relative velocity and meridional velocity distributions were extracted, and have been compared to the one-dimensional predictions in Figure 4.24. To highlight the

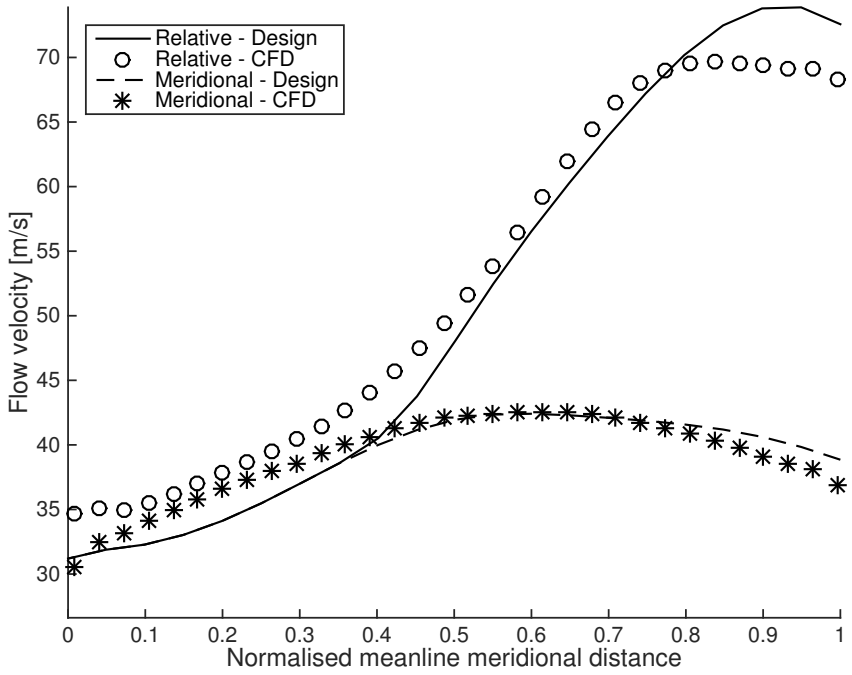

Figure 4.24: Comparison between the velocity distributions predicted by the one-dimensional model and the results obtained for the no clearance CFD simulation.

deviation observed for the CFD simulation that considered the clearance gap, the relative flow angles for both the clearance and no clearance simulations have been compared to the blade angle distribution in Figure 4.25.

For the first 40% of the rotor passage there is a large discrepancy between the velocity distributions predicted by CFD and the one-dimensional model. This discrepancy is because the one-dimensional model assumes that the flow remains aligned with blade, whilst in reality the flow enters the rotor with a certain amount of incidence. For the first 35% of the rotor passage the blade angle remains at 0°, and therefore it takes a while for the flow and blade to begin to align. Furthermore, whilst the blade angle remains at 0° the one-dimensional model assumes that the flow through the rotor is fully radial, explaining why the meridional and relative velocities predicted by the one-dimensional model remain the same until 35% of the path length. At 35% of the meridional path length the blade begins to turn, and shortly afterwards the flow aligns with the blade. The flow then remains closely aligned with the blade until around 90% of the path length, where the CFD results start to deviate from the one-dimensional predictions. Upon inspection of the geometry, it was found that this is the approximate location of the rotor throat. Therefore the sudden expansion from the throat to the rotor exit causes a deviation in the flow angle, resulting

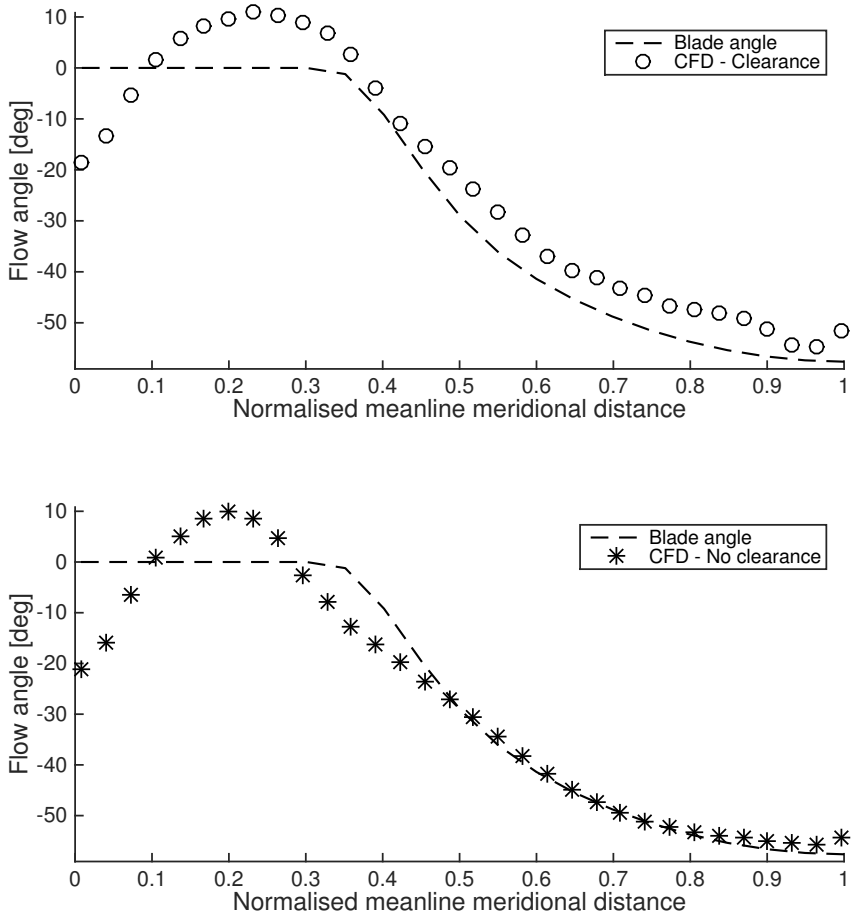

Figure 4.25: Comparison between blade angle and the flow angles for the clearance and no clearance CFD simulations.

in the slight reduction in relative velocity compared to the one-dimensional predictions.

The bottom plot in Figure 4.25 clearly demonstrates where the flow remains aligned with the blade, and where it deviates. From this it is clear that the locations where there is a significant deviation in Figure 4.24 directly correlate to the locations where the flow is not aligned with the blade. The top plot in Figure 4.24 demonstrates the deviation that is introduced by considering the clearance gap, highlighting why the one-dimensional model is not appropriate for accurately capturing the three-dimensional flow field. To visualise this deviation a comparison between the relative Mach number distributions at the rotor trailing edge for the no clearance and clearance simulations is shown in Figure 4.26. This shows the complex three-dimensional nature of the flow that exists for both simulations. However, the introduction of the clearance gap has created additional secondary flow features, which further complicate the flow pattern. This has introduced a counter-rotating vortex that results in an area with a relatively lower velocity. This comparison provides

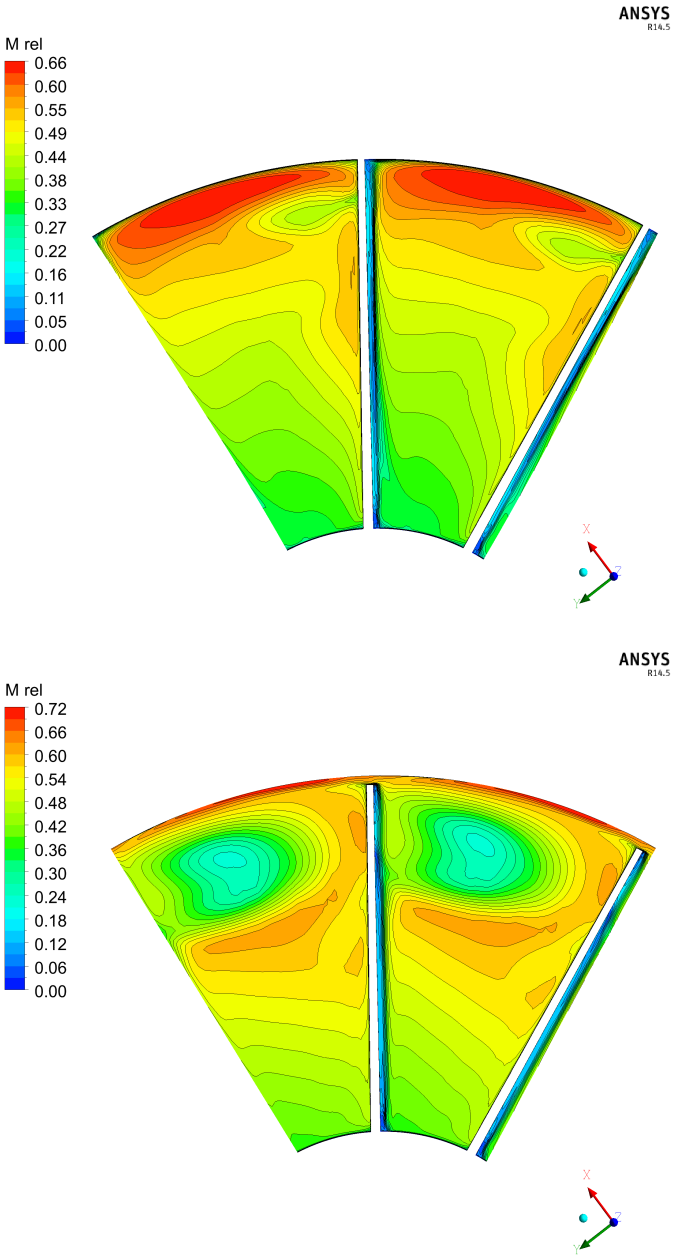

Figure 4.26: Contours of relative Mach number at the rotor outlet for the R245fa turbine. Top: no clearance; Bottom: clearance.

a visual representation of the source of deviation in flow angle away from the blade angle that has been discussed throughout this chapter.

In summary, despite its shortcomings in capturing the complex nature of the flow at the rotor discharge, the one-dimensional meanline model described in Section 4.3.2 seems sufficiently accurate in evaluating the rotor passage velocity distribution to be useful as a preliminary design aid. This allows the designer to quickly iterate through the design process, alerting the designer to any potential problems, before moving forward with more complex design and analysis methods.

4.7 Conclusion

A model for the design of radial inflow turbines operating with organic fluids was presented in this chapter. The design method considers the one-dimensional design of the rotor and stator, in addition to generating the full three-dimensional turbine geometry, thus extending, and improving upon, existing methods found within the literature. Alongside this, a novel method to determine the meanline velocity distribution within the rotor has been included, allowing quick assessment of the turbine geometry before moving into a more detailed design phase.

Two candidate turbines have been developed, operating with air and R245fa respectively, and both designs have been analysed using ANSYS CFX. This chapter has demonstrated the use of this CFD solver for real gas applications, with the inclusion of property tables generated using REFPROP, in addition to comparing steady and unsteady simulations. Overall, the results validate the design method with only small differences between the intended performance and that predicted using CFD. For both designs the aerodynamic total-to-static efficiency is around 85%. The same CFD results have also validated the method used to predict the rotor meanline velocity distribution.

Despite validating the design methodology, the CFD results have also shown further improvements that could be made to the turbine design to further improve performance. This includes increasing the stator leading edge radius, reducing the relative flow angle at the rotor inlet, and implementing an alternative camberline to improve blade loading. None the less, using the developed design methodology a turbine with a reasonable performance has been obtained, which was the objective of this phase of the project.

Chapter 5

Application of similitude theory to ORC turbines

5.1 Introduction

In Chapter 3 a thermodynamic model was presented, which can be used to determine the optimal cycle configuration for a given heat source and heat sink. In this model the assumption of a constant turbine efficiency is suitable since the turbine is then effectively designed to achieve this specified efficiency. Another interesting modelling scenario is to determine the optimal cycle conditions when using an existing ORC turbine. In this instance, it is not suitable to assume a constant turbine efficiency, so off-design models are required. These models must either use similitude theory to non-dimensionalise the turbine performance map, or use one-dimensional loss models. Since loss models are based on empirical data obtained for ideal gases, and there is not yet sufficient experimental data to develop these models for real gases, similitude theory is the more suitable choice. However, the use of similitude theory to predict ORC turbine performance has not been validated within the literature, and those that have used it have not demonstrated the most appropriate implementation.

This chapter presents a significant contribution to the research community by demonstrating the correct implementation of similitude theory to ORC turbines, and investigates the applicability of similitude to ORC turbines. The CFD analysis of the ORC turbine conducted in Chapter 4 has been extended to obtain a complete performance map, and this performance map is non-dimensionalised according to similitude theory. This map is

then used to predict turbine performance over a range of different operating conditions, whilst operating with three different working fluids, namely R245fa, R123 and R1234yf. These results are used to investigate the accuracy of the existing theory, and this has led to the development of a modified similitude theory, which is accurate over a wider range of operating conditions. The research completed in this chapter is supported by a publication in the Journal of Engineering for Gas Turbines and Power (White and Sayma, 2015b).

5.2 Similitude theory

A turbine's performance is described by the isentropic enthalpy change across it Δh_s, the power output W, and the isentropic efficiency η. These three parameters are expressed as a function of the turbine diameter D, rotational speed N, mass flow rate $\dot{m}$, and the fluid thermodynamic properties at the turbine inlet. Here ρ_{01}, a_{01} and μ denote the stagnation density, stagnation speed of sound and dynamic viscosity respectively at the turbine inlet, and these can be found using a suitable equation of state when the total inlet temperature T_{01} and pressure P_{01} are known. The performance parameters can be expressed in the following functional relationship:

$$[\Delta h_\mathrm{s},\ \eta,\ W] = f\left(D,\ N,\ \dot{m},\ a_{01},\ \rho_{01},\ \mu\right) \tag{5.1}$$

Dimensional analysis reduces these parameters to Equation 5.2. The parameters on the left hand side are the head coefficient, isentropic efficiency and power coefficient respectively. The first term on the right hand side is the flow coefficient, the second is the Reynolds number and the third is the blade Mach number.

$$\left[\frac{\Delta h_\mathrm{s}}{N^2D^2},\ \eta,\ \frac{W}{\rho_{01}N^3D^5}\right] = f\left(\frac{\dot{m}}{\rho_{01}ND^3},\ \frac{\rho_{01}ND^2}{\mu},\ \frac{ND}{a_{01}}\right) \tag{5.2}$$

The terms Δh_s and η may be expressed in terms of total-to-total, or total-to-static conditions, and either choice is suitable so long as it is used consistently. The convention within radial turbine design is to consider the total-to-static performance of the turbine, although for the closed ORC, total-to-total conditions might be more appropriate. Within this chapter the method will initially be implemented considering total-to-static conditions. However, after completing this analysis the total-to-total conditions will be revisited to

ensure that the same conclusions are valid.

The isentropic enthalpy drop Δh_s is directly related to the turbine pressure ratio. Depending on whether total-to-total or total-to-static conditions have been selected will determine whether this pressure ratio is total-to-total or total-to-static. For an ideal gas the relationship between the isentropic enthalpy change and the pressure ratio can be expressed using isentropic relationships. For a real gas, the pressure ratio can be obtained using a suitable equation of state. The specified inlet conditions immediately provide the total inlet enthalpy h_{01} and entropy s_{01}, whilst the isentropic enthalpy drop supplies the enthalpy following an isentropic expansion. This in turn supplies the outlet pressure and therefore pressure ratio. This has been demonstrated for the total-to-static case by Equations 5.3 - 5.6. The procedure is the same for total-to-total, although the terms $h_{5\mathrm{ss}}$, P_5 and $\mathrm{PR_{ts}}$ will be replaced by $h_{05\mathrm{ss}}$, P_{05} and $\mathrm{PR_{tt}}$ respectively.

$$[h_{01},\ s_{01},\ a_{01},\ \rho_{01}] = \mathrm{EoS}(T_{01},\ P_{01},\ \mathrm{fluid}) \tag{5.3}$$

$$h_{5\mathrm{ss}} = h_{01} - \Delta h_\mathrm{s} \tag{5.4}$$

$$P_5 = \mathrm{EoS}(h_{5\mathrm{ss}},\ s_{01},\ \mathrm{fluid}) \tag{5.5}$$

$$\mathrm{PR_{ts}} = \frac{P_{01}}{P_5} \tag{5.6}$$

It should be noted that for ideal gas applications, alternative expressions for the flow coefficient and blade Mach number are obtained by using ideal gas relationships for the density ($\rho = P/RT$) and speed of sound ($a = \sqrt{\gamma RT}$)). This defines the performance parameters in terms of the turbine inlet total temperature and total pressure. For ideal gas applications Reynolds number effects are quoted to be small and are neglected (Moustapha et al., 2003). Therefore it is assumed that the head coefficient, isentropic efficiency and power coefficient all remain constant when the flow coefficient and blade Mach number also remain constant. Furthermore, when considering the performance of a single turbine operating with air, the turbine diameter D and fluid properties (R and γ) remain constant. This reduces Equation 5.2 to the most widely used form of similitude theory, which describes how the pressure ratio and isentropic efficiency of the turbine vary with the reduced flow coefficient, and reduced blade Mach number. This is defined by Equation 5.7 for the total-to-static implementation. Here the performance terms are referred to as reduced coefficients to distinguish them from the coefficients defined in Equation 5.2. It

should of course be noted that these reduced parameters are no longer non-dimensional.

$$\left[\frac{P_{01}}{P_5},\ \eta_{\mathrm{ts}}\right] = f\left(\frac{\dot{m}\sqrt{T_{01}}}{P_{01}},\ \frac{N}{\sqrt{T_{01}}}\right) \tag{5.7}$$

Since the real fluids found in ORCs do not obey the ideal gas law, Equation 5.7 is not applicable. Instead the equation of state is used to directly calculate the density and speed of sound when supplied with the total inlet temperature and pressure. Neglecting Reynolds number effects, the equivalent to Equation 5.7 for real gases is obtained and is expressed by Equation 5.8. This form can be used to describe how the reduced head coefficient and isentropic efficiency of a particular turbine vary with the reduced flow coefficient and reduced blade Mach number.

$$\left[\frac{\Delta h_{\mathrm{s}}}{a_{01}^2},\ \eta_{\mathrm{ts}}\right] = f\left(\frac{\dot{m}}{\rho_{01} a_{01}},\ \frac{N}{a_{01}}\right) \tag{5.8}$$

Using Equation 5.8 it is now possible to scale an existing turbine map, obtained at defined inlet conditions, to different inlet conditions using different working fluids. For a change in total inlet conditions or working fluid, the new mass flow rate, rotational speed and isentropic enthalpy drop are easily determined. Denoting the original and new operating points with the subscripts 'A' and 'B' respectively, this scaling is as follows:

$$N_{\mathrm{B}} = \left(\frac{a_{01,\mathrm{B}}}{a_{01,\mathrm{A}}}\right) N_{\mathrm{A}} \tag{5.9}$$

$$\dot{m}_{\mathrm{B}} = \left(\frac{\rho_{01,\mathrm{B}}}{\rho_{01,\mathrm{A}}}\frac{a_{01,\mathrm{B}}}{a_{01,\mathrm{A}}}\right) \dot{m}_{\mathrm{A}} \tag{5.10}$$

$$\Delta h_{\mathrm{s,B}} = \left(\frac{a_{01,\mathrm{B}}}{a_{01,\mathrm{A}}}\right)^2 \Delta h_{\mathrm{s,A}} \tag{5.11}$$

$$\eta_{\mathrm{B}} = \eta_{\mathrm{A}} \tag{5.12}$$

Although Reynolds number effects are often neglected for ideal gas turbines, it may not be suitable to immediately make this same assumption for real gas turbines. Therefore the scaling should be expanded to include the Reynolds number. Doing so, the Reynolds number term can be combined with the blade Mach number, which results in a single expression that relates only the thermodynamic properties of the working fluid at the original and new operating points (Equation 5.13). This relationship determines the required inlet conditions to maintain the same Reynolds number, provided that the rotational speed has

been appropriately scaled using Equation 5.9. In this case the variation in this relationship and the variation in the Reynolds number is the same. Therefore, when the deviation in Reynolds number is discussed it is synonymous with the deviation in this relationship.

$$\left(\frac{\rho_{01}a_{01}}{\mu}\right)_{\mathrm{A}} = \left(\frac{\rho_{01}a_{01}}{\mu}\right)_{\mathrm{B}} \tag{5.13}$$

For a selected fluid, this expression can be calculated over a range of operating pressures and temperatures, and the percentage deviation from an original operating point can be obtained. This has been demonstrated in Figure 5.1 for the ORC turbine developed in Chapter 4. The working fluid is R245fa and the black dot corresponds to the ORC turbine design inlet conditions, corresponding to total inlet conditions of $T_{01} = 350$ K and $P_{01} = 623.07$ kPa. Keeping the same working fluid, the percentage deviation in Reynolds number from Equation 5.13 over a range of alternative inlet conditions has been calculated and displayed as a contour plot. It should be clarified that these deviation lines are not lines of constant pressure, despite looking similar.

Overall, Figure 5.1 shows a single line along which the Reynolds number will be matched as long as the rotational speed has been appropriately scaled. For a given total

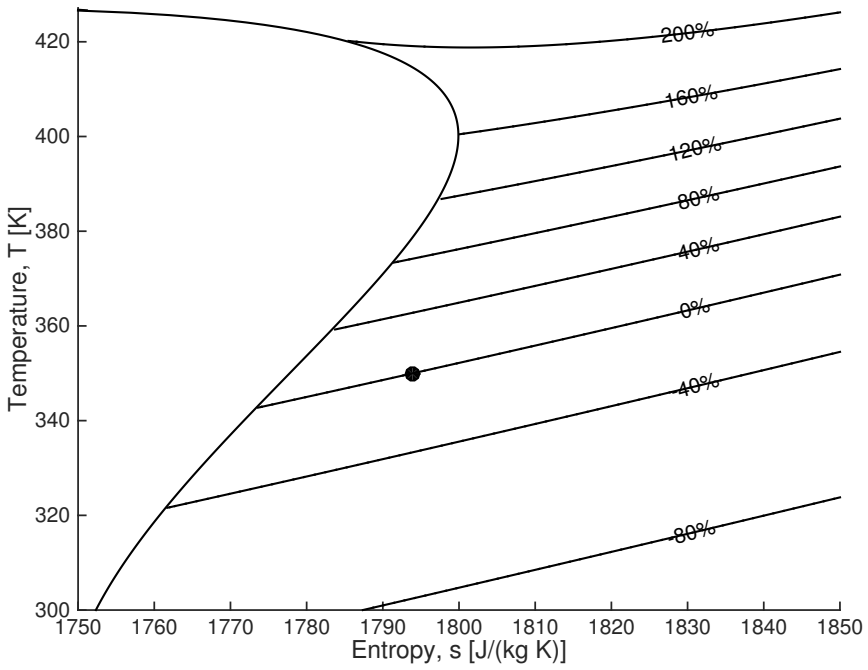

Figure 5.1: Deviation in Reynolds number with variations in turbine total inlet conditions for R245fa assuming that the blade Mach number has been conserved.

inlet temperature, the entropy and therefore total pressure required to maintain the same Reynolds number is immediately defined. The mass flow rate, rotational speed, isentropic enthalpy drop and efficiency then follow from Equations 5.9 - 5.12. For a system designer this is restrictive since for a given total inlet temperature there is only one pressure that can be selected to conserve the Reynolds number. As conditions move further away from the original design point, the deviation in Reynolds number increases. The main aim of this chapter is to investigate and establish if there is a limit to how much deviation in Reynolds number can be introduced before the accuracy of similitude theory predictions becomes unacceptable. In doing so, the applicability of similitude theory to subsonic ORC turbines could be established.

To assess the source of the Reynolds number deviation the variations in density, speed of sound and dynamic viscosity have been investigated in Figure 5.2. Again, these variations are expressed as a percentage deviation from the original design point. To help describe the behaviour shown in Figure 5.2 it is also helpful to introduce the compressibility factor z, which is defined by Equation 5.14 where R is the gas constant for the particular fluid considered. The compressibility factor helps to quantify the real gas effects common within ORC working fluids. It measures how ideal the behaviour of a gas is at a given thermodynamic state, with Equation 5.14 reducing to the ideal gas law at $z = 1$. Figure 5.2D displays contours of the compressibility factor, and shows the introduction of significant real gas effects as the critical point is approached.

$$z = \frac{P}{\rho R T} \tag{5.14}$$

Equation 5.14 and Figure 5.2D can be used to explain the behaviour shown in Figures 5.2A-C. Firstly, the range of temperatures considered ranges from 300 K up to 427 K, and for these temperatures the saturation pressure ranges from 159 kPa to 3640 kPa. Clearly, a much larger variation in pressure is observed than for the temperature, and since $\rho = P/zRT$, a large change in pressure must result in a large change in density. Furthermore, as the pressure increases, the rate of reduction in z is greater than the rate of increase in T. This leads to an even greater increase in density as the critical point is approached.

The behaviour observed for the speed of sound can be explained by assuming that

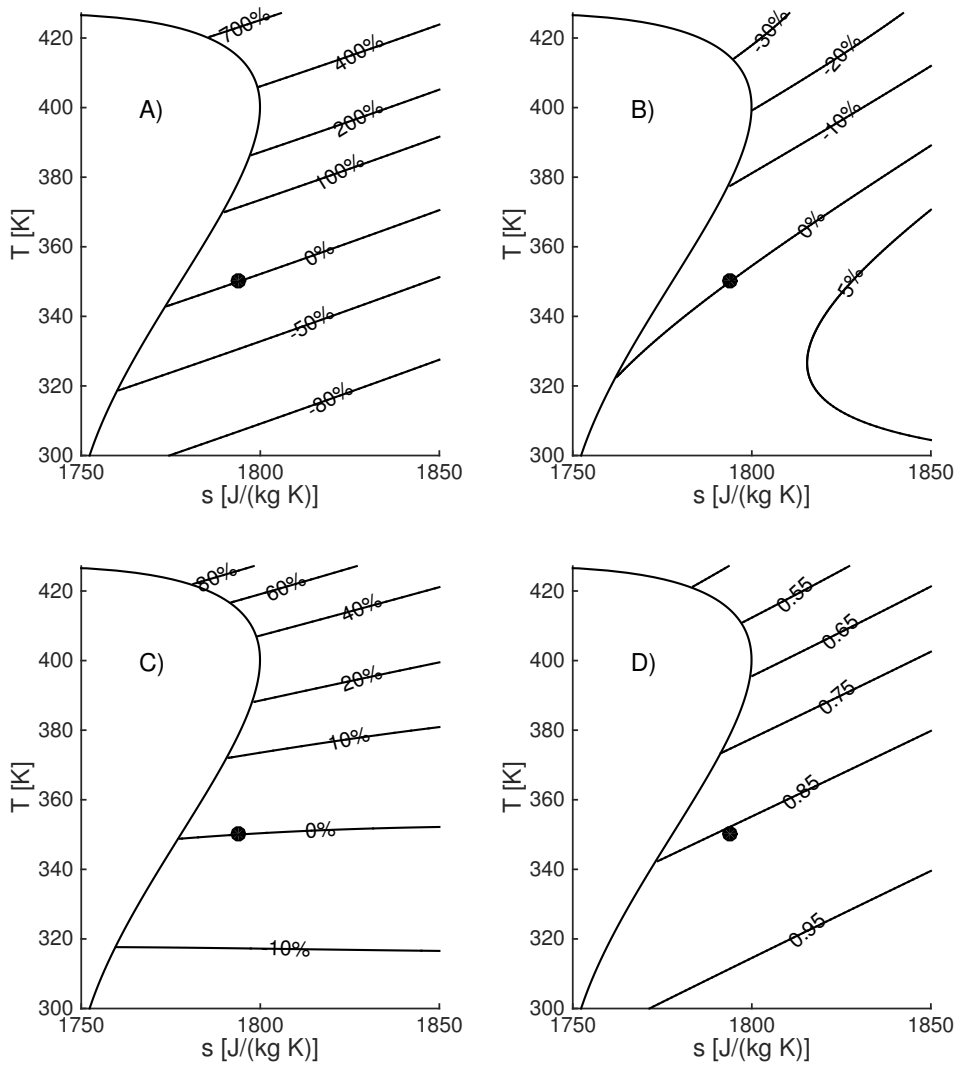

Figure 5.2: Variation in thermodynamic properties over a range of operating conditions for superheated R245fa between operating point and design point. A) Percentage deviation in density. B) Percentage deviation in speed of sound. C) Percentage deviation in dynamic viscosity. D) Variation in compressibility factor.

$a^2 = kP/\rho$. For an ideal gas k is the ratio of specific heats whilst $P/\rho = RT$. This results in an expression that shows the speed of sound to be a strong function of temperature, namely $a = \sqrt{\gamma RT}$. For an ORC working fluid neither of these formulations are valid. However it has been shown that k can be considered as a polytropic index that can be determined numerically using a linear regression (Wheeler and Ong, 2013). Using this method it can be shown that for R245fa over the range of conditions considered, the value of the polytropic index reduces as the critical point is approached. Furthermore, following from the previous discussion, the ratio P/ρ must also reduce leading to a reduction in the speed of sound as the critical point is approached. From Figure 5.2C it is clear that the

dynamic viscosity is a strong function of temperature.

Overall, both the density and dynamic viscosity increase towards the critical point, whilst the speed of sound reduces. The net effect of reducing speed of sound and increasing dynamic viscosity is to reduce the Reynolds number. However, since the Reynolds number is rising, the significant increase in density must cause the observed deviation in Reynolds number. Therefore the Reynolds number is clearly dependent upon the density of the fluid, and the result of real gas effects near the critical point is to increase the deviation in Reynolds number even further. This is an important factor that might be the cause of any observed deviation in similitude predictions at high deviations in Reynolds number. This discussion also explains why the deviation lines shown in Figure 5.1 resemble constant pressure lines.

5.3 ORC turbine performance mapping

The work completed in Chapter 4 developed a candidate ORC turbine, and a CFD simulation was setup to evaluate the turbine performance at the design point. To investigate the application of similitude theory for the performance prediction of ORC turbines, this CFD analysis should be extended to consider off-design operation. Having already ensured that a suitable mesh and fluid property table size are used, and also having confirmed the suitability of steady-state simulations, it is easy to evaluate off-design performance. For this the same steady-state simulation was performed over a range of total-to-static pressure ratios at 80%, 100% and 120% of the design rotational speed. This correlated to rotational speeds of $30,000$ rpm, $37,525$ rpm and $45,000$ rpm. The inlet boundary condition remained fixed at the turbine total inlet conditions ($T_{01} = 350$ K, $P_{01} = 623.07$ kPa), whilst the outlet static pressure was set according to the desired total-to-static pressure ratio.

After completing each simulation, REFPROP was used to calculate the total enthalpy at the turbine inlet and outlet (h_{01} and h_{05}), and the turbine inlet entropy s_{01}, using the mass averaged total temperatures and pressures from the CFD results. The isentropic static enthalpy $h_{5\text{ss}}$, and isentropic total enthalpy $h_{05\text{ss}}$, at the turbine outlet were then obtained from the area and mass averaged static and total outlet pressures, and determined inlet entropy s_{01}. This allowed the turbine isentropic total-to-total efficiency η_{tt} and total-

to-static efficiency η_{ts} to be calculated using Equations 2.11 and 2.12 respectively.

From the CFD results the reduced head and flow coefficients, and reduced blade Mach numbers were then calculated according to Equation 5.8. These data points were then curve fitted to generate smooth performance curves. For the curve fit that models the relationship between the reduced head and flow coefficients for each reduced blade Mach number a second order power law was found to offer the best fit. This relationship is given by Equation 5.15 where the coefficients a, b and c need to be determined for each constant blade Mach number.

$$\left(\frac{\dot{m}}{\rho_{01}a_{01}}\right) = a\left(\frac{\Delta h_s}{a_{01}^2}\right)^b + c \tag{5.15}$$

For the total-to-static isentropic efficiency the best fit was achieved when modelling it as a second order polynomial function of the total-to-static isentropic velocity ratio ν_{ts}. The representation of η_{ts} as a function of ν_{ts} is common practice within the radial turbine community, and the conversion from the reduced head coefficient to ν_{ts} is simple since $\nu_{ts} = u_4/\sqrt{2\Delta h_s}$ and $u_4 = \pi r_4 N/30$. The curve fit for each reduced blade Mach number is therefore given by Equation 5.16, where a, b and c are to be determined. After generating these curve fits it is a simple matter to convert the performance curve back into the form of η_{ts} as a function of the reduced head coefficient.

$$\eta_{ts} = a\nu_{ts}^2 + b\nu_{ts} + c \tag{5.16}$$

The resulting performance maps for the candidate ORC turbine using the curve fits described by Equations 5.15 and 5.16 are shown in Figures 5.3 and 5.4 respectively. It can be observed in these figures that the performance curves have been extrapolated beyond the range of the CFD data points. This may introduce some uncertainty in predictions made at these extreme operating points. However, for realistic applications turbine operation should be centred around the area where sufficient CFD data has been obtained.

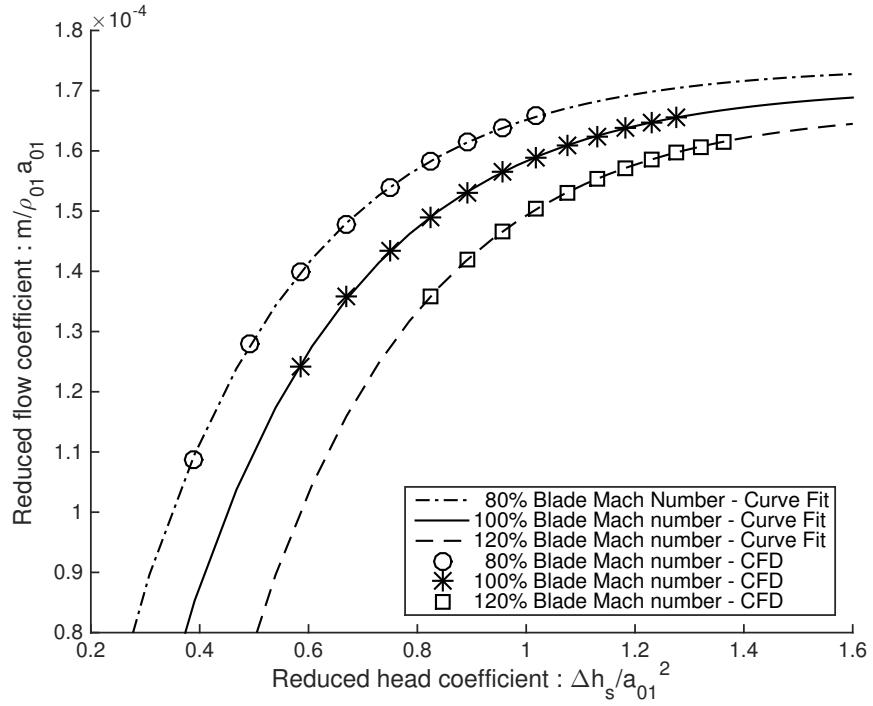

Figure 5.3: Variation of reduced flow coefficient with reduced head coefficient at 80%, 100% and 120% design blade Mach number for the candidate ORC turbine.

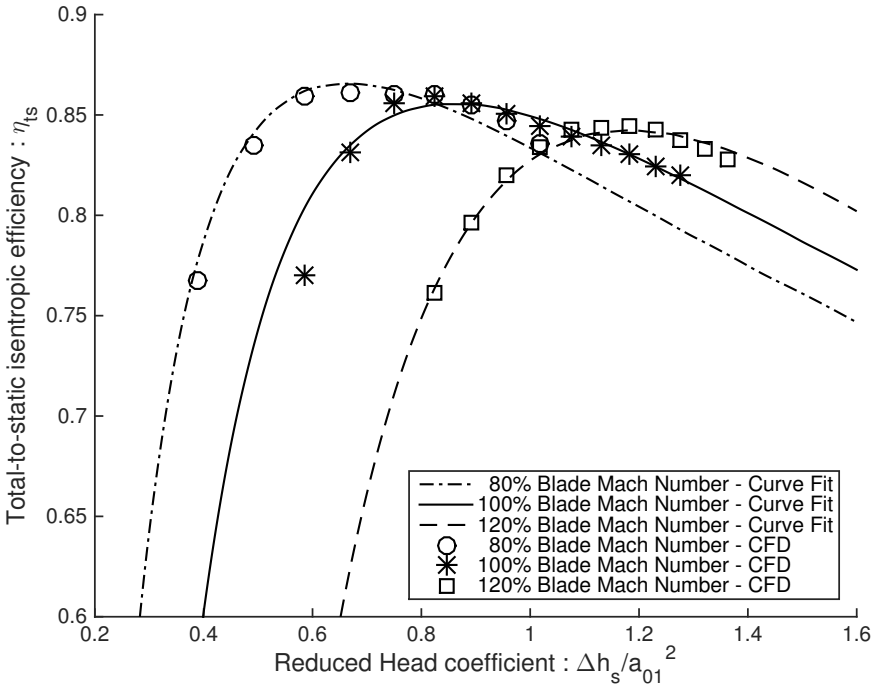

Figure 5.4: Variation of isentropic total-to-static efficiency with reduced head coefficient at 80%, 100% and 120% design blade Mach number for the candidate ORC turbine.

5.4 Similitude scaling case study: R245fa

Having constructed the turbine performance map for the candidate turbine, it is now possible to evaluate whether similitude can predict the performance of this turbine when the operating conditions, or working fluid changes. The first case study considered has been designed to evaluate turbine performance when using the same working fluid but at different turbine inlet conditions. This would be a typical application within ORC cycle analysis where the same turbine and working fluid may be optimised for a variety of different heat sources and sinks. A group of 8 operating points have been selected ranging from turbine inlet temperatures of 305 K up to 420 K, with total inlet pressures ranging from 127 kPa to 2963 kPa. These points correspond to deviations in Reynolds number between -75% and $+200\%$ respectively. The operating points are summarised in Table 5.1, and each operating point has been given a case number, and these case numbers correspond to dots shown in Figure 5.5. Here the case 'D' refers to the original design point. These 8 operating points were considered as they cover the range of total inlet temperatures and pressures that may be experienced within a low temperature, subcritical ORC utilising R245fa, and this spread is demonstrated in Figure 5.5. Cases 1 and 2 are perhaps the least practically viable due to the low turbine inlet temperatures. Nonetheless, their inclusion permits an investigation into similitude theory at a -75% deviation in Reynolds number.

In order to investigate the accuracy of similitude theory, the same CFD setup described previously has been used to generate the performance map for each case listed in Table 5.1. The inlet boundary conditions were set according to the corresponding total

Table 5.1: Thermodynamic summary of the operating points selected for the R245fa similitude theory study.

Case	T_{01} K	P_{01} kPa	ρ_{01} kg m^3	a_{01} m s^{-1}	μ Pa s^{-1} $\times 10^{-5}$	%Re deviation
1	305	127.2	7.1	137.3	1.07	-75%
2	315	133.8	7.2	139.9	1.10	-75%
D	350	623.1	33.5	133.9	1.23	0%
3	360	652.4	33.6	137.2	1.27	-0%
4	375	1239.5	69.7	124.6	1.37	$+75\%$
5	385	1292.2	68.9	129.2	1.40	$+75\%$
6	400	2088.0	127.8	112.0	1.58	$+150\%$
7	410	2146.4	120.9	119.8	1.60	$+150\%$
8	420	2963.2	202.1	100.9	1.87	$+200\%$

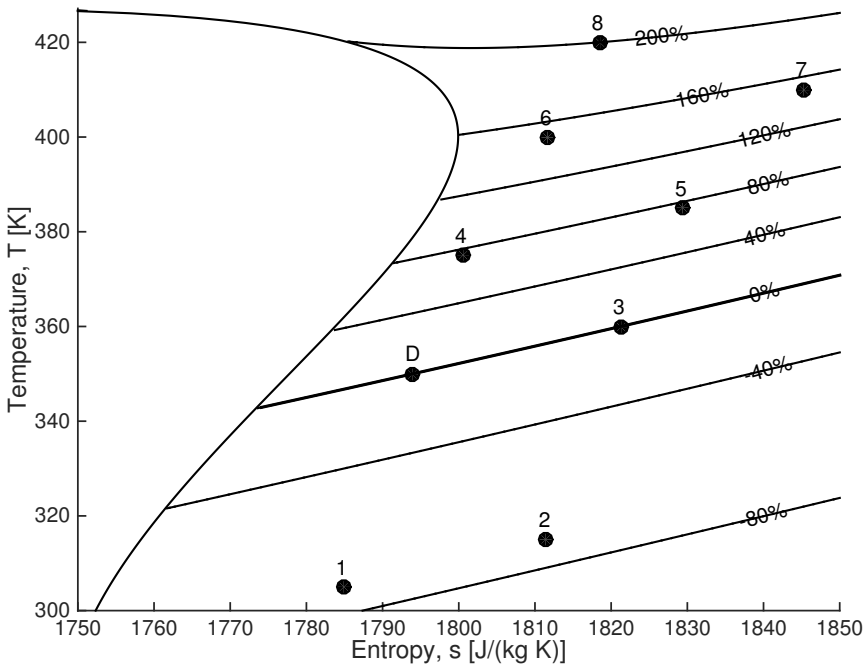

Figure 5.5: Turbine total inlet conditions for the 8 cases defined for the R245fa similitude theory study.

inlet conditions, and the same approach angle upstream of the stator leading edge was assumed. The reduced blade Mach numbers obtained for the design point supplied the rotor rotational speeds for each case using the corresponding speed of sound values in Table 5.1. The CFD setup was then run for a range of pressure ratios at each reduced blade Mach number, and for each case number. The total and static properties were then extracted from the CFD results and the values for the reduced head and flow coefficients, along with the isentropic total-to-static efficiency, were determined.

For each case at 80%, 100% and 120% of the design reduced blade Mach number, the same pressure ratio values were converted into their respective reduced head coefficients. These reduced head coefficients then provided estimates for the reduced flow coefficient, and total-to-static efficiency through interpolation of the non-dimensional performance map obtained using similitude theory (Figures 5.3 and 5.4). Having obtained both the similitude predictions and the performance data predicted by CFD, the results can be compared and this comparison is shown in Figures 5.6 and 5.7 for all cases. Error bands corresponding to $\pm 2\%$ and $\pm 5\%$ deviation have been included for clarity.

From these figures it is clear that cases with a Reynolds number deviation between -75% and $+75\%$ (cases 1 to 5) all lie within the $\pm 2\%$ bands. This suggests that the

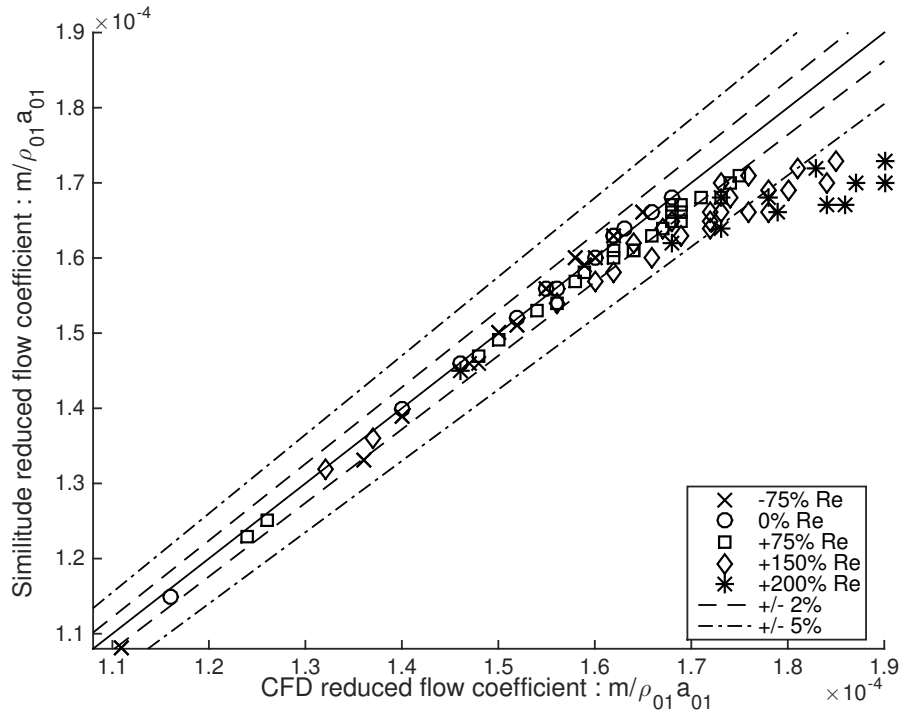

Figure 5.6: Comparison between the flow coefficient predicted by similitude theory and the flow coefficient found from the CFD results for the R245fa operating points.

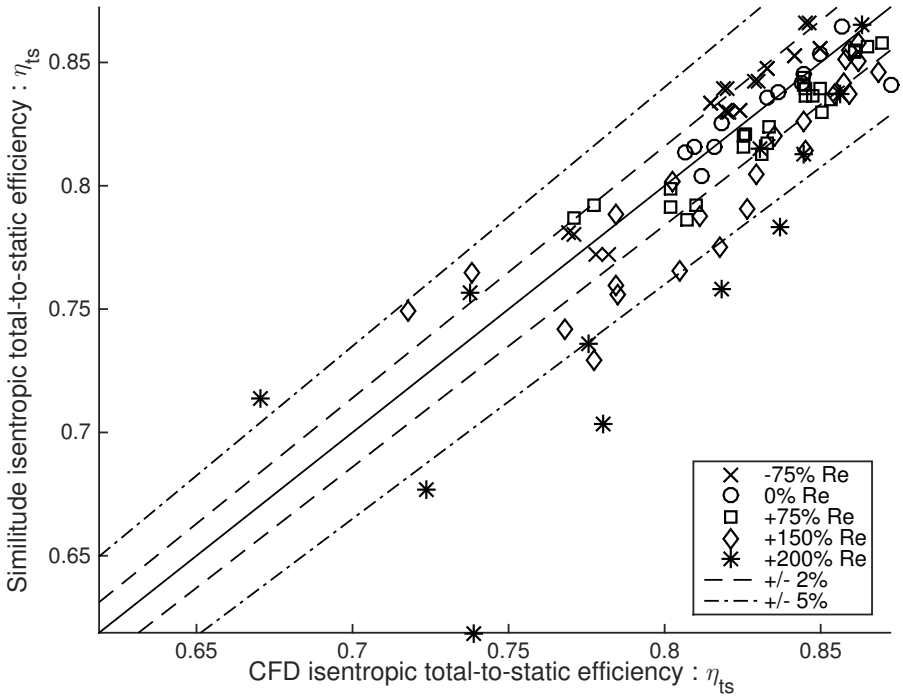

Figure 5.7: Comparison between the isentropic total-to-static isentropic efficiency predicted by similitude theory and the efficiency found from the CFD results for the R245fa operating points.

current similitude theory accurately predicts the mass flow rate and isentropic efficiency for this turbine operating with R245fa, as long as the change in the total inlet conditions does not cause a deviation in Reynolds number that is greater than ±75%. Furthermore, for these cases the isentropic efficiency is found to remain high, ranging from $\eta_{ts} = 75\%$ to $\eta_{ts} = 85\%$. This suggests that this candidate turbine could perform well over the range of operating points considered within cases 1-5.

For higher deviations in Reynolds number of +150% and +200% (cases 6-8) the deviation is more pronounced, with similitude theory under predicting the mass flow rate. Referring to Figure 5.3 it is clear that higher flow coefficients correspond to higher head coefficients, which in turn means that turbine operation is closer to the choking point. Figure 5.6 therefore suggests that as the turbine approaches, or exceeds, the choking pressure ratio, the error in similitude predictions increases. It is however, interesting to note that at low flow coefficients similitude theory accurately predicts the mass flow rate and efficiency for these high Reynolds deviation cases. This shows that similitude may still be applicable to high Reynolds number deviations, so long as the flow conditions within the turbine remain far from the choking point.

For the cases with higher flow coefficients the CFD results continually predict a higher mass flow rate than similitude theory. Figure 5.7 shows that cases 6 to 8 generally correspond to lower isentropic efficiencies suggesting that the turbine is operating at more significant off-design conditions. Furthermore it was found that the +150% and +200% Reynolds number deviation data points that show the lowest efficiencies in Figure 5.7 correspond to the data points with the highest flow coefficients in Figure 5.6. This confirms that the deviation observed in Figure 5.6 increases as the operating conditions move further away from the design point. Within the context of thermodynamic analysis, and developing a practical system, this suggests that cases 6 to 8 may benefit from an alternative turbine design that would operate more efficiently at these conditions.

Another interesting discussion point is the relationship between the head coefficient and pressure ratio. As observed from Figure 5.2, increasing the inlet temperature and pressure reduces the speed of sound. To maintain the head coefficient, the isentropic enthalpy drop, and therefore pressure ratio, must reduce. When moving from the design point to case 8, the design total-to-static pressure ratio reduces from 2.5 to 1.8. Within a practical ORC application, increases in inlet temperature and pressure permit higher pressure ratios

resulting in better cycle efficiencies and a better utilisation of the heat source. However these results show that for a higher pressure ratio, the efficiency is significantly penalised by operating at off-design. This further confirms that implementing this turbine for these conditions would not be appropriate.

For the sake of completing this analysis, the source of the deviation for cases 6-8 has been investigated further. The first step was to consider any uncertainties that may have caused this observed deviation. The initial data points used to construct the performance map did not extend beyond a head coefficient of 1.4. Therefore extrapolation of these curves may have introduced some uncertainty into the similitude predictions. Furthermore, the CFD analysis undertaken was comprised of a steady-state analysis using a mixing plane to simulate rotor-stator interface. This model has been validated for the subsonic design point, but may introduce discrepancies for supersonic flow as the influence of shock waves generated upstream of the rotor cannot traverse across the rotor-stator boundary.

To confirm the suitability of the steady-state CFD simulations for supersonic operating points the same unsteady simulation setup previously described in Section 4.6.2, was run for a number of additional operating points. Following from the sensitivity study, the number of time steps per blade pass was set to 25. The operating points selected were the points that show the highest deviation in Figure 5.6. These points correspond to case 8 where the head coefficient is high, with choked or supersonic flow expected. The comparison between the steady and unsteady results is shown in Table 5.2. The percentage differences for the mass flow rate and isentropic efficiency remain below 0.65% and 1.85% respectively. These deviations were not considered significant enough and therefore it is concluded that the steady-state simulation is sufficiently accurate for the purpose of this research. The reductions in isentropic efficiency found for the unsteady simulations are similar to those found by Wheeler and Ong (2014). They studied the unsteady flows within transonic ORC turbines and found a reduction in efficiency between 1.25% and 1.5%.

Table 5.2: Comparison between steady and unsteady CFD simulations for case 8.

Blade Mach number	Head coefficient	$\dot{m}$			η_{ts}		
		Steady	Unsteady	% Diff.	Steady	Unsteady	% Diff.
80%	1.863	3.865	3.875	+0.259	66.94	65.82	−1.706
100%	2.151	3.870	3.882	+0.292	72.28	70.97	−1.842
120%	2.403	3.780	3.805	+0.644	73.92	72.91	−1.382

Having verified the steady-state simulation, the steady CFD results for cases 6 to 8 have been compared with the non-dimensional performance curves used for similitude theory (Figure 5.8). Similitude theory predicts that above a non-dimensional head coefficient of around 1.6 choking is expected, whilst the CFD results show that above this head coefficient the mass flow rate, and therefore flow coefficient, continues to rise. For each case, the CFD results show a smooth variation of data points for each constant blade Mach number, with the flow choking at a higher flow coefficient than that predicted by similitude. This suggests that the deviation is a more fundamental issue with similitude theory not accurately predicting the choking mass flow rate. Figure 5.8 also shows that at head coefficients below 1 the CFD results match well with the non-dimensional performance curves. This confirms the suitability of similitude for the high Reynolds number cases, provided the flow remains subsonic.

Overall, it is clear that the current similitude theory is only accurate for a certain range of operating conditions. To consider possible improvements to the current similitude theory, it is helpful to consider that the choking mass flow rate is defined by Equation 5.17 where a^* and ρ^* are the static speed of sound and density at the choking point, and A is the throat area.

$$\dot{m} = \rho^* a^* A \tag{5.17}$$

Since the throat area cannot change the expression $\dot{m}/\rho^* a^*$ must remain constant for all fluids and turbine inlet conditions. Upon inspection it is clear that this expression is identical to the reduced flow coefficient defined in Equation 5.8, expect that it uses the static throat conditions instead of the turbine total inlet conditions. This suggests that applying similitude theory using these parameters would maintain the choking mass flow rate and lead to more accurate predictions for the turbine performance. This new formulation of similitude theory, again neglecting turbine diameter, but including the Reynolds number and power coefficient, is given by Equation 5.18.

$$\left[\frac{\Delta h_\mathrm{s}}{a^{*2}},\ \eta,\ \frac{W}{\rho^* a^{*3}}\right] = f\left(\frac{\dot{m}}{\rho^* a^*},\ \frac{\rho^* a^*}{\mu},\ \frac{N}{a^*}\right) \tag{5.18}$$

To obtain values for ρ^* and a^* an iterative procedure is required since neither the static temperature or static pressure at the choked stator throat is known. Based on a

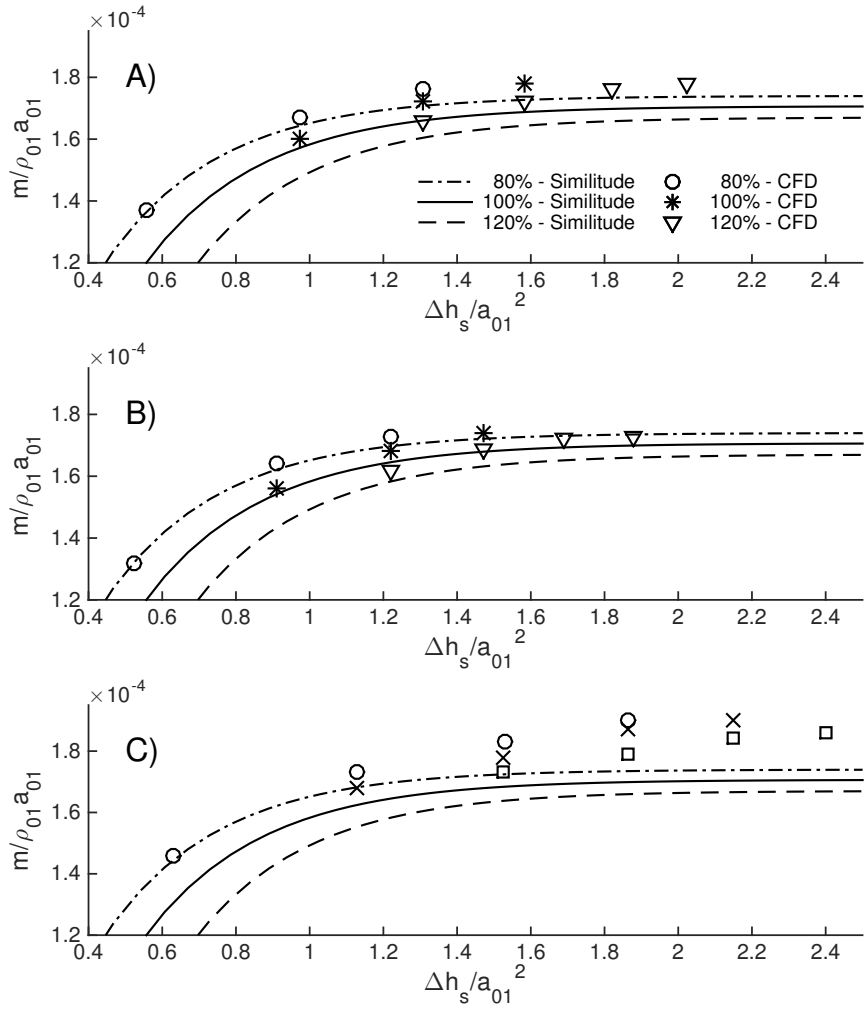

Figure 5.8: Comparison between the CFD results for R245fa cases 6-8 and the non-dimensional performance curves used during the application of similitude theory. A) Case 6; B) Case 7; C) Case 8.

total inlet temperature and pressure, the inlet entropy s_{01}, total enthalpy h_{01} and speed of sound a_{01} are known. Setting $a^* = a_{01}$ determines the static enthalpy since $h^* = h_{01} - 1/2\ a^{*^2}$, whilst it is assumed that flow from the stator inlet to the throat is isentropic ($s^* = s_{01}$). This allows a new guess of a^* to be calculated as a function of h^* and s^*, and this process is repeated until convergence. In reality the flow between the stator inlet and throat will not be isentropic. However, since the flow is assumed to approach the stator blade at the optimal incidence angle any incidence loss should be minimal. Furthermore, by comparison to the entropy generated due to the mixing of the stator vane wakes downstream of the stator throat and any shock waves generated during supersonic expansion, any total pressure profile loss should be minimal. Therefore the change in a^* and ρ^* should be minimal.

Table 5.3: Comparison between total inlet and static throat thermodynamic conditions.

Case	a_{01}	a^*	a^*/a_{01}	ρ_{01}	ρ^*	ρ^*/ρ_{01}
1	137.3	136.3	0.99	7.1	4.3	0.61
2	139.9	138.9	0.99	7.2	4.4	0.61
D	133.9	137.2	1.02	33.5	20.2	0.60
3	137.2	140.3	1.02	33.6	20.3	0.60
4	124.6	132.7	1.07	69.7	41.2	0.59
5	129.2	136.4	1.06	68.9	40.8	0.59
6	112.0	125.3	1.12	127.8	73.5	0.58
7	119.8	131.2	1.10	120.9	70.2	0.58
8	100.9	116.4	1.15	202.1	113.9	0.56

Using the method outlined the values the values for a^* and ρ^* have been calculated for the original design case and the 8 cases defined for the similitude study. These values are shown in Table 5.3. From this table it is clear that as the total inlet conditions move closer towards the critical point, the ratio of a^*/a_{01} increases, whilst the the ratio ρ^*/ρ_{01} reduces. Referring back to Figure 5.2 this was to be expected since the speed of sound reduces and the density increases as the critical point is approached.

To investigate the suitability of the updated similitude theory the original turbine performance maps (Figures 5.3 and 5.4) must first be rescaled according to the throat static properties for the design case. This is a simple scaling that obtains the new performance maps in terms of the new reduced head coefficients, flow coefficients and blade Mach numbers defined by the static throat conditions instead of the total inlet conditions. This scaling is summarised as follows:

$$\frac{\Delta h_s}{a^{*^2}} = \left(\frac{\Delta h_s}{a_{01}^2}\right)\left(\frac{a_{01}}{a^*}\right)^2 \tag{5.19}$$

$$\frac{\dot{m}}{\rho^* a^*} = \left(\frac{\dot{m}}{\rho_{01} a_{01}}\right)\left(\frac{\rho_{01} a_{01}}{\rho^* a^*}\right) \tag{5.20}$$

$$\frac{N}{a^*} = \left(\frac{N}{a_{01}}\right)\left(\frac{a_{01}}{a^*}\right) \tag{5.21}$$

For the initial similitude theory study using total inlet conditions the CFD results were obtained at specific rotational speeds that maintained the reduced blade Mach number, namely at 80%, 100% and 120% of N/a_{01}. However, for the updated similitude theory the definition of the blade Mach numbers have changed to N/a^*, and therefore a direct comparison between the CFD results and the new performance map is no longer possible.

Table 5.4: Reduced blade Mach numbers (N/a^*) obtained using the updated similitude theory for the CFD results that were obtained at rotational speeds that maintained the original blade Mach numbers (N/a_{01}). Results are expressed as a percentage of the reduced blade Number at the original turbine design point.

Case	% $(N/a^*)_D$		
	80% N/a_{01}	100% N/a_{01}	120% N/a_{01}
1	82.8	103.5	124.1
2	82.8	103.5	124.3
D	80.0	100.0	120.0
3	80.3	100.5	120.5
4	77.0	96.2	115.4
5	77.6	97.1	116.4
6	73.0	91.4	109.6
7	74.7	93.4	112.0
8	70.6	88.4	106.0

To clarify this point consider the data listed in Table 5.4 for case 1. For this case, the rotational speeds selected for the CFD analysis were selected to maintain the original blade Mach numbers based on the total inlet speed of sound a_{01}. However, using the new similitude theory, a^* now replaces a_{01} which means that the updated blade Mach numbers at which CFD data has been obtained are no longer at 80% and 100% and 120% of N/a^* but instead are at 82.74%, 103.50% and 124.12% of N/a^*. Since the performance maps have not been obtained at these alternative blade Mach numbers, an interpolation method has been developed. This uses the available performance data at known reduced blade Mach numbers to predict the turbine performance at other reduced blade Mach numbers.

Before implementing this interpolation method it was important to obtain data points for additional reduced blade Mach numbers, which will provide a greater accuracy when completing the interpolation. Two additional rotational speeds have been selected, namely 50% and 150% of the original design value, and this corresponded to rotational speeds of $18,762$ rpm and $56,288$ rpm respectively. At these rotational speeds, and for the design point total inlet conditions ($T_{01} = 350$ K, $P_{01} = 623.07$ kPa), the CFD simulations were run over a range of pressure ratios and the mass flow rates and turbine efficiencies were calculated. The results were then converted to the reduced head and flow coefficients using the throat static conditions, and then curve fitted using Equations 5.15 and 5.16. The resulting curves are shown in Figures 5.9 and 5.10, along with the previously obtained curves that have now been scaled according to Equations 5.19 - 5.21.

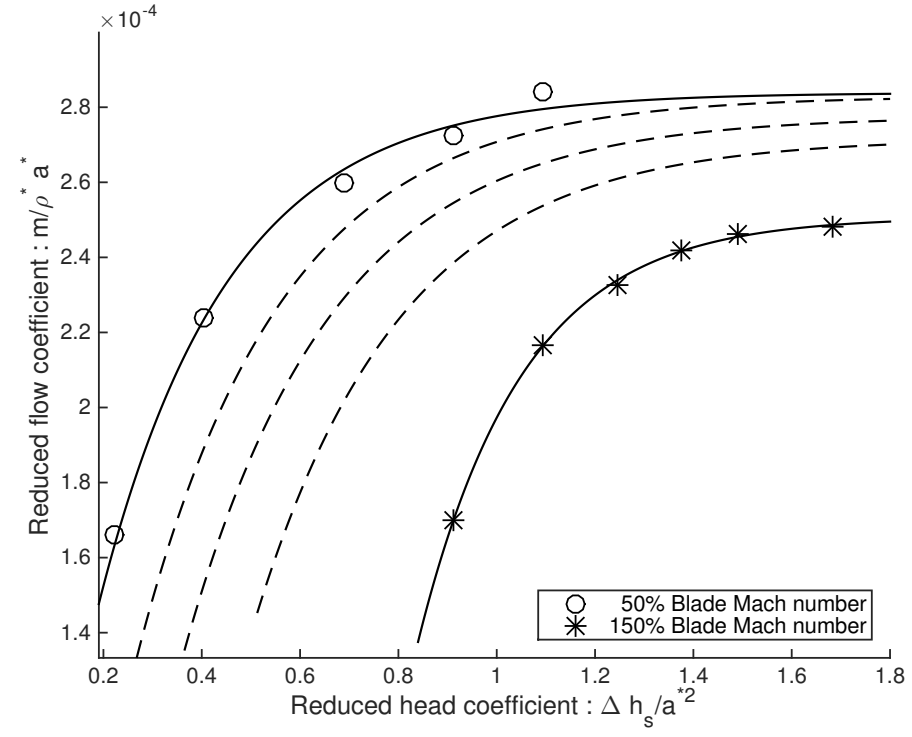

Figure 5.9: Variation of reduced flow coefficient with reduced head coefficient at 50% and 150% design blade Mach number for the candidate ORC turbine.

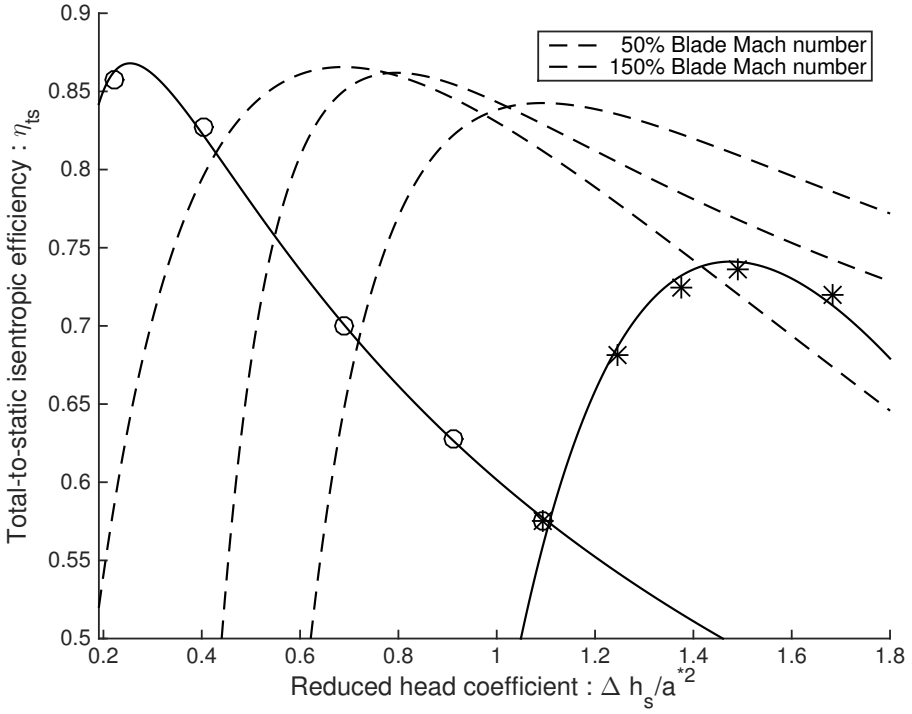

Figure 5.10: Variation of isentropic total-to-static efficiency with reduced head coefficient at 50% and 150% design blade Mach number for the candidate ORC turbine.

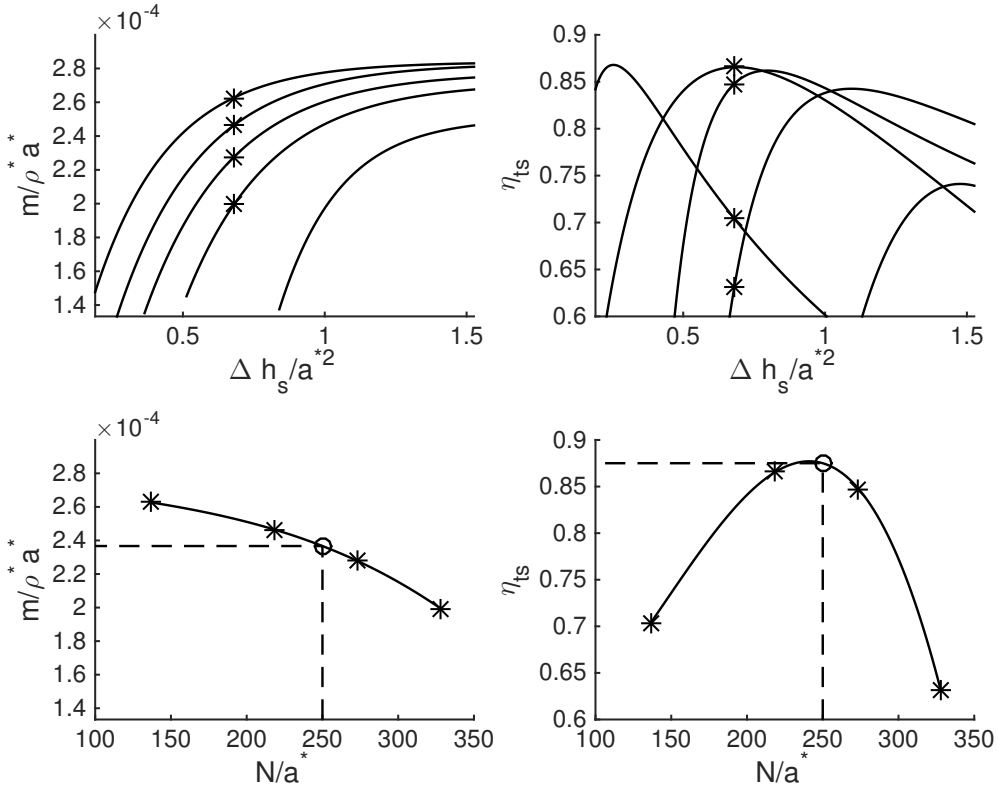

Figure 5.11: Interpolation method to determine turbine performance at alternative blade Mach numbers.

With two more reduced blade Mach number lines added to the turbine performance map, the interpolation that is used to obtain the similitude prediction using the updated similitude theory can be described. This description is accompanied by Figure 5.11 which illustrates this process. Considering a single data point at which the mass flow rate and total-to-static isentropic efficiency have been obtained for a defined total-to-static pressure ratio and rotational speed, the reduced head coefficient and reduced blade Mach number can immediately be obtained using the known values of a^* and ρ^*. For this head coefficient, the reduced flow coefficient and isentropic efficiency at 50%, 80%, 100%, 120% and 150% of the design point blade Mach number can easily be obtained, as demonstrated by the dots in the top graphs of Figure 5.11. These data points can then be plotted as a function of blade Mach number, as shown in the bottom graphs of Figure 5.11. These data points are then connected using a cubic spline, and interpolation of this cubic spline allows the flow coefficient and isentropic efficiency to be calculated for any blade Mach number.

This interpolation process has been repeated for every CFD data point that was obtained for each case. The final comparisons between the performance predicted directly

from the CFD results, and the predictions made using the updated similitude theory are shown in Figure 5.12 and 5.13 respectively. It is clear from this comparison that there is a significant improvement in the accuracy of the similitude predictions when using the updated similitude performance map. The flow coefficient predictions continually remain within the ±2% error bands so long as the flow coefficient does not exceed 2.7×10^{-4}, whilst most efficiency predictions also remain within the ±2% error bands.

To investigate the deviation observed for flow coefficients above 2.7×10^{-4} a stator only simulation was setup using the same stator mesh and general CFD setup as before. Since this simulation only considered the stator, the outlet of the CFD domain was positioned at a radius equal to the rotor inlet radius, and the static pressure was varied over a range of stator total-to-static pressure ratios. The flow coefficient and Mach numbers at the stator outlet and throat were then obtained from the simulation results, in addition to the total pressure loss coefficient Y. Y quantifies total pressure losses and is defined as the reduction in total pressure from the inlet to either the stator throat or outlet radius, divided by the difference between the total and static pressures at stator throat or outlet radius. The general expression for calculating Y is given by Equation 5.22. The stator only CFD analysis was completed for cases 1, 3, 6 and 8 and the results are shown in Figure 5.14.

$$Y = \frac{P_{0,\text{in}} - P_{0,\text{out}}}{P_{0,\text{out}} - P_{\text{out}}} \tag{5.22}$$

The first comment is that for all cases considered, the total pressure loss coefficient between the stator inlet and stator throat remains below 0.03. This corresponds to no more than a 1.2% reduction in the product of a^* and ρ^* compared to the isentropic values. It is interesting to note that the loss coefficient reduces as the flow coefficient increases, with values between 0.01 and 0.02 obtained for supersonic operating points. This will result in an even smaller deviation from the isentropic values, confirming the isentropic assumption used to obtain a^* and ρ^*.

In comparison, the total pressure loss coefficient for the whole stator shows much more variation. There are small variations until sonic conditions at the stator outlet are reached, but then after choking it rapidly increases. Sonic conditions at the stator outlet are obtained at a flow coefficient of approximately 2.7×10^{-4}, and this corresponds to

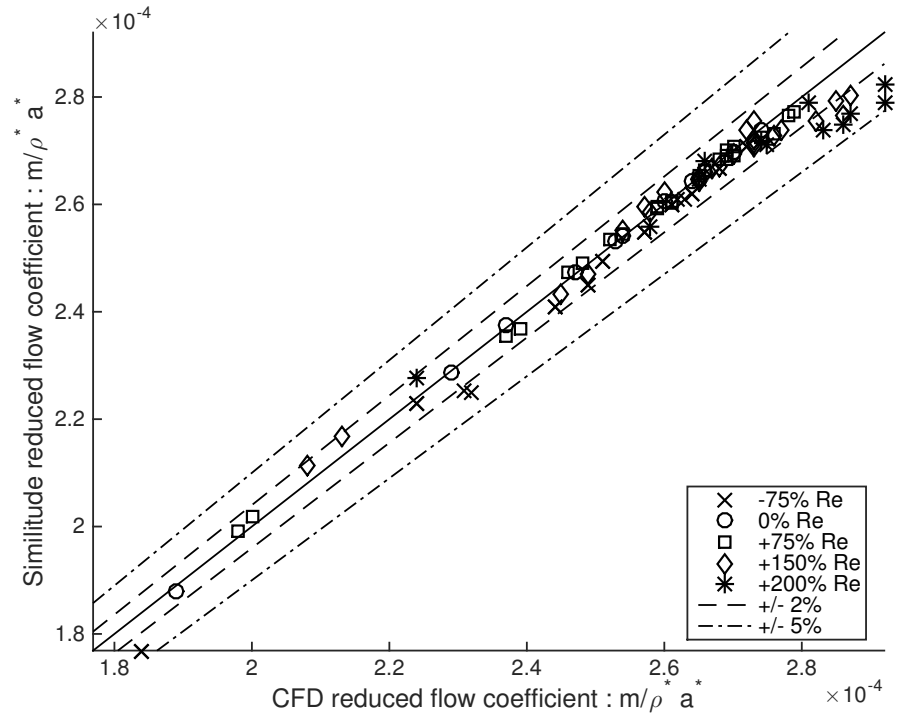

Figure 5.12: Comparison between the flow coefficient predicted by the updated similitude theory and the flow coefficient found from the CFD results for the R245fa operating points.

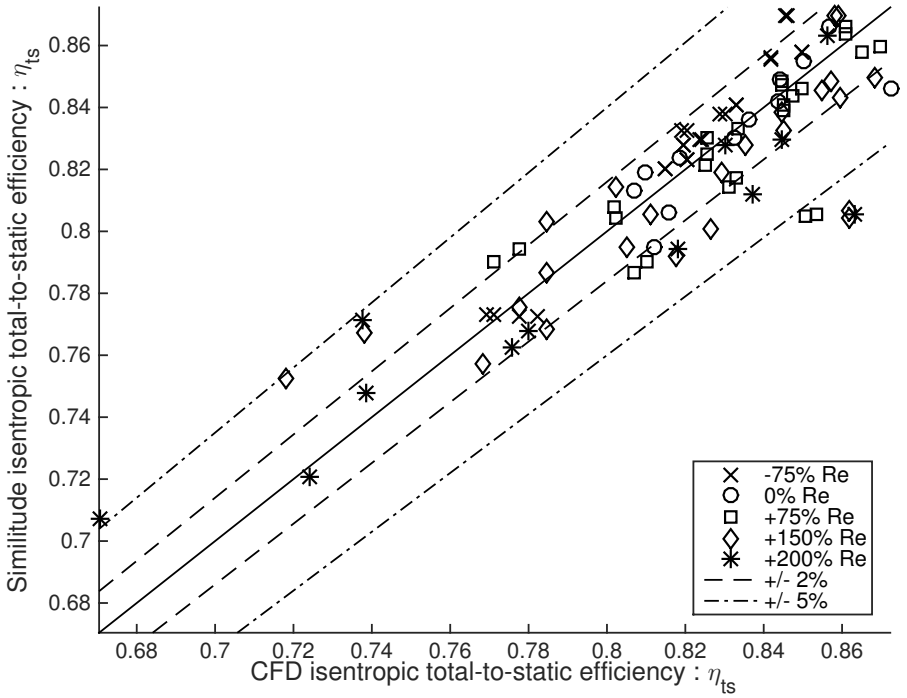

Figure 5.13: Comparison between the isentropic total-to-static isentropic efficiency predicted by the updated similitude theory and the efficiency found from the CFD results for the R245fa operating points.

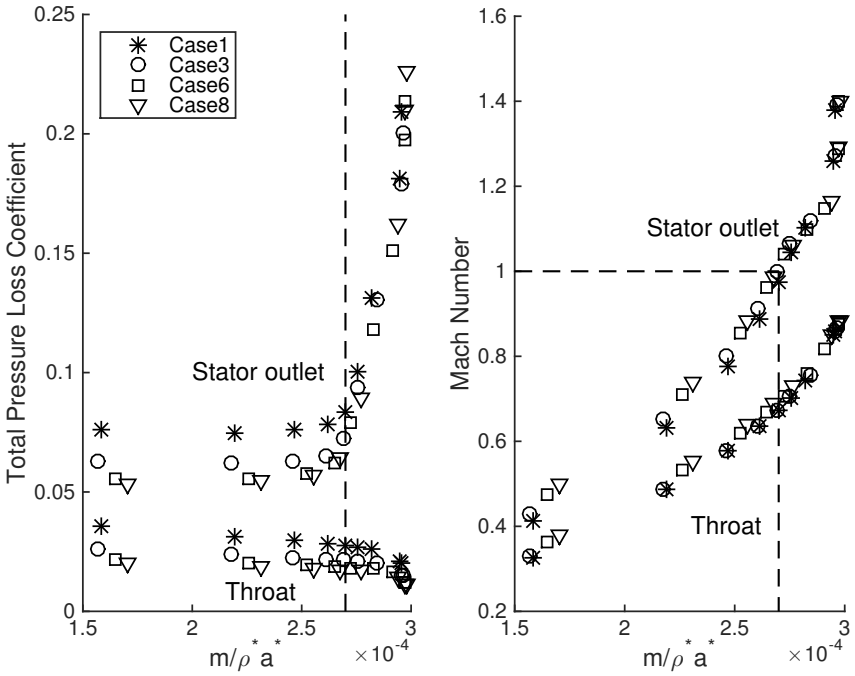

Figure 5.14: Summary of the stator vane performance over a range of flow coefficients. Bottom group of data points refers to the throat whilst the top group of data points refers to the stator outlet set at the rotor inlet radius. The dashed lines represent the change from subsonic to supersonic operation.

the point at which deviations between similitude and CFD predictions are introduced in Figure 5.12. This suggests that the modified similitude theory accurately predicts the performance of the turbine right up until the point at which sonic conditions are achieved at the stator outlet/rotor inlet.

It is interesting to note that the stator throat Mach number remains subsonic even as the stator outlet Mach number exceeds 1. This shows that the flow does not choke at the stator throat, but instead chokes further downstream. In fact it is sometimes feasible to design for supersonic conditions by allowing this to happen (Moustapha et al., 2003). However, this introduces uncertainty in the choking location, which may explain the observed deviation between the similitude and CFD predictions.

Figure 5.15 displays the Mach number distribution within the stator at one of the most extreme off-design conditions considered within this study. The results shown refer to the rotor and stator unsteady simulation at 120% of the design rotational speed, as defined in Table 5.2. This study consisted of four stator blades and three rotor blades although the rotor domain has been removed for clarity. Furthermore, this also explains

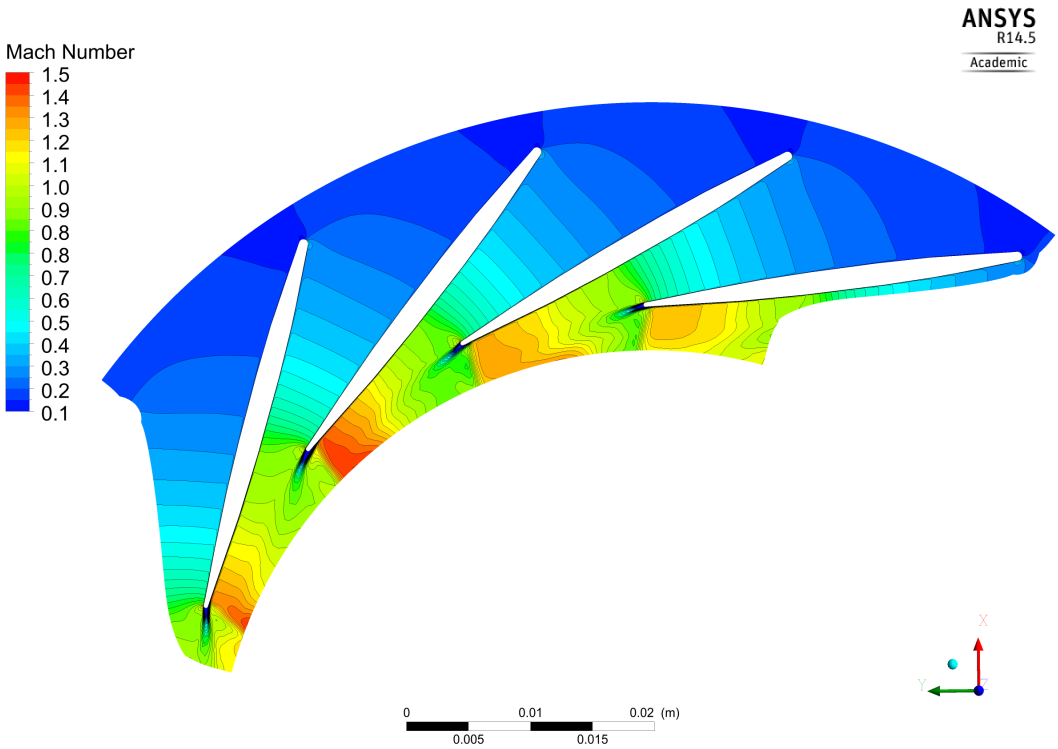

Figure 5.15: Distribution of Mach number within the turbine stator for case 8 with a flow coefficient of 2.87×10^{-4}.

why the flow pattern observed is not periodic. At this operating point, the flow coefficient is 2.87×10^{-4}. This figure clearly shows how the flow remains subsonic at the throat but then chokes further downstream.

The increasing total pressure loss coefficient for supersonic outlet conditions suggests there are high total pressure losses resulting from shock waves. This is again shown in Figure 5.15. Towards the trailing edge of the stator blade, on the suction side, there is a sudden visible change in Mach number corresponding to the shock wave. The introduction of supersonic flow, and the associated shock waves, again confirms that at these conditions the turbine is operating at off-design, and that the stator may require re-design. It could be concluded that the deviations observed between similitude and CFD predictions are a consequence of operating this existing subsonic turbine at supersonic conditions, as opposed to a more fundamental issue with the similitude theory. To investigate this further additional turbine geometry, consisting of a supersonic stator design, should be developed and analysed. Overall, from this investigation it can be concluded that within the range of operating conditions that would be considered sensible operating points for this turbine within an ORC, the modified similitude theory can successfully predict the

turbine performance.

To further verify the accuracy of the modified similitude theory, the analysis outlined throughout this section was repeated for total-to-total conditions. In this instance the isentropic enthalpy drop across the turbine and turbine isentropic efficiency are both measured in total-to-total terms instead of total-to-static. For this formulation the turbine performance maps must first be reformulated based on these conditions. Using the CFD results that were used to generate the original performance map, the turbine isentropic total-to-total efficiency at each combination of pressure ratio and rotational speed was calculated according to Equation 2.11. This was done using the mass averaged total temperatures and pressures at the turbine inlet and outlet. The same second order power and polynomial curve fits were used to generate the performance curves, and these curves were then non-dimensionalised according to Equation 5.18, where $\Delta h_{\mathrm{s}} = h_{01} - h_{05\mathrm{ss}}$ and $\eta = \eta_{\mathrm{tt}}$. The CFD results obtained for each case defined in Table 5.1 were then compared to the similitude predictions made using this new performance map and the results are shown in Figures 5.16 and 5.17.

From these results it clear that similitude theory predictions for the reduced flow coefficient continually match the CFD results, right up until the choked flow coefficient is reached. In terms of the total-to-total efficiency, the majority of operating points are within the $\pm 2\%$ error bands, and all operating points are within the $\pm 5\%$ error bands. At this point, it should again be reiterated that the efficiency values shown in Figure 5.17 are aerodynamic efficiencies based on the rotor, stator and clearance gap only. Therefore, total pressure losses within the volute, windage losses and mechanical losses are not taken into consideration, explaining why relatively high isentropic efficiency values are obtained.

Ultimately, as expected, the results shown in Figures 5.16 and 5.17 are very similar to Figures 5.12 and 5.13. This confirms that the modified similitude theory can be formulated using both total-to-total, and total-to-static conditions.

5.5 Similitude scaling case studies: R123 and R1234yf

One of the key aspects within ORC design is the selection of a suitable working fluid, and this often requires a parametric investigation considering a range of candidate fluids. It is therefore important to predict the performance of a given turbine when the working fluid

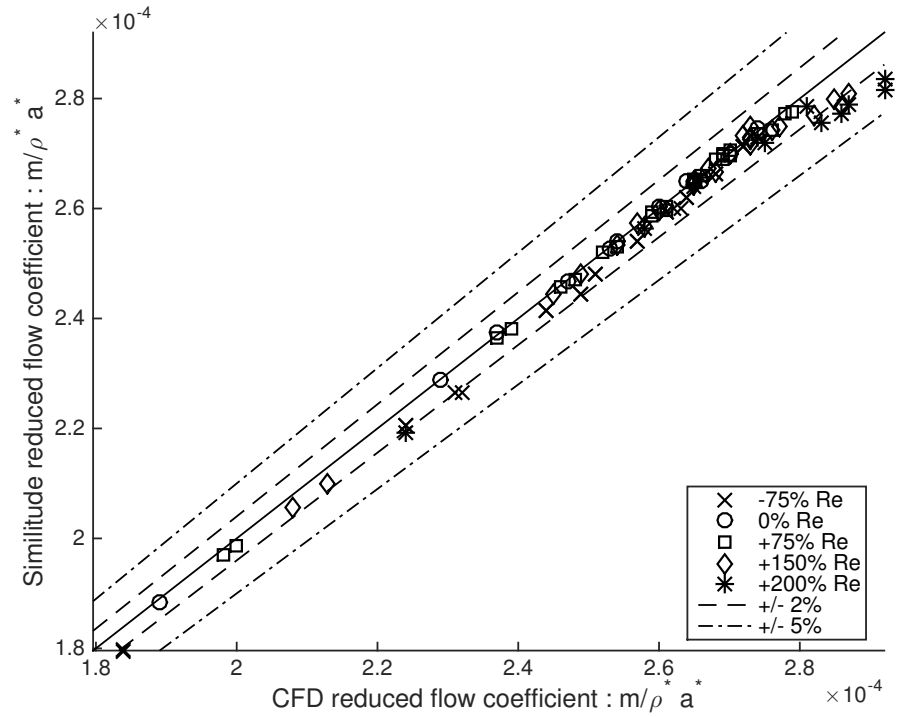

Figure 5.16: Comparison between the flow coefficient predicted by the updated similitude theory and the flow coefficient found from the CFD results for the R245fa operating points. Based on total-to-total conditions.

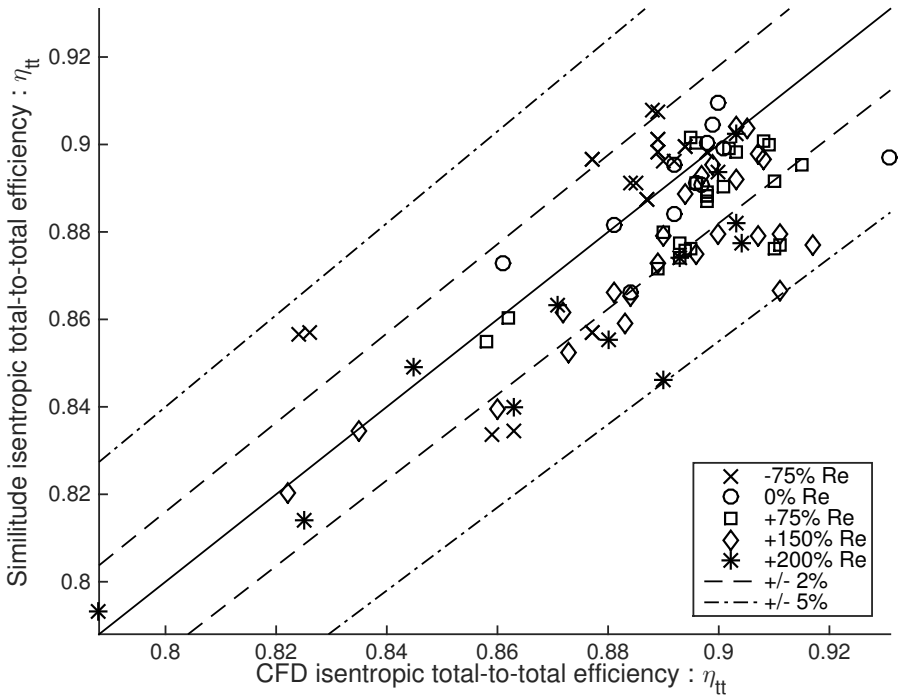

Figure 5.17: Comparison between the isentropic total-to-total isentropic efficiency predicted by the updated similitude theory and the efficiency found from the CFD results for the R245fa operating points.

changes. To do this two alternative working fluids have been selected. R123 is another commonly used low temperature ORC working fluid, whilst R1234yf may be considered a next generation fluid to be employed within ORCs. For both fluids, a number of operating points have been selected, and these cover the same deviations in Reynolds as selected for the R245fa case study. Table 5.5 summarises the total inlet conditions for the R123 and R1234yf studies, whilst Figure 5.18 displays these inlet conditions on the respective T-s diagrams for R123 and R1234yf. Again, the selected operating points cover the range of operating temperatures and pressures that could be expected within a subcritical ORC using these working fluids. R123 has a higher critical temperature, whilst R1234yf has a lower critical temperature than R245fa, resulting in a different range of temperatures for these two working fluids.

Table 5.5: Turbine inlet conditions for the R123 and R1234yf similitude studies.

		R123		R1234yf	
Case	% Re	T_{01} K	P_{01} kPa	T_{01} K	P_{01} kPa
1	−75%	320	131.4		
2	−75%	335	140.9		
3	0%	370	641.4	305	577.7
4	0%	385	682.1	315	610.8
5	+75%	400	1272.6	330	1159.5
6	+75%	415	1346.9	340	1222.8
7	+150%	430	2146.6	350	1903.3
8	+150%	440	2207.8	360	1996.7
9	+200%	455	3153.1	362	2586.2

For each operating point in Table 5.5 the performance over a range of pressure ratios and rotational speeds has been predicted using the same steady-state CFD simulation as previously outlined for the R245fa turbine. Real fluid property tables were generated for R123 and R1234yf using REFPROP, whilst the choked flow properties a^* and ρ^* were obtained using the same iteration procedure previously described in Section 5.4. After determining these parameters the reduced head and flow coefficients, along with the isentropic total-to-static efficiency were determined. The performance map, non-dimensionalised according to the updated similitude theory, was then used to predict the flow coefficient and isentropic total-to-static efficiency at the same reduced head coefficient and blade Mach number. The results for R123 are shown in Figures 5.19 and 5.20, whilst the results for R1234yf are shown in Figures 5.21 and 5.22.

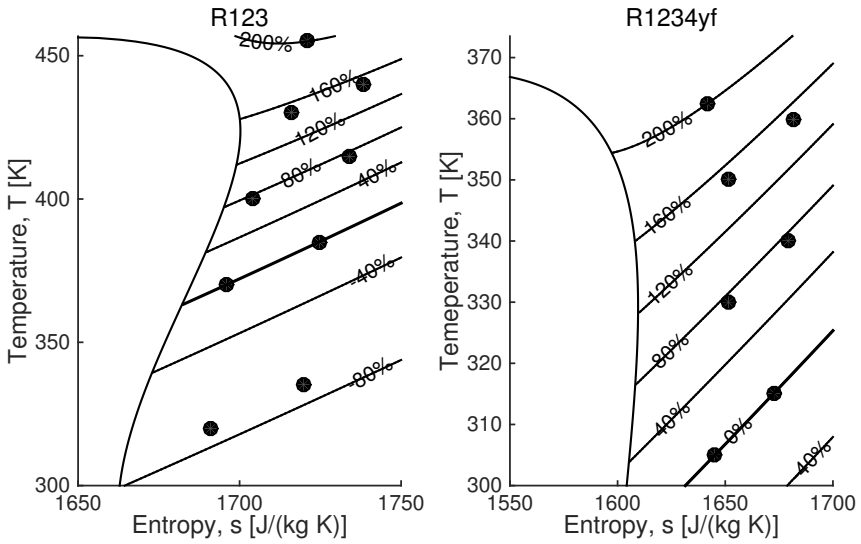

Figure 5.18: Turbine inlet conditions for the R123 and R1234yf similitude studies overlaid onto contours showing the percentage deviation in Reynolds number.

For both studies the most striking conclusion is the similarity between these results and the results obtained for R245fa. For all cases with flow coefficients below 2.7×10^{-4}, the turbine performance is accurately predicted to within $\pm 2\%$. Beyond this point increased deviation is observed, again attributed to operating at supersonic conditions. These points are again accompanied with lower turbine efficiencies, confirming that this design may be unsuitable for these operating conditions. From this analysis, it seems that the proposed modification to similitude theory can accommodate changes in working fluid.

5.6 Conclusions

In this chapter the suitability of applying similitude theory to predict radial turbine performance within a low-temperature ORC has been investigated. The CFD analysis completed in Chapter 4 has been extended to obtain the complete performance map for the ORC turbine, operating with R245fa as the working fluid. Similitude theory was then used to non-dimensionalise this performance map, and this map was used to predict turbine performance for alternative inlet conditions but with the same working fluid. These predictions were then compared with additional CFD simulations. It was concluded that the original similitude theory using total inlet conditions can only be relied upon provided that the flow remains subsonic and that the deviation in the turbine Reynolds number is between $\pm 75\%$.

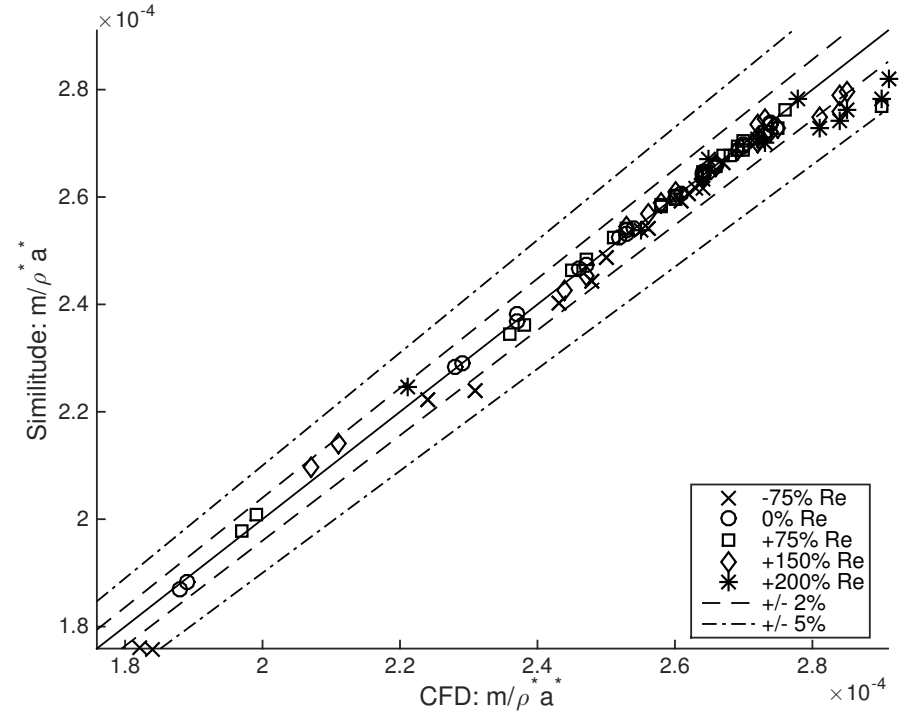

Figure 5.19: Comparison between the flow coefficient predicted by the updated similitude theory and the flow coefficient from the CFD results for the R123 operating points.

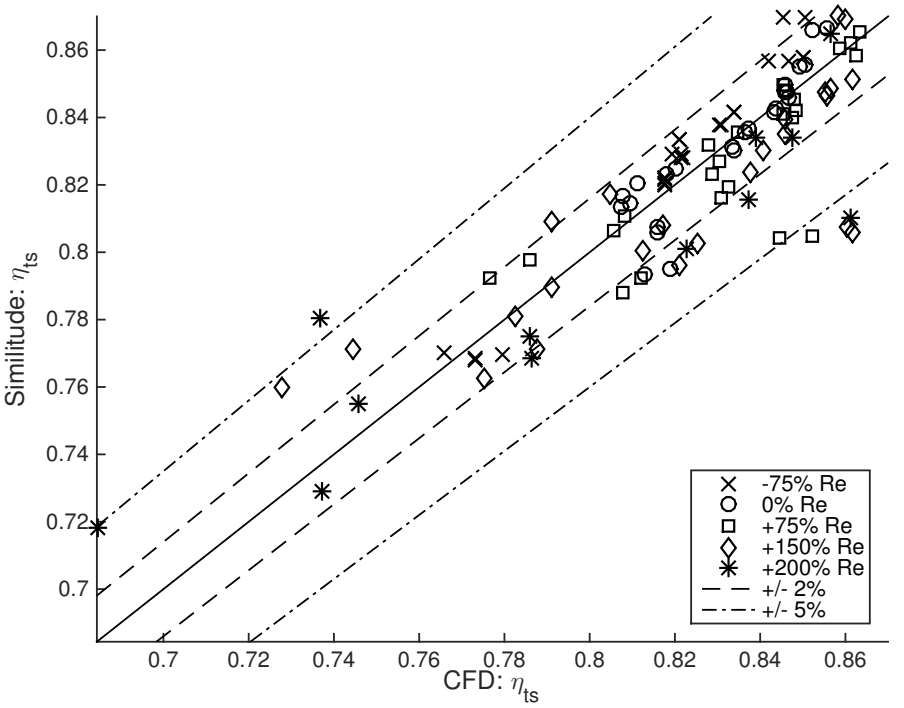

Figure 5.20: Comparison between the isentropic total-to-static isentropic efficiency predicted by the updated similitude theory and the efficiency found from the CFD results for the R123 operating points.

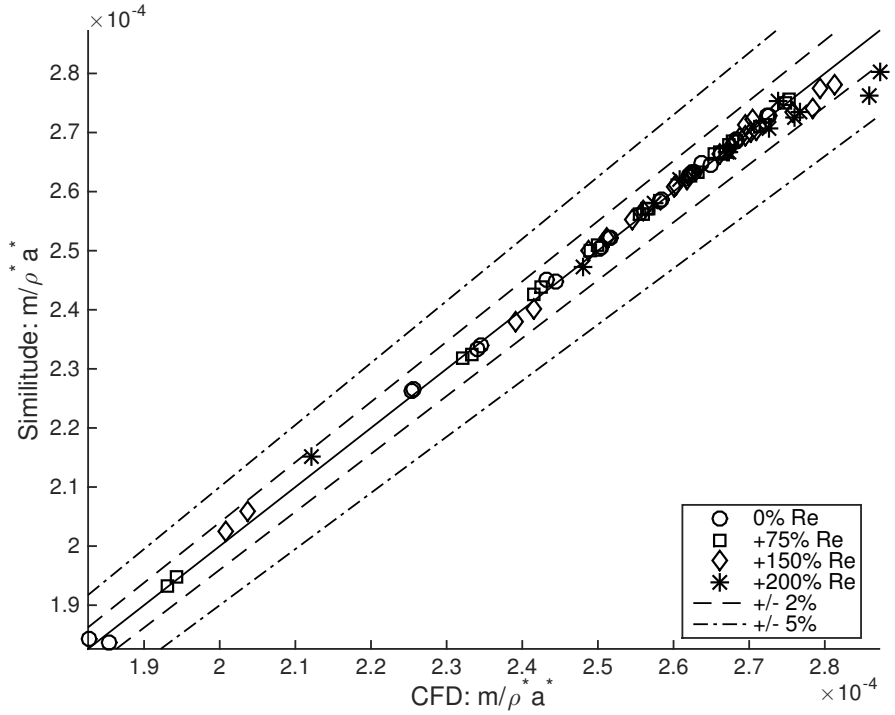

Figure 5.21: Comparison between the flow coefficient predicted by the updated similitude theory and the flow coefficient from the CFD results for the R1234yf operating points.

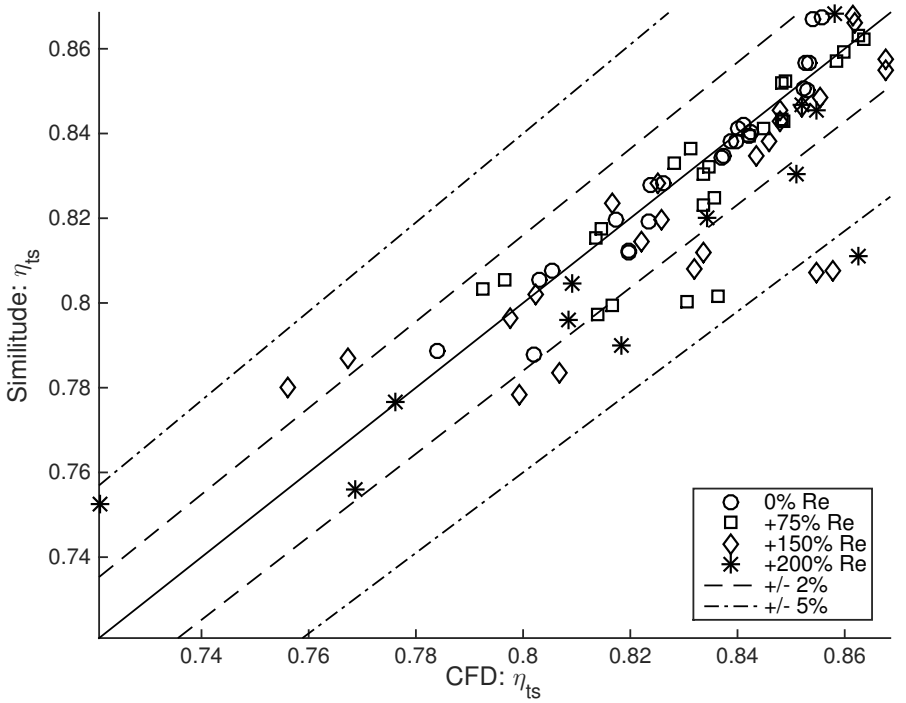

Figure 5.22: Comparison between the isentropic total-to-static isentropic efficiency predicted by the updated similitude theory and the efficiency found from the CFD results for the R1234yf operating points.

To improve the accuracy of similitude theory at higher deviations in the Reynolds number a modified similitude theory has been suggested. This model uses the flow conditions at the stator throat instead of the total inlet conditions. This modification was implemented to conserve the choked mass flow rate. This new formulation provided accurate predictions right up to the choking flow coefficient to within $\pm 2\%$ for all cases considered. As the head coefficient exceeds the choked conditions, deviations are introduced due to the presence of supersonic flow. However, at these conditions, the turbine was found to operate at more extreme off-design conditions suggesting that it would be more suitable to implement an alternative turbine design. It has been concluded that within the range of operating conditions that would be considered sensible operating points for this turbine within an ORC, similitude theory can successfully predict the turbine performance.

The proposed similitude theory analysis was then repeated for two more working fluids, namely R123 and R1234yf, and the same results were found, thus validating the updated similitude theory for the three working fluids considered. However, future work should extend this analysis to confirm its suitability to a wider range of organic fluids and, in particular, working fluids used within higher temperature ORC applications. It should also be extended to consider a variety of turbine geometries, designed for higher pressure ratios operating under supersonic conditions.

Chapter 6

Implementation of turbine performance map

6.1 Introduction

Throughout this research the distinction between designing optimal components for a particular application, and optimising existing components to obtain the best performance has been discussed. Generally, the former may lead to high cost, bespoke systems. However, for an ORC system to be economically viable for small-scale applications it is reasonable to assume that the same system must be implemented within a number of different applications. This allows the key component, the turbine, to be manufactured on a relatively large scale but then implemented into a range of different cycles. In this instance cycle analysis should be coupled to turbine models to account for off-design performance, where the search for optimal cycle conditions may move the turbine performance away from design conditions.

The chapter builds on the previous three chapters by implementing the modified similitude theory developed in Chapter 5 within a cycle analysis model similar to that presented in Chapter 3. The aim of this chapter is to confirm the suitability of implementing the candidate turbine design, developed in Chapter 4, within a number of different ORC applications, utilising a range of different heat source conditions. Not only will this further validate the suitability of the developed turbine, but it will also demonstrate whether the economy of scale of small-scale ORC systems can be improved.

Within this chapter the developed model is summarised before considering a partic-

ular case study. After demonstrating how the model can be used to obtain the optimal operating point for a given heat source and working fluid, the model is ran for a range of heat source temperatures and working fluids and the range of potential applications for this candidate turbine is established. This chapter is also supported by a conference paper, presented at the 9th International Conference on Compressors and their Systems (White and Sayma, 2015c)

6.2 Turbine modelling

The performance of the candidate turbine was analysed in Chapter 5, and the non-dimensional performance maps were constructed. Having validated that these performance maps can be used when the operating conditions and working fluid changes it is now suitable to use this performance map within further optimisation studies. However it should be noted that this performance map was generated using CFD simulations that consisted of the stator, rotor and the shroud clearance gap only. As noted previously, any total pressure losses upstream of the stator leading edge, or downstream of the rotor trailing edge have been neglected. Furthermore parasitic losses such as windage loss behind the rotor back face have also been ignored. Before completing further cycle analysis studies it is therefore important to account for such losses and adjust the performance map accordingly.

6.2.1 Windage losses

Windage loss is a parasitic loss that absorbs some of the work produced by the rotor, thereby reducing the turbine efficiency and the power produced. For the rotating rotor a clearance gap must exist behind the rotor back face and the rotor casing, and within this clearance space the circulation of fluid and the development of boundary layers on the rotor and casing walls result in a loss mechanism.

The power lost due to windage W_{w} is approximated using Equation 6.1, where C_{w} is a torque loss coefficient, ρ_4 is the density at the rotor inlet, ω is the rotational speed in rad s^{-1} and r_4 is the rotor inlet radius. This power loss can then be expressed as an

enthalpy loss Δh_{w} by dividing by the mass flow rate $\dot{m}$.

$$W_{\mathrm{w}} = \frac{1}{2} C_{\mathrm{w}} \rho_4 \omega^3 r_4^5 \tag{6.1}$$

$$\Delta h_{\mathrm{w}} = \frac{W_{\mathrm{w}}}{\dot{m}} \tag{6.2}$$

In order to determine the torque loss coefficient C_{w}, Glassman (1972) completed a comprehensive study on windage losses, and found that four different flow regimes can occur. These are laminar and turbulent flow, both with merged and separated boundary layers respectively. The flow within the clearance gap is laminar for $\mathrm{Re} < 10^5$, and turbulent for $\mathrm{Re} > 10^5$, where Re is the rotational Reynolds number and is determined from Equation 6.3.

$$\mathrm{Re} = \frac{\rho_4 u_4 r_4}{\mu_4} \tag{6.3}$$

The ratio of the clearance gap to the turbine inlet radius establishes whether the boundary layers are merged or separated, with small ratios corresponding to the merged case, and larger ratios corresponding to the separated case. Again, following from Dixon (2010), the clearance gap was assumed to be 0.4mm. The turbine inlet radius is 33.34 mm resulting in a clearance gap to radius radius of 0.012, which is sufficiently small to assume merged boundary layers. For this candidate turbine the Reynolds number at the design point is $\mathrm{Re} = 8.36 \times 10^6$, and therefore the flow is fully turbulent. For this case C_{w} is given by Equation 6.4, where ϵ is the specified clearance gap (Glassman, 1972).

$$C_{\mathrm{w}} = \frac{0.0622}{\left(\frac{\epsilon}{r_4}\right)^{\frac{1}{4}} \mathrm{Re}^{\frac{1}{4}}} \tag{6.4}$$

6.2.2 Diffuser design

Within radial turbine design it is often beneficial to employ a diffuser downstream of the rotor to reclaim some of the kinetic energy contained with the flow, reducing the flow velocity whilst increasing the static pressure. The design and analysis work completed thus far has not considered the effect of a diffuser. Therefore it is necessary to first design a diffuser with a suitable area ratio, based on the original turbine design point, before considering how this diffuser performs during off-design.

For this analysis a simple straight sided, conical diffuser has been defined, and the notation used to describe this geometry is shown in Figure 6.1. The diffuser geometry is controlled by two design parameters, the area ratio $A_{\mathrm{R}} = A_7/A_6$, and the diffuser divergence angle θ. The diffuser divergence angle is a critical parameter governing diffuser performance, and Aungier (2006) suggested that optimal performance is obtained when $2\theta = 11°$. For a specified area ratio A_{R}, and the known rotor outlet dimensions r_6 and b_6, the diffuser outlet dimensions r_7 and b_7, and the volute axial length z, and flow path length L can be easily determined after some simple algebra.

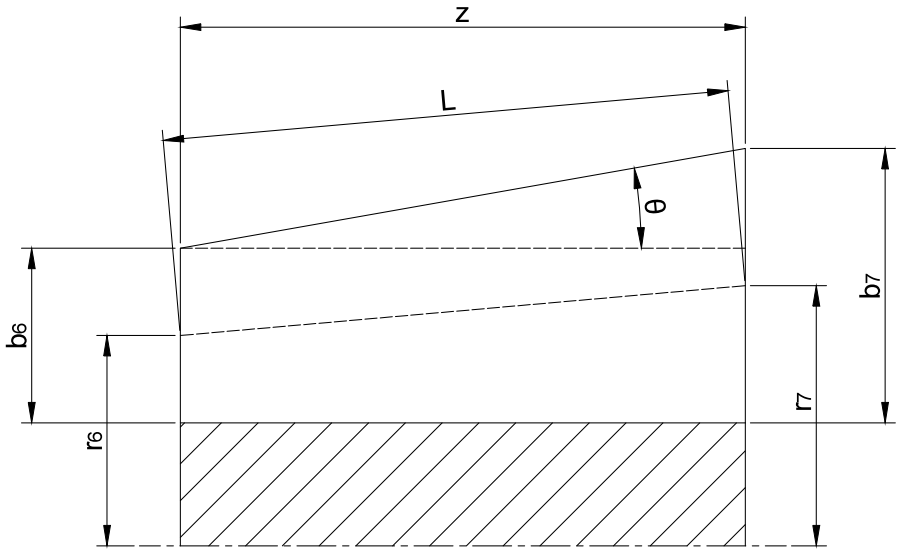

Figure 6.1: Schematic of the defined diffuser geometry.

It should be noted that here the subscript '6' has been used to describe the rotor outlet, whilst in Chapter 4 the rotor outlet was described using the subscript '5'. The reason for this is to account for the abrupt area expansion that occurs at the rotor trailing edge. Locations 5 and 6 therefore refer to the fluid conditions immediately before and after this abrupt area change. Since both locations refer to the same location it is inferred that $r_6 = r_5$ and $b_6 = b_5$. Across this sudden change in area the tangential velocity component and total enthalpy will remain the same, i.e $c_{\theta 6} = c_{\theta 5}$ and $h_{06} = h_{05}$. However the meridional velocity will suddenly reduce, and this will be accompanied with a total pressure loss. This total pressure loss is accounted for by the total pressure loss coefficient, Y, and is given by Equation 6.5 (Aungier, 2006). Here α, P_0 and P represent the absolute flow angle, total pressure and static pressure respectively, and BK_5 is the blockage factor at the rotor outlet. The subscript $6'$ corresponds to the conditions that would result if

the abrupt area expansion was isentropic (i.e. $P_{06'} = P_{05}$), and these conditions can be determined by applying an iterative mass balance using the known flow area. The use of Equation 6.5 to arrive at the final conditions downstream of the rotor trailing edge also requires iteration, with an initial guess of $P_{06} = P_{05}$.

$$Y = \left[\frac{1}{(1 - \mathrm{BK}_5)} \cos \alpha_{6'}^2\right]^2 \left(\frac{P_{06'} - P_{6'}}{P_{06} - P_6}\right) \tag{6.5}$$

Considering the turbine design completed in Chapter 4, the design point conditions at the rotor outlet correspond to $T_{05} = 327.47$ K, $P_{05} = 259.62$ kPa, $c_5 = 39.23$ m s^{-1}, and $\alpha_5 = 0.00°$. Using these conditions, and the known rotor outlet geometry, Equation 6.5 can be used to determine the fluid conditions immediately downstream of the rotor trailing edge. With these known conditions a parametric study over a range of diffuser area ratios A_R was then completed to establish the most suitable diffuser geometry for this turbine. For a range of values for A_R the diffuser geometry was constructed according to Figure 6.1. The diffuser performance analysis described in the next section (Section 6.2.3) was then completed. The results from this study are shown in Figure 6.2. The top plot displays the resulting diffuser geometry as viewed on the meridional plane, whilst the bottom plot shows how the total-to-total and total-to-static efficiencies change with an increasing diffuser area ratio.

From Figure 6.2 it is clear that an increasing area ratio results in a larger diffuser, and an increased total-to-static turbine efficiency. This was to be expected as an increasing area must be accompanied with a reduction in the flow velocity, and an increase in static pressure. As with any real flow process the diffusion process is not isentropic, leading to a slight reduction in the turbine total-to-total efficiency. Furthermore, as the area ratio increases, the diffuser flow path length must increase resulting in a thicker boundary layer at the diffuser discharge. This explains why the total-to-total efficiency continues to fall as the diffuser area ratio is increased. From Figure 6.2 it is evident that the majority of the energy recovery occurs for an area ratio below 2.5. The baseline value for η_ts without a diffuser was 85.76%. For $A_\mathrm{R} = 2.5$, this increases to 88.14% corresponding to an increase of 2.38%. By comparison, for $A_\mathrm{R} = 4$ this increases to 88.39% which is only a 0.15% increase in the overall turbine total-to-static efficiency compared to an A_R of 2.5. Clearly the increased diffuser length it not justified. Proceeding with this analysis, a diffuser area

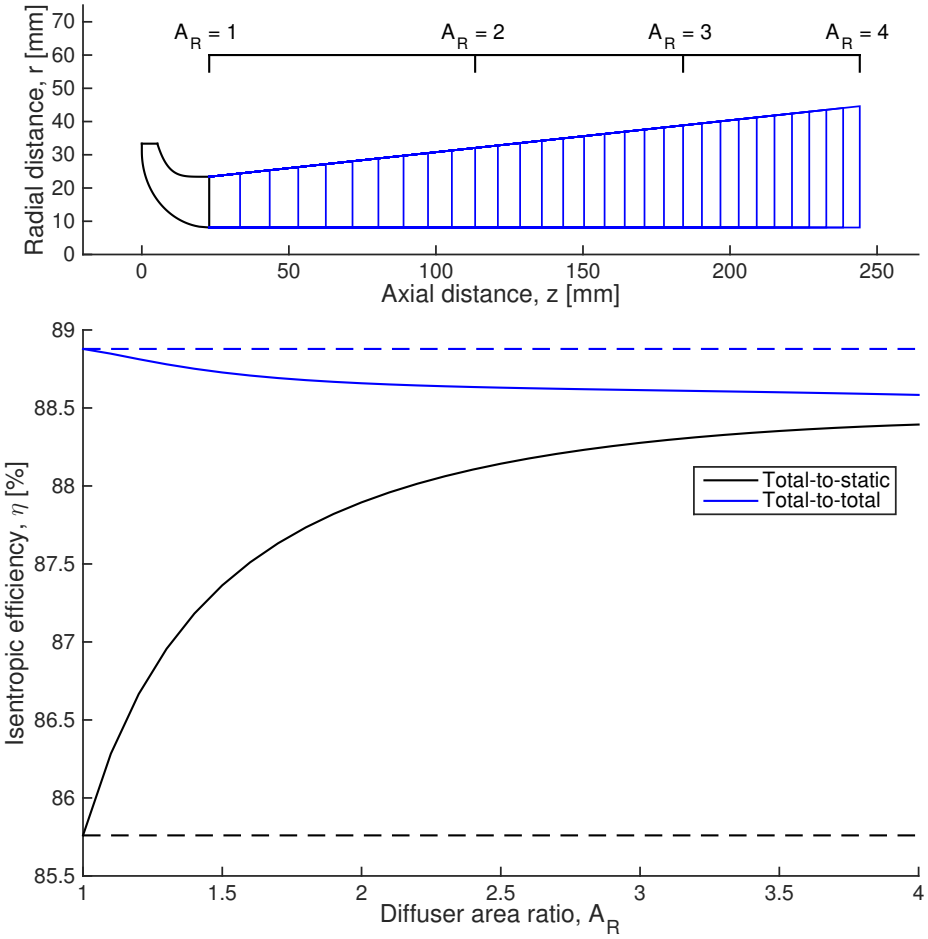

Figure 6.2: Parametric study on the effect of the diffuser area ratio on turbine performance.

ratio of $A_{\mathrm{R}} = 2.5$ has been selected for this candidate turbine.

It is worth pointing out that the analysis conducted within this section is based on a diffuser model developed mainly for ideal gas turbines, and therefore the suitability of these models for organic fluids has not been validated. It would therefore be interesting to investigate the suitability of these models in more detail in the future. Having said this, in Chapter 5 it was shown that the compressibility factor reduces as the critical point is approached. Therefore at the turbine outlet, after the expansion, the compressibility factor will be closer to 1, and the fluid behaviour may be closer to that of an ideal gas.

6.2.3 Diffuser performance analysis

The diffuser performance analysis consists of an empirical correlation used to calculate the boundary layer blockage at the diffuser discharge, and is implemented according to

Aungier (2006). The diffuser blockage Δ is given by Equation 6.6

$$\Delta = [K_1 + K_2(D-1)] \frac{LA_6}{A_7 b_6} \tag{6.6}$$

Where,

$$K_1 = 0.005 + \frac{K_\theta - 1}{5} \tag{6.7}$$

$$K_2 = \frac{2\theta \left(1 - \frac{2\theta}{22K_\theta}\right)}{125K_\theta} \tag{6.8}$$

$$D = \frac{(\sqrt{P_{\text{vr}}} + 1)^2}{4} \tag{6.9}$$

For optimal conditions, corresponding to $2\theta = 11°$, $K_\theta = 1$. P_{vr} is the ideal diffuser pressure ratio and is defined by Equation 6.10, where $P_{7'}$ is the static pressure at the diffuser discharge following an isentropic diffusion process and assuming no blockage. This can be obtained by performing an iterative mass balance at the diffuser discharge assuming $P_{07} = P_{06}$, $h_{07} = h_{06}$, $\Delta = 0$, and applying conservation of angular momentum ($r_6 c_{\theta 6} = r_7 c_{\theta 7}$).

$$P_{\text{vr}} = \frac{P_{06} - P_6}{P_{07} - P_{7'}} \tag{6.10}$$

Once Δ is known the mass balance can be repeated accounting for the loss in geometrical area, and the actual static pressure at the diffuser discharge, P_7, is determined. The total pressure that corresponds to this static pressure can then be determined after some iteration.

6.2.4 Updated turbine performance map

Using the loss models described in the previous subsections, the non-dimensionalised turbine performance map obtained in Chapter 5 can now be updated to account for these additional losses. To do so the turbine inlet conditions were set to the original design point, corresponding to $T_{01} = 350$ K and $P_{01} = 623.07$ kPa, and the turbine performance reevaluated over a range of operating conditions. Since turbine performance is being considered within a closed thermodynamic cycle the performance map will be evaluated in terms of the total-to-total conditions instead of the total-to-static. However, since the diffuser

loss model requires details on the static conditions at the rotor outlet, the total-to-static performance map is also required, but for this analysis only.

Firstly, to account for losses upstream of the stator leading edge, a total pressure drop of $\Delta P_{\mathrm{v}} = 1\%$ was assumed within the volute. This immediately determined the total conditions at the stator inlet.

$$P_{02} = P_{01}(1 - \Delta P_{\mathrm{v}}) \tag{6.11}$$

$$[T_{02}, s_{02}, \rho_{02}, a_{02}] = \mathrm{EoS}(P_{02}, h_{01}, \mathrm{fluid}) \tag{6.12}$$

Since the performance map was obtained without taking the volute into account, it should be noted that the turbine performance map applies to these updated stator inlet conditions (location 2) instead of the original design inlet conditions (location 1). Therefore the choked throat static conditions, a^* and ρ^*, should be obtained by assuming an isentropic expansion from location 2 to the stator throat. An array of head coefficients ranging from 0 to 1.6 can then be constructed, and this can be converted into the isentropic total-to-total enthalpy from the stator inlet to the rotor outlet. At each head coefficient the working fluid mass flow rate, total-to-total efficiency and total-to-static efficiency, can all be established at 50%, 80%, 100%, 120% and 150% of the design rotational speed through interpolation of the turbine performance map.

With the performance data known, the total conditions at the rotor outlet can be obtained. It should be stated that the results from the CFD analysis used to construct the performance maps were taken slightly downstream of the rotor trailing edge. These results therefore correspond to location 6 so the abrupt expansion loss at the rotor trailing edge has already been taken into consideration. The total conditions are therefore as follows:

$$h_{06\mathrm{ss}} = h_{02} - \Delta h_{0\mathrm{ss}} \tag{6.13}$$

$$P_{06} = \mathrm{EoS}(h_{06\mathrm{ss}}, s_{02}, \mathrm{fluid}) \tag{6.14}$$

$$h_{06} = h_{02} - \eta_{\mathrm{tt}}(h_{02} - h_{06\mathrm{ss}}) \tag{6.15}$$

$$s_{06} = \mathrm{EoS}(P_{06}, h_{06}, \mathrm{fluid}) \tag{6.16}$$

The known enthalpy drop and total-to-static efficiency, can then be used to determine

the static conditions at the rotor outlet.

$$\Delta h_{\mathrm{ss}} = \frac{h_{02} - h_{06}}{\eta_{\mathrm{ts}}} \tag{6.17}$$

$$h_{6\mathrm{ss}} = h_{02} - \Delta h_{\mathrm{ss}} \tag{6.18}$$

$$P_6 = \mathrm{EoS}(h_{6\mathrm{ss}}, s_{02}, \mathrm{fluid}) \tag{6.19}$$

$$[h_6, \rho_6] = \mathrm{EoS}(P_6, s_{06}, \mathrm{fluid}) \tag{6.20}$$

With the known total and static enthalpy the absolute velocity c_6 can be determined. Furthermore, a mass balance with the known static density ρ_6 supplies the meridional velocity $c_{\mathrm{m}6}$, which in turn supplies the tangential velocity $c_{\theta 6}$ and absolute flow angle α_6. The diffuser loss model, described in Section 6.2.3, can then be applied using the diffuser geometry that corresponds to a diffuser area ratio of $A_{\mathrm{R}} = 2.5$. This then supplies the total and static conditions at the diffuser discharge. Finally the windage model, described in Section 6.2.1 can be applied to determine the enthalpy loss Δh_{w}.

The isentropic total-to-total and total-to-static enthalpy drops can now be recalculated considering the upstream and downstream pressure losses. These are now the enthalpy drops associated with an isentropic expansion from the defined inlet conditions (T_{01}, P_{01}) to the diffuser discharge total and static pressures pressures respectively.

$$h_{07\mathrm{ss}} = \mathrm{EoS}(P_{07}, s_{01}, \mathrm{fluid}) \tag{6.21}$$

$$h_{7\mathrm{ss}} = \mathrm{EoS}(P_7, s_{01}, \mathrm{fluid}) \tag{6.22}$$

$$\Delta h_{0\mathrm{ss}} = h_{01} - h_{07\mathrm{ss}} \tag{6.23}$$

$$\Delta h_{\mathrm{ss}} = h_{01} - h_{7\mathrm{ss}} \tag{6.24}$$

The isentropic total-to-total and total-to-static efficiencies can now be reformulated accounting for the windage loss and are given as follows.

$$\eta_{\mathrm{tt}} = \frac{(h_{01} - h_{07}) - \Delta h_{\mathrm{w}}}{\Delta h_{0\mathrm{ss}}} \tag{6.25}$$

$$\eta_{\mathrm{ts}} = \frac{(h_{01} - h_{07}) - \Delta h_{\mathrm{w}}}{\Delta h_{\mathrm{ss}}} \tag{6.26}$$

The choked flow parameters, a^* and ρ^*, associated with the turbine inlet conditions can then be obtained iteratively, and the performance map can be non-dimensionalised

according to the updated similitude theory (Equation 5.18). The final performance maps are shown in Figures 6.3 and 6.4, where they are also compared to the original performance data obtained from the CFD simulations.

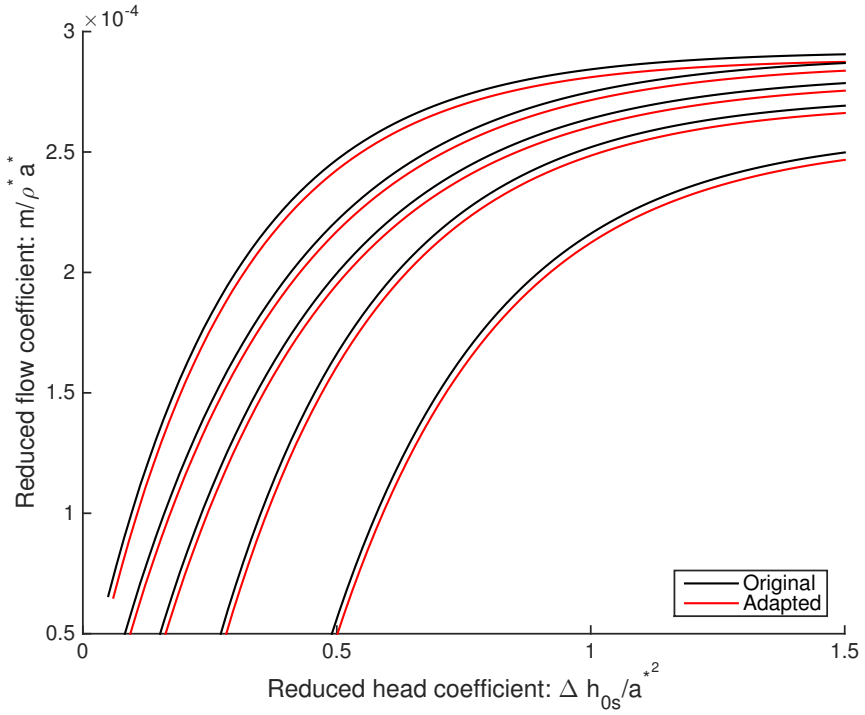

Figure 6.3: Updated turbine performance map showing relationship between the reduced head coefficient and reduced flow coefficient for different reduced rotational speeds.

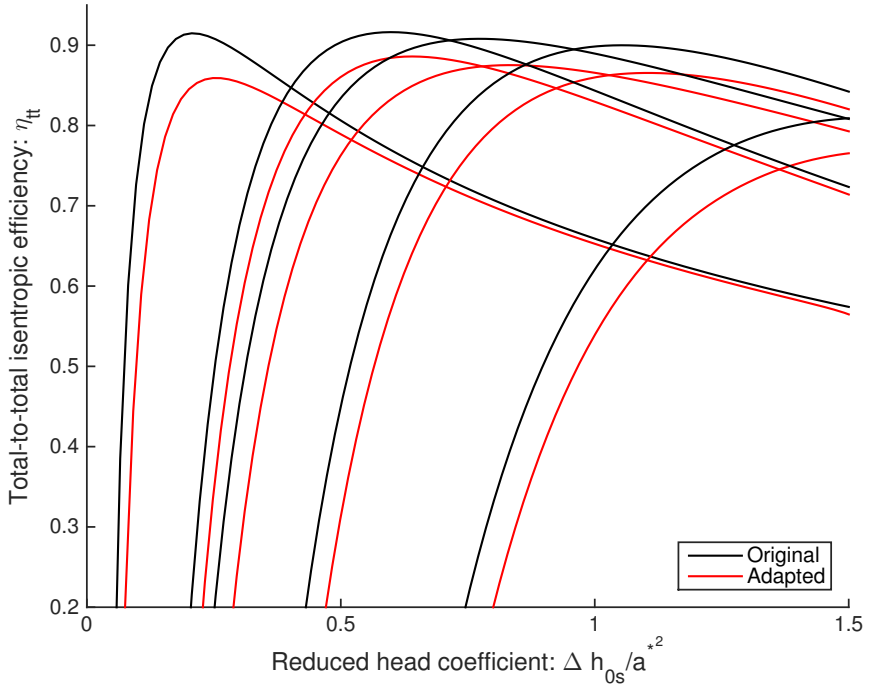

Figure 6.4: Updated turbine performance map showing relationship between the reduced head coefficient and turbine efficiency for different reduced rotational speeds.

6.3 Thermodynamic modelling

A simple thermodynamic model has been developed which can be used to investigate the range of operating conditions where the developed candidate turbine could be effectively utilised within an ORC. The aim of this model is to determine, when supplied with a heat source at a particular temperature, the optimal heat source mass flow rate that can be effectively converted into useful power using this existing turbine. Following from Chapter 3 a simple subcritical ORC without a regenerator has been considered. Not only does this simplify the analysis, but it would also ease manufacture and reduce the overall cost of the system. Furthermore, since the main focus within this chapter is to investigate the interaction between turbine performance and cycle performance, additional aspects such as the required heat transfer areas, and the pump performance are not considered.

The thermodynamic modelling follows that outlined in Section 3.3.1, with the working fluid properties at the pump inlet, evaporator inlet and turbine inlet being calculated based on a specified condensation temperature T_{w1}, pressure ratio PR, and amount of superheat ΔT_{sh}. The required heat transfer areas are not considered within this analysis, so the evaporator model is restricted to a simple energy balance when supplied with the evaporator pinch point $\mathrm{PP_h}$. Since the aim of this analysis is to determine the optimal heat source mass flow rate at a given heat source temperature that can be converted into power using this turbine, the heat source mass flow rate is unknown. However, for specified ORC conditions, the ratio of the working fluid mass flow rate $\dot{m}_{\mathrm{w}}$, to the heat source mass flow rate $\dot{m}_{\mathrm{h}}$ can be determined and is given by Equation 6.27, where the subscripts have the meanings outlined in Figure 3.2.

$$\frac{\dot{m}_{\mathrm{w}}}{\dot{m}_{\mathrm{h}}} = \frac{h_{\mathrm{h1}} - h_{\mathrm{h3}}}{h_{\mathrm{w3}} - h_{\mathrm{w2'}}} \tag{6.27}$$

With the turbine inlet conditions defined, T_{w3} and P_{w3}, the choked flow conditions, a^* and ρ^* can be obtained. The outlet pressure P_{w4} defined by the ORC pressure ratio then provides the reduced head coefficient $(h_{\mathrm{w3}} - h_{\mathrm{w4s}})/a^{*^2}$. Referring to Figure 6.3, this value of the head coefficient allows the minimum and maximum flow coefficients to be obtained, which correspond to the minimum and maximum rotational speeds. These minimum and maximum flow coefficients can be converted into the physical mass flow rate limits for the turbine and an array of mass flow rates is constructed between these two

limits. Then, for each value of $\dot{m}_{\mathrm{w}}$, the reduced rotational speed can be obtained through interpolation Figure 6.3. The reduced flow coefficient and reduced rotational speed then supplies the turbine efficiency η_{t} through interpolation of Figure 6.4, which then leads to the determination of the turbine outlet conditions. For each value of $\dot{m}_{\mathrm{w}}$, $\dot{m}_{\mathrm{h}}$ is supplied by Equation 6.27. Ultimately, the result of this model is that for specified values for T_{w1}, PR, ΔT_{sh} and PP_{h} there is a range of heat source mass flow rates that can be accommodated using this existing turbine design.

To complete the analysis, an energy balance within the condenser is completed, assuming a condenser pinch point PP_{c}, which in turn provides the required cooling mass flow rate. Having completed the cycle analysis, the performance of the cycle is assessed in terms of the net power produced W_{n}, and the ORC thermal efficiency η_{o}.

Although evaluating the cycle performance in terms of the net power and cycle efficiency is useful, it does not give a clear indication of whether implementing the candidate turbine within a particular application is a feasible solution. In other words, could the system performance be improved if an alternative turbine was implemented? To do this an additional comparison has been introduced which compares the net power produced by the turbine to the maximum net power that could be produced using the same heat source with a turbine operating at an optimal efficiency. For fixed values of T_{w1}, ΔT_{sh} and PP_{h}, with a fixed heat source temperature and mass flow rate, there exists an optimal pressure ratio at which optimal power can be produced. This optimum exists because, whilst a higher pressure increases the cycle efficiency, a higher pressure ratio must also lead to a higher evaporation temperature. A higher evaporation temperature leads to a smaller temperature drop within the heat source, leading to a smaller ORC mass flow rate. Since the net work is the product of the net power per unit mass and the mass flow rate, there is a trade-off between maximising the cycle efficiency, and maximising the amount of heat that is absorbed by the working fluid.

This optimal pressure ratio and corresponding net power has been investigated and the results are shown in Figure 6.5 for a range of heat source conditions. Here the following assumptions have been made: $T_{\mathrm{w1}} = 313$ K, $\Delta T_{\mathrm{sh}} = 10$ K, $\mathrm{PP}_{\mathrm{h}} = 15$ K, $\eta_{\mathrm{p}} = 70\%$ and $\eta_{\mathrm{t}} = 85\%$. The top graph shows how the optimum changes for a range of heat source temperatures, all with a fixed heat source mass flow rate of $\dot{m}_{\mathrm{h}} = 1.0$ kg s^{-1}. Clearly as the heat source temperature rises the optimal pressure ratio increases, as expected. The

bottom graph shows that for a fixed heat source temperature of $T_{h1} = 380$ K, the optimum changes with changes in the heat source mass flow rate. Evidently, the optimal pressure ratio is independent of the heat source mass flow rate, and the net power increases linearly with increasing heat source mass flow rate. Therefore when supplied with a heat source flow rate and heat source temperature Figure 6.5 can be used to obtain the maximum potential power that could be obtained for a turbine operating with a fixed efficiency of $\eta_t = 85\%$. Here, 85% was selected as a maximum turbine efficiency as this was considered to be an achievable target at design point. It should be noted that when comparing the actual net power produced by the turbine to the maximum power, if the actual power is greater, this is the result of the turbine operating at a higher efficiency than 85%.

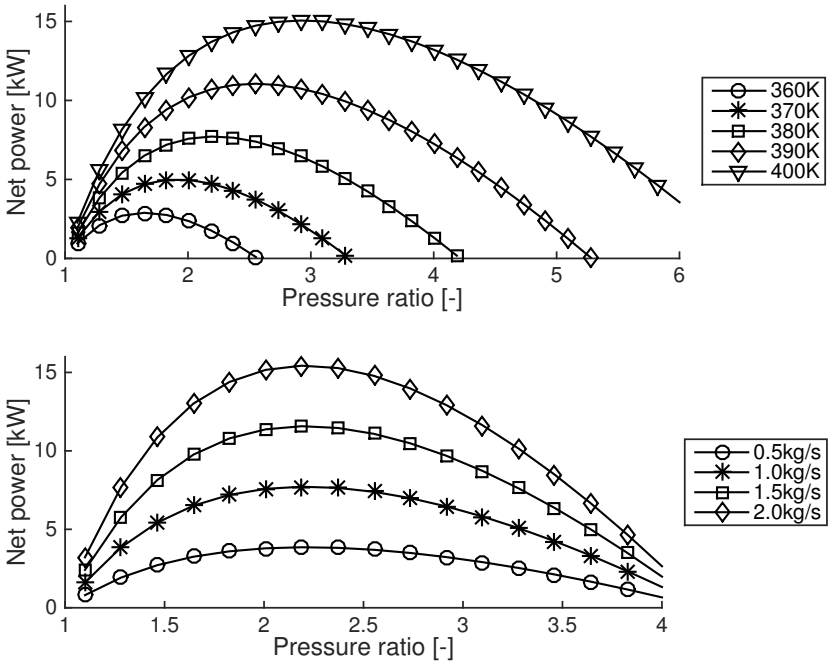

Figure 6.5: Variation in net power produced as a function of pressure ratio for different heat source conditions. Top: fixed heat source mass flow rate of 1.0kg/s; Bottom: fixed heat source temperature of 380K.

6.4 R245fa case study

To demonstrate the model described in the previous section a case study has been considered. A low temperature heat source of pressurised water at $T_{h1} = 380$ K and $P_h = 400$ kPa has been defined and the ORC working fluid has been kept as the original turbine

design working fluid, namely R245fa. A number of the ORC thermodynamic variables have been fixed according to the values listed in Table 6.1. This is because the focus of this investigation is on the turbine performance and therefore the impact of variations in pump and heat exchanger performance, although important, have been neglected. T_{w1} and PP_c dictate the condenser area and the heat sink mass flow rate. The heat sink temperature is set at $T_{c1} = 288$ K, whilst setting $T_{w1} = 313$ K and $PP_c = 10$ K corresponds to an approximate 15 K rise in the heat sink temperature through the condenser. The value for PP_h has been estimated to be 15 K; both pinch points dictate the size of the heat exchangers, and represent a trade-off between performance and cost. The values selected have been found to provide a reasonable balance between these two aspects. It has been widely shown that superheating is not necessary for organic fluids, but a small superheat of $\Delta T_{sh} = 2$ K has been selected to ensure that the fluid is fully vaporised at the turbine inlet. This is included as a safety margin since expansion within the stator would in fact prevent droplets from entering the rotor. However, the inclusion of a small superheat is not expected to impact the final results. Since the pump work is much smaller than the turbine work the impact of variations in pump efficiency are expected to be negligible; therefore the pump efficiency is assumed to be constant at $\eta_p = 70\%$.

Table 6.1: Fixed inputs for the R245fa case study.

Parameter		Value	Units
Heat source fluid		water	
Heat source temperature	T_{h1}	380	K
Heat source pressure	P_h	400	kPa
Heat sink fluid		water	
Heat sink temperature	T_{c1}	288	K
Heat sink pressure	P_c	101	kPa
Pump isentropic efficiency	η_p	70	%
Condensation temperature	T_{w1}	313	K
Amount of superheat	ΔT_{sh}	2	K
Evaporator pinch point	PP_h	15	K
Condenser pinch point	PP_c	10	K

With the fixed inputs in Table 6.1 defined the ORC model was then run over a range of ORC pressure ratios, and a range of possible working fluid mass flow rates were established at each pressure ratio. At each combination of working fluid mass flow rate and pressure ratio the corresponding heat source flow rate was then calculated allowing the maximum

potential power for that heat source mass flow rate to be obtained. The result of this analysis is a performance map that shows the variation of the net power, as a percentage of the maximum potential power, with pressure ratio and $\dot{m}_{\mathrm{w}}$ (Figure 6.6). The black lines, overlaid on the contour plot, indicate the resulting heat source mass flow rate in kg s^{-1}.

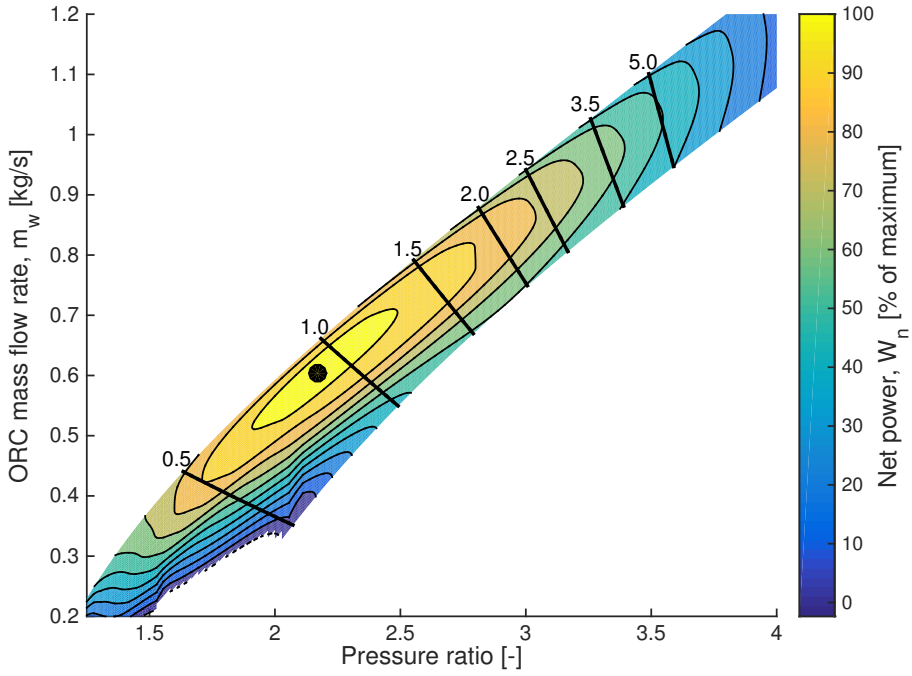

Figure 6.6: Contour of the net power produced by an ORC operating with the candidate turbine as a percentage of the maximum potential power. Heat source of water at 380K, and R245fa as working fluid. The black lines indicate the heat source mass flow rate in kg/s, whilst the black dot represents the point of optimal operation.

Figure 6.6 is useful since, for a specified heat source mass flow rate at 380K, it is easy to assess the feasibility of using this turbine. For example, for a heat source mass flow rate of around 1.0kg/s, with a pressure ratio of 2.2, the turbine efficiency is high and 100% of the maximum potential net power can be achieved. The optimal operating point is shown as a black dot, and this corresponds to PR = 2.17, $\dot{m}_{\mathrm{w}} = 0.60$ kg s^{-1} and $\dot{m}_{\mathrm{h}} = 0.91$ kg s^{-1}. At this operating condition the turbine operates at 88.7% of the design reduced rotational speed (N/a^*), which is well within feasible limits.

Clearly, as the heat source mass flow rate increases or decreases beyond this optimal point, the ORC performance deteriorates leading to a lower percentage of the maximum power being produced. To evaluate this in more detail the performance data shown in

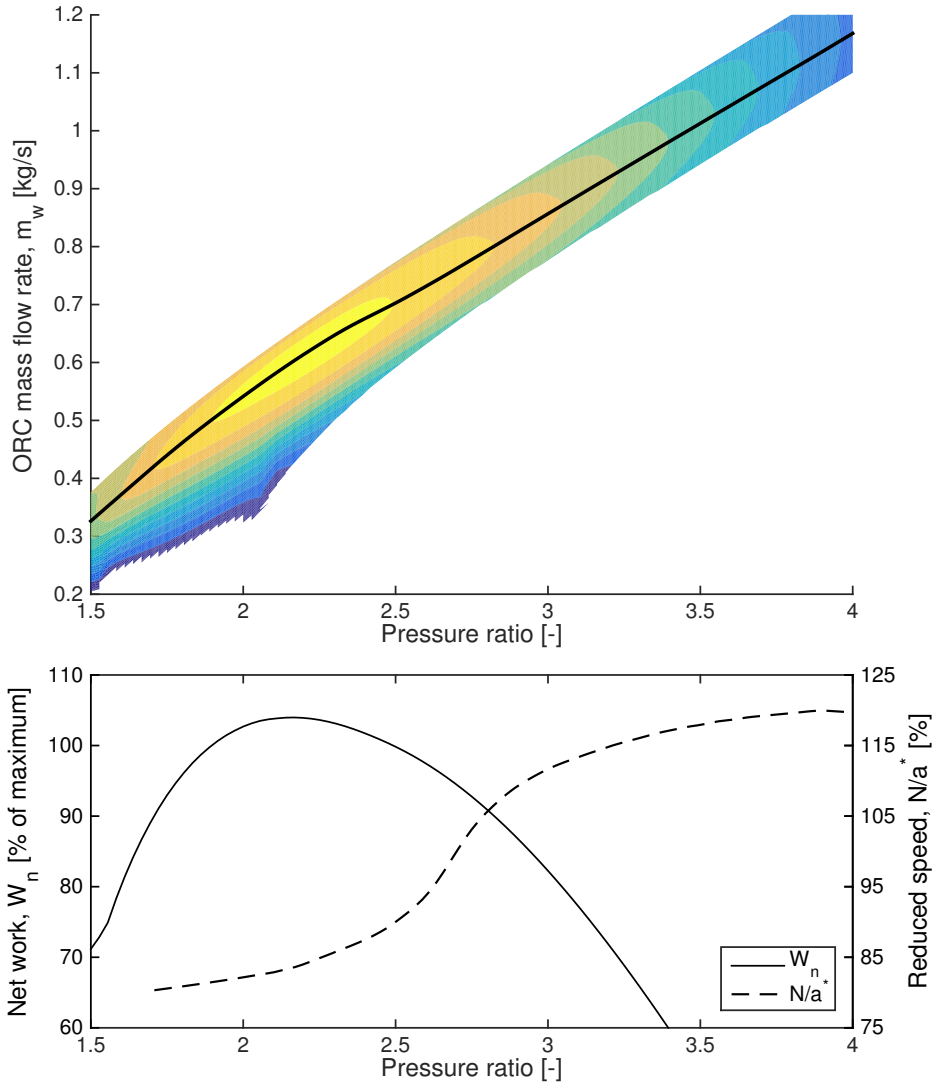

Figure 6.7: The optimal percentage of net work and the corresponding reduced rotational speed for the candidate turbine operating with R245fa for a heat source of 380K over a range of ORC pressure ratios.

Figure 6.6 has been re-analysed to produce Figure 6.7. Here, at each pressure ratio, the operating point that results in the highest percentage of the maximum is obtained, and this results in a single line that cuts across the performance contour as shown by the black line in the top plot of Figure 6.7. The corresponding ORC and heat source mass flow rates, net work as a percentage of the maximum and the reduced rotational speed can then be determined and the latter two of these parameters are shown in the bottom plot. These results show that for this heat source at 380 K, this existing turbine, operating with R245fa, can effectively operate between pressure ratios of around 1.75 and 2.75. This corresponds to heat source mass flow rates between around 0.5 kg s^{-1} and 1.75 kg s^{-1}, whilst the reduced rotational speed of the turbine remains between 80% and

110% of the design value, which is within a feasible range. Within these conditions the net power produced should remain above 90% of the maximum potential power that could be produced. At alternative heat source conditions an alternative turbine design may offer a better performance, and further analysis would be required to establish whether the improved performance would outweigh the increased costs of developing an alternative design.

Although the analysis completed is very useful, the results obtained only apply to one particular heat source temperature. However, in reality to improve the economy of scale of small machines it would be beneficial to employ the same turbine within a range of different applications where both the heat source mass flow rate and heat source temperature may change. The analysis completed thus far has therefore been repeated at heat source temperatures of $T_{\mathrm{h1}} = 360$ K and $T_{\mathrm{h1}} = 400$ K. These temperatures were considered to span the range of feasible heat source temperatures that could be effectively converted into power using this turbine. Below 360 K the cycle efficiency would reduce, significantly impacting the economic feasibility of such a system. Comparatively, above 400 K the pressure ratio would increase, increasing the likelihood of supersonic flows within the stator. For applications such as these it might be more suitable to implement a turbine design with a supersonic stator design. For these two heat source temperatures the same fixed inputs defined in Table 6.1 were selected, and the same analysis was completed over a range of pressure ratios. The results for the 360 K and 400 K cases are shown in Figures 6.8 and 6.9 respectively. Again, the black dots represent the points of optimal operation where the maximum percentage of the maximum power is produced. The operating conditions at these optimal operating points, along with the optimal operating point for the 380 K heat source are summarised in Table 6.2.

As the heat source temperature reduces to 360 K, the optimal pressure ratio, mass flow rate and therefore power output all reduce. At the optimal operating point the power produced is only 3.61 kW. Furthermore, as a result of the low heat source temperature, and the low Carnot efficiency, the thermal efficiency of the cycle is inevitably low at $\eta_{\mathrm{o}} = 4.31\%$. Although the turbine operates under favourable conditions, leading to a high turbine efficiency, and a feasible reduced rotational speed, it is questionable whether such a system would be feasible to implement. These results therefore validate that selecting 360 K as a bottom limit for the heat source temperature was a suitable choice.

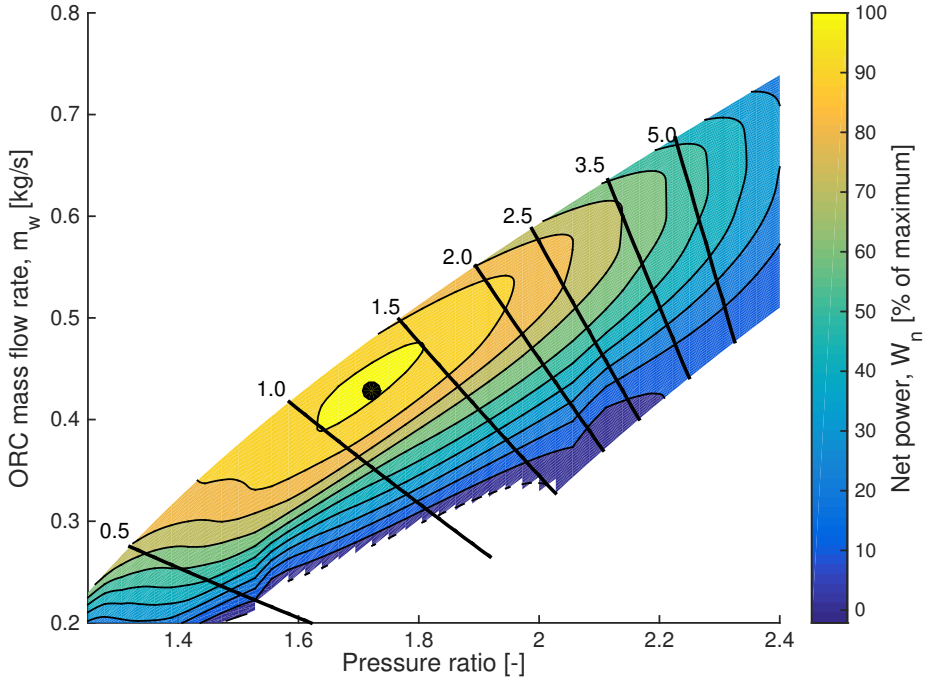

Figure 6.8: Contour of the net power produced by an ORC operating with the candidate turbine as a percentage of the maximum potential power. Heat source of water at 360K, and R245fa as working fluid. The black lines indicate the heat source mass flow rate in kg/s, whilst the black dot represents the point of optimal operation.

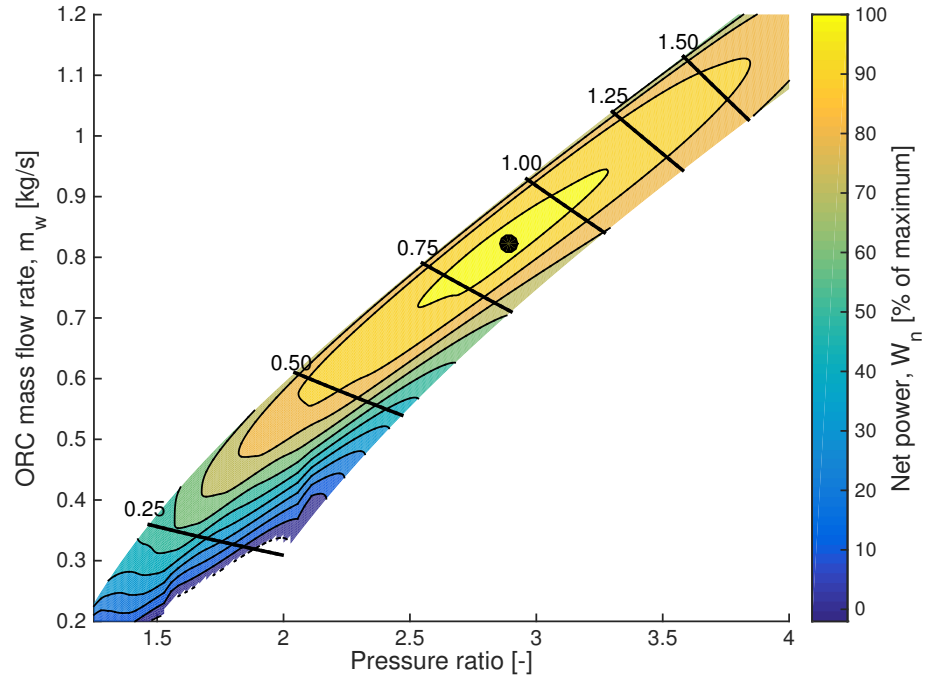

Figure 6.9: Contour of the net power produced by an ORC operating with the candidate turbine as a percentage of the maximum potential power. Heat source of water at 400K, and R245fa as working fluid. The black lines indicate the heat source mass flow rate in kg/s, whilst the black dot represents the point of optimal operation.

Table 6.2: Summary of optimal operating points for R245fa case study.

Heat source temperature	T_{h1}	360	380	400	K
Pressure ratio	PR	1.72	2.17	2.89	
ORC mass flow rate	$\dot{m}_{\mathrm{w}}$	0.43	0.60	0.82	kg s^{-1}
Heat source mass flow rate	$\dot{m}_{\mathrm{h}}$	1.21	0.91	0.86	kg s^{-1}
Turbine rotational speed	N	30,900	32,900	41,900	RPM
Turbine efficiency	η_{t}	87.5	88.3	87.1	%
ORC efficiency	η_{o}	4.31	6.05	7.91	%
Net power	W_{n}	3.61	7.36	13.56	kW
Net power/max. power	$W_{\mathrm{n}}/W_{\mathrm{max}}$	102.2	104.0	102.5	%
Reduced head coefficient	$\Delta h_{\mathrm{s}}/a^{*2}$	0.54	0.77	1.07	
Reduced flow coefficient	$\dot{m}_{\mathrm{w}}/\rho^{*}a^{*}$	2.21	2.50	2.56	$\times 10^{-4}$
Reduced rotational speed	N/a^{*}	227.4	242.7	310.2	

For the higher heat source temperature of 400 K the results are much more favourable. The optimal operating point corresponds to a pressure ratio of 2.89, whilst the increasing heat source temperature results in a higher Carnot efficiency, and a higher thermal of efficiency of $\eta_{\mathrm{o}} = 7.91\%$. The net power from the cycle is also higher at 13.56 kW, which is much more in line with the intended power production at the original design point. The turbine efficiency is again high, leading to around 100% of the maximum power being produced, thus suggesting that the performance of this cycle could not be improved by considering alternative expander designs. At the optimal operating point the reduced rotational speed is around 113% of the design reduced speed. The flow coefficient is also approaching the choked flow coefficient, confirming that the turbine would be approaching choked operation.

Referring to Table 6.2 the flow coefficient and reduced rotational speed both increase as the heat source temperature increases. This was expected, but suggests that any further increase in heat source temperature would result in an even larger flow coefficient and reduced rotational speed. At these conditions the turbine operation may no longer be feasible, requiring alternative turbine designs to be considered. This therefore supports the selection of 400 K as a maximum heat source temperature.

Overall, the results obtained for the three heat source temperatures have shown that this turbine, operating with R245fa, could be effectively utilised in different ORC applications with heat source temperatures ranging between 360 K and 400 K. To ensure optimal operation the heat source mass flow rate should be between 0.82 kg s^{-1} and 1.21 kg s^{-1}.

To estimate performance away from the optimal operating points, the method described in relation to Figure 6.7 can be repeated for the other heat source temperatures. Alongside these temperatures, the analysis can also repeated for an even greater number of heat source temperatures and this leads to production of Figure 6.10. At each heat source temperature the black line shown in the top plot of Figure 6.7 is obtained, and the variation in heat source mass flow rate and the reduced rotational speed along each line is obtained. This allows the net power, as a percentage of the maximum, to be presented on a contour plot as a function of heat source temperature and heat source mass flow rate. The black lines overlaid onto this plot are the constant speed lines ranging between 80% and 120% of the design reduced rotational speed.

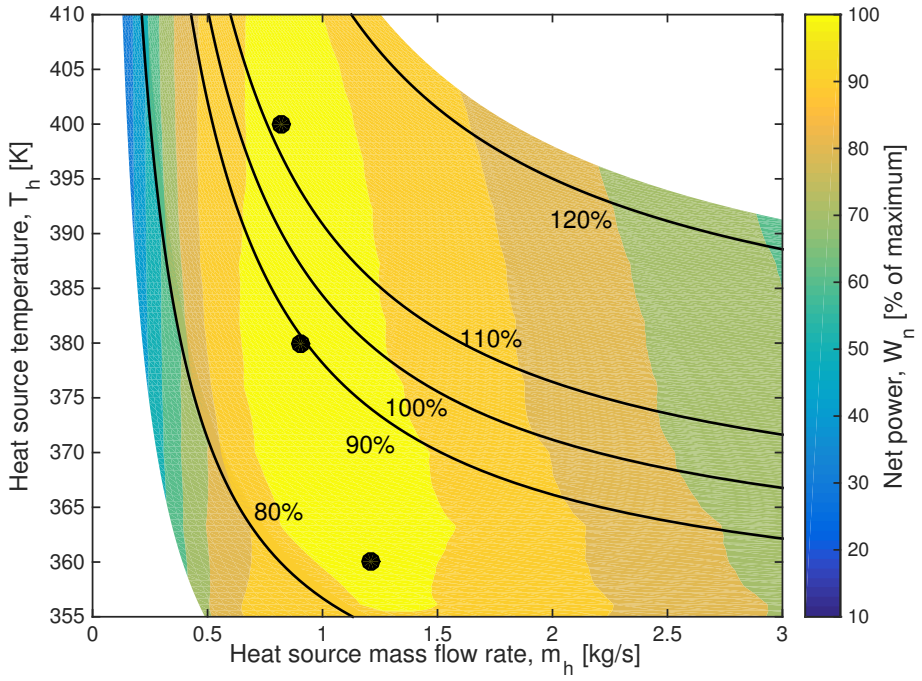

Figure 6.10: Contour plot showing the percentage of maximum power that can be obtained using the candidate turbine design operating with R245fa for a range of heat source conditions. The black lines indicate the percentage of the design reduced rotational speed, whilst the black dots correspond to the optimal points discussed in Table 6.2.

Ultimately, this figure can be used to give an indication of where it might be suitable to implement this existing turbine. For a given heat source temperature and mass flow rate the net power, as a percentage of the maximum, and the reduced rotational speed can be estimated by reading from this chart. Based on these values it is then possible to decide whether using this existing turbine design is feasible. It should be noted that this map was

obtained assuming constant values for the condensation temperature, amount of superheat and the evaporator pinch point. None the less, Figure 6.10 is an interesting result from this research, which highlights how it might be possible to use the same combination of turbine and working fluid within a range of different ORC applications, thus improving the economy of scale for these small-scale machines.

6.5 Alternative working fluids

In addition to applying the analysis to different heat source temperatures, the effect of changing the working fluid has also been investigated. The same model was ran for a range of working fluids at the same three heat source temperatures. Following from the analysis completed in Chapter 3 the same group of working fluids have been considered, namely the 15 working fluids listed in Table 3.8. For each combination of working fluid and heat source temperature the performance contour plot was obtained (i.e. Figure 6.6). This then allowed the optimal operating point, and therefore optimal heat source mass flow rate, to be obtained.

Figure 6.11 summarises the results from this analysis in terms of the optimal heat source mass flow rate and the net power produced for each working fluid. The top-right plot in Figure 6.11 summarises all of the results, with each marker representing the result obtained for a particular working fluid at the respective heat source temperature. The remaining plots expand these results, showing which working fluid each marker represents.

The most striking observation from this figure is the large spread of heat source mass flow rates that can be effectively utilised by this turbine. For example, for a heat source temperature of 400K this same turbine can effectively convert a heat source ranging from 0.52 kg s^{-1} to 1.65 kg s^{-1}, with power outputs between 7.88 kW and 30.24 kW, by simply changing the work. Furthermore, across all of the operating points shown in Figure 6.11, the location of the optimal point is consistently close to 100% of the maximum potential power, thus corresponding to turbine isentropic efficiencies close to 85%. This confirms that at the corresponding heat source conditions, the ORC is operating at an optimal pressure ratio that corresponds to the optimal head coefficient for the candidate turbine. In other words, for the same heat source conditions it would be unlikely that an alternative turbine would offer much improvement on the turbine, and cycle, performance.

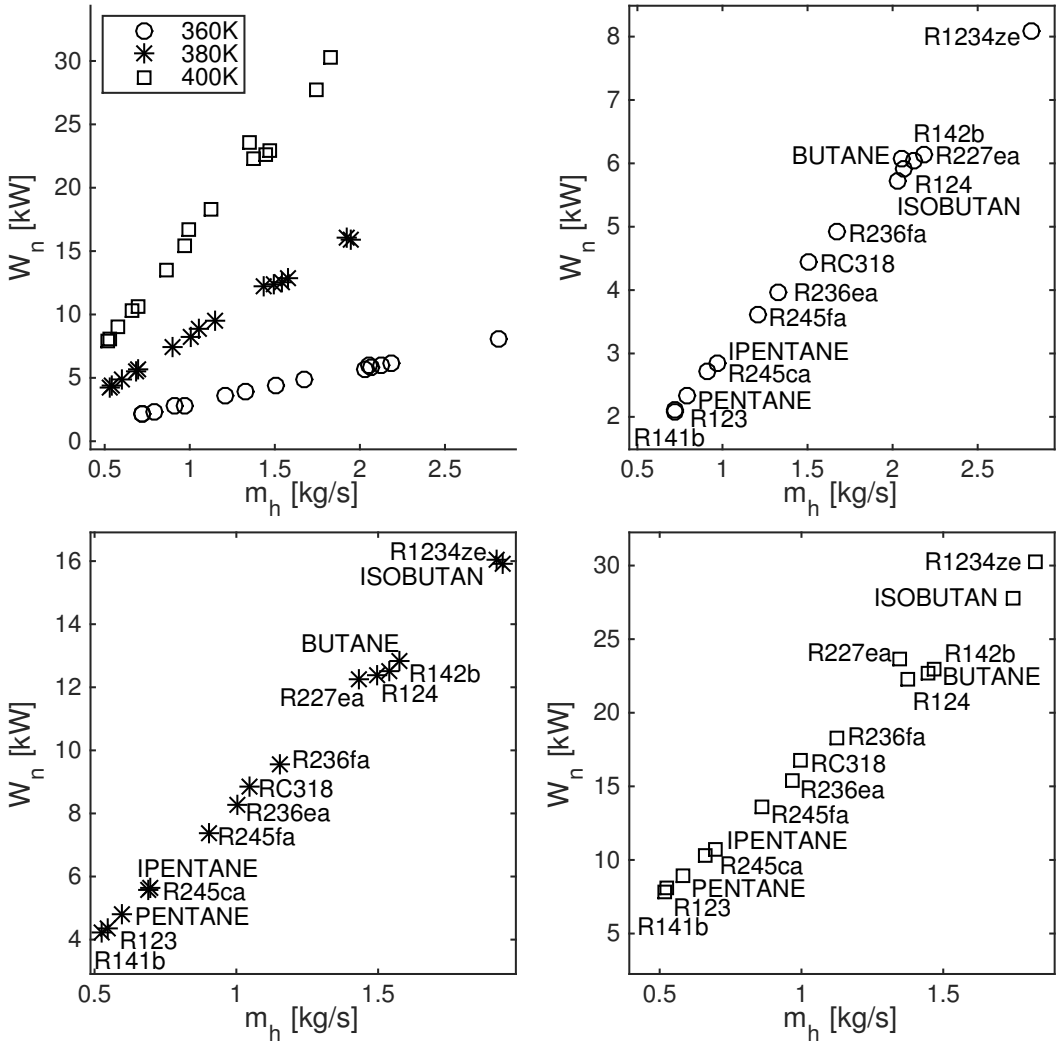

Figure 6.11: Cycle analysis results showing the heat source mass flow rates that can be accommodated by an ORC utilising the candidate turbine at each combination of heat source temperature and working fluid. Top left: summary of all results; top right: 360K; bottom left; 380K; bottom right; 400K.

To demonstrate this point further, the operating points obtained have been plotted on the non-dimensional turbine performance maps in Figure 6.12. Clearly, as the heat source temperature increases the optimal pressure ratio, and therefore head coefficient increases. Then as the head coefficient increases, the optimal reduced rotational speed is selected to ensure the optimal turbine efficiency. The reduced rotational speed remains between 81.6% and 115.7% of the original design, confirming feasible turbine operation. Figure 6.12 also further validates the selection of the heat source temperatures of 360 K and 400 K as the limits of operation for this turbine. Clearly, for lower heat source temperatures optimal operating points would shift to the left leading to lower reduced rotational speeds, and low

turbine efficiencies. A similar scenario can be seen for increasing head coefficients which correspond to higher heat source temperatures. It should also be noted that the maximum flow coefficient for all the cases considered is 2.6×10^{-6}. In Chapter 5 the choking point for this turbine was found to be at a flow coefficient of 2.7×10^{-6}. This confirms that for all operating points shown in Figure 6.11 the turbine operation remains subsonic, thus confirming it is valid to use the modified similitude theory.

The resulting cycle efficiencies are shown in Figure 6.13. As expected cycle efficiency increases with increasing heat source temperature, however there is only a small variation in cycle efficiency amongst the different working fluids. This is largely due to the optimal

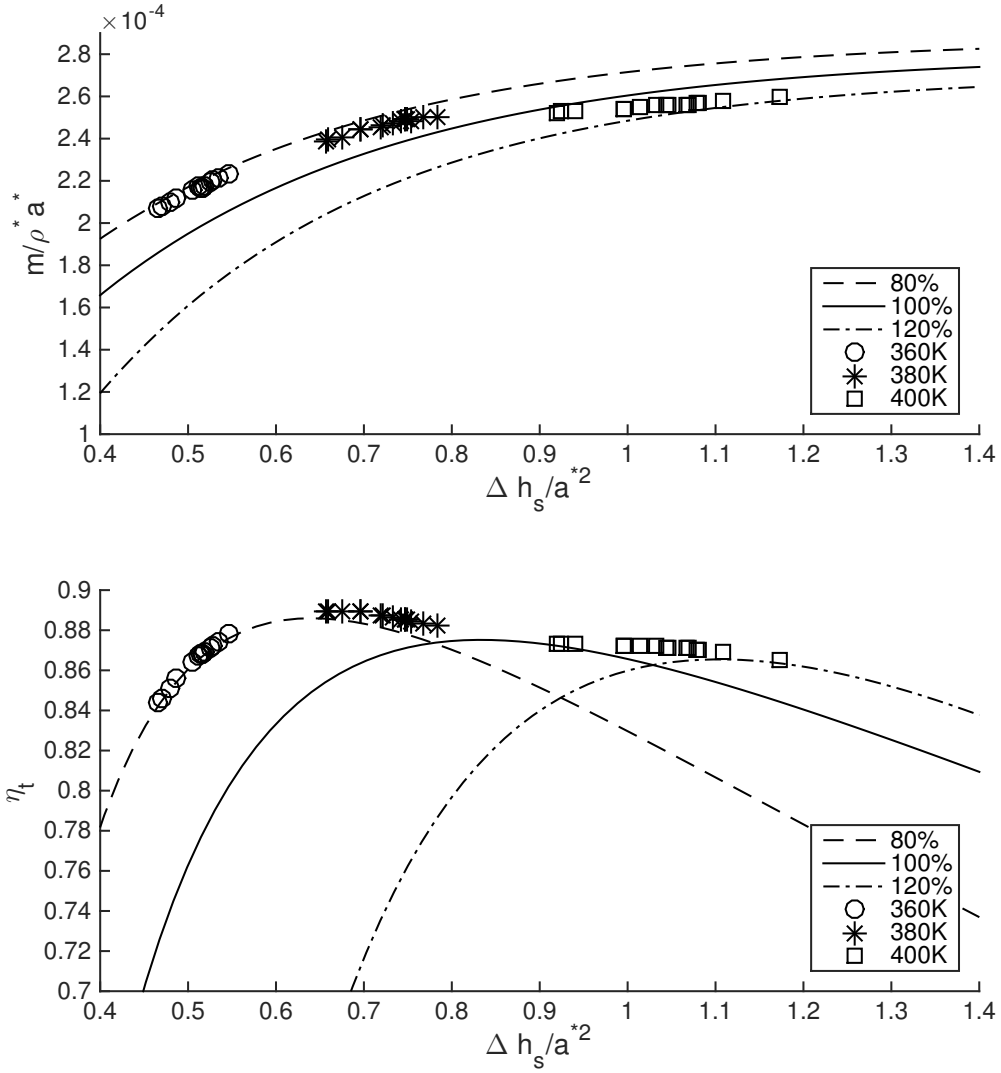

Figure 6.12: Results from each combination of heat source temperature and working fluid overlaid onto the turbine performance map.

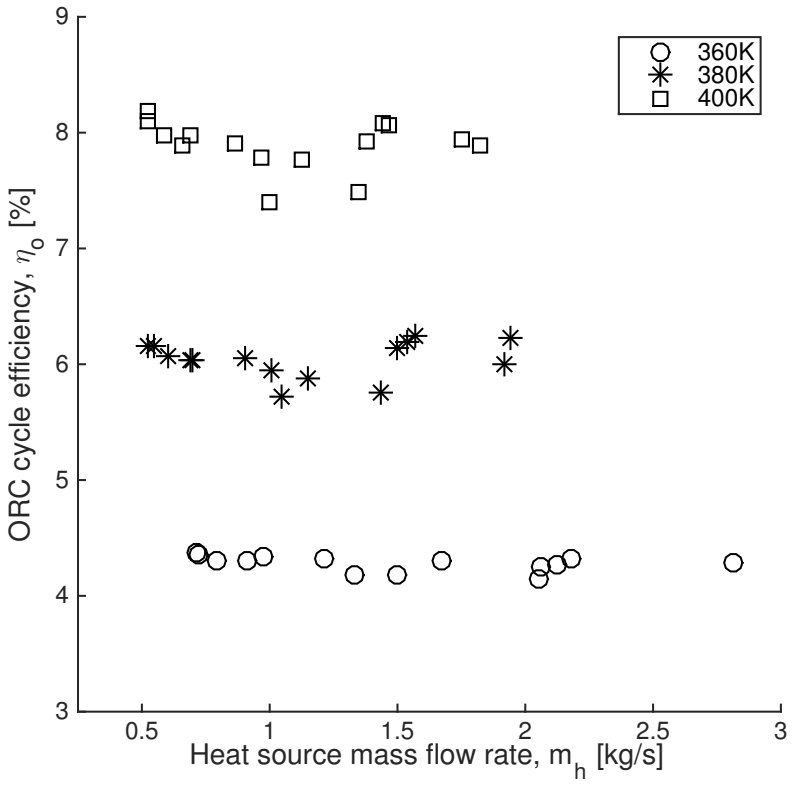

Figure 6.13: Cycle analysis results showing variation in cycle at the three different heat source temperatures.

pressure ratio for a given heat source temperature being independent of the working fluid mass flow rate. Again, it could be debated that at heat source temperatures of around 360 K, the cycle efficiency is too low to develop an economically feasible system.

Overall, Figure 6.11 suggests that the same turbine can be utilised within a number of different ORC applications by selecting a suitable working fluid to match the heat source temperature and mass flow rate. For example, for a heat source of 1.0 kg s^{-1} at 380 K, R245fa could be selected as the working fluid and the net power would be around 8 kW. However, for a heat source of around 1.75 kg s^{-1} at 400 K, R1234ze or isobutane could be selected and the net power output would be around 30 kW. Ultimately, this allows the same turbine to be produced on a relatively large scale, thus improving the economy of scale, which therefore improves the economic feasibility of implementing such a system.

It should be noted that additional mechanical factors, such as the bearing system and generator, are not taken into consideration during this study, and this may limit the feasibility of using the same turbine assembly across a wide range of power outputs. However in these instances, even if modifications to the mechanical design may be required,

the costs associated with the aerodynamic design and manufacture of the stator and rotor assembly can still be avoided. Furthermore, for the purpose of this study a wide range of working fluids were considered, which in reality may not be suitable to implement due to availability, cost and legislative restrictions. None the less, this work may be a novel contribution to the ORC community demonstrating how non-dimensional turbine maps can be implemented within cycle analysis studies, and ultimately, how it might be possible to improve the economy of scale of small-scale ORC systems.

6.6 Conclusions

This chapter has extended work on the development of a radial turbine for low temperature ORC applications by developing a modelling method that combines the turbine's performance map, with the modified similitude model and a thermodynamic analysis of the cycle. When supplied with a particular heat source temperature, this model can establish the range of heat source mass flow rates that can be effectively converted into power using an ORC that incorporates this existing turbine design. It has been shown that when provided with a particular heat source temperature and working fluid there is an optimal heat source mass flow rate that can be accommodated by this design. This fact has been used to show that the same turbine can be effectively utilised within a range of different ORC applications, simply by changing the working fluid. This is a significant result, since it allows the same turbine design to be produced on a relatively large scale, but implemented into a variety of applications, thus improving the economy of scale. The results indicate that the candidate turbine developed in Chapter 4 can be used for heat source temperatures ranging from 360K to 400K, with mass flow rates between 0.45kg/s and 2.7kg/s. The resulting power output ranges from around 2.0 kW and 30 kW, depending on the working fluid selected. These results also demonstrate the correct implementation of the modified similitude theory within a cycle analysis model, whilst the results confirm the suitability of the candidate turbine developed for low temperature ORC applications. Further work should extend this model to include off-design models of the other cycle components such as the pump and heat exchangers.

This page is left intentionally blank.

Chapter 7

Conclusions and recommendations for further work

7.1 Conclusions

The aim of this project has been to investigate and develop design and analysis modelling methods for turboexpanders implemented within small-scale low temperature ORCs. To achieve this goal, a number of project objectives were defined in Chapter 1, which are reproduced here for clarity:

- To design and implement an ORC design tool that builds on existing models within the literature by combining thermodynamic analysis, component design and multi-objective optimisation into a single ORC model.
- To design and implement a turbine design model suitable for the development of ORC specific turboexpanders. This model will be used to develop and validate a candidate turbine design for small-scale low temperature ORCs.
- To investigate the off-design behaviour of ORC turboexpanders, and to develop suitable models to predict off-design behaviour within ORC thermodynamic models.

Alongside the formation of these objectives, a comprehensive literature review was undertaken, and this acted to reinforce these objectives whilst highlighting particular aspects that should be considered in order to achieve these objectives. The deliverables from this thesis will now be evaluated against each of these objectives, and the corresponding comments made during the literature review.

7.1.1 Development of the ORC model

The literature review demonstrated the importance of thermodynamic modelling, component modelling, optimisation and working fluid selection to the design and analysis of low temperature ORCs. Building from this, an ORC model is developed in Chapter 3 that combines all of these aspects into a single model. The developed model is then applied to a particular case study. A prominent challenge in multi-objective optimisation is correctly quantifying the trade-off between system performance and complexity, where system performance is measured in terms of net work output and system complexity corresponds to larger heat exchangers and increasing turbine rotational speed. This trade-off is discussed throughout Chapter 3, but ultimately, a major outcome of this chapter, in addition to the ORC model, is the proposed novel multi-objective function that addresses this trade-off without relying on the availability of suitable economic models. Through the delivery of this ORC model it is apparent that the first objective has therefore been achieved.

To demonstrate the developed model, a case study was completed whereby the optimisation was performed for a range of different working fluids. The results demonstrate that whilst the multi-objective optimisation can determine the optimal operating condition for a particular working fluid, it is not suitable to compare different working fluids in terms of the resulting objective function value. It is therefore recommended that the ORC model and optimisation procedure is run for each working fluid, and the designer can then select the final working fluid based on their own selection criteria, such as fluid availability, cost and the fluids environmental properties. The final results from this study confirmed R245fa to be a suitable working fluid for low temperature ORCs.

7.1.2 Development of the turbine design model

Moving on from thermodynamic analysis, the second objective is delivered in Chapter 4 where a turbine design model is described that is suitable for ORC radial turbines. The literature review indicated that such a design methodology needs to incorporate a suitable equation of state to accurately predict fluid properties, and that it is important to consider the three-dimensional geometry within preliminary design. Not only have both of these aspects been addressed, but a novel method to predict the meanline relative velocity distribution within the rotor has also been included which enables more rapid design iteration before proceeding with more advanced design methods.

In Chapter 4 two design case studies were considered and two candidate turbine designs were obtained using the developed turbine design model. Within the literature review the suitability of the commercial CFD code, ANSYS CFX, for the analysis of ORC turbines was demonstrated, and therefore it was suitable to use CFX for the validation of these candidate turbine designs. This therefore allowed this thesis to demonstrate the correct implementation of a suitable equation of state into a three-dimensional RANS simulation of an ORC stator and rotor assembly, complete with clearance gap. Ultimately, the simulation results for both turbines validated the design model with only small deviations between the intended and achieved aerodynamic isentropic efficiencies being observed at the design point. Similar simulations were also used to validate the meanline model used to predict the relative velocity distribution within the rotor.

7.1.3 Investigating the off-design behaviour of ORC turbines

From the literature review it was clear that there is a need for component off-design models to be incorporated into ORC thermodynamic models, and it was also highlighted that there is currently a lack of off-design models for ORC turboexpanders. This area is particularly pertinent for small-scale systems, where it is important to improve the economy of scale by developing standardised solutions that can operate within a range of different applications. This requirement for off-design models led to the investigation of similitude theory for the performance prediction of ORC radial turbines, presented in Chapter 5. The key outcome from this chapter is a modified similitude theory that uses the estimated choked flow conditions instead of using the turbine total inlet conditions. To arrive at this modification the non-dimensional performance map for the candidate turbine developed in Chapter 4 was first constructed. This then allowed predictions made using the original similitude theory to be compared to additional CFD simulations. It was shown that the original similitude model was only suitable within a narrow range of operating conditions, and that this model did not conserve the choked mass flow rate. After developing the modified similitude theory, further CFD simulations of the ORC turbine operating with R245fa, R123 and R1234yf were conducted, and this led to the successful validation of the modified similitude theory. This modified model is accurate right up until the choking point, predicting both mass flow rate and turbine efficiency to within $\pm 2\%$.

In Chapter 6 the correct implementation of similitude theory into an ORC thermodynamic model is demonstrated, thus achieving the third and final objective of this thesis. This coupling of off-design models for the turbine with thermodynamic models allows system designers to arrive at optimal system configurations that will obtain the best performance from a particular heat source. The developed model is then used within a number of case studies where the optimal operating point is established for a range of different working fluids at three different heat source temperatures, namely 360, 380 and 400 K. From these results it is demonstrated that the developed turbine can be effectively implemented into ORC systems that utilise heat source temperatures within this range. Furthermore, this same turbine can also convert a range of different heat source mass flow rates into useful power by selecting a suitable working fluid. This is an interesting contribution to the ORC community, demonstrating how the economy of scale of these small-scale systems might be improved.

7.2 Further work

Despite completing this research project, and successfully delivering the three key objectives, a number of improvements and recommendations for future work can be made.

7.2.1 Improvements to the ORC model

The ORC model developed in Chapter 3 could be further developed in a number of ways. First and foremost, it would be advantageous to replace the existing counter-flow double pipe heat exchanger models with models for more realistic geometries such as a shell-and-tube or a plate heat exchanger model. Within this thesis the purpose of the heat exchanger models was to allow the quantification of the heat exchanger area, such that it can be included within a multi-objective optimisation. However, replacing the existing models would allow for a more accurate prediction of the required heat transfer area. The challenges to be overcome would be implementing a suitable discretisation method to account for the variation in fluid properties in these more complex geometries, and also determining the accuracy of existing empirical heat transfer correlations using experimental data.

Alongside implementing alternative heat exchanger sizing models, it is also important

to develop suitable off-design models for the heat exchangers and pump. The development of such models would complement the work conducted in Chapter 6 by allowing an investigation into how feasible it is to implement a complete system, comprised of existing components, into a range of different applications operating under different conditions, and with different working fluids.

Ultimately the ORC model was developed with a modular structure with the intention that in the future further modifications could be implemented into the existing model with relative ease.

7.2.2 Improvements to the turbine model and candidate design

Potential improvements in terms of turbine design can be categorised into improvements in the candidate radial turbine developed, and improvements in the turbine design model. In terms of the turbine design, a number of improvements to the developed turbine have already been discussed in Chapter 4. For example, the stator leading edge radius could be increased whilst the relative flow angle at the rotor inlet could be reduced to reduce incidence losses in the stator and rotor respectively. It might also be suitable to reduce the rotor blade chord length, in a bid to improve the blade loading profile. As mentioned, the aim of the work conducted in of Chapter 4 was not to obtain a fully optimised design, but of course this further optimisation would benefit both the turbine performance in addition to the overall ORC thermal efficiency.

In terms of the turbine design model, it would be useful to include more detailed methods to assess turbine performance within the preliminary design phase without requiring more advanced three-dimensional CFD simulations. Although the use of one-dimensional loss models has been avoided within this thesis, loss models do have a place in ORC radial turbine design if they can be sufficiently validated, or developed using suitable experimental data. This will make preliminary design easier, as certain designs can be rejected based on their predicted performance. The development of a suitable throughflow code may also be beneficial to assess the blade loading profile in the preliminary design phase, although ultimately, with the development of real gas CFD solvers and suitable test rigs to provide suitable experimental data for validation, it will be interesting to turn to the inverse design method to arrive at ORC turbine designs.

7.2.3 Improvements to off-design modelling of ORC turbines

Of the work conducted throughout this thesis, the modification to similitude theory to make it applicable for the performance prediction of subsonic ORC turbines is perhaps the most interesting contribution. It would therefore be very interesting to extend this analysis further. The most simple extension would be to consider a wider range of working fluids. Following this, the suitability of similitude theory to higher temperature ORCs should be investigated, thus extending the analysis to supersonic ORC turbines, and the working fluids used for these higher temperature applications. This would also require the turbine design model to be modified since supersonic stator passages would be required. Another interesting study would be to investigate if similitude theory can be used to scale an existing turbine design to larger power outputs. In Chapter 5 the rotor diameter was neglected because the same turbine was considered. However, if the scaling could be extended to include diameter this could further streamline the design process, and could further help reduce the economy of scale of small-scale ORCs.

7.2.4 Development of experimental test rigs

As a general comment, the field of small-scale ORC systems generally suffers from a lack of experimental data suitable for model validation. From Chapter 2 it is clear that a number of experimental test rigs have been developed, but few provide sufficient data for model validation. All three areas of future work discussed would benefit from suitable experimental data. This is therefore an area that future research into ORC systems should be focussed on.

Bibliography

Air Squared (2015). Scroll expanders. `http://airsquared.com/products/scroll-expanders/`. Last accessed on 17th July, 2015.

Angelino, G., Gaia, M., and Macchi, E. (1984). A review of Italian activity in the field of organic Rankine cycles. In *Proceedings of the International VDI-Seminar*, Zurich, Switzerland.

ANSYS (2013). ANSYS CFX-solver modeling guide.

ASHRAE (2009). *2009 ASHRAE Handbook - Fundamentals (SI Edition)*. American Society of Heating, Refrigerating and Air-Conditioning Engineers, Inc., Atlanta, 1st edition.

ASHRAE (2010). *2010 ASHRAE Handbook - Refrigeration (SI Edition)*. American Society of Heating, Refrigerating and Air-Conditioning Engineers, Inc., Atlanta, 1st edition.

Atkinson, M. J. (1998). *The design of efficient radial turbines for low power applications*. Phd, University of Sussex.

Atlas Copco (2012). Delivering complete ORC solutions. `http://www.atlascopco-gap.com/fileadmin/download/brochure/AC-ORC-BRO.pdf`. Last accessed on 17th July, 2015.

Aungier, R. H. (2006). *Turbine aerodynamics: Axial-flow and radial-inflow turbine design and analysis*. American Society of Mechanical Engineers, New York, 1st edition.

Badr, O., O'Callaghan, P., Hussein, M., and Probert, S. (1984). Multi-vane expanders as prime movers for low-grade energy organic Rankine-cycle engines. *Applied Energy*, 16(1):129–146.

Badr, O., Probert, S. D., and O'Callaghan, P. W. (1985). Selecting a working fluid for a Rankine-cycle engine. *Applied Energy*, 21(1):1–42.

Bao, J. and Zhao, L. (2013). A review of working fluid and expander selections for organic Rankine cycle. *Renewable and Sustainable Energy Reviews*, 24(1):325–342.

Bell, I. H., Wronski, J., Quoilin, S., and Lemort, V. (2014). Pure and pseudo-pure fluid thermophysical property evaluation and the open-source thermophysical property library coolprop. *Industrial and Engineering Chemistry Research*, 53(6):2498–2508.

BEP (2015). E-Rational - Green electricity out of low temperature waste heat. `http://e-rational.net`. Last accessed on 17th July, 2015.

Borsukiewicz-Gozdur, A. (2013). Pumping work in the organic Rankine cycle. *Applied Thermal Engineering*, 51(1):781–786.

Bracco, R., Clemente, S., Micheli, D., and Reini, M. (2013). Experimental tests and modelization of a domestic-scale ORC (Organic Rankine Cycle). *Energy*, 58(1):107–116.

Calise, F., Capuozzo, C., Carotenuto, A., and Vanoli, L. (2013). Thermoeconomic analysis and off-design performance of an organic Rankine cycle powered by medium-temperature heat sources. *Solar Energy*, 103(1):595–609.

Calnetix (2014). `http://www.calnetix.com`. Last accessed on 17th July, 2015.

Campana, F., Bianchi, M., Branchini, L., De Pascale, A., Peretto, A., Baresi, M., Fermi, A., Rossetti, N., and Vescovo, R. (2013). ORC waste heat recovery in European energy intensive industries: Energy and GHG savings. *Energy Conversion and Management*, 76(1):244–252.

Casati, E., Vitale, S., Pini, M., Persico, G., and Colonna, P. (2014). Centrifugal Turbines for Mini-ORC Power Systems. *Journal of Engineering for Gas Turbines and Power*, 136(12):11.

Casella, F., Mathijssen, T., Colonna, P., and Buijtenen, J. V. (2013). Dynamic Modeling of Organic Rankine Cycle Power Systems. *Journal of Engineering for Gas Turbines and Power*, 135(4):12.

Cengel, Y. (2008). *Introduction to thermodynamics and heat transfer*. McGraw-Hill, New York, 2nd edition.

Cengel, Y. A. and Boles, M. A. (2007). *Thermodynamics: An engineering approach*. McGraw-Hill Higher Education, New York, 6th edition.

Chen, H., Goswami, D. Y., and Stefanakos, E. K. (2010). A review of thermodynamic cycles and working fluids for the conversion of low-grade heat. *Renewable and Sustainable Energy Reviews*, 14(1):3059–3067.

Chys, M., van den Broek, M., Vanslambrouck, B., and De Paepe, M. (2012). Potential of zeotropic mixtures as working fluids in organic Rankine cycles. *Energy*, 44(1):623–632.

Clemente, S., Micheli, D., Reini, M., and Taccani, R. (2012). Energy efficiency analysis of Organic Rankine Cycles with scroll expanders for cogenerative applications. *Applied Energy*, 97(1):792–801.

Colonna, P., Casati, E., Trapp, C., Mathijssen, T., Larjola, J., Turunen-Saaresti, T., and Uusitalo, A. (2015). Organic Rankine Cycle Power Systems: from the Concept to Current Technology, Applications and an Outlook to the Future. *Journal of Engineering for Gas Turbines and Power*, 137(10):19.

Colonna, P., Gallo, M., Casati, E., and Mathijssen, T. (2013). Flexible asymmetric shock tube (FAST) set-up: Status and first experiences. In *Proceedings of the 2nd Interntional Seminar on ORC Power Systems*, Rotterdam, Netherlands.

Colonna, P., Rebay, S., Harinck, J., and Guardone, A. (2006). Real-gas effects in ORC turbine flow simulations: Influence of thermodynamic models on flow fields and performance parameters. In *European Conference on Computational Fluid Dynamics*, Delft, The Netherlands.

Costall, A., Gonzalez Hernandez, A., Newton, P., and Martinez-Botas, R. (2015). Design methodology for radial turbo expanders in mobile organic Rankine cycle applications. *Applied Energy*, In press:15.

Dai, Y., Wang, J., and Gao, L. (2009). Parametric optimization and comparative study of organic Rankine cycle (ORC) for low grade waste heat recovery. *Energy Conversion and Management*, 50(1):576–582.

Declaye, S., Quoilin, S., Guillaume, L., and Lemort, V. (2013). Experimental study on an open-drive scroll expander integrated into an ORC (Organic Rankine Cycle) system with R245fa as working fluid. *Energy*, 55(1):173–183.

Department of Energy and Climate Change (2014). The potential for recovering and using surplus heat from industry. Technical report, DECC, London, UK.

Dixon, S. (2010). *Fluid mechanics and thermodynamics of turbomachinery*. Butterworth-Heinemann, Oxford, UK, 7th edition.

Dunham, J. and Panton, J. (1973). Experiments on the design of a small axial turbine. In *Conference on Heat and Fluid Flow in Steam and Gas Turbine Plant*, pages 55–63, Coventry, UK.

Electratherm (2015). `https://electratherm.com`. Last accessed on 17th July, 2015.

Emery, J. C., Herrig, J., Erwin, J. R., and Felix, A. R. (1957). Systematic two-dimensional cascade tests of NACA 65-series compressor blades at low speeds. Technical report, NACA, Cranfield, UK.

ENEFTECH (2010). `http://www.eneftech.com`. Last accessed on 17th July, 2015.

Erbas, M. and Biyikoglu, A. (2015). Design and multi-objective optimization of organic Rankine turbine. *International Journal of Hydrogen Energy*, In Press:9.

Exergy (2014). Geothermal. `http://www.exergy-orc.com`. Last accessed on 17th July, 2015.

Fiaschi, D., Manfrida, G., and Maraschiello, F. (2012). Thermo-fluid dynamics preliminary design of turbo-expanders for ORC cycles. *Applied Energy*, 97(1):601–608.

Fiaschi, D., Manfrida, G., and Maraschiello, F. (2015). Design and performance prediction of radial ORC turboexpanders. *Applied Energy*, 138(1):517–532.

Galiana, F. J. D., Wheeler, A. P. S., and Ong, J. (2015). A study of the trailing-edge losses in organic Rankine cycle turbines. In *Proceedings of ASME Turbo Expo 2013: Turbine Technical Conference and Exposition*, Montreal, Canada.

General Electric (2014). Clean Cycle II J-Series. `https://www.ge-distributedpower.com/products/heat-recovery-solutions/clean-cycle`. Last accessed on 17th July, 2015.

Ghiaasiaan, S. M. (2007). *Two-phase flow, boiling, and condensation: In conventional and miniature systems*. Cambridge University Press, Cambridge, UK, 1st edition.

Glassman, A. J. (1972). Turbine design and application. Technical report, NASA, Washington, US.

Glassman, A. J. (1976). Computer program for design analysis of radial-inflow turbines. Technical report, NASA, Cleveland, US.

GMK (2011). `http://www.gmk.info`. Last accessed on 17th July, 2015.

Guangbin, L., Yuanyang, Z., Yunxia, L., and Liansheng, L. (2010). Simulation of the dynamic processes in a scroll expander-generator used for small-scale organic Rankine cycle system. *Proceedings of the Insitution of Mechanical Engineers Part A: Journal for Power and Energy*, 225(1):141–149.

Harinck, J., Pasquale, D., Pecnik, R., Buijtenen, J. V., and Colonna, P. (2013). Performance improvement of a radial organic Rankine cycle turbine by means of automated computational fluid dynamic design. *Proceedings of the Institution of Mechanical Engineers, Part A: Journal of Power and Energy*, 227(6):637–645.

Harinck, J., Turunen-Saaresti, T., Colonna, P., Rebay, S., and van Buijtenen, J. (2010). Computational study of a high-expansion ratio radial organic Rankine cycle turbine stator. *Journal of Engineering for Gas Turbines and Power*, 132(5):6.

He, C., Liu, C., Gao, H., Xie, H., Li, Y., Wu, S., and Xu, J. (2012). The optimal evaporation temperature and working fluids for subcritical organic Rankine cycle. *Energy*, 38(1):136–143.

Hettiarachchi, M. H., Golubovic, M., Worek, W. M., and Ikegami, Y. (2007). Optimum design criteria for an Organic Rankine cycle using low-temperature geothermal heat sources. *Energy*, 32(1):1698–1706.

Hoffren, J., Talonpoika, T., Larjola, J., and Siikonen, T. (2002). Numerical Simulation of Real-Gas Flow in a Supersonic Turbine Nozzle Ring. *Journal of Engineering for Gas Turbines and Power*, 124(4):395–403.

Hu, D., Li, S., Zheng, Y., Wang, J., and Dai, Y. (2015). Preliminary design and off-design performance analysis of an Organic Rankine Cycle for geothermal sources. *Energy Conversion and Management*, 96(1):175–187.

Hung, T. (2001). Waste heat recovery of organic Rankine cycle using dry fluids. *Energy Conversion and Management*, 42(5):539–553.

Hung, T. C., Shai, T., and Wang, S. K. (1997). A review of organic Rankine cycles (ORCs) for the recovery of low-grade waste heat. *Energy*, 22(7):661–667.

Husband, W. W. and Beyene, A. (2008). Feasibility Study of Low Grade Heat Recovery Rankine Cycle Using Ozone Neutral Refrigerant. In *Proceedings of ASME Turbo Expo 2008: Power for Land, Sea and Air*, Berlin, Germany.

Infinity Turbines (2015). `http://www.infinityturbine.com`. Last accessed on 17th July, 2015.

Inoue, N., Kaneko, A., Watanabe, H., and Uchimura, T. (2007). Development of Electric Power Generation Unit Driven by Waste Heat (Study on Working Fluids and Expansion Turbines). In *Proceedings of ASME Turbo Expo 2007: Power for Land, Sea amd Air*, page 12, Montreal, Canada.

James, F. (1994). MINUIT - Function minimization and error analysis.

Johnston, J. R. (2001). *Evaluation of Expanders for Use in a Solar-Powered Rankine Cycle Heat Engine*. Master, Ohio State University.

Kang, S. H. (2012). Design and experimental study of ORC (organic Rankine cycle) and radial turbine using R245fa working fluid. *Energy*, 41(1):514–524.

Karellas, S., Schuster, A., and Leontaritis, A.-D. (2012). Influence of supercritical ORC parameters on plate heat exchanger design. *Applied Thermal Engineering*, 33-34(1):70–76.

Klonowicz, P., Heberle, F., Preiß inger, M., and Brüggemann, D. (2014). Significance of loss correlations in performance prediction of small scale, highly loaded turbine stages working in Organic Rankine Cycles. *Energy*, 72(1):322–330.

Kofskey, M. G. and Wasserbauer, C. A. (1966). Experimental performance evaluation of a radial inflow turbine over a range of specific speeds. Technical report, NASA, Cleveland, US.

Lang, W., Colonna, P., and Almbauer, R. (2013). Assessment of Waste Heat Recovery From a Heavy-Duty Truck Engine by Means of an ORC Turbogenerator. *Journal of Engineering for Gas Turbines and Power*, 135(4):10.

Larjola, J. (1995). Electricity from industrial waste heat using high-speed organic Rankine cycle (ORC). *International Journal of Production economics*, 41(1-3):227–235.

Larsen, U., Pierobon, L., Haglind, F., and Gabrielii, C. (2013). Design and optimisation of organic Rankine cycles for waste heat recovery in marine applications using the principles of natural selection. *Energy*, 55(1):803–812.

Leibowitz, H., Smith, I. K., and Stosic, N. (2006). Cost Effective Small Scale ORC Systems for Power Recovery From Low Grade Heat Sources. In *2006 ASME International Mechanical Engineering Congress and Exposition*, Chicago, USA.

Lemmon, E. W., Huber, M. L., and McLinden, M. O. (2013). NIST standard reference database 23: Reference fluid thermodynamic and transport properties-REFPROP.

Lemort, V., Quoilin, S., Cuevas, C., and Lebrun, J. (2009). Testing and modeling a scroll expander integrated into an Organic Rankine Cycle. *Applied Thermal Engineering*, 29(14-15):3094–3102.

Li, J., Pei, G., Ji, J., Bai, X., Li, P., and Xia, L. (2014). Design of the ORC (organic Rankine cycle) condensation temperature with respect to the expander characteristics for domestic CHP (combined heat and power) applications. *Energy*, 77(1):579–590.

Li, J., Pei, G., Li, Y., Wang, D., and Ji, J. (2012). Energetic and exergetic investigation of an organic Rankine cycle at different heat source temperatures. *Energy*, 38(1):85–95.

Li, J., Pei, G., Li, Y., Wang, D., and Ji, J. (2013). Examination of the expander leaving loss in variable organic Rankine cycle operation. *Energy Conversion and Management*, 65(1):66–74.

Liu, W., Meinel, D., Wieland, C., and Spliethoff, H. (2014). Investigation of hydrofluoroolefins as potential working fluids in organic Rankine cycle for geothermal power generation. *Energy*, 67(1):106–116.

Luján, J., Serrano, J., Dolz, V., and Sánchez, J. (2012). Model of the expansion process for R245fa in an organic Rankine cycle (ORC). *Applied Thermal Engineering*, 40:248–257.

Manente, G., Toffolo, A., Lazzaretto, A., and Paci, M. (2013). An Organic Rankine Cycle off-design model for the search of the optimal control strategy. *Energy*, 58(1):97–106.

Maxxtec (2014). `http://www.maxxtec.com/en/`. Last accessed on 17th July, 2015.

McLinden, M. O., Kazakov, A. F., Steven Brown, J., and Domanski, P. A. (2014). A thermodynamic analysis of refrigerants: Possibilities and tradeoffs for Low-GWP refrigerants. *International Journal of Refrigeration*, 38(1):80–92.

Moustapha, H., Zelesky, M. F., Baines, N. C., and Japikse, D. (2003). *Axial and radial turbines*. Concepts ETI, Norwich, US.

Nguyen, V., Doherty, P., and Riffat, S. (2001). Development of a prototype low-temperature Rankine cycle electricity generation system. *Applied Thermal Engineering*, 21(2):169–181.

Nusbaum, W. J. and Kofskey, M. G. (1969). Cold performance evaluation of 4.97 inch radial-inflow turbine designed for single-shaft Brayton cycle space-power system. Technical report, NASA, Washington, USA.

ORMAT (2015). ORMAT Technologies Inc. `http://www.ormat.com`. Last accessed on 17th July, 2015.

Orosz, M., Mueller, A., and Quoilin, S. (2009). Small Scale Solar ORC system for distributed power. In *Solar Paces Conference*, Berlin, Germany.

Pan, L. and Wang, H. (2013). Improve analysis of Organic Rankine Cycle based on radial flow turbine. *Applied Thermal Engineering*, 61(2):606–615.

Papadopoulos, A. I., Stijepovic, M., and Linke, P. (2010). On the systematic design and selection of optimal working fluids for Organic Rankine Cycles. *Applied Thermal Engineering*, 30(6-7):760–769.

Pasquale, D., Ghidoni, A., and Rebay, S. (2013). Shape Optimization of an Organic Rankine Cycle Radial Turbine Nozzle. *Journal of Engineering for Gas Turbines and Power*, 135(4):13.

Pei, G., Li, J., Li, Y., Wang, D., and Ji, J. (2011). Construction and dynamic test of a small-scale organic rankine cycle. *Energy*, 36(5):3215–3223.

Persico, G., Pini, M., Dossena, V., and Gaetani, P. (2015). Aerodynamics of centrifugal turbine cascasdes. *Journal of Enginering for Gas Turbines and Power*, 137(11):11.

Peterson, R. B., Wang, H., and Herron, T. (2008). Performance of a small-scale regenerative Rankine power cycle employing a scroll expander. *Proceedings of the Institution of Mechanical Engineers Part A Journal of Power and Energy*, 222(3):271–282.

Pierobon, L., Nguyen, T. V., Larsen, U., Haglind, F., and Elmegaard, B. (2013). Multi-objective optimization of organic Rankine cycles for waste heat recovery: Application in an offshore platform. *Energy*, 58(1):538–549.

Pini, M., Persico, G., Casati, E., and Dossena, V. (2013). Preliminary Design of a Centrifugal Turbine for Organic Rankine Cycle Applications. *Journal of Engineering for Gas Turbines and Power*, 135(4):9.

Qiu, G. (2012). Selection of working fluids for micro-CHP systems with ORC. *Renewable Energy*, 48(1):565–570.

Qiu, G., Liu, H., and Riffat, S. (2011). Expanders for micro-CHP systems with organic Rankine cycle. *Applied Thermal Engineering*, 31(16):3301–3307.

Qiu, G., Shao, Y., Li, J., Liu, H., and Riffat, S. B. (2012). Experimental investigation of a biomass-fired ORC-based micro-CHP for domestic applications. *Fuel*, 96(1):374–382.

Quoilin, S., Declaye, S., Tchanche, B. F., and Lemort, V. (2011). Thermo-economic optimization of waste heat recovery Organic Rankine Cycles. *Applied Thermal Engineering*, 31(14-15):2885–2893.

Quoilin, S., Lemort, V., and Lebrun, J. (2010). Experimental study and modeling of an Organic Rankine Cycle using scroll expander. *Applied Energy*, 87(4):1260–1268.

Quoilin, S., van den Broek, M., Declaye, S., Dewallef, P., and Lemort, V. (2013). Techno-economic survey of organic Rankine cycle (ORC) systems. *Renewable and Sustainable Energy Reviews*, 22(1):168–186.

Rahbar, K., Mahmoud, S., and Al-Dadah, R. K. (2014). Mean-line modeling and CFD analysis of a miniature radial turbine for distributed power generation systems. *International Journal of Low-Carbon Technologies*, In Press.:12.

Rahbar, K., Mahmoud, S., Al-Dadah, R. K., and Moazami, N. (2015). Parametric analysis and optimization of a small-scale radial turbine for Organic Rankine Cycle. *Energy*, 83(1):696–711.

Rashidi, M. M., Beg, O. a., Parsa, a. B., and Nazari, F. (2011). Analysis and optimization of a transcritical power cycle with regenerator using artificial neural networks and genetic algorithms. *Proceedings of the Institution of Mechanical Engineers, Part A: Journal of Power and Energy*, 225(6):701–717.

Reinker, F., Hasselmann, K., aus der Wiesche, S., and Kenig, E. Y. (2015). Thermodynamics and fluid mechanics of a closed blade cascade wind tunnel for organic vapors. In *Proceedings of ASME Turbo Expo 2015: Turbine Technical Conference and Exposition*, Montreal, Canada.

Rödder, M., Neef, M., Laux, C., and Priebe, K. P. (2015). Systematic fluid selection for organic Rankine cycles (ORC) and performance analysis for a combined high and temperature low temperature cycle. In *Proceedings of ASME Turbo Expo 2015: Turbine Technical Conference and Exposition*, Montreal, Canada.

Rodgers, C. and Geiser, R. (1987). Performance of a high-efficiency radial/axial turbine. *Journal of Turbomachinery*, 109(2):151–154.

Rohlik, H. E. (1968). Analytical determination of radial inflow turbine design geometry for maximum efficiency. Technical report, NASA, Cleveland, USA.

Roy, J., Mishra, M., and Misra, A. (2010). Parametric optimization and performance ana-

lysis of a waste heat recovery system using Organic Rankine Cycle. *Energy*, 35(12):5049–5062.

Saitoh, T., Yamada, N., and Wakashima, S. (2007). Solar Rankine Cycle System Using Scroll Expander. *Journal of Environment and Engineering*, 2(4):708–719.

Saleh, B., Koglbauer, G., Wendland, M., and Fischer, J. (2007). Working fluids for low-temperature organic Rankine cycles. *Energy*, 32(7):1210–1221.

Sauret, E. and Gu, Y. (2014). Three-dimensional off-design numerical analysis of an organic Rankine cycle radial-inflow turbine. *Applied Energy*, 135(1):202–211.

Sauret, E. and Rowlands, A. S. (2011). Candidate radial-inflow turbines and high-density working fluids for geothermal power systems. *Energy*, 36(7):4460–4467.

Smith, I. K., Stosic, N., and Kovacevic, A. (2005). Screw Expanders Increase Output and Decrease the Cost of Geothermal Binary Power Plant Systems. In *Geothermal Resources Council Annual Meeting*, Reno, USA.

Spinelli, A., Pini, M., Dossena, V., Gaetani, P., and Casella, F. (2013). Design, Simulation, and Construction of a Test Rig for Organic Vapors. *Journal of Engineering for Gas Turbines and Power*, 135(4):10.

Srinivasan, K. K., Mago, P. J., and Krishnan, S. R. (2010). Analysis of exhaust waste heat recovery from a dual fuel low temperature combustion engine using an Organic Rankine Cycle. *Energy*, 35(6):2387–2399.

Stosic, N., Smith, I., and Kovacevic, A. (2003). Optimisation of screw compressors. *Applied Thermal Engineering*, 23(10):1177–1195.

Sun, J. and Li, W. (2011). Operation optimization of an organic rankine cycle (ORC) heat recovery power plant. *Applied Thermal Engineering*, 31(11-12):2032–2041.

Tchanche, B. F., Lambrinos, G., Frangoudakis, A., and Papadakis, G. (2011). Low-grade heat conversion into power using organic Rankine cycles - A review of various applications. *Renewable and Sustainable Energy Reviews*, 15(8):3963–3979.

Tchanche, B. F., Papadakis, G., Lambrinos, G., and Frangoudakis, A. (2009). Fluid selection for a low-temperature solar organic Rankine cycle. *Applied Thermal Engineering*, 29(11-12):2468–2476.

Triogen (2012). `http://www.triogen.nl`. Last accessed on 17th July, 2015.

Turboden (2013). Turboden - Organic Rankine cycle turbogenerators for clean energy production. `www.turboden.eu`. Last accessed on 30th June, 2015.

Uusitalo, A., Turunen-Saaresti, T., Honkatukia, J., Colonna, P., and Larjola, J. (2013). Siloxanes as Working Fluids for Mini-ORC Systems Based on High-Speed Turbogenerator Technology. *Journal of Engineering for Gas Turbines and Power*, 135(4):9.

Vaja, I. and Gambarotta, A. (2010a). Dynamic Model of an Organic Rankine Cycle System. Part I - Mathematical Description of Main Components. In *ECOS Vol. III Cycles & Buildings*, pages 35–42, Lausanne, Switzerland.

Vaja, I. and Gambarotta, A. (2010b). Internal Combustion Engine (ICE) bottoming with Organic Rankine Cycles (ORCs). *Energy*, 35(2):1084–1093.

Vélez, F., Segovia, J. J., Martín, M. C., Antolín, G., Chejne, F., and Quijano, A. (2012). A technical, economical and market review of organic Rankine cycles for the conversion of low-grade heat for power generation. *Renewable and Sustainable Energy Reviews*, 16(6):4175–4189.

Ventura, C. A. M., Jacobs, P. A., Rowlands, A. S., Petrie-Repar, P., and Sauret, E. (2012). Preliminary design and performance estimation of radial inflow turbines: an automated approach. *Journal of Fluids Engineering*, 134(3):13.

Wang, E., Zhang, H., Fan, B., Ouyang, M., Zhao, Y., and Mu, Q. (2011). Study of working fluid selection of organic Rankine cycle (ORC) for engine waste heat recovery. *Energy*, 36(5):3406–3418.

Wang, H., Peterson, R. B., and Herron, T. (2009). Experimental performance of a compliant scroll expander for an organic Rankine cycle. *Proceedings of the Institution of Mechanical Engineers, Part A: Journal of Power and Energy*, 223(7):863–872.

Wang, J., Yan, Z., Wang, M., Li, M., and Dai, Y. (2013a). Multi-objective optimization of an organic Rankine cycle (ORC) for low grade waste heat recovery using evolutionary algorithm. *Energy Conversion and Management*, 71(1):146–158.

Wang, X., Liu, X., and Zhang, C. (2013b). Performance Analysis of Organic Rankine Cycle With Preliminary Design of Radial Turbo Expander for Binary-Cycle Geothermal Plants. *Journal of Engineering for Gas Turbines and Power*, 135(8):8.

Wang, Z., Zhou, N., Guo, J., and Wang, X. (2012). Fluid selection and parametric optimization of organic Rankine cycle using low temperature waste heat. *Energy*, 40(1):107–115.

Watanabe, I., Ariga, I., and Mashimo, T. (1971). Effect of dimensional parameters of impellers on performance characteristics of a radial-inflow turbine. *Journal of Engineering for Gas Turbines and Power*, 93(1):22.

Watson, N. and Janota, M. S. (1982). *Turbocharging the internal combustion engine*. MacMilan, 1st edition.

Wei, D., Lu, X., Lu, Z., and Gu, J. (2007). Performance analysis and optimization of organic Rankine cycle (ORC) for waste heat recovery. *Energy Conversion and Management*, 48(4):1113–1119.

Wei, D., Lu, X., Lu, Z., and Gu, J. (2008). Dynamic modeling and simulation of an Organic Rankine Cycle (ORC) system for waste heat recovery. *Applied Thermal Engineering*, 28(10):1216–1224.

Wheeler, A. P. S. and Ong, J. (2013). The role of dense gas dynamics on organic Rankine cycle turbine performance. *Journal of Engineering for Gas Turbines and Power*, 135(10):9.

Wheeler, A. P. S. and Ong, J. (2014). A study on the three-dimensional unsteady real-gas flows within a transonic ORC turbine. In *Proceedings of the ASME Turbo Expo 2014*, Dusseldorf, Germany.

White, M. and Sayma, A. I. (2015a). System and component modelling and optimisation for an efficient 10 kWe low-temperature organic Rankine cycle utilising a radial inflow expander. *Proceedings of the Institution of Mechanical Engineers, Part A: Journal of Power and Energy*, In Press.:15.

White, M. and Sayma, A. I. (2015b). The application of similitude theory for the performance prediction of radial turbines within small-scale low-temperature organic Rankine cycles. *Journal of Engineering for Gas Turbines and Power*, 137(12):10.

White, M. and Sayma, A. I. (2015c). The impact of component performance on the overall cycle performance of small-scale low temperature organic Rankine cycles. In *9th International Conference on Compressors and their Systems*, London, UK.

White, M. and Sayma, A. I. (2015d). The one-dimensional meanline design of radial turbines for small scale low temperature organic Rankine cycles. In *Proceedings of ASME Turbo Expo 2015: Turbine Technical Conference and Exposition*, Montreal, Canada.

Whitfield, A. and Baines, N. C. (1990). *Design of Radial Turbomachines*. Longman, London, UK, 1st edition.

Wood, H. J. (1963). Current technology of radial-inflow turbines for compressible fluids. *Journal of Engineering Power*, 85(1):72–83.

Yamamoto, T., Furuhata, T., Arai, N., and Mori, K. (2001). Design and testing of the Organic Rankine Cycle. *Energy*, 26(3):239–251.

Zhang, J., Zhang, W., Hou, G., and Fang, F. (2012). Dynamic modeling and multivariable control of organic Rankine cycles in waste heat utilizing processes. *Computers & Mathematics with Applications*, 64(5):908–921.

Zhang, X., He, M., and Wang, J. (2014). A new method used to evaluate organic working fluids. *Energy*, 67(1):363–369.

Appendix A

Heat transfer and pressure drop correlations

A.1 Heat transfer correlations

The calculation of the evaporator and condenser heat transfer areas rely on the prediction of the local heat transfer coefficients using empirical correlations. The Gnielinski correlation is used for all single-phase heat transfer, whilst the Chen and Shah correlations are used for two-phase evaporation and condensation respectively. These correlations have been selected, and implemented, following the guidelines found in Ghiaasiaan (2007).

Gnielinski's Correlation

The Gnielinski correlation is the preferred correlation used for single-phase turbulent flow within tubes. The Gnielinski correlation finds the Nusselt number Nu, which can be rearranged to find the local heat transfer coefficient α.

$$\mathrm{Nu} = \frac{\left(\frac{f}{8}\right)(\mathrm{Re} - 1000)\mathrm{Pr}}{1 + 1.2\left(\frac{f}{8}\right)^{0.5}(\mathrm{Pr}^{\frac{2}{3}} - 1)} \tag{A.1}$$

$$\alpha = \frac{\mathrm{Nu}\ k}{d_\mathrm{h}} \tag{A.2}$$

Where f is the Petukhov friction factor, Re is the Reynolds number, Pr is the Prandtl number, d_h is the hydraulic diameter and k is the fluid thermal conductivity. For the correlation to be applicable $0.5 \leq \mathrm{Pr} \leq 2000$ and $3 \times 10^3 < \mathrm{Re} < 5 \times 10^6$.

The Prandtl number is the ratio of momentum to thermal diffusivity and is given as a function of the specific heat c_p, dynamic viscosity μ and k.

$$\mathrm{Pr} = \frac{c_\mathrm{p}\mu}{k} \tag{A.3}$$

The Reynolds number is the ratio of inertial to viscous forces and is given by Equation A.4 where ρ is the density and c is the fluid velocity. Considering mass continuity, the product ρc (referred to as the mass flux) can be described by the ratio of the mass flow rate and area. Therefore an alternative form of the Reynolds number is obtained.

$$\mathrm{Re} = \frac{\rho c d_\mathrm{h}}{\mu} = \frac{\dot{m} d_\mathrm{h}}{\mu A} \tag{A.4}$$

For the double-pipe heat exchanger arrangement the area and hydraulic diameter used in Equations A.2 and A.4 depends upon whether the fluid stream is in the inner pipe or the outer annular space. For flow through the inner pipe:

$$d_\mathrm{h} = d_\mathrm{i} \tag{A.5}$$

$$A = \left(\frac{\pi}{4}\right) d_\mathrm{i}^2 \tag{A.6}$$

For flow through the annular space:

$$d_\mathrm{h} = d_\mathrm{o} - (d_\mathrm{i} + 2t) \tag{A.7}$$

$$A = \left(\frac{\pi}{4}\right) (d_\mathrm{o}^2 - (d_\mathrm{i} + 2t)^2) \tag{A.8}$$

The Petukhov friction factor f is found based on the Reynolds number.

$$f = (0.790 \ln \mathrm{Re} - 1.64)^{-2} \tag{A.9}$$

All thermophysical properties used within the calculation of these non-dimensional parameters are evaluated at the bulk mean fluid temperature.

Chen's Correlation

Chen's correlation for saturated flow boiling remains one of the most successful correlations for saturated boiling. The ORC working fluid local heat transfer coefficient α_w due to

boiling is thought to be the summation of forced convection α_{fc} and nucleate boiling terms α_{nb}.

$$\alpha_{\mathrm{w}} = \alpha_{\mathrm{nb}} + \alpha_{\mathrm{fc}} \tag{A.10}$$

α_{fc} is obtained using Equations A.11 and A.12, where the 'l' subscript refers to the Reynolds and Prandtl numbers based on the saturated liquid properties. The vapour quality q is used to scale the saturated liquid Reynolds number.

$$\frac{\alpha_{\mathrm{fc}} d_{\mathrm{h}}}{k_{\mathrm{l}}} = 0.023 \mathrm{Re}^{0.8} \mathrm{Pr_l}^{0.4} F \tag{A.11}$$

$$\mathrm{Re} = \mathrm{Re_l}(1-q) \tag{A.12}$$

The term F is found using the Matinelli parameter (Equation A.14), where the subscript 'v' refers to the saturated vapour properties.

$$F = \begin{cases} 1 & \text{for } \dfrac{1}{X_{\mathrm{tt}}} < 0.1 \\ 2.35\left(0.213 + \dfrac{1}{X_{\mathrm{tt}}}\right)^{0.736} & \text{for } \dfrac{1}{X_{\mathrm{tt}}} > 0.1 \end{cases} \tag{A.13}$$

$$X_{\mathrm{tt}} = \left(\frac{\rho_{\mathrm{v}}}{\rho_{\mathrm{l}}}\right)^{0.5} \left(\frac{\mu_{\mathrm{l}}}{\mu_{\mathrm{v}}}\right)^{0.1} \left(\frac{1-q}{q}\right)^{0.9} \tag{A.14}$$

α_{nb} is found using Equation A.15, where σ is the surface tension, h_{lv} is the latent heat of vaporisation, and S is Chen's suppression factor given by Equation A.16. The temperature difference ΔT is the difference between the evaporator wall temperature and the bulk fluid temperature, whilst the pressure difference ΔP is the difference between the fluid saturation pressure that corresponds to the wall temperature and the bulk fluid pressure.

$$\alpha_{\mathrm{nb}} = 0.00122 \left[\frac{k_{\mathrm{l}}^{0.79} c_{\mathrm{p,l}}^{0.45} \rho_{\mathrm{l}}^{0.49}}{\sigma^{0.5} \mu_{\mathrm{l}}^{0.29} h_{\mathrm{lv}}^{0.24} \rho_{\mathrm{v}}^{0.24}}\right] \Delta T^{0.24} \Delta P^{0.75} S \tag{A.15}$$

$$S = \left[1 + (2.56 \times 10^{-6})(\mathrm{Re_l} F^{1.25})^{1.17}\right]^{-1} \tag{A.16}$$

Where,

$$\Delta T = T_{\text{wall}} - T$$

$$\Delta P = P_{\text{wall}} - P$$

From Equation A.15 it is clear that the wall temperature needs to be determined in order to calculate α_{w}. This can be determined by considering the heat transfer processes that exist. A simplified schematic of the double-pipe counter flow heat exchanger is shown in Figure A.1, which shows the wall temperature T_{wall}, and the mean bulk temperatures for the two fluid streams, T_{h} and T_{w}. For this configuration T_{wall} can be approximated using Equation A.17 where Q is already known from the heat source mass flow rate and change in enthalpy, and $A = 2\pi d_{\text{i}} L$.

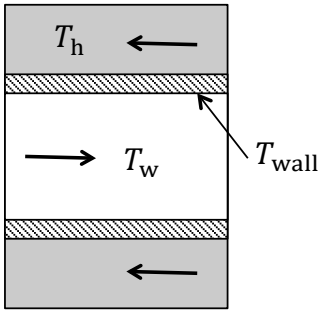

Figure A.1: Simplified schematic of the evaporator geometry.

$$Q = UA(T_{\text{h}} - T_{\text{wall}}) \tag{A.17}$$

Recalling that the overall heat transfer coefficient U is derived by considering convective and conductive heat transfer processes as thermal resistances, the heat transfer between the heat source fluid and the inner side of the wall consists of a convection term on the outer wall of the pipe, and conduction term through the pipe. Recalling Equation 3.25 from Chapter 3 the first term can be removed. The resulting expression can then be

combined with Equation A.17 to obtain an expression for T_{wall}.

$$T_{\text{wall}} = T_{\text{h}} - \frac{Q}{2\pi L}\left(\frac{1}{(d_{\text{i}}+2t)}\frac{1}{\alpha_{\text{h}}} + \frac{\ln\left(\frac{d_{\text{i}}+2t}{d_{\text{i}}}\right)}{k_{\text{wall}}}\right) \tag{A.18}$$

From this expression it is clear that T_{wall} is a function of the pipe length L, which has not yet been determined. The final determination of the evaporator length therefore requires iteration using Equations 3.23, 3.25, A.15 and A.18.

Shah's Correlation

Shah's correlation is one of the most widely used correlations for condensation of a pure saturated vapour in horizontal tubes. It is based on a two-phase multiplier concept in which the two-phase heat transfer of the working fluid α_{w} is the heat transfer coefficient for a saturated liquid α_{l}, multiplied by a function of the vapour quality q.

$$\frac{\alpha_{\text{w}}}{\alpha_{\text{l}}} = (1-q)^{0.8} + \frac{3.8q^{0.76}(1-q)^{0.04}}{\left(\frac{P}{P_{\text{cr}}}\right)^{0.38}} \tag{A.19}$$

Where P_{cr} is the fluid critical pressure, and α_{l} is obtained using the Dittus-Boelter correlation for single-phase flow. The subscript 'l' again denotes that saturated liquid properties should be used.

$$\frac{\alpha_{\text{l}} d_{\text{h}}}{k_{\text{l}}} = 0.023\text{Re}_{\text{l}}^{0.8}\text{Pr}_{\text{l}}^{0.4} \tag{A.20}$$

For the correlation to be applicable; $10.8 < \rho u < 1599$ kg m^2 s^{-1}; $\text{Re}_{\text{l}} > 350$; $0.02 < P/P_{\text{cr}} < 0.44$; $\text{Pr}_{\text{l}} > 0.5$; and $0 < q < 1$.

A.2 Pressure drop correlations

Within the ORC cycle analysis and heat exchanger sizing, there are assumed to be no pressure losses within the system. However, an additional model to estimate pressure drops within the heat exchangers is ran after all other calculations have been preformed. This has been included as a design check and becomes necessary when variable heat exchanger diameters are considered within the sizing optimisation. If pressure drops are

neglected, the optimisation will converge to a solution with very small pipe diameters since this reduces heat exchanger area, whilst increasing heat transfer due to a larger Reynolds number. However, in reality such a design would incur very large pressure drops which would have a significant effect on cycle efficiency due to large pump work requirements.

For this case an additional user input is required which is the maximum allowable pressure drop within the heat exchangers ΔP_{max}. After the heat exchanger area for each heat transfer phase has been calculated, the total pressure drop within each fluid is calculated. If each fluid experiences a pressure drop less than the specified maximum the design is considered to be a viable solution.

$$\Delta P_{\text{ph}} + \Delta P_{\text{ev}} + \Delta P_{\text{su}} < \Delta P_{\text{max}} \tag{A.21}$$

$$\Delta P_{\text{pc}} + \Delta P_{\text{co}} < \Delta P_{\text{max}} \tag{A.22}$$

$$\Delta P_{\text{h}} < \Delta P_{\text{max}} \tag{A.23}$$

$$\Delta P_{\text{c}} < \Delta P_{\text{max}} \tag{A.24}$$

Single-phase flow pressure drop

The pressure loss for a single-phase internal flow of any flow regime through a pipe of length L can be expressed by Equation A.25. This is determined by the friction factor (Equation A.9), the ratio of the pipe length to the hydraulic diameter, and $\rho_{\text{av}} c^2/2$ which is the dynamic pressure. This equation is suitable for the calculation of the pressure drop within the preheat, superheat and precooling stages for the working fluid, and for the complete heat source and heat sink fluid flows.

$$\Delta P = f \frac{L}{d_{\text{h}}} \frac{\rho_{\text{av}} c^2}{2} \tag{A.25}$$

Where;

$$\rho_{\text{av}} = \frac{\rho_{\text{in}} + \rho_{\text{out}}}{2} \tag{A.26}$$

$$c = \frac{\dot{m}}{\rho_{\text{av}} A} \tag{A.27}$$

Two-phase flow pressure drop

Within the evaporation and condensation heat transfer stages, the working fluid is two-phase and an alternative pressure drop calculation is required. There are a number of correlations within the literature, however the Müller-Steinhagen and Heck correlation has been proven to provide suitably accurate results.

$$\frac{\Delta P}{L} = \Lambda(1-q)^{1/3} + \left(\frac{\mathrm{d}P}{\mathrm{d}z}\right)_{\mathrm{zo}} q^3 \tag{A.28}$$

Where;

$$\Lambda = \left(\frac{\mathrm{d}P}{\mathrm{d}z}\right)_{\mathrm{lo}} + 2\left[\left(\frac{\mathrm{d}P}{\mathrm{d}z}\right)_{\mathrm{zo}} - \left(\frac{\mathrm{d}P}{\mathrm{d}z}\right)_{\mathrm{lo}}\right] q \tag{A.29}$$

$$\left(\frac{\mathrm{d}P}{\mathrm{d}z}\right)_{\mathrm{lo}} = f_{\mathrm{l}} \frac{2G^2}{d_{\mathrm{h}}\rho_{\mathrm{l}}} \tag{A.30}$$

$$\left(\frac{\mathrm{d}P}{\mathrm{d}z}\right)_{\mathrm{zo}} = f_{\mathrm{v}} \frac{2G^2}{d_{\mathrm{h}}\rho_{\mathrm{v}}} \tag{A.31}$$

$$f = \frac{0.079}{\mathrm{Re}^{0.25}} \tag{A.32}$$

$$\mathrm{Re} = \frac{G d_{\mathrm{h}}}{\mu} \tag{A.33}$$

$$G = \rho c = \frac{\dot{m}}{A} \tag{A.34}$$

The friction factors for the liquid and vapour phases are found by calculating the Reynolds number using the liquid and vapour viscosity of the fluid respectively.

This page is left intentionally blank.

Appendix B

Turbine three-dimensional design

B.1 Construction of the rotor

The three-dimensional construction of the rotor requires the definition of the meridional profile curves, rotor camberline and the blade thickness distributions on the hub and shroud profiles. As discussed previously, the approach adopted combines aspects from both Atkinson (1998) and Aungier (2006).

Meridional profile curves

The meridional profile of the rotor is defined on a two-dimensional plane with axial distance z along the x-axis and radius r along the y-axis. The hub and shroud profile curves are defined on this plane, and connect the rotor inlet and rotor outlet together. These profile curves are summarised in Figure B.1. The design program follows Aungier (2006) by using a circular arc and a straight section to construct the hub profile, denoted $r_{\mathrm{h}}(z)$, where the radius of the circular arc is set to the smallest value of the two distances, L or $(r_4 - r_{5\mathrm{h}})$. The shroud profile is determined using the power law given by Equation B.1, where the power factor n can be varied by the designer allowing direct control over the passage area distribution. Equation B.1 is valid within the range $0 \leq z \leq (L - b_4)$, where $z = 0$ is taken at the rotor outlet, as suggested in Figure B.1.

$$r_s(z) = r_{5\mathrm{t}} + (r_4 - r_{5\mathrm{t}}) \left(\frac{z}{L - b_4} \right)^n \tag{B.1}$$

At any axial distance z, the lengths of the hub and shroud profile curves from the rotor

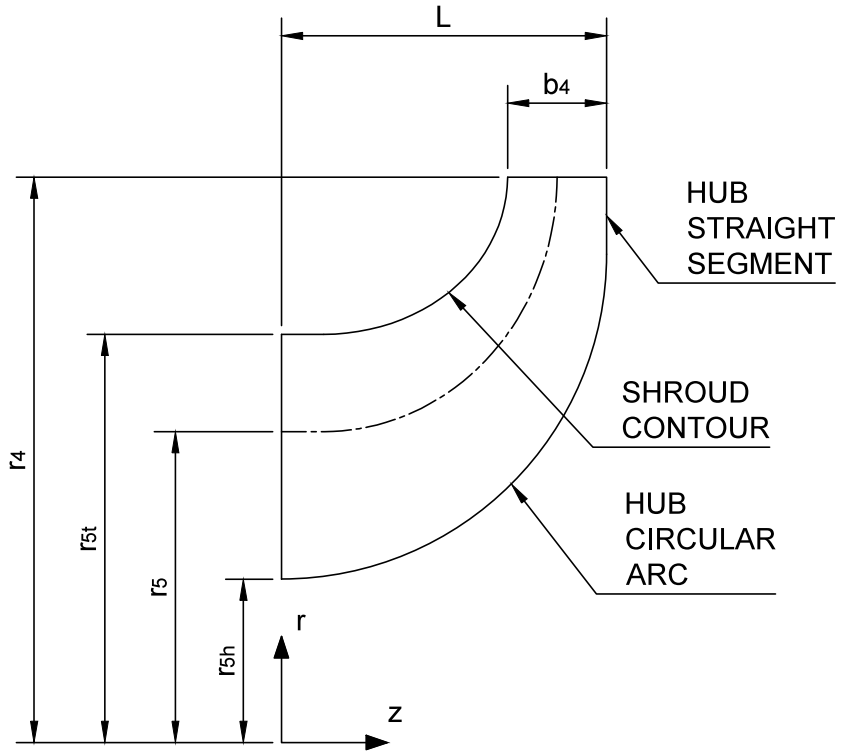

Figure B.1: Schematic of the hub and shroud meridional profiles.

outlet to that axial location, are denoted as the meridional distributions $M_{\mathrm{h}}(z)$ and $M_{\mathrm{s}}(z)$. These values are obtained through the numerical integration of Equation B.2 along the hub and shroud profile curves respectively.

$$dM = \sqrt{dr^2 + dz^2} \tag{B.2}$$

Rotor camberline

A camberline describes the variation in the blade polar angle θ along a meridional path M. For a generalised rotor design, two camberline functions can be defined which describe the polar angle variation along the hub and shroud meridional paths respectively. However, for structural considerations radial turbine blades are typically assumed to be radially fibered, which means that at any axial distance along the blade the polar angle remains constant for any radius. This simplifies the camberline construction since the camberline only needs to be defined on one profile curve. The convention is to define this along the shroud profile.

Aungier (2006) suggests a fourth order polynomial to describe the shroud polar angle distribution θ_s as a function of the shroud meridional distance M_s (Equation B.3). This function is defined as a function of the meridional path length instead of the axial length z. However, since M_s is a function z_s, the conversion from $\theta_s(M_s)$ to $\theta_s(z_s)$ is simple. The parameter $M_{s,max}$ is the total meridional path length of the shroud profile.

$$\theta_s(M_s) = a_1 M_s + a_2 M_s^3 + a_3 M_s^4 \tag{B.3}$$

Where,

$$a_1 = \frac{\tan \beta_{5t}}{r_{5t}}$$
$$a_2 = \frac{-a_1}{M_{s,max}}$$
$$a_3 = \frac{-a_2}{2M_{s,max}}$$
$$M_{s,max} = \max(M_s)$$

The variation in the shroud blade angle $\beta_s(M_s)$ is given by differentiating Equation B.3 with respect to M_s.

$$\frac{\tan \beta_s(M_s)}{r_s(M_s)} = \frac{d\theta_s}{dM_s} = a_1 + 3a_2 M_s^2 + 4a_3 M_s^3 \tag{B.4}$$

One disadvantage of Equation B.3 is that it allows no control over the amount of blade overlap. As an alternative Atkinson (1998) considers a second order polynomial which uses an input value for the blade overlap angle α_{bo}. This fomulation determines the variation in the product $r_s\theta_s$ as a function of the shroud axial distance z_s (Equation B.5).

$$r_s\theta_s(z_s) = a_1 + a_2 z_s + a_3 z_s^2 \tag{B.5}$$

Where,

$$a_1 = r_{5t}\left(\alpha_{bo} + \frac{360}{Z_R}\right)$$
$$a_2 = -\tan \beta_{5t}$$
$$a_3 = \frac{a_2^2}{4a_1}$$

The variation in the rotor shroud blade angle $\beta_s(z_s)$ is given by differentiating Equation B.5 with respect to z_s.

$$\tan\beta_s(z_s) = \frac{d(r_s\theta_s)}{dz_s} = a_1 + 2a_2 z_s \tag{B.6}$$

With the camberline defined using either Equation B.3 or B.5, the hub blade angle distribution $\beta_h(z_h)$ can easily be obtained. Recalling that for a radially fibered turbine blade the ratio $\tan\beta/r$ remains constant for all radii at any given value of z, $\beta_h(z_h)$ is given by Equation B.7. Since the shroud is only defined between $0 \leq z \leq L - b_4$, $\beta_h(z_h)$ is set to zero if z_h is greater than $L - b_4$. For values below this, the shroud properties are found by inputting z_h into Equation B.1 and the corresponding camberline function (Equation B.3 or B.5).

$$\tan\beta_h(z_h) = \begin{cases} \left(\frac{\tan\beta_s(z_h)}{r_s(z_h)}\right) r_h(z_h) & \text{if } z_h < L - b_4 \\ 0 & \text{if } z_h \geq L - b_4 \end{cases} \tag{B.7}$$

Rotor blade thickness distributions

Blade thickness distributions are constructed on the hub and shroud profile curves respectively, and are defined by the manual input of thickness values at 20%, 40%, 60% and 80% of the the relevant axial distance. For the hub this distance is the full axial length of the rotor L, whilst for the shroud it is defined as $L - b_4$. The rotor blade thicknesses at the rotor inlet and rotor outlet have already been determined by the defined blade thickness ratios. The blade thickness distributions on the hub and shroud are then constructed using a cubic spline that passes through these defined points.

Geometrical construction of the rotor

With the meridional profiles, camberline and blade thicknesses defined the full rotor geometry can be constructed. At any point on the meridional profile, the two-dimensional location can be translated into the three-dimensional co-ordinate system by rotating that point around the z-axis by the corresponding camber angle. This creates a single surface which can be offset by the specified blade thickness distribution to create the pressure and suction blade surfaces. For a full description of this process refer to Aungier (2006).

B.2 Construction of the stator

The geometrical construction of the stator airfoil was shown in Figure 4.2, and consists of a thickness distribution imposed onto a parabolic-arc camberline. The implementation of which follows that presented by Aungier (2006). All of the parameters used to define this stator blade airfoil are expressed in non-dimensional form by normalising each term by the chord length c. This permits a generalised airfoil shape to be defined that can be applied to any application. The chord length is determined by the ratio S_3/c which is specified as an input to the stator design model. Therefore once stator outlet radius r_3, has been defined the airfoil can be fully dimensionalised and constructed.

Stator camberline

The stator blade airfoil is constructed using a parabolic-arc camberline, which is described by Equation B.8, where x and y are the co-ordinates, c is the chord length, and a and b are the horizontal and vertical distances from the leading edge to the location of maximum camber respectively. These parameters were defined in Figure 4.2.

$$x^2 + \frac{c-2a}{b}xy + \frac{(c-2a)^2}{4b^2}y^2 - cx - \frac{c^2-4ac}{4b}y = 0 \tag{B.8}$$

The blade angles at the leading and trailing edges are defined as χ_1 and χ_2, and are related to a, b and c through Equations B.9 and B.10 respectively. The blade angles are then related to the full blade camber angle θ by Equation B.11.

$$\tan\chi_1 = \frac{4b}{4a-c} \tag{B.9}$$

$$\tan\chi_2 = \frac{4b}{3c-4a} \tag{B.10}$$

$$\theta = \chi_1 + \chi_2 \tag{B.11}$$

Combining Equations B.8 - B.11 a relationship between b and θ is obtained. This allows the designer to directly control the blade camber angle, instead of defining b.

$$\frac{b}{c} = \frac{\sqrt{1 + (4\tan\theta)^2\left(\frac{a}{c} - \left(\frac{a}{c}\right)^2 - \frac{3}{16}\right)} - 1}{4\tan\theta} \tag{B.12}$$

Stator blade thickness distribution

The thickness distribution is constructed by an exponential function that is defined by the thicknesses at the leading and trailing edges, t_{le} and t_{te}, the maximum blade thickness t_{max}, and the horizontal distance from the leading edge to the point of maximum blade thickness, d. At any x location, the thickness t is given by the following:

$$t = t_{\text{ref}} + (t_{\text{max}} - t_{\text{ref}})\xi^e \tag{B.13}$$

$$t_{\text{ref}} = t_{\text{le}} + (t_{\text{te}} - t_{\text{le}})x \tag{B.14}$$

Where,

$$\xi = \begin{cases} x & \text{for } x \leq d \\ \dfrac{1-x}{1-d} & \text{for } x > d \end{cases} \tag{B.15}$$

$$e = \begin{cases} \dfrac{1-x}{1-\xi} & \text{for } x \leq d \\ \dfrac{x}{1-\xi} & \text{for } x > d \end{cases} \tag{B.16}$$

Stator blade setting angle

As mentioned in Section 4.4.2 an iterative process is required to determine the stator setting angle γ_3, which results in the required stator throat width. Once the stator blade airfoil is defined it can be positioned at the stator outlet radius r_3 and rotated about the trailing edge based on an initial guess for γ_3. A second blade is then constructed by rotating this first stator blade about the origin by $\theta = 2\pi/Z_{\text{N}}$. The throat width, which is the minimum distance between these two airfoils, can then be determined numerically and is denoted at o. The next guess for the stator setting angle is then given by Equation B.17, where o_{th} is the required throat width. The stator can then be reconstructed, and this process can be repeated until convergence is achieved.

$$\sin\gamma_3 \rightarrow \sin\gamma_3 \left(\frac{o}{o_{\text{th}}}\right) \tag{B.17}$$

Appendix C

Validation of turbine design model for ideal gases

C.1 Ideal gas turbine design

The thermodynamic specification for this test turbine was specified in Table 4.2. The isentropic stator efficiency was set according to the approximation recommended by Aungier (2006) (Equation 4.71). This resulted in a value of $\eta_N = 91.62\%$.

Since the purpose of this work was to validate the design methodology instead of obtaining a fully optimised turbine design, a parametric study was completed to establish the rotor one-dimensional design. The aim was to achieve a rotor geometry which should achieve reasonable performance. The parameters considered for this parametric study are listed in Table C.1, along with the minimum and maximum values, and the array size. The limits shown are all set according to recommendations made by Dixon (2010), who also derives the relationship $\alpha_4 = 90 - \beta_4/2$. Using this relationship, β_4 can be calculated based on α_4 which reduces the number of variables, thus simplifying the parametric study.

Table C.1: Air parametric study inputs.

Parameter		Minimum	Maximum	Array size
Isentropic velocity ratio	ν_{ts}	0.65	0.75	11
Rotor inlet absolute flow angle	α_4	50°	80°	8
Rotor velocity ratio	ϕ	0.7	0.9	11
Rotor outlet/inlet diameter ratio	ϵ	0.44	0.67	10
Rotor outlet hub/shroud ratio	λ	0.4	0.7	7

Table C.2: Turbomachinery inputs for the air turbine case study.

Parameter		Value
Isentropic velocity ratio	ν_{ts}	0.730
Rotor inlet absolute flow angle	α_4	71.43°
Rotor inlet relative flow angle	β_4	−37.14°
Rotor velocity ratio	ϕ	0.84
Rotor outlet/inlet diameter ratio	ϵ	0.517
Rotor outlet hub/shroud ratio	λ	0.400
Blade number	Z_{R}	12
Rotor inlet blade thickness	t_4/r_4	0.04
Rotor outlet hub blade thickness	$t_{5\text{h}}/r_4$	0.02
Rotor outlet shroud blade thickness	$t_{5\text{t}}/r_4$	0.02

For each combination of inputs shown in Table C.1 the one-dimensional rotor design was completed and the turbine geometry was recorded. The blade number and blade thickness ratios remains constant through this study. The resulting rotor geometries were screened by considering the absolute flow angle at the rotor outlet α_5, and the meridional velocity ratio ξ. It is important to ensure minimal swirl at the rotor exit ($\alpha_5 = 0°$), whilst maintaining a meridional velocity ratio close to 1 (Moustapha et al., 2003). After this screening the final set of design inputs were selected (Table C.2). The resulting turbine is summarised in Table C.3.

This design was selected because the specific speed N_{s} and specific diameter D_{s} are both within the optimal range considering for radial turbines, and correlate well to the selected isentropic total-to-static efficiency. Furthermore, both the flow coefficient and and degree of reaction are both within limits recommended by Aungier (2006). The flow through the rotor remains subsonic so shock losses will be avoided. The resulting turbine rotor is 79.08 mm in diameter with a rotational speed of 135, 587 rpm. A structural analysis of the rotor would be required to confirm the suitability of this design but this is beyond the scope of this project. However, for the purposes of validating the aerodynamic design method it was assumed that this design was adequate.

The rotor three-dimensional design was established through the manual variation of the meridional profile curves, camberline and blade thickness distributions. These were controlled using the shroud meridional curve power factor n, the axial length ratio Γ and the blade thickness spline points. The camberline was defined by Equation B.3. A manual iteration of these parameters was undertaken, coupled with the method to determine the

Table C.3: Outputs from the design program for the air turbine case study.

Parameter		Value	Units
Performance parameters			
Isentropic efficiency (tt)	η_{tt}	88.72	%
Work output	W_{t}	25.13	kW
Rotational speed	N	135,587	rpm
Specific speed	N_{s}	0.567	
Specific diameter	D_{s}	3.643	
Degree of reaction	R	0.608	
Blade loading coefficient	Ψ	0.797	
Flow coefficient	Φ	0.285	
Meridional velocity ratio	ξ	1.065	
Rotor dimensions			
Inlet radius	r_4	39.541	mm
Inlet blade height	b_4	4.360	mm
Outlet hub radius	$r_{5\mathrm{h}}$	10.730	mm
Outlet shroud radius	$r_{5\mathrm{t}}$	26.826	mm
Rotor flow angles			
Outlet absolute flow angle	α_5	0.000	°
Outlet hub relative flow angle	$\beta_{5\mathrm{h}}$	-43.611	°
Outlet shroud relative flow angle	$\beta_{5\mathrm{t}}$	-67.223	°
Rotor Mach numbers			
Inlet Mach number	Ma_4	0.771	
Outlet shroud Mach number	$\mathrm{Ma}_{5\mathrm{t}}$	0.749	

passage area distribution and predict the meanline velocity distribution. This was also combined with preliminary CFD analysis to evaluate the mass flow rate through the rotor at the design pressure ratio and rotational speed. The final geometrical inputs used to construct the 3D rotor are summarised in Table C.4, whilst Figures C.1 and C.2 show the resulting rotor geometry.

Table C.4: Rotor geometrical inputs for the air turbine case study.

Axial length ratio	Γ	1.5
Shroud profile power factor	n	4.5
Camberline function		Equation B.3

Hub		Shroud	
Location	Thickness (mm)	Location	Thickness (mm)
$0.2L$	1.00	$0.2(L-b_4)$	0.95
$0.4L$	1.20	$0.4(L-b_4)$	1.10
$0.6L$	1.40	$0.6(L-b_4)$	1.25
$0.8L$	1.60	$0.7(L-b_4)$	1.43

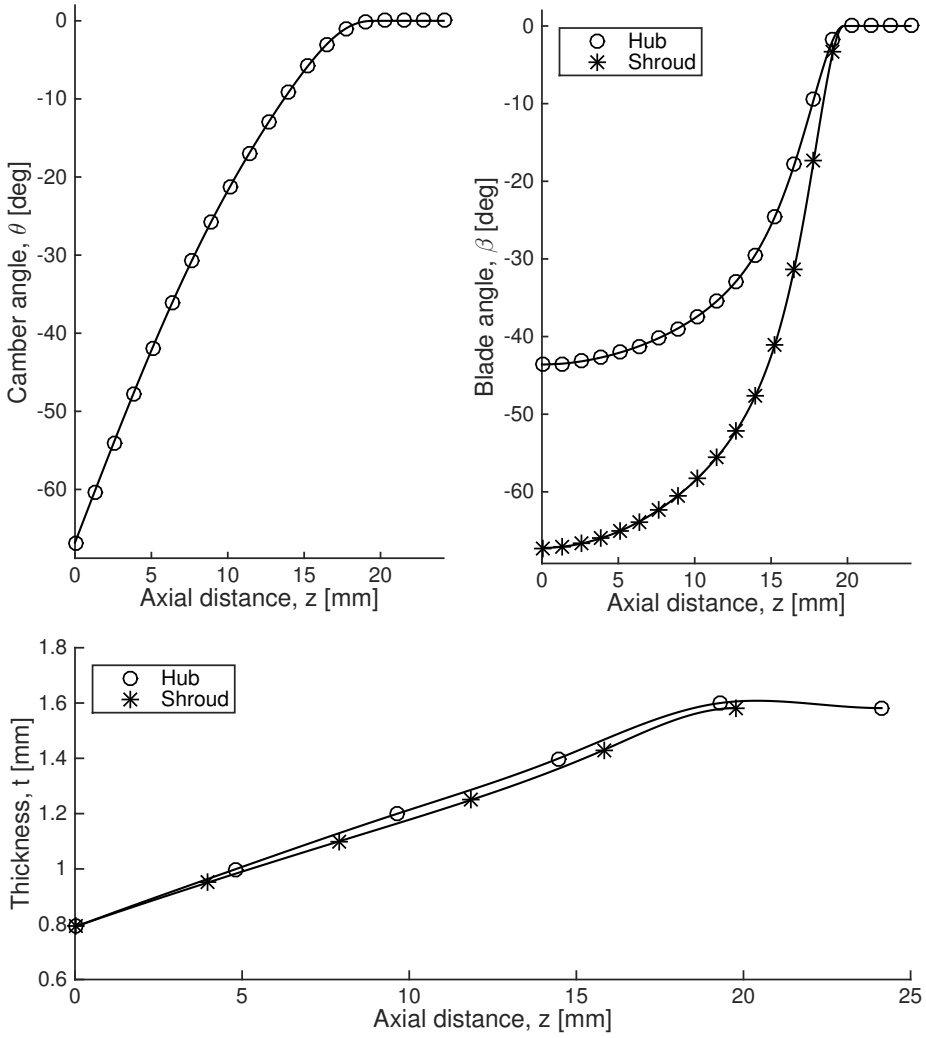

Figure C.1: Camberline distribution and thickness distributions for the air turbine.

The default inputs in Table 4.1 were used to construct the stator, and this was originally completed with an stator-rotor interspace parameter of 2. However, it was found that this resulted in a small distance between the stator outlet radius and the rotor inlet radius. Whilst this is not a physical problem, it could result in numerical issues within the CFD solver since the rotor inlet domain radius would be very close to the rotor leading edge. To avoid this the stator-rotor interspace parameter was therefore increased to 3, and the stator was reconstructed.

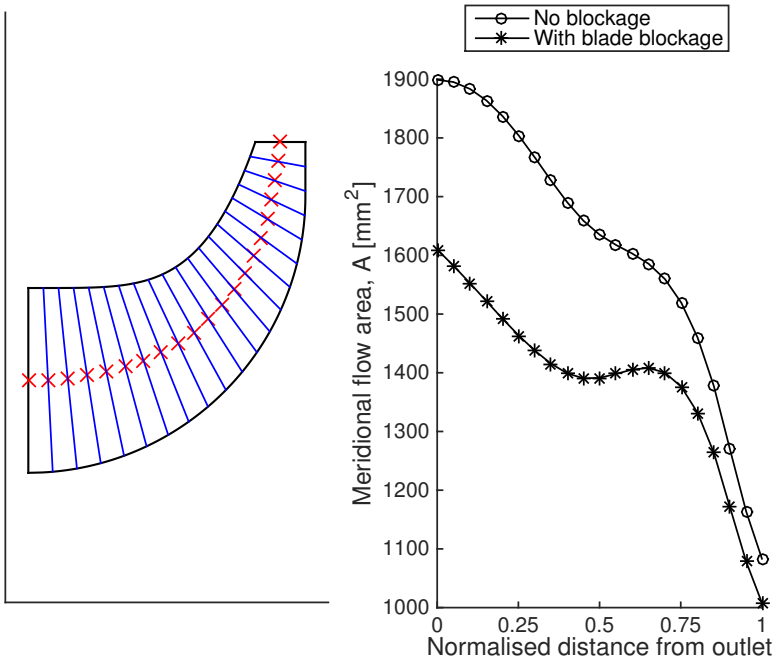

Figure C.2: Rotor quasi-normals and passage area distribution for the air turbine.

C.2 CFD validation

To validate the turbine performance at the design point a steady state simulation of the rotor, stator and clearance gap was setup using ANSYS CFX. This simulation was setup using the same setup as described for the ORC turbine (Section 4.6.2), although here the ideal gas model was used instead of generating fluid property tables using REFPROP. The ratio of specific heats was set to 1.34, corresponding to the average of the expected inlet and outlet conditions. The final, grid-independent, single passage stator and rotor meshes consisted of 3.7×10^5 and 4.7×10^5 nodes respectively.

The results from this simulation are compared to the design values in Table 4.3. To allow a suitable comparison the rotor outlet design values at the mid-span have been estimated by conserving rothalpy, and assuming a constant static pressure and meridional velocity across the rotor discharge. For the CFD results total conditions and temperatures are mass flow averaged, whilst static pressure and velocities are area averaged. The flow angles are then obtained from the area averaged meridional and tangential velocity components.

The blade loading diagrams for the stator and rotor are shown in Figures C.3 and C.4 respectively. Figure C.5 displays the contours of relative Mach number and the relative

Table C.5: Summary of the design point CFD results for the air turbine case study.

Parameter		Design	CFD	Units
Rotor leading edge				
Total temperature	T_{04}	1073.00	1071.23	K
Total pressure	P_{04}	272.15	272.37	kPa
Static temperature	T_4	975.78	960.99	K
Static pressure	P_4	186.32	178.24	kPa
Absolute velocity	c_4	472.12	495.69	m s^{-1}
Absolute flow angle	α_4	71.43	71.85	°
Rotor trailing edge				
Total temperature	T_{05}	851.32	850.66	K
Total pressure	P_{05}	99.20	101.89	kPa
Static temperature	T_5	839.78	831.99	K
Static pressure	P_5	94.10	93.36	kPa
Absolute velocity	c_5	160.06	201.33	m s^{-1}
Absolute flow angle	α_5	0.00	14.98	°
Performance summary				
Rotational speed	N	135,587	135,587	rpm
Mass flow rate	$\dot{m}$	0.100	0.104	kg s^{-1}
Pressure ratio (ts)	PR_{ts}	3.0	3.0	
Isentropic efficiency (ts)	η_{ts}	85.00	84.74	%
Isentropic efficiency (tt)	η_{tt}	88.70	91.01	%

velocity vectors that were predicted by the CFD simulation at the mid-span. Ultimately, the discussion surrounding these figures is the same as the discussion for the ORC turbine. Despite achieving a reasonable flow field through the stator and rotor there is an obvious recirculation behind the rotor leading edge due to a large incidence angle. Furthermore

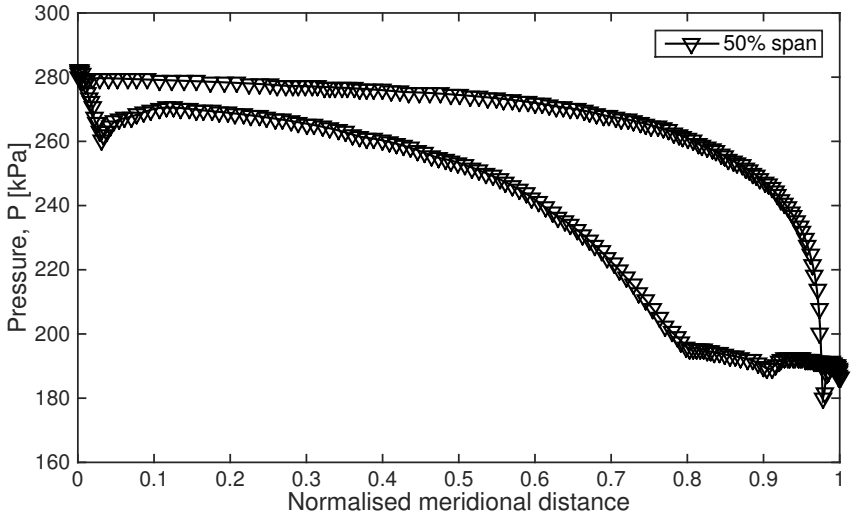

Figure C.3: Air stator blade loading at 50% span.

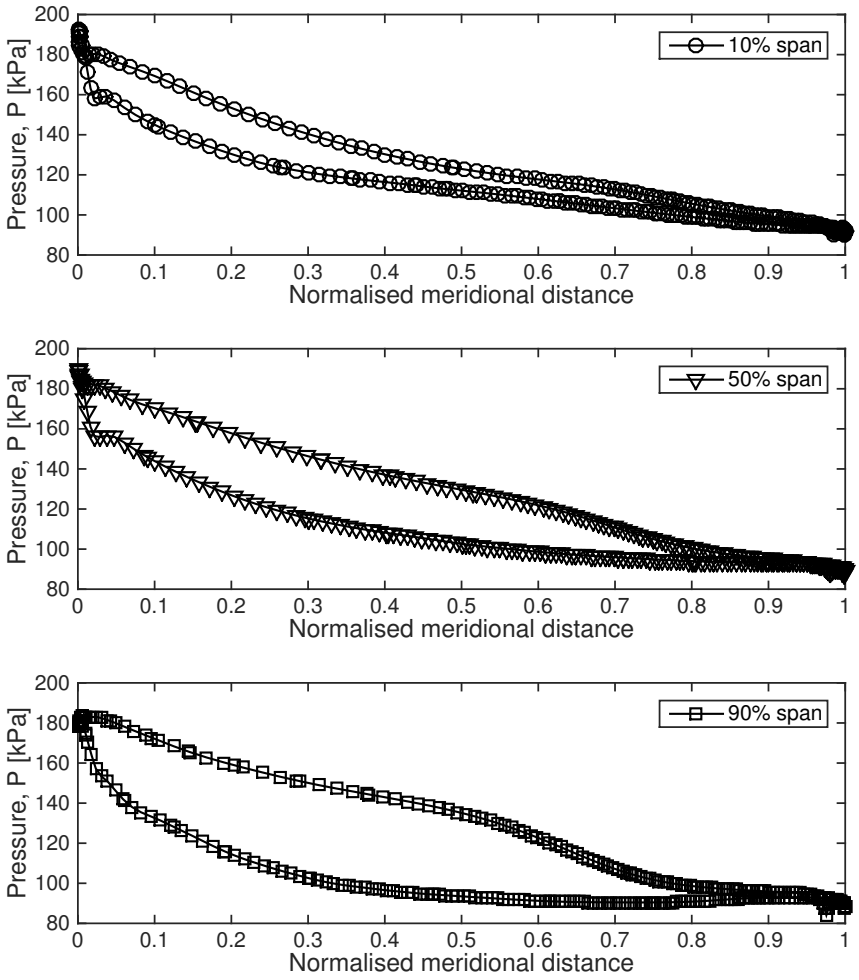

Figure C.4: Air blade loading at 10%, 50% and 90% span.

the resulting rotor blade has a large overlap and large chord length which has resulted in a relatively low blade loading, particularly towards towards the second half of the rotor passage. It should be reiterated that the purpose of this analysis was not to obtain a fully optimised design, but if further optimisation was to be completed it would be sensible to reduce this incidence angle and rotor blade chord length to further improve performance.

The CFD results were also used to determine the velocity distributions through the rotor passage to enable validation of the method to predict the meanline velocity distribution within the rotor. However, as for the ORC turbine, large discrepancies were found due to the deviation between the blade and flow angles, and therefore the CFD simulation was re-ran without including the clearance gap. Figure C.6 shows a comparison of the resulting velocity distributions for the relative and meridional velocities, whilst the blade angles and flow angles predicted by the CFD simulations are compared in Figure C.7.

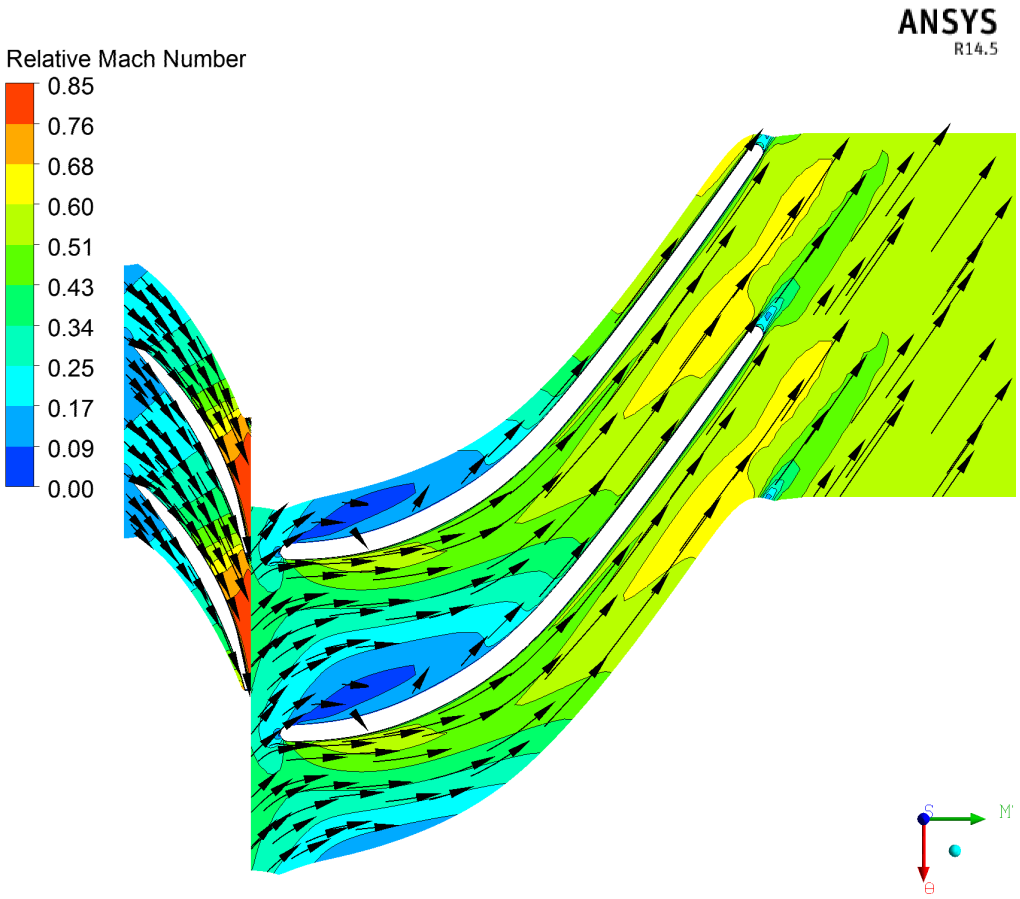

Figure C.5: Contour of relative Mach number and relative velocity vectors on the midspan of the air turbine.

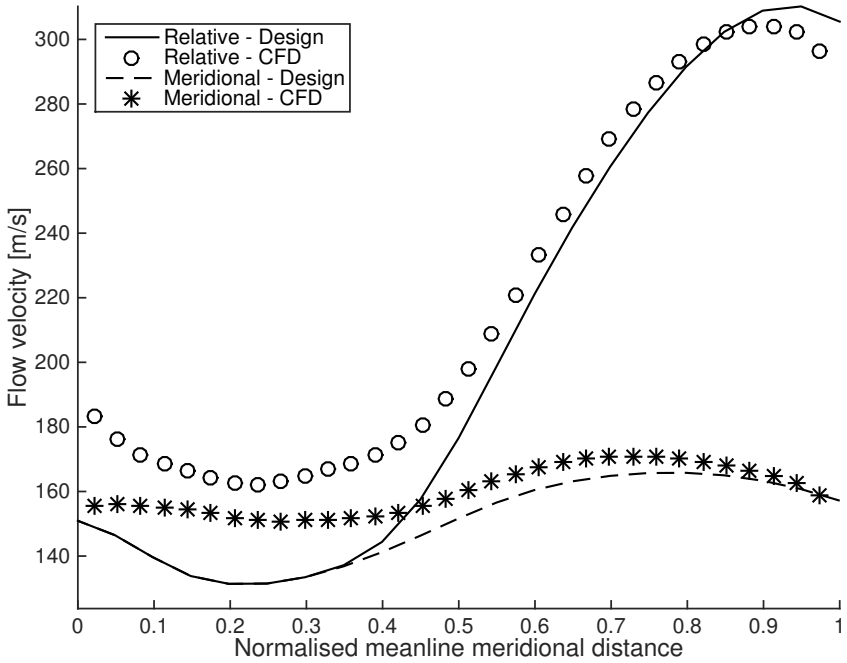

Figure C.6: Comparison between the velocity distributions predicted by the one-dimensional model and the results obtained for the no clearance simulation.

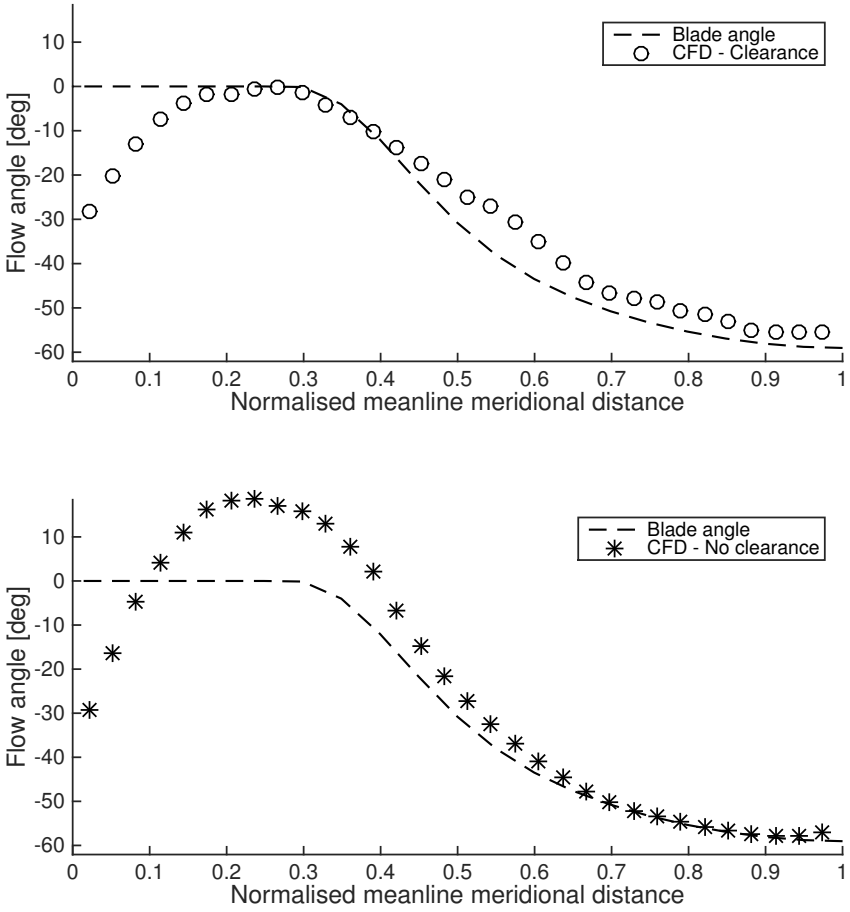

Figure C.7: Comparison between the blade angle and flow angles for the for the clearance and no clearance CFD simulations.

For the first 40% of the rotor passage there is a large discrepancy between the velocity distributions. This is attributed to the flow entering the rotor with a certain amount of incidence such that the flow and blade angles are not aligned. The consequence of this is that the relative velocity must increase as observed within the CFD results shown in Figure C.6. After 30% of the meridional path length, the blade turns, and by 40% the flow is starting to align with the blade. For the rest of the rotor passage, the no clearance CFD results agree well with the one-dimensional predictions, with both results predicting a similar distribution shape. Figure C.7 shows that the flow and blade angles are closely aligned for the second half of the rotor passage, although some deviation at the rotor discharge is observed. This is caused by the sudden expansion between the rotor throat and rotor exit. From Figure C.7 the additional deviation caused by introducing the clearance gap is clearly highlighted.

Despite its shortcomings, it is clear that the one-dimensional meanline model is suf-

ficiently accurate in evaluating the rotor passage within the preliminary design of an air turbine. This allows the designer to quickly iterate and move towards a suitable rotor three-dimensional passage design before considering more complex design methods. This therefore further validates the turbine design model for ideal gas turbines.

Appendix D

Cubic equations of state

Cubic equations of state provide an alternative method to predict fluid properties instead of using REFPROP. These equations give the pressure P as a function of the temperature T and the specific volume v of the fluid. The equations are also based on the specific gas constant of the fluid R, the critical temperature T_c, the critical pressure P_c and the acentric factor ω.

Peng-Robinson

The Peng-Robinson cubic equation of state is given by Equation D.1.

$$P = \frac{RT}{v-b} - \frac{a}{v^2+2bv-b^2} \tag{D.1}$$

Where;

$$a = a_0\left(1+n\left(1-\sqrt{\frac{T}{T_c}}\right)\right)^2 \tag{D.2}$$

$$a_0 = \frac{0.45724R^2T_c^2}{P_c} \tag{D.3}$$

$$b = \frac{0.0778RT_c}{P_c} \tag{D.4}$$

$$n = 0.37464 + 1.54226\omega - 0.26993\omega^2 \tag{D.5}$$

Redlich-Kwong-Soave

The Redlick-Kwong-Soave cubic equation of state is given by Equation D.6.

$$P = \frac{RT}{v-b} - \frac{a}{v(v+b)} \tag{D.6}$$

Where;

$$a = a_0 \left(1 + n\left(1 - \sqrt{\frac{T}{T_c}}\right)\right)^2 \tag{D.7}$$

$$a_0 = \frac{0.42747 R^2 T_c^2}{P_c} \tag{D.8}$$

$$b = \frac{0.08664 R T_c}{P_c} \tag{D.9}$$

$$n = 0.480 + 1.574\omega - 0.176\omega^2 \tag{D.10}$$

Redlich-Kwong-Aungier

The Redlick-Kwong-Aungier cubic equation of state is given by Equation D.11. This equation also requires the specific volume of the fluid at the critical point v_c.

$$P = \frac{RT}{v-b+c} - \frac{a}{v(v+b)} \tag{D.11}$$

Where;

$$a = a_0 \left(\frac{T}{T_c}\right)^{-n} \tag{D.12}$$

$$a_0 = \frac{0.42747 R^2 T_c^2}{P_c} \tag{D.13}$$

$$b = \frac{0.08664 R T_c}{P_c} \tag{D.14}$$

$$c = \frac{RT_c}{P_c + \dfrac{a_0}{v_c(v_c+b)}} + b + v_c \tag{D.15}$$

$$n = 0.4986 + 1.1735\omega + 0.4754\omega^2 \tag{D.16}$$

Determining the internal energy, enthalpy and entropy

After selecting the desired cubic equation of state it is then possible to calculate the remaining thermodynamic properties, namely the internal energy e, enthalpy h and entropy s. To do this a function to describe the variation in specific heat capacity at constant volume and at zero pressure $c_{\mathrm{v}0}$, must first be determined. This is done using by fitting a polynomial function to data obtained from REFPROP.

By then considering a reference data point ($T_{\mathrm{ref}},\ v_{\mathrm{ref}}$), the change in internal energy from this reference point to any required operating point can be determined by considering three thermodynamic processes. Firstly, the fluid is assumed to expand from the reference point to an infinite volume (i.e. zero pressure) under a constant temperature. The fluid is then assumed to heat up from the reference temperature to the known temperature of the fluid under constant volume. Then, finally, the fluid is assumed to compress from an infinite volume, to the known fluid volume under constant temperature. These three processes can be expressed mathematically as follows;

$$\begin{aligned} e - e_{\mathrm{ref}} = &\int_{v_{\mathrm{ref}}}^{\infty} \left(T \left(\frac{dP}{dT} \right)_{\mathrm{v}} - P \right) dv \Bigg|_{T=T_{\mathrm{ref}}} + \int_{T_{\mathrm{ref}}}^{T} c_{\mathrm{v}0} dT \\ &- \int_{v}^{\infty} \left(T \left(\frac{dP}{dT} \right)_{\mathrm{v}} - P \right) dv \Bigg|_{T=T} \end{aligned} \tag{D.17}$$

The change in entropy is calculated in a similar fashion;

$$\begin{aligned} s - s_{\mathrm{ref}} = &\int_{v_{\mathrm{ref}}}^{\infty} \left(\frac{dP}{dT} \right)_{\mathrm{v}} dv \Bigg|_{T=T_{\mathrm{ref}}} + \int_{T_{\mathrm{ref}}}^{T} \frac{c_{\mathrm{v}0} + R}{T} dT \\ &- R \ln \left(\frac{P}{P_{\mathrm{ref}}} \right) - \int_{v}^{\infty} \left(\frac{dP}{dT} \right)_{\mathrm{v}} dv \Bigg|_{T=T} \end{aligned} \tag{D.18}$$

Based on the change in internal energy, the change in enthalpy can easily be determined by considering the pressure and volume of the fluid at the desired operating point, and at the defined reference point.

$$h - h_{\mathrm{ref}} = (e - e_{\mathrm{ref}}) + Pv - P_{\mathrm{ref}} v_{\mathrm{ref}} \tag{D.19}$$